Adsorption, Diffusion and Reaction Studies of Hydrocarbons on Zeolite Catalysts

Sander van Donk

ISBN 90-393-3213-4

Drukkerij Ponsen & Looijen, Wageningen

Adsorption, Diffusion and Reaction Studies of Hydrocarbons on Zeolite Catalysts

Adsorptie, Diffusie en Reactie Studies van Koolwaterstoffen op Zeoliet Katalysatoren

(met een samenvatting in het Nederlands)

Proefschrift

ter verkrijging van de graad van doctor aan de Universiteit Utrecht
op gezag van de Rector Magnificus, Prof. Dr. W.H. van Gispen,
ingevolge het besluit van het College voor Promoties in het openbaar te verdedigen op
maandag 2 december 2002 des middags te 16:15 uur

door

Sander van Donk

geboren op 28 oktober 1973 te Hillegom

Promotor: Prof. Dr. Ir. K.P. de Jong
Faculteit Scheikunde, Universiteit Utrecht

Copromotor: Dr. J.H. Bitter
Faculteit Scheikunde, Universiteit Utrecht

The research described in this thesis was financially supported by the
Netherlands Organization for Scientific Research – Chemical Sciences (NWO-CW)

Talk about a dream
Try to make it real

Bruce Springsteen (Badlands)

Voor jou, lieve mam!

Promotiecommissie

Promotor:	Prof. Dr. Ir. K.P. de Jong (Universiteit Utrecht)
Copromotor:	Dr. J.H. Bitter (Universiteit Utrecht)
Leescommissie:	Prof. Dr. Ir. D.C. Koningsberger (Universiteit Utrecht) Prof. Dr. Ir. B.M. Weckhuysen (Universiteit Utrecht) Prof. Dr. L.W. Jenneskens (Universiteit Utrecht)
Overige leden:	Prof. Dr. Ir. H. van Bekkum (Technische Universiteit Delft) Prof. Dr. J.A. Lercher (Technische Universiteit München) Dr. E.T.C. Vogt (Akzo Nobel Catalysts)

Contents

1

General Introduction on Zeolites and Catalysis

- Scope of this Thesis -

Abstract

Zeolites are crystalline microporous minerals, built up of silicon, aluminum and oxygen atoms. A brief historical overview and a short general introduction on the structure and application of zeolites are given. The concept of catalysis is introduced and the use and operation of zeolites as active and selective catalysts in hydrocarbon reactions is exemplified. In view of the further contents of this thesis, short introductions on the occurrence and measurement of adsorption, diffusion and coke formation on zeolites are presented.

Zeolites

History and application

Zeolites are crystalline minerals that are broadly present in nature and have been known to mankind for almost 250 years. It was the Swedish mineralogist Axel Fredrick Crønstedt in 1756 who discovered that the natural occurring mineral, nowadays known as stilbite, lost large amounts of steam upon heating. Therefore he named the material 'zeolite' which emerges from the classical Greek, where ζεω (zeo) means 'to boil' and λιθος (lithos) means 'stone' [1]. Nowadays, zeolites are available on a large scale and in a variety of applications. The major use of zeolites is as ion exchangers in laundry detergents where they remove calcium and magnesium from water by exchanging it for sodium present in the zeolite. Furthermore, zeolites are applied as adsorbents in the purification of gas streams to remove water and volatile organic species, and in the separation of different isomers and gas-mixtures, moreover they are applied in the clean up of radioactive waste [2,3]. However, in this thesis the focus will entirely be on the application of zeolites as catalysts for the conversion of hydrocarbons.

Structure

Zeolite structures consist of silicon cations (Si^{4+}) and aluminum cations (Al^{3+}) that are surrounded by four oxygen anions (O^{2-}). Each oxygen anion connects two cations and this yields a macromolecular three-dimensional framework, with net neutral SiO_2 and negatively charged AlO_2^- tetrahedral building blocks. The negative charge arises from the difference in formal valency between the silicon- and aluminum cations, and will be located on one of the oxygen anions connected to an aluminum cation. Commonly, the negative charge is compensated by additional non-framework cations like sodium (Na^+), which is generally present after the synthesis of the zeolite. However for catalysis applications, sodium ions are mostly replaced by protons (H^+) that form a bond with the negatively charged oxygen anions of the zeolite [4]. This results in Brønsted OH acid sites, as displayed in figure 1, that have proven to be highly active in catalyzing cracking and isomerization reactions [5].

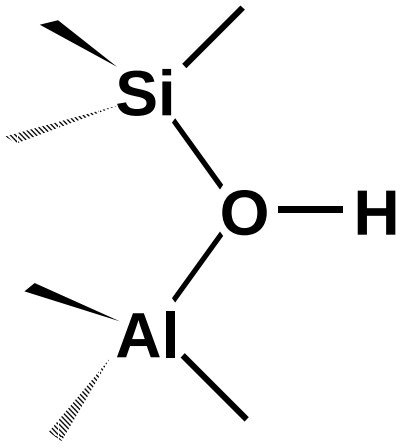

Figure 1. Brønsted acid site as present in a zeolite.

The zeolite structure consists of a pore system with channels in one, two or three dimensions and additionally inner cavities may be present. The diameters of the pores and cavities range from 3 Å to 12 Å, which coincides with the dimensions of many hydrocarbon molecules for which they are applied as adsorbents and catalysts. The exact diameter of the pore depends on the coordination and the amount of cations and anions present in the ring. In figure 2 (on the next page) the structures of four different zeolites are displayed [6]. Zeolite Y (FAU) is a three-dimensional zeolite with large cavities present in the structure that are interconnected by 12 membered ring (MR) channels, which means that there are 12 cations (Si^{4+} and Al^{3+}) and 12 O^{2-} anions present in the ring. Ferrierite (FER) is a two-dimensional zeolite with 10 MR main channels, which are interconnected via smaller 8 MR side channels. Another zeolite containing 10 MR channels is ZSM-5 (MFI). For this zeolite the straight 10 MR channels are interconnected by 10 MR zig-zag channels, which makes this zeolite three-dimensional. Mordenite (MOR) is a 12 MR zeolite with the channels running in only one dimension. The 12 MR channels contain small 8 MR side-pockets.

In this thesis the main focus will be on the zeolites mordenite and ferrierite, which will be used as catalysts for the skeletal isomerization of *n*-hexane and *n*-butene, respectively.

Catalysis

The role of a catalyst

A catalyst as defined by the Swedish chemist Jöns Jacob Berzelius in 1836, is a material that changes the rate of establishing chemical equilibrium without itself being changed or consumed [7]. Catalysis is an exceptional phenomenon in the sense that very small quantities of catalyst can convert thousands or millions of times their own weight of chemicals. Another important feature of a catalyst is the ability to direct a chemical reaction such that only the preferred product is obtained quickly and purely, which brings about economic and environmental benefits. Concisely, the role of a catalyst is to accelerate a chemical reaction that is thermodynamically feasible and to provide selectivity towards the formation of the preferred product.

The valuable role of catalysis is further emphasized by the fact that many of the products currently available to people are made with the assistance of one or more catalysts in order to minimize environmental pollution [8]. In that sense catalysis is an essential technology for the manufacturing of various chemicals, materials and food. But it is also largely applied in fuel cells, combustion devices and pollution control systems.

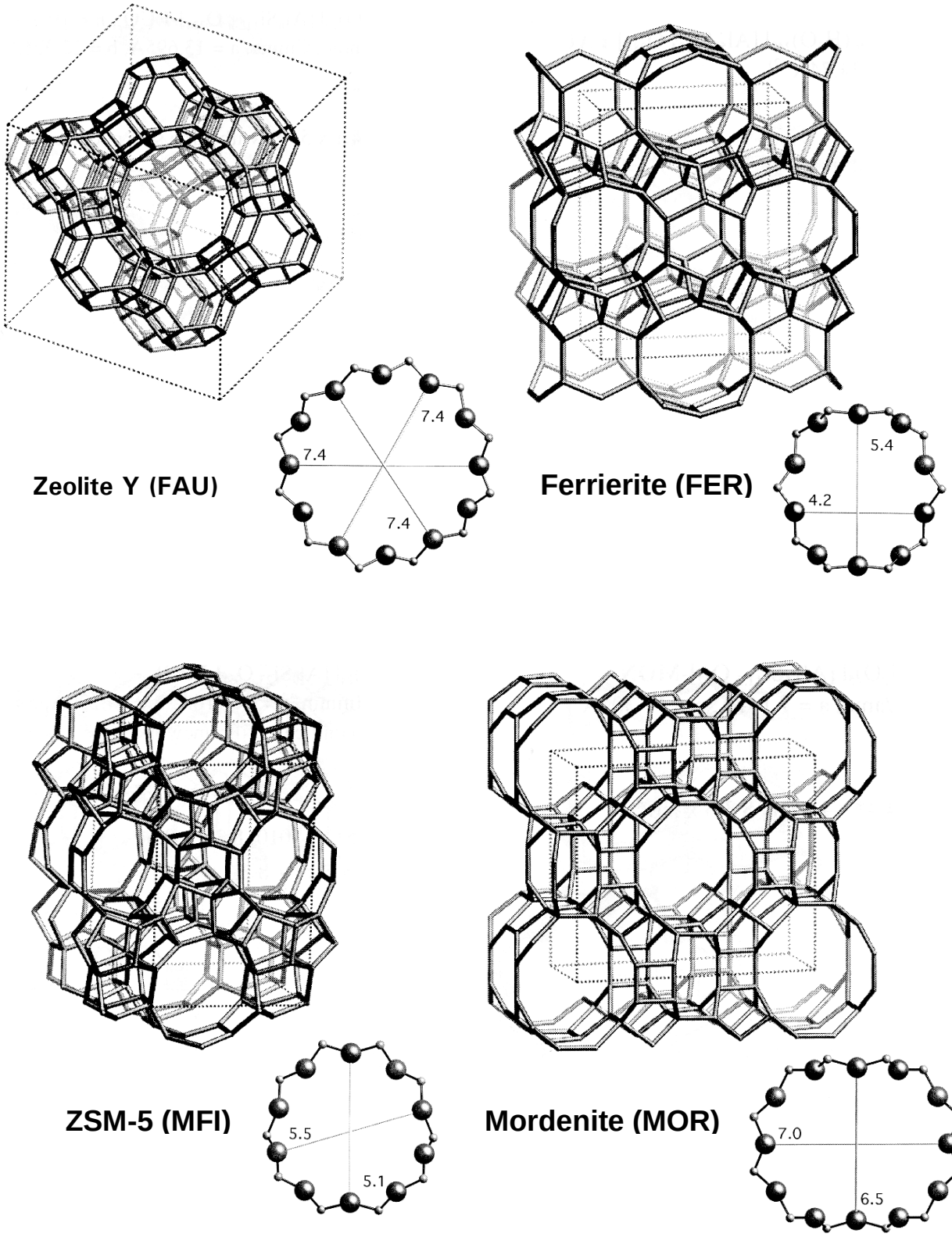

Figure 2. Framework structures of zeolite Y (FAU), ferrierite (FER), ZSM-5 (MFI) and mordenite (MOR). For each zeolite the ring structure of the main channel with its size is also visualized; the small dots represent the silicon or aluminum cation and the large ones the oxygen anion.

Zeolite catalysts

Compared to other types of catalysts, zeolites exhibit exceptional properties with respect to both activity and selectivity because of their ability to adsorb and transform molecules in their inner pore volume. An important class of reactions performed by zeolites is the acid-catalyzed reactions. For that the zeolite framework needs to contain protons, as depicted in figure 1, which give rise to a high Brønsted acidity. This is exploited in many organic reactions, including crude oil cracking, isomerization and fuel synthesis. After the introduction or deposition of metals into the framework, zeolites can also act as a matrix accommodating oxidation and/or reduction reactions. For all these types of reactions the major benefit lies in the unique microporous structure of the used zeolite. The shape and size of the particular pore system exerts a steric influence on the reaction, controlling the adsorption of reactants and desorption of products. Therefore zeolites are often said to induce shape selectivity, which makes it possible to orient hydrocarbon transformations in a direction other than it would take if no such micropores were available [9].

The prominent role of zeolites in catalysis started around 45 years ago with the introduction of the first synthetic zeolites [2]. A breakthrough herein was the industrial application of the man-made zeolites X and Y in the cracking of heavy crude oil into lighter highly valuable products, resulting in a major increase in the yield of gasoline [10,11]. Nowadays, synthetic zeolites are applied in industry catalyzing numerous reactions, mainly in the field of oil refining and basic petrochemistry [2]. For overviews on this we refer to Maxwell and Stork [12] and Blauwhoff *et al.* [13]. The two major catalytic processes in the oil industry that make use of zeolites are fluid catalytic cracking and hydrocracking of heavy oil fractions over catalysts containing zeolite Y as the main component. At present the hydroisomerization of light alkanes over mordenite catalysts plays a key-role as an environmental friendly way to enhance the octane quality of the gasoline. This is mainly induced by the rapid phase-out of lead additives and the fact that alternative octane boosting chemicals like methyl-*tert*-butyl-ether (MTBE) and ethyl-*tert*-butyl-ether (ETBE) have become environmentally disfavored because of groundwater contamination [12,14].

Scope of this thesis

Diffusion in zeolites

Diffusional behavior of hydrocarbons in zeolites has been studied extensively over the years [15-17]. As mentioned before, the micropore diameters of zeolites and the sizes of the molecules for which they are largely applied as catalysts have similar dimensions. The migration of molecular species through the zeolite occurs therefore in

close contact with the micropore walls. As a direct consequence, the order of diffusion coefficients lies beyond the molecular and Knudsen diffusion regimes that are typically displayed by porous media having much larger pore sizes. Paul B. Weisz [15] introduced the term "configurational diffusion" to cover the intracrystalline migration of molecules in zeolite micropores. The driving force for configurational diffusion is a concentration gradient over the inner zeolite crystal and its coefficients span a region of more than 10 orders of magnitude, *i.e.* 10^{-8} – 10^{-20} m^2s^{-1}. This actual number is mainly determined by the size and nature of the sorbate molecules, the zeolite pore-structure and the applied temperature [17].

In many cases the low effective diffusivity in zeolite crystals limits the reaction rate and yields rather high values for the diffusional time constant. An excellent way to overcome diffusion limitation in zeolite micropores is the generation of mesopores, *i.e.* pores with a diameter between 2.0 and 50 nm. In this way the micropores of the zeolite are effectively shortened and the accessibility of the crystals is largely enhanced, because the diffusion in the mesopores is several orders of magnitude higher than in the micropores [15]. Moreover, the creation of mesopores in zeolite crystals increases the number of pore mouths that are exposed to the reactant [18]. This is schematically depicted in figure 3.

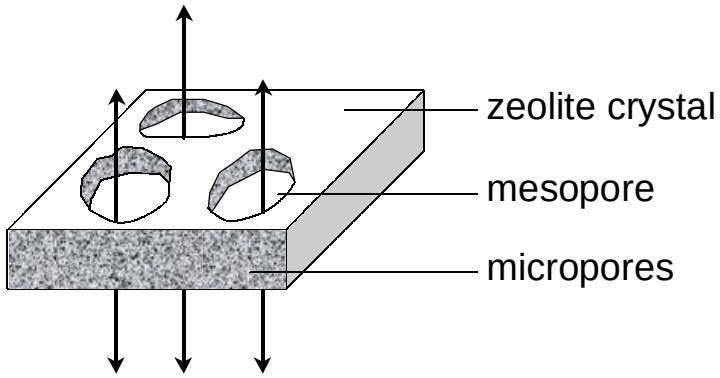

Figure 3. Schematic picture of a zeolite crystal containing micro- and mesopores.

Lately, numerous examples have become available in which the impact of mesopores on the overall reaction was illustrated. In **chapter 2** of this thesis, the different routes presented in literature for the generation and characterization of mesopores in zeolite crystals will be reviewed. The beneficial effect that the presence of mesopores brings about for cracking reactions and fine chemical synthesis over zeolite Y, and for cumene production and alkane hydroisomerization over mordenite will be discussed.

Measurement of adsorption, diffusion and reaction in zeolites

In literature, various experimental procedures are described to establish diffusion coefficients in zeolites. For an up-to-date and comprehensive overview on this we refer

to Ruthven and Post [17]. In general, the available experimental methods can be divided into macroscopic- and microscopic techniques. Gravimetric, volumetric and piezometric uptake measurements are the most simple and straightforward macroscopic techniques in which the sorption rate of molecules is detected by a microbalance or a pressure-recording device. An alternative approach has been developed by Karge and Niessen [19], who studied the uptake rate of hydrocarbons using *in situ* infrared (IR) spectroscopy to monitor the appearance of a characteristic IR-band with time. The main advantage of this approach is that by careful selection of the IR bands the sorption of more than one component can be studied.

The disadvantage with the various uptake methods as described above is that a large part of the sorbent molecules bypasses the zeolite bed. This may introduce problems with respect to the accuracy of the obtained data due to the presence of film diffusion, intra-particle gradients and/or heat effects. Moreover, because of the relatively slow response of most uptake techniques, reliable measurements are only obtained for systems with a high characteristic time for diffusion. This implies that only systems with low intracrystalline diffusion coefficients can be studied or if otherwise, samples with large zeolite crystals must be used. To overcome these problems, Eic and Ruthven [20] developed the Zero Length Column (ZLC) method. In this method the zeolite sample is equilibrated with the sorbate molecules. Subsequent purging of the sample with an inert gas desorbs the molecules and their concentration is followed chromatographically. By using very high purge rates, mass and heat transfer problems can be eliminated.

The best known microscopic method to determine diffusion in zeolites is Pulsed Field Gradient – Nuclear Magnetic Resonance (PFG-NMR) spectroscopy, as developed by Kärger and Pfeifer [21]. In this method the zeolite sample is brought at steady state conditions with sorbed molecules and excited with a standard radio frequency. Subsequently the movement of individual molecules is determined by applying two successive magnetic field gradient pulses with equal magnitude but opposite sign. If the particles have not moved in between the two pulses, the effect of both pulses is exactly cancelled out. However, if movement has occurred there is a change in the signal and from this the self-diffusion of the molecules in the zeolite can be derived. It is important to realize that the self-diffusivities as determined by PFG-NMR studies do not necessarily result in similar diffusivities as are derived from uptake and ZLC measurements. In the latter case the measurement of diffusion is only possible in the presence of a concentration gradient, while in the case of self-diffusion one looks at the mean square displacement of molecules under a constant concentration.

Most of the applied methods yield data for the diffusion of single components at low temperatures. For catalysis research, however, it would be of interest to perform uptake and/or desorption measurements in a fixed bed reactor at higher temperatures

and with multicomponent systems, *i.e.* reactants and products. Hershkowitz and Madiara [22] demonstrated that by the use of a tapered element oscillating microbalance (TEOM) adsorption and reaction could be monitored simultaneously in a quantitative way while deviations from plug-flow are minimized. Chen *et al.* [23,24] performed transient uptake measurements in a TEOM and derived numerical values for the diffusional time constant. More recently, Zhu *et al.* [25,26] showed that the TEOM can be easily used for both transient uptake and desorption experiments as well as for steady state and equilibrium adsorption measurements. In both cases diffusion coefficients could be derived, which were in good agreement with earlier results obtained using the ZLC method [27].

In **chapter 3** of this thesis the experimental background and application of the TEOM is further introduced and illustrated with two examples. In **chapter 4** the TEOM is applied to perform uptake measurements under full catalytic conditions. In this way the effect of acid leaching on the diffusion and hydroisomerization of *n*-hexane over Pt/H-mordenite has been determined. In **chapter 5**, a new approach using adsorption and diffusion of hydrocarbons is introduced to verify the extent of accessibility of the zeolite micropore volume.

Formation of carbonaceous deposits in zeolites

Hydrocarbon conversions over zeolite catalysts often suffer from the concurrent formation of carbonaceous deposits or so-called coke [28]. The extent to which carbonaceous deposits are formed depends on several factors, like the nature of reactants and products, temperature and reaction time. For zeolites, the majority of the coke is deposited inside the zeolite micropores and its formation and nature is largely determined by the pore topology and the amount, location and strength of the acid sites [29,30]. In literature, good overviews on the formation and characterization of coke on zeolites are presented by Karge [31] and Bibby *et al.* [32].

The coke molecules trapped in the zeolite micropores are not always inert and therefore may participate in the catalytic reaction [33]. In most cases this provokes a decrease in the catalytic activity and selectivity. However, occasionally the deposition of carbonaceous species induces a beneficial effect, which is the case in the skeletal isomerization of *n*-butene to isobutene over the zeolite ferrierite. For this reaction, numerous studies have indicated that the formation of carbonaceous deposits gives rise to high isobutene selectivities [34-37].

In the early nineties the Shell-group discovered the exceptional selectivity and stability of the zeolite ferrierite [38]. Over the last decade, the skeletal isomerization of butenes has received much interest, not only from an industrial point of view but also scientifically, since it is a demanding reaction to catalyze. Especially much discussion is on the exact role of the carbonaceous deposits and the nature of the active sites for

isobutene formation. In **chapter 6** of this thesis a comprehensive review on the beneficial and harmful effects of carbonaceous deposits in butene skeletal isomerization is presented.

Measurement of the amount of carbonaceous deposits

The amount of coke formed during hydrocarbon conversions can be established after the reaction, hence by using *ex situ* methods like X-ray Photoelectron Spectroscopy (XPS) [39,40], Temperature Programmed Oxidation (TPO) [41,42] and IR spectroscopy by analysis of the coke-band of the spent catalyst in [43]. Moreover, the amount of carbonaceous deposits can be monitored during reaction by the use of a conventional microbalance [36,37,44]. In such measurements, however, the reactants are not forced to flow through the catalyst bed like in a fixed bed reactor. As a consequence, the relation between the amount of coke and the catalytic action can not be fully assessed.

Hershkowitz and Madiara [22], Fung *et al.* [45] and Chen *et al.* [23,46] demonstrated that it is possible to quantitatively monitor the formation rate and amount of coke *in situ* by using a TEOM, in which all properties of a down-flow fixed bed reactor are preserved. In **chapters 7 and 8** of this thesis a catalysis set-up including a TEOM is applied to correlate the rate and amount of carbonaceous deposits formed on ferrierite with its catalytic performance in the skeletal isomerization of *n*-butene to isobutene.

Measurement of the nature and location of carbonaceous deposits

The chemical nature of carbonaceous species and its location in the zeolite crystals can be determined after or during a catalytic reaction, hence *ex situ* or *in situ*. Various spectroscopies are available to characterize the deposited coke *ex situ*, like IR [43], ultraviolet-visible (UV-VIS) [47] electron paramagnetic resonance (EPR) [48] and ^{13}C-NMR [48,49]. However, even more information on the relation between the catalytic behavior and the nature of the coke is obtained when the spectroscopic techniques can be applied *in situ*, as is the case for IR [43,50,51], UV-VIS [50], EPR [52] and ^{13}C-NMR spectroscopy [53,54]. In **chapter 7** of this thesis, *in situ* IR spectroscopy is applied to establish the nature of the carbonaceous deposits and the number of Brønsted acid sites during butene skeletal isomerization over ferrierite. Moreover, it is demonstrated that it is possible to distinguish the differently located Brønsted acid sites in the ferrierite structure during reaction, hence as a function of the amount of carbonaceous deposits. In this way also information on the location of the carbonaceous deposits in the ferrierite crystals is obtained.

Another way to establish the location of deposits and/or the availability of Brønsted acid and Lewis acid sites in a zeolite is the use of probe molecules [55]. By using d_3-acetonitrile as a probe molecule, Jolly *et al*. [56] showed in an IR study that it is

possible to distinguish between zeolite acid sites and adsorbed carbenium ions. In **chapter 8** of this thesis d_3-acetonitrile is applied as a probe molecule to determine the number and nature of the active sites on aged and highly selective ferrierite using IR spectroscopy.

To directly determine the location of the carbonaceous deposits inside the zeolite pore network, ^{129}Xe-NMR [48,57] has proven to be a highly suitable technique. However, it does not give any indication on the nature of the coke. Electron energy-loss spectroscopy performed in a scanning transmission electron microscope (STEM-EELS) has also been applied to determine the location of the coke and in particular whether it was deposited on the outside or inside of the zeolite crystal [58]. The elegance of this technique is that it also allows characterization of deposits at different locations in the crystal. In **chapter 9** of this thesis STEM-EELS measurements are performed on aged crystals of the zeolite ferrierite. Due to recent technical developments, it is demonstrated to be possible to obtain highly detailed spatial information. In this way the influence of the pore structure on the location and nature of the carbonaceous deposits in zeolite crystals can be unraveled.

References

1. A.F. Crønstedt, Akad. Handl. Stockholm 18 (1756) 120.
   [Source: E.M. Flanigen, in "Introduction to Zeolite Science and Practice" (H. van Bekkum, E.M. Flanigen, P.A. Jacobs and J.C. Jansen, Eds.) 2nd edition, Elsevier Science, Amsterdam (2001)].
2. J. Weitkamp, Solid State Ion. 131 (2001) 175.
3. E.M. Flanigen, in "Introduction to Zeolite Science and Practice" (H. van Bekkum, E.M. Flanigen, P.A. Jacobs and J.C. Jansen, Eds.) 2nd edition, Elsevier Science, Amsterdam (2001).
4. J.W. Ward, J. Catal. 9 (1967) 225.
5. W.O. Haag, R.M. Lago and P.B. Weisz, Nature 309 (1984) 589.
6. Atlas of Zeolite Framework Types (Ch. Baerlocher, W.M. Meier and D.H. Olson, Eds.) 5th edition, Elsevier, Amsterdam (2001).
7. J.J. Berzelius, Ann. Chim. Phys. 61 (1836) 146.
8. G. Centi, P. Ciambelli, S. Perathoner and P. Russo, Catal. Today 75 (2002) 3.
9. C.R. Marcilly, Top. Catal. 13 (2000) 357.
10. C.J. Plank, E.J. Rosinski and W.P. Hawthorne, Ind. Eng. Chem. Prod. Res. Dev. 3 (1964) 165.
11. A. Humphries, D.H. Harris and P. O'Connor, Stud. Surf. Sci. Catal. 76 (1993) 41.
12. I.E. Maxwell and W.H.J. Stork, in "Introduction to Zeolite Science and Practice" (H. van Bekkum, E.M. Flanigen, P.A. Jacobs and J.C. Jansen, Eds.) 2nd edition, Elsevier Science, Amsterdam (2001).
13. P.M.M. Blauwhoff, J.W. Gosselink, E.P. Kieffer, S.T. Sie and W.H.J. Stork, in "Catalysis and Zeolites Fundamentals and Applications" (J. Weitkamp and L. Puppe, Eds.) Springer-Verlag, Berlin (1999).

14. A. Rhodes, Oil & Gas J. April 5 (1999) 39.
15. P.B. Weisz, Chemtech 3 (1973) 498.
16. J. Kärger and D.M. Ruthven, "Diffusion in Zeolites and Other Microporous Materials", John Wiley and Sons, New York (1992).
17. D.M. Ruthven and M.F.M Post, in "Introduction to Zeolite Science and Practice" (H. van Bekkum, E.M. Flanigen, P.A. Jacobs and J.C. Jansen, Eds.) 2nd edition, Elsevier Science, Amsterdam (2001).
18. A. Corma, Chem. Rev. 97 (1997) 2373.
19. H.G. Karge and W. Niessen, Catal. Today 8 (1991) 451.
20. M. Eic and D.M. Ruthven, Zeolites 9 (1988) 40.
21. J. Kärger and H. Pfeifer, Zeolites 7 (1987) 90.
22. F. Hershkowitz and P.D. Madiara, Ind. Eng. Chem. Res. 32 (1993) 2969.
23. D. Chen, PhD Thesis, NTNU Trondheim (1998).
24. D. Chen, H.P. Rebo, K. Moljord and A. Holmen, Chem. Eng. Sci. 51 (1996) 2687.
25. W. Zhu, PhD Thesis, Delft University of Technology (2002).
26. W. Zhu, F. Kapteijn and J.A. Moulijn, Micropor. Mesopor. Mat. 47 (2001) 157.
27. C.L. Cavalcante and D.M. Ruthven, Ind. Eng. Chem. Res. 34 (1995) 185.
28. H.G. Karge, in "Introduction to Zeolite Science and Practice" (H. van Bekkum, E.M. Flanigen, P.A. Jacobs and J.C. Jansen, Eds.) 2nd edition, Elsevier Science, Amsterdam (2001).
29. M. Guisnet and P. Magnoux, Appl. Catal. 54 (1989) 1.
30. A. K. Gosh and R.A. Kydd, J. Catal. 100 (1986) 185.
31. H.G. Karge, in "Introduction to Zeolite Science and Practice" (H. van Bekkum, E.M. Flanigen, P.A. Jacobs and J.C. Jansen, Eds.) 2nd edition, Elsevier Science, Amsterdam (2001).
32. D.M. Bibby, R.F. Howe and G.D. McLellan, Appl. Catal. A Gen. 93 (1992) 1.
33. M. Guisnet, J. Mol. Catal. A Chem. 182-183 (2002) 367.
34. H.H. Mooiweer, K.P. de Jong, B. Kraushaar-Czarnetzki, W.H.J. Stork and B.C.H. Krutzen, Stud. Surf. Sci. Catal. 84 (1994) 2327.
35. M. Guisnet, P. Andy, N.S. Gnep, C. Travers and E. Benazzi, Stud. Surf. Sci. Catal. 105 (1997) 1365.
36. K.P. de Jong, H.H. Mooiweer, J.G. Buglass and P.K. Maarsen, Stud. Surf. Sci. Catal. 111 (1997) 127.
37. W-Q. Xu, Y-G. Yin, S.L. Suib and C-L. O' Young, J. Phys. Chem. 99 (1995) 758.
38. P. Grandvallet, K.P. de Jong, H.H. Mooiweer, A.G.T.G. Kortbeek and B. Kraushaar-Czarnetzki, Shell, Eur. Patent no. 501577 (1992).
39. B.A. Sexton, A.E. Hughes and D.M. Bibby, J. Catal. 109 (1988) 126.
40. M. Stöcker, Micropor. Mat. 6 (1996) 235.
41. V.R. Choudhary, P. Devadas P, S.D. Sansare and M. Guisnet, J. Catal. 166 (1997) 236.
42. G.N. Brasco and R.A. Comelli, Catal. Lett. 71 (2001) 111.
43. H.G. Karge and E. Boldingh, Catal. Today 3 (1988) 379.
44. J. Biswas, P.G. Gray and D. Do, Appl. Catal. 31 (1987) 249.
45. S.C. Fung, C.A. Querini, K. Liu, D.S. Rumschitzki and T.C. Ho, Stud. Surf. Sci. Catal. 88 (1994) 305.
46. D. Chen, A. Gronvold, H.P. Rebo, K. Moljord and A. Holmen, Appl. Catal. A Gen. 137 (1996) L1.

47. H. Foerster, I. Kiricsi and J. Seebode, Stud. Surf. Sci. Catal. 37 (1988) 435.
48. A.R. Pradhan, T.S. Lin, W.H. Chen, S.J. Jong, J.F. Wu, K.J. Chao and S.B. Liu, J. Catal. 184 (1999) 29.
49. C.E. Snape, B.J. McGhee, S.C. Martin and J.M. Andresen, Catal. Today 37 (1997) 285.
50. C. Paze, B. Sazak, A. Zecchina, and J. Dwyer, J. Phys. Chem. B 103 (1999) 9978.
51. A. Vimont, O. Marie, J.P. Gilson, J. Saussey, F. Thibault-Starzyk and J.C. Lavalley, Stud. Surf. Sci. Catal. 126 (1999) 147.
52. D.B. Lukyanov, Stud. Surf. Sci. Catal. 122 (1999) 299.
53. M. Hunger and T. Horvath, J. Catal. 167 (1997) 187.
54. A. Philippou, J. Dwyer, A.Ghanbari-Siahkali, C. Paze and M.W. Anderson, J. Mol. Catal. A Chem. 174 (2001) 223.
55. J.A. Lercher, C. Gründling and G. Eder-Mirth, Catal. Today 27 (1996) 353.
56. S. Jolly, J. Saussey and J.C. Lavalley, Catal. Lett. 24 (1994) 141.
57. M.A. Springuel-Huet, J.L. Bonardet, A. Gédéon and J. Fraissard, Langmuir 13 (1997) 1229.
58. P. Gallezot, C. Leclercq, M. Guisnet and P. Magnoux, J. Catal. 114 (1988) 100.

2

Generation, Characterization and Impact of Mesopores in Zeolite Catalysts

- a Review -

Abstract

Amongst the current developments in the field of hierarchical pore structures, the creation of mesopores in zeolite crystals is the most frequently employed way to combine micropores with mesopores in one material. In this review an overview is presented of the different approaches to generate and characterize mesopores in zeolite crystals and establish their impact on the catalytic action. Mesopores can be created via several routes from which steaming and acid leaching are the most frequently applied. Novel approaches using secondary carbon templates that are removed after synthesis have recently been launched. For the characterization of mesopores, nitrogen physisorption and electron microscopy are commonly used. More recently, it was shown that electron tomography, a form of three-dimensional transmission electron microscopy, is able to reveal the three-dimensional shape, size and connectivity of the mesopores. The effect of the presence of mesopores for catalysis is demonstrated for several industrially applied processes that make use of zeolite catalysts: the cracking of heavy oil fractions and synthesis of fine chemicals over zeolite Y, and the production of cumene and hydroisomerization of alkanes over mordenite. For these processes, the mesopores ensure an optimal accessibility and transport of reactants and products, while the zeolite micropores induce the preferred shape-selective properties.

Introduction

Zeolites are crystalline microporous materials that are widely applied as catalysts in industries like oil refining, basic petrochemistry and fine chemistry [1]. They exhibit unique properties with respect to both activity and selectivity. Activity is mostly determined by the zeolite Brønsted acid sites and by the active metal-phase that may be present in the zeolite. Selectivity is provided by the zeolite micropores that may range in size from 3 Å to 12 Å. The shape and size of the micropores may induce various kinds of shape selectivity as recently reviewed by Marcilly [2]. Besides the highly favorable role in providing shape selectivity, the presence of micropores in some cases limits the catalytic performance of zeolites [3]. Cause for this is the restricted molecular transport rate inside the zeolite crystal, induced by the similarity between the size of the involved hydrocarbons and the micropore diameter. Accordingly, the migration of hydrocarbons through the micropores of a zeolite occurs in close contact with the micropore walls. The values for zeolite intracrystalline diffusion coefficients are therefore several orders of magnitudes lower than those for the molecular and Knudsen diffusion regimes that are typically displayed in meso- and macroporous media [4-6]. In hydrocarbon transformations over zeolites, both the conversion-level and selectivity may be largely dependent on the time that the hydrocarbon molecules spend inside the zeolite crystal. In general one can state that only in the case that the time for diffusion is substantially lower than the time needed for the intrinsic chemical reaction, no limiting effect of diffusion on the overall conversion will be observed and the micropore area of the zeolite is optimally used.

The occurrence of diffusion limitation can be used to the benefit of the catalytic process, *e.g.* to enhance the selectivity of the reaction. This is for example illustrated in the toluene disproportionation and xylene isomerization reaction over ZSM-5, where the diffusion of the desired product *p*-xylene is much faster, *i.e.* the diffusional time constant is much lower, than that of the unwanted products *o*-xylene and *m*-xylene. The large difference in diffusivity results in an effective trapping of the unwanted isomers, which only can leave the zeolite micropores easily if they are converted to *p*-xylene. Consequently the selectivity to *p*-xylene improves with increasing zeolite crystal size [7,8] and is substantially higher than one would expect from the thermodynamic equilibrium.

Nevertheless, in most cases the effective low diffusivity in zeolite crystals limits the reaction rate and yields rather high values for the diffusional time constant. However, the enhancement of intracrystalline diffusion inside a zeolite micropore at a given temperature and pressure seems rather impossible without changing the internal pore architecture. An alternative solution to minimize diffusion limitation is the reduction of the intracrystalline diffusion pathlength. The concept of decreasing the crystal size,

i.e. reducing the intracrystalline diffusion pathlength, in order to improve the catalytic performance has been demonstrated for mordenite [9], zeolite Y [10], ZSM-5 [11,12] and zeolite beta [13]. The beneficial effect of the use of small zeolite crystals on the overall reaction rate is twofold. First, smaller crystals have shorter intracrystalline diffusion pathlengths, hence the reaction products are released more rapidly. Accordingly less secondary reactions like coke formation and cracking are observed. Second, per weight amount of zeolite, more micropore entrances are present. This induces a higher accessibility of the zeolite crystals and therefore may result in a net increase in the overall activity. Corma *et al.* [14] showed that it is even possible to delaminate a zeolite precursor and thereby synthesize small sheets of zeolite that are highly accessible.

In practice the application of small or delaminated zeolite crystals may not always be feasible. Therefore the synthesis of new zeolite materials containing extra-large micropores that enhance a better diffusional transport has recently drawn attention. In this respect, Davis *et al.* [15,16] presented two new one-dimensional zeolites and recently Corma *et al.* [17] introduced a new three-dimensional zeolite with highly accessible large cavities present. An alternative route to prepare materials with an enhanced accessibility is the combination of micropores and mesopores (diameter between 2 and 50 nm) in one material, since the diffusion in mesopores is several orders of magnitude faster than in micropores [4]. To meet this goal, some recent studies have applied 'intercrystalline' approaches in which zeolite material is assembled into ordered mesoporous structures. This can be either established by the deposition of small zeolite crystals on the walls of the mesopores [18], or by the recrystallization of the amorphous mesopore walls into zeolite material while retaining the ordered mesoporous structure [19,20]. However, a more generally applied strategy to attain materials that combine zeolite micropores with mesopores is the 'intracrystalline' approach, in which mesopores are created in the zeolite crystals. In this way the micropores of the zeolite are effectively shortened and their molecular accessibility is largely enhanced. The creation of mesopores in zeolite crystals is equivalent to increasing the external surface area of the zeolite, in this respect that a larger number of pore mouths is made accessible to the reactant [21].

Lately, numerous examples have become available in which the impact of mesopores on the overall reaction was exposed. In this review we will give a comprehensive overview of the different 'intracrystalline' approaches presented in literature for the generation and characterization of mesopores in zeolite crystals. As well, we will demonstrate the beneficial effect that the presence of mesopores comprises for some industrially applied zeolite catalyzed processes. In that context we will discuss zeolite Y catalysts, which are largely applied in cracking reactions and more recently

also in some manufacturing processes for fine chemicals; and zeolite mordenite, which is applied in the production of cumene and the hydroisomerization of alkanes.

Generation of mesopores in zeolites

Steaming

The most renowned way to create mesopores in zeolites is by hydrothermal treatment in the presence of steam. Although thermal treatments without steam can also create defects in the zeolite structure [22], the use of steam greatly enhances the mobility of aluminum and silicon species. Almost all the work on steaming of zeolites has been performed on zeolite Y [23-34], although examples of the steaming of mazzite [35], omega [36], mordenite [37], ferrierite [38] and ZSM-5 [39] are known. The steaming is usually performed at temperatures above 500°C while the zeolite is in the ammonium (or hydrogen) form. During the contacting with steam hydrolysis of Al-O-Si bonds takes place. The aluminum is finally expelled from the framework causing a vacancy (hydroxyl nest) or partial amorphization of the framework. The amorphous material is a source of mobile silicon species, which can heal the vacancies in the framework left by the expelled aluminum atoms. Thus part of the vacancies are filled while others grow to form mesopores, as depicted in figure 1 [40]. In regions of high

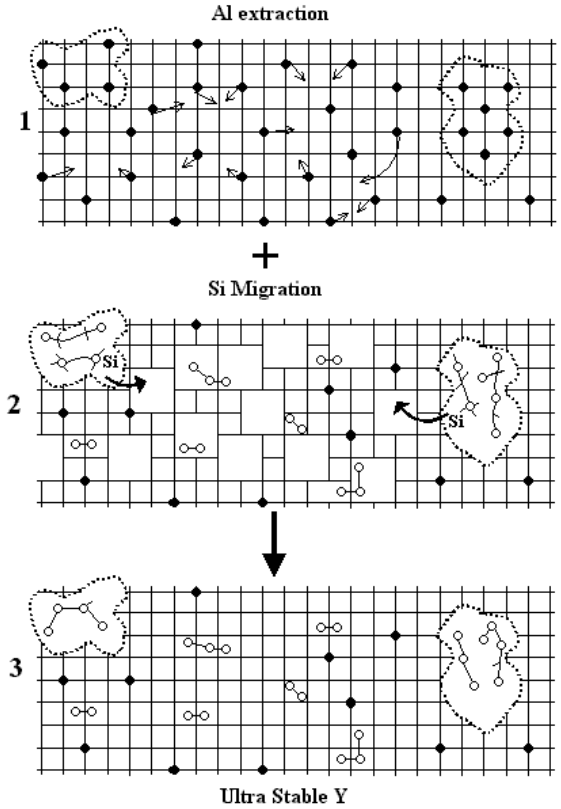

Figure 1. Schematic picture of the formation of mesopores (adapted from Marcilly [40]). The grid denotes the zeolite framework, the black dots are framework aluminum atoms, the open circles are aluminum atoms extracted from the framework and the dotted lines indicate the mesopores.

defect concentrations spherical mesopores can coalesce to form channels [34]. Many of the mesopores formed during the steaming are filled with debris from the partial amorphization of the framework and the extraction of aluminum from the framework. The extraframework material in the micro- and mesopores can be extracted by mild acid leaching. Zeolite Y with very high mesopore volumes of almost exclusively cylindrical mesopores can be obtained after a special hydrothermal treatment at temperatures above 100°C and pressures above 1 bar [41,42]. This hydrothermal treatment deviates from steaming, which is performed with gaseous steam at atmospheric pressures.

Although the created mesopores are beneficial, the main disadvantage of steaming is the partial amorphization of the zeolite framework. Not only the relative crystallinity drops with increasing severity of the treatment leading to a decreased amount of the active phase, also part of the micropores and mesopores are filled with amorphous debris leading to a partial blockage of active sites. In table 1 the drop of the relative crystallinity and the increase of the mesopore volume with increasing treatment are shown for a series of Y zeolites [42]. In this table also the deposition of amorphous material on the external surface and in the micropores is evident from the surface enrichment in aluminum and the lower measured micropore volume compared to the calculated micropore volume that is expected on the basis of the crystallinity, sodium content and unit cell size of the materials (see table 1: V_{micro} and V_{micro} calc.). Upon acid leaching the amorphous material is removed from the meso- and micropores (see table 1: V_{micro} and V_{micro} calc. of XVUSY). Another side effect of steaming is that the number and nature of the acid sites is changed by the extraction of aluminum. If only steaming and no acid leaching is applied the bulk Si/Al ratio remains the same, but the framework Si/Al ratio increases. Although these changes of the acid sites can be very important for the catalytic activity and deactivation behavior of the catalyst, this is beyond the scope of this review.

Table 1. Physical properties of NaY, USY (steamed), XVUSY (steamed twice and acid leached) and High-Meso VUSY (special hydrothermal treatment, see text).

	Si/Al bulk (at/at)	Si/Al XPS (at/at)	a_0 (nm)	%Y[a]	V_{micro}[b] (ml/g)	V_{micro} calc.[c] (ml/g)	V_{tot}-V_{micro} (ml/g)[d]	S_T[e] (m^2/g)
NaY	2.6	2.8	2.469	100	0.34	0.34	0.05	8
USY	2.6	1.1	2.450	87	0.26	0.32	0.11	63
XVUSY	39.3	71.3	2.423	72	0.28	0.27	0.25	120
HMVUSY	20.0	1.4	2.427	71	0.15	0.26	0.47	146

a) Relative crystallinity determined with XRD; data from manufacturer b) Micropore volume from t-plot c)Expected micropore volume if all micropores are empty; calculated by correcting V_{micro} of NaY for crystallinity, a_0 and sodium weight of USY and XVUSY and HMVUSY d) $V_{meso} + V_{macro}$ e) sum of external and mesopore surface area calculated from t-plot

Acid leaching

The purpose of acid leaching can be the removal of non-framework material created during the steaming process or the direct creation of mesopores, *i.e.* without the use of steam. The first method is frequently applied because during steaming material is extracted from the framework and subsequently deposited in the micro- and mesopores and on the external surface of the zeolite crystals. A mild acid-leaching step, with either inorganic acids such as diluted nitric acid or organic (complexing) acids such as oxalic acid, dissolves this extra-framework material. In this case the mesopores are not actually formed during the acid leaching process. Rather, the mesopores formed during the steaming process are emptied, resulting in a higher mesopore volume compared to zeolites that have only been steamed. [25-27,29]

In the second method, mesopores are created by direct acid leaching (without steaming). During the severe treatments with strong inorganic acids, aluminum is removed from the framework. The effectiveness of this technique depends on the zeolite used. Especially in the case of mordenite direct acid treatments are used to generate mesopores [43-48]. It has also been claimed that mesopores can be formed in zeolite beta by direct attack with a strong acid [49,50], although it is difficult to separate these intracrystalline mesopores from the mesopores between the very small zeolite beta crystals.

The nature of the acid used can be of great influence on the final mesopore structure. Treating calcined mordenite with acid resulted in a much higher bulk Si/Al ratio and less mesopores in the case of oxalic acid compared to nitric acid. This is thought to be caused by the higher pH of the oxalic acid solution and the ability of the oxalate ions to form a complex with the aluminum ions [51]. One of problems with acid leaching is that the Si/Al ratio is changed. With mild acid leaching after steaming the framework Si/Al ratio (obtained after steaming) is not changed if performed carefully [25,26]. However, if mesopores are created by direct attack of the zeolite with acid, the framework Si/Al ratio increases resulting in a loss of active sites. For several purposes one would like to separate the contributions of the changes of the acid sites and the generation of mesopores in order to study their influence on catalytic reactions. With acid leaching both variables are changed at the same time, thus complicating the interpretation of the activity of the catalyst.

Base leaching

To our knowledge only few examples are known of treating a zeolite with a base in order to generate mesopores. Matsukata *et al.* [52,53] treated ZSM-5 crystals with a NaOH solution, resulting in a partial dissolution of the zeolite crystals. Higher NaOH concentrations and prolonged contact of the zeolites with the NaOH solution resulted in an increase of the external surface and mesopore volume. Recently they have

extended the experiments to the base leaching of USY [54]. Besides treatment of ZSM-5 with NaOH [55] also treatment of 10-membered ring zeolites like ferrierite with alkali aluminates [56] is known in patent literature to increase the porosity of the zeolites. In these cases, however, an additional acid treatment was performed after the base treatment to dissolve amorphous material in the pores.

Chemical treatment

Extraction of aluminum from the framework of zeolite Y by reaction with $SiCl_4$ results in the formation of mesopores [57], although it has also been reported that it is possible to obtain a dealuminated zeolite Y without mesopores after reaction with $SiCl_4$ [24]. Extraction of aluminum from zeolite Y with EDTA [17] or $(NH_4)_2SiF_6$ [58] results in the formation of mesopores. However, it is known that the zeolite structure collapses if the rate of extraction of aluminum by EDTA is much faster than the migration of silicon in the framework [59].

Creating mesopores during synthesis

Recently researchers from Haldor Topsøe developed a method to create mesopores in zeolite crystals during the synthesis [60]. First they synthesized zeolite crystals around a template carbon source, viz. carbon black particles [61] or carbon nanotubes [62]. During the subsequent calcination of the material the carbon is burned away, resulting in mesopores in the zeolite crystallites. This strategy enables one to tune the size, shape and connectivity of the mesopore system in the zeolite by choosing the proper carbon source. This also allows one to vary the Si/Al ratio and the mesopore system independently.

Characterization of mesopores in zeolites

Nitrogen physisorption

The most widely applied technique to study the size and surface area of mesopores in zeolites is nitrogen physisorption. Already from the shape of the nitrogen adsorption and desorption isotherm valuable information on the presence and shape of the mesopores can be deduced. In figure 2, the curves for the nitrogen adsorption and desorption of some different Y zeolites are displayed. The NaY zeolite without mesopores will give a type I isotherm, while after the formation of mesopores a combination of type I and IV isotherms is found as is observed for the three USY samples. The existence of a hysteresis loop in the isotherms is indicative for the presence of mesopores, whereas the shape of the hysteresis loop is related to the shape of the mesopores [25,29,42]. Roughly, a vertical hysteresis loop is indicative of

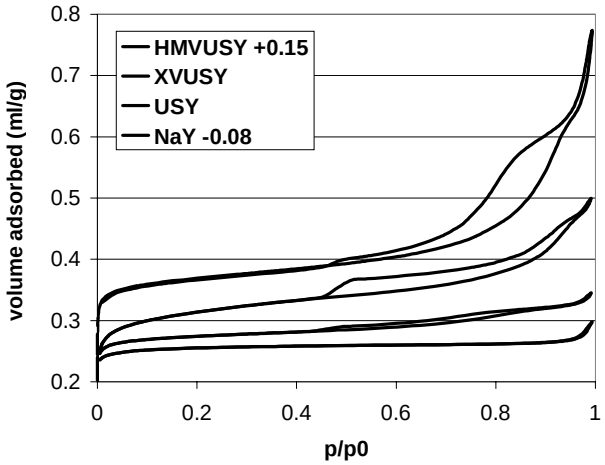

Figure 2. Nitrogen adsorption and desorption isotherms on a series of Y zeolites.

cylindrical mesopores, whereas a horizontal hysteresis loop indicates inkbottle-type mesopores. However, since most mesopore systems have a broad variation in pore shapes and sizes, this should be treated with caution. From the presence and shapes of the hysteresis loops in figure 2, it is obvious that by varying the steaming treatment different amounts and forms of mesopores can be created.

For the analysis of the nitrogen physisorption data several methods are available. Very often only the BET surface of the materials is given. Since for microporous materials the boundary conditions for multilayer adsorption are not fulfilled, the reported BET areas have no physical meaning. They should be understood as a number proportional to the total micropore volume rather than the specific surface area [63]. A valuable tool for the analysis of the external surface area is the t-plot method. The external surface area is the total surface area of all meso- and macropores. If the crystallite size remains the same during the formation of mesopores the difference between the external surface areas of the parent and the treated zeolite is the surface area of the mesopores created. Hudec *et al.* [45] showed that upon acid leaching of an H-mordenite, the BET surface area remained almost unaltered, while the external surface area increased due to the formation of mesopores. Another method that is often applied is the BJH (Barret-Joyner-Halenda) method, which uses the desorption branch of the nitrogen isotherms to calculate the pore size distribution and the adsorbed volume. Up to ca. 4 nm diameter the BJH method gives a reasonable good pore size distribution based on the Kelvin equation. However, below a pore diameter of 2 nm the Kelvin equation is not valid anymore and also, the area between 2 and 4 nm is prone to errors if a hysteresis loop is present [29,64]. In that case a huge amount of nitrogen is released at once between a relative pressure of 0.38 and 0.44, which is visible as the closing of the hysteresis loop in the isotherm. The BJH method correlates the volume of released nitrogen via the Kelvin equation to pores of 3-4 nm diameter. This is not always correct, since also inkbottle type of pores with pore necks smaller than 4

nm diameter release their nitrogen between a relative pressure of 0.38 and 0.44. Many examples are known where people claim that uniform pores of 4 nm diameter are formed, which do not change during more severe treatments. This often leads to discrepancies with TEM images shown [29,53,65]. Sometimes the BJH method is applied to the adsorption branch of the nitrogen isotherm. However, many programs treat the adsorption isotherm as if it was a desorption isotherm in order to apply the BJH method. Because this gives errors in the calculated pore size distribution, care should be taken when the BJH method is applied to the adsorption branch.

Mercury porosimetry

In the IUPAC's Recommendations for the Characterization of Porous Solids it is stated that "mercury porosimetry is widely accepted as a standard measure of total pore volume and pore size distribution in the macro- and mesopore ranges" [66]. Nevertheless, only two examples are known to us where researchers used mercury porosimetry to study the intracrystalline mesopores of zeolites with mercury porosimetry. Lohse *et al.* [23] used mercury porosimetry in addition to adsorption measurements of hexane to show that upon steaming of zeolite Y a mesopore system

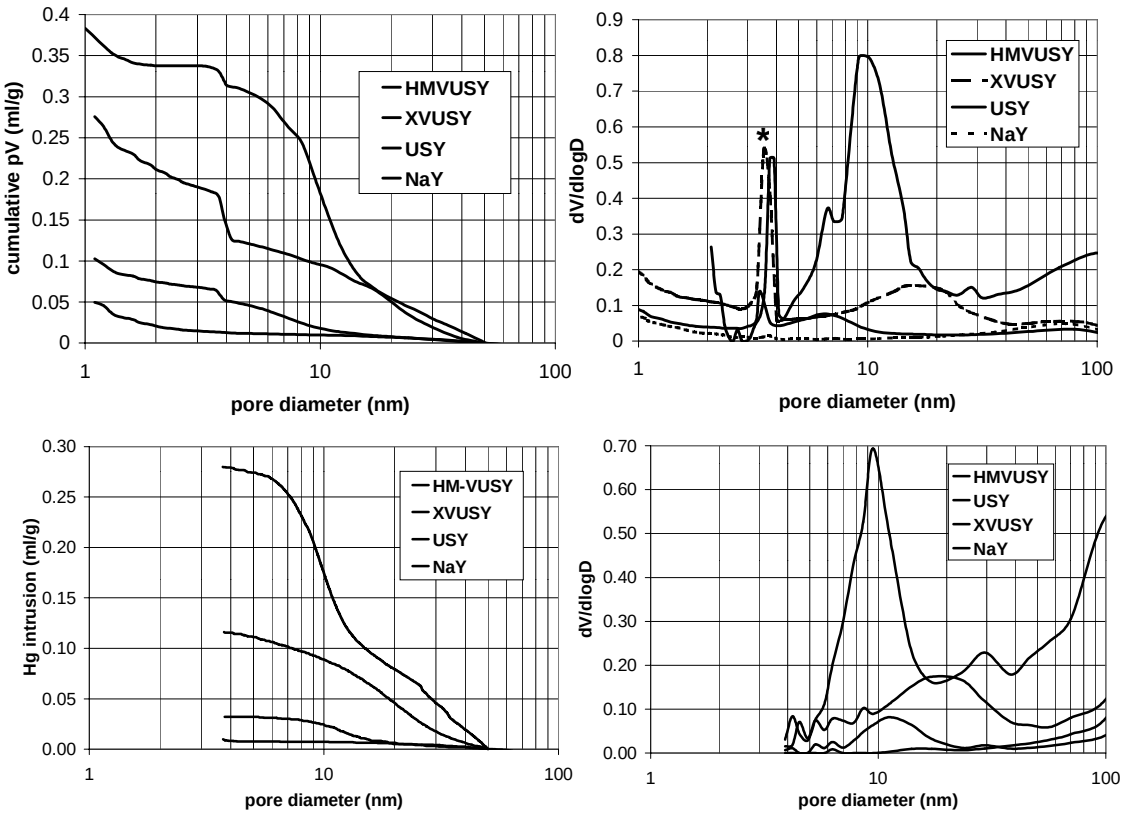

Figure 3. Cumulative nitrogen desorption (upper left) and pore size distribution, calculated from the desorption isotherm using the BJH method (upper right); and cumulative mercury intrusion (bottom left) and calculated pore size distribution (bottom right).

with pores of 10 nm diameter is formed. After extraction of extra-framework material with an acid, the pore diameter increased to 20 nm. More recently Janssen *et al.* [42] used mercury porosimetry as an extension to nitrogen physisorption measurements to differentiate between cylindrical mesopores and mesopores connected to the external surface by micropores only (cavities). The results are displayed in figure 3. From this it is clear that nitrogen physisorption probes both the micro- and the mesopores, while mercury could penetrate only in pores with diameters larger than 4 nm (at the applied pressures). After steaming of zeolite Y the relative volume fraction of the mesopores (4-20 nm in diameter) that were cavities inside the crystals amounted to 20 vol%, while after more severe steaming combined with acid leaching even 29 vol% of the mesopores (with diameters of 4-40 nm) were cavities inside the crystals.

Electron Microscopy

Although Scanning Electron Microscopy (SEM) has been used to assess the formation of mesopores by studying the roughening of the surface of zeolite crystals after acid treatments [51], Transmission Electron Microscopy (TEM) is the most frequently used electron microscopy technique in the study of mesopore formation. In the transmission electron microscope an image is formed that is a projection of the mass-density encountered by the electrons moving through the sample. Therefore, a mesopore will show up as a white area in a TEM image since it has a reduced mass-density. This has indeed been observed for zeolite Y [27,29,30,32-34,49,65], mordenite [47,48], ZSM-5 [53,61,62], ferrierite [38], mazzite [35] and zeolite omega [36]. In order to increase the visibility of the mesopores in the TEM images, the crystallites are often cut into thin slices using a microtome. However, this gives rise to fracturing of the crystals. Although these fractures are often aligned parallel to each other, they may hinder the interpretation of the TEM image. Because the image formed is a projection of the mass-density of the entire crystallite the exact shape and size of the mesopores is often obscured. After steaming of zeolite Y the observed mesopores appear spherical [27,30,65], although Choi-Feng *et al.* [33] have demonstrated very nicely that in regions with high defect concentrations the mesopores 'coalesce' to form channels. Pellet *et al.* [38] and Ajot *et al.* [49] have shown that the mesopores in steamed ferrierite and zeolite Y respectively appear 'structured'. The observed mesopores were square rather than spherical. Also cylindrical mesopores have been observed with TEM. Both after leaching of ZSM-5 with NaOH [53] as well as after templating mesopores in silicalite with carbon nanotubes [62] cylindrical mesopores were clearly visible in the TEM images. Also Sasaki *et al.* [32] clearly showed the presence of cylindrical mesopores in steamed zeolite Y.

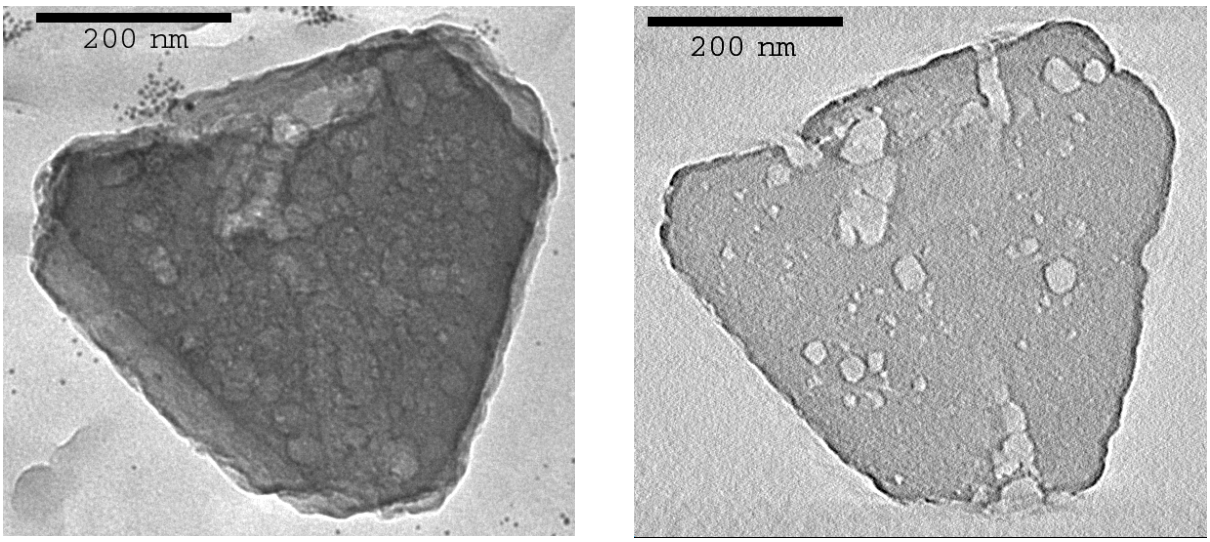

Figure 4. Conventional TEM image of severely steamed and subsequently acid leached zeolite Y (left) and slice through the 3D-TEM reconstruction of the same crystal (right) showing the mesopores in the crystal as lighter gray-tones.

In order to get three-dimensional information on the shape of the mesopores Pellet *et al.* looked at their ferrierite platelets both side-on as well as top-on [38]. However, this was done on different crystals and also the projection of mesopores on top of each other obscured a clear interpretation of the shape of the mesopores. Sasaki *et al.* [32] tilted a steamed zeolite Y crystal from 0° to 50° in their electron microscope, while collecting an image every 10 degrees. From these subsequent images it is clear that two round pores that were visible in the crystallite in one orientation showed up as cylindrical pores by tilting over 50 degrees. More recently electron tomography, a form of 3D-TEM, has been used to characterize the mesopores in an acid-leached mordenite and a steamed zeolite Y [67,68]. With electron tomography a series of TEM images (tilt series) is taken over a large angular range (typically from –70° to +70° with 1° increment). From these data a 3D-reconstruction of the crystal is calculated as a stack of very thin slices (ca. 2 nm). The tilt series already gives valuable information on the shape of the mesopores, but the slices through the 3D-reconstruction really show the mesopores with great clarity and provide information on the three-dimensional shape and connectivity of the mesopores. In figure 4 a conventional TEM image of a severely steamed and acid leached Y zeolite and a thin slice through the 3D-TEM reconstruction of the same crystal are given. Although the presence of mesopores can be seen as lighter areas in the conventional TEM image, the mesopores are much clearer (light areas) in the 3D-TEM slice. From the study of subsequent 3D-TEM slices it is clear that many of these mesopores are cavities inside the zeolite [68].

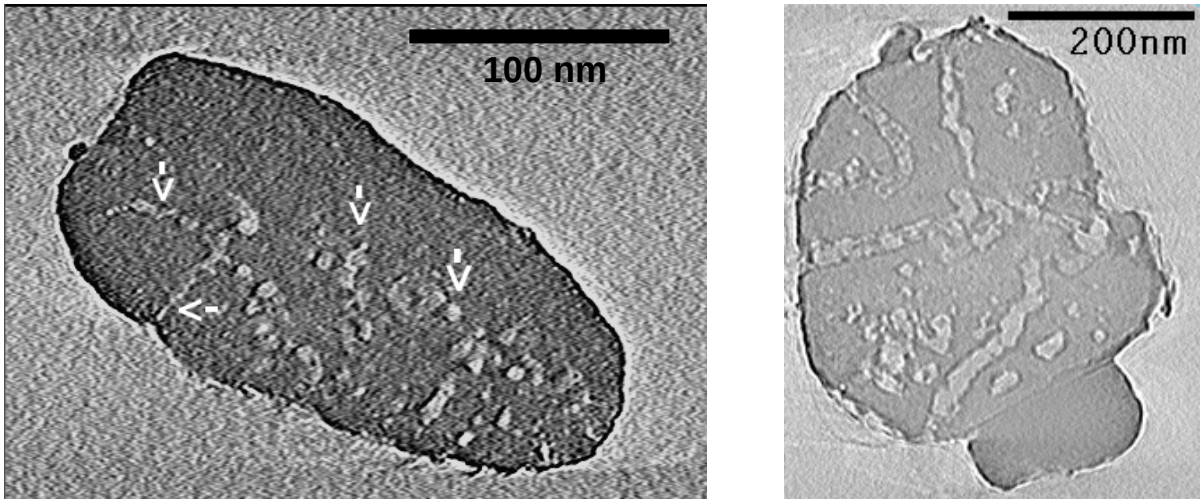

Figure 5. Slices through the crystallites of an acid leached mordenite (left) and a special hydrothermal treated zeolite Y (HMVUSY, right) based on 3D-TEM reconstructions, showing the mesopores in the crystal as lighter gray-tones.

In figure 5, 3D-TEM slices showing cylindrical mesopores in zeolites are given for an acid leached mordenite [67] and a special hydrothermally treated zeolite Y [42]. A system of interconnected cylindrical mesopores is expected to enhance accessibility much more than mesoporous cavities inside the crystal [42].

Transport and reaction in zeolites containing mesopores

The beneficial role of mesopores in zeolite Y catalysts

Zeolite Y catalysts are largely used in hydrocracking and fluid catalytic cracking (FCC) of large bulky molecules of heavy oil fractions into smaller molecules. Nace [69] demonstrated the limited accessibility of the zeolite Y micropores for the larger molecules present in the feed. Therefore the zeolite is commonly combined with an amorphous matrix that cracks the large molecules in smaller ones, which are then able to access the zeolite micropore system. Additionally, in order to optimize the catalyst performance, the zeolite is steam dealuminated to high Si/Al ratios. The dealumination procedure initiates changes in both acidity as well as in the morphology of the zeolite [32,34,70-76]. From literature, it is obvious that large part of the research has been focussed on explaining the enhanced activity by changes in acidity of the dealuminated zeolite Y catalysts [75,77-79]. However, since diffusion limitation may play a major role in the cracking of large molecules over zeolite Y, morphology changes like mesopore formation largely enhance the activity [22,70,72-74,80-86]. Even more so because of the recent trends in FCC reactor and catalyst design resulting in reduced contact times

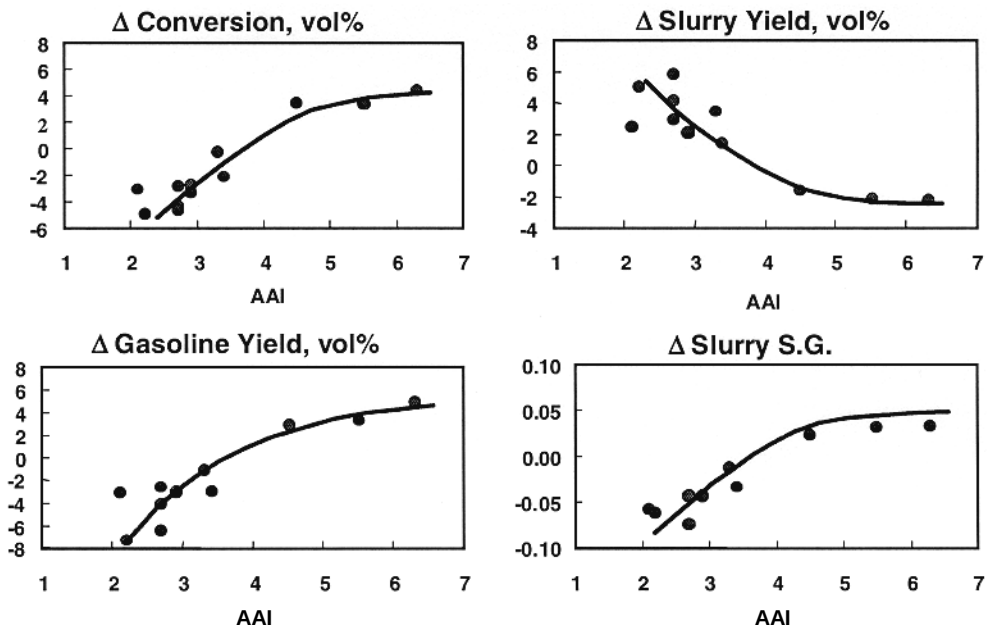

Figure 6. Performance of a FCC catalyst as a function of accessibility, adapted from [86].

between the catalyst and the hydrocarbons. Accordingly, the mass transfer rates of the reactant into and products out of the zeolite crystals have become more dominant in determining the overall cracking rate [81-83,86]. In addition, the use of heavier and more contaminated feedstocks, containing large bulky molecules and heavy metals, often induce a decrease in accessibility by pore plugging and/or film-formation [83,84]. At Akzo Nobel it has been demonstrated that zeolite Y catalysts displaying a high initial accessibility are less subject to deactivation with time on stream [81,82,86]. In order to increase the initial accessibility, the presence of mesopores is one of the important requirements. The concept of increasing the accessibility of the FCC catalyst and the influence on its catalytic performance has recently been demonstrated by Hakuli *et al.* [86] and is displayed in figure 6. The enhanced conversion and gasoline yield and the lower slurry yield clearly indicate the beneficial effect of the use zeolite Y catalysts containing mesopores in the cracking of today's oil fractions.

Corma [21,70] showed the favorable effect of the combination of micro- and mesopores in zeolite crystals, by comparing the cracking activity of two dealuminated zeolite Y catalysts. The first catalyst (Y1) had little mesoporosity and an intact micropore system, and the second catalyst (Y2) contained a high amount of mesopores and a micropore system that was partly destroyed. As is displayed in figure 7, it was revealed that for the cracking of the relatively small molecule *n*-heptane, which can easily migrate in the micropores, Y1 displayed a higher activity than Y2 as a result of the higher intact micropore system. However, for the cracking of vacuum gas oil, containing mostly molecules that are too large to penetrate into zeolite micropores, Y2

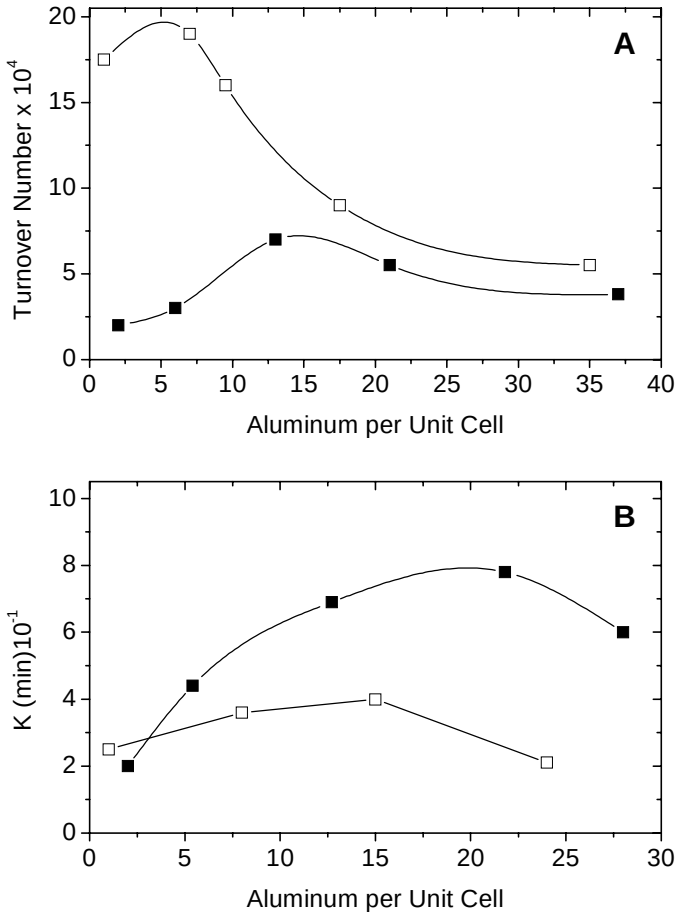

Figure 7. (A) Cracking of *n*-heptane and (B) cracking of vacuum gas oil over dealuminated USY catalysts. Y1 (□) contains little mesoporosity and an intact micropore system; Y2 (■) contains a high amount of mesopores and a partly destroyed micropore system; adapted from [21].

displayed a significantly higher conversion than Y1. A comparable study was performed by Sato *et al.* [22] for the hydrocracking of diphenylmethane (DPM) and triphenylmethane (TPM) over two different zeolite Y catalysts, one without (Y1) and one with mesopores (Y2). In figure 8 it is shown that for the hydrocracking of diphenylmethane, which has a smaller molecular size and therefore is able to diffuse into the zeolite Y micropores, both catalysts exhibited similar activities. On the other hand the hydrocracking of triphenylmethane, which is larger in molecular size and cannot diffuse into the micropores, resulted in a four times higher activity for the catalyst containing mesopores. Falabella *et al.* [74] found similar results by comparing the initial cracking rate of 1,3,5-tri-isopropylbenzene over zeolite Y catalysts with different mesoporosities. In this case the used probe molecule was too large to enter the micropores of zeolite Y and accordingly it was found that catalysts with a higher mesopore volume displayed a higher initial cracking activity.

The examples above illustrate that the most favorable zeolite Y cracking catalysts must combine micropores with mesopores. An example of a theoretically ideal cracking catalyst was imagined by Mann [87] and is displayed in figure 9, in which also the presence of macropores is visualized. The macro- and mesopores induce a high

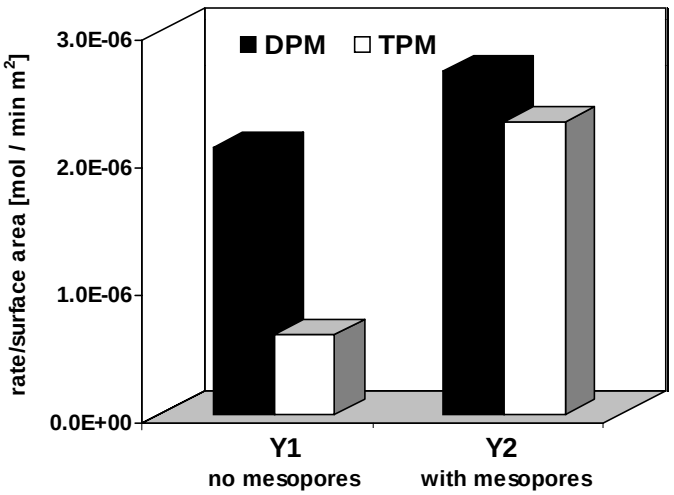

Figure 8. Reaction rate per total surface area for the hydrocracking of diphenylmethane (DPM) and triphenylmethane (TPM) over two zeolite Y catalysts, one without (Y1) and one with mesopores (Y2); adapted form [22].

accessibility of the micropores, enhance diffusion of reactants and products and provide a high surface area in order to crack large molecules.

Compared to the frequent use of zeolites in hydrocarbon processing industries, their use in the industrial synthesis of fine chemicals is small. One of the main reasons for this is the fact that the organic chemicals that need to be synthesized are often too bulky to be built in and/or desorb from the zeolite micropore system [88]. Hence, diffusion limitation effects play a major role. Nevertheless, in some cases successful industrial application has been accomplished. Based on the work by Corma *et al.* [89], Rhodia has commercialized the synthesis of acetoveratrole using dealuminated zeolite Y catalysts [90]. Moreover, at Dupont it was found that dealuminated zeolite Y is a selective catalyst for the manufacturing of 1,4-bis(4-phenoxybenzoyl)benzene, which is a monomer for the building of various aromatic polyketons [91]. For both of these reactions it is stated that diffusion limitations may be present and that catalysts with

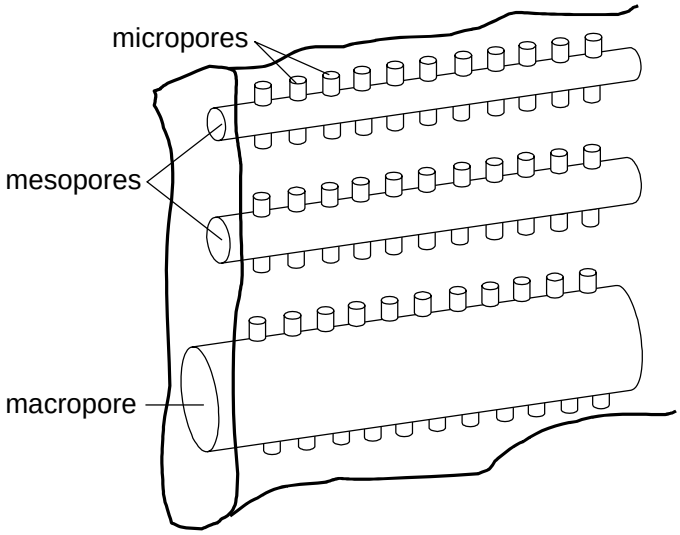

Figure 9. Idealized catalyst pore structure for a cracking catalyst, adapted from [87].

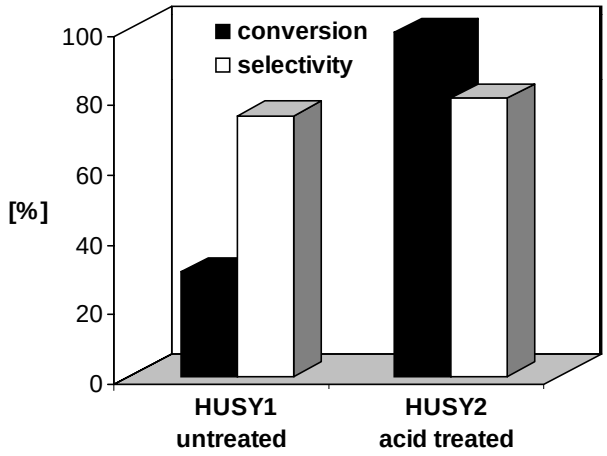

Figure 10. Influence of acid treatment on the performance of HUSY catalysts in the isomerization of of α-pinene oxide at 273 K, adapted from [92].

high external surface areas are preferential. More recently Hölderich *et al.* [92] emphasized the beneficial role of mesopores in zeolite Y for the selective isomerization of α-pinene oxide. As depicted in figure 10, it was found that dealuminated Y zeolites exhibit high selectivity towards the preferred campholenic aldehyde. After exposing the sample to a mild acid treatment (HUSY2), a much higher activity as well as a slightly enhanced selectivity was observed. This was explained by the fact that the mesopores formed during the steaming process are emptied by the acid treatment, resulting in a higher mesopore volume compared to the sample that was only steamed (HUSY1). It was stated that the mesopores allows a good diffusional transport of large organic molecules, even at the low temperatures that are often favored in fine chemical synthesis.

The beneficial role of mesopores in mordenite catalysts

In general, mordenite catalysts undergo rapid deactivation because of their one-dimensional 12 membered ring pore structure. However, it has been shown that by applying dealumination procedures, mordenite catalysts can be used with high profitability in industrial processes. DOW Chemical applies mordenite catalysts in the production of cumene [93,94] and Shell introduced Pt/mordenite catalysts for the hydroisomerization of linear alkanes to branched ones [95].

Cumene (or isopropylbenzene) is produced by the acid alkylation of benzene with propylene and subsequently used for the production of phenol and acetone. Almost all the applied industrial processes make use of two stages, *i.e.* alkylation and transalkylation, which produces a di-isopropylbenzene (DIPB). The current two-stage DOW-process uses two different deeply dealuminated mordenite catalysts with very high Si/Al ratios of 78 and 54 respectively, prepared by several acid leaching and steaming treatments [43]. The high activity and stability of the dealuminated mordenite catalysts were explained by several factors [93]. First, it is generally established that the

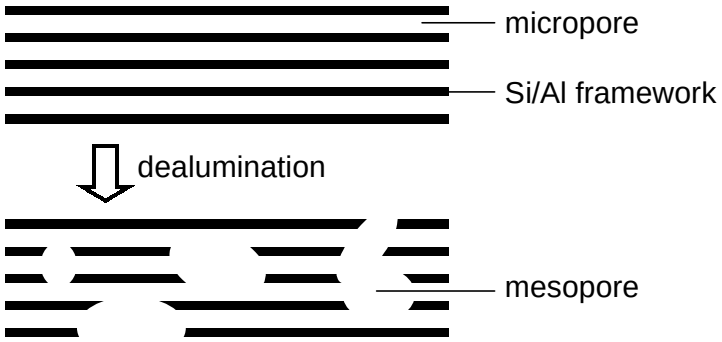

Figure 11. Schematic visualization showing the effect of mesopore creation in zeolite mordenite, adapted from [44].

concentration of Al cations in the framework largely determines the acid strength of the Brønsted acid sites [96]. After dealumination, the net number of Brønsted sites is lower, but the acid strength of the remaining Brønsted sites is enhanced by the fact that only a small number of aluminum cations is placed in the next nearest neighbor positions [97]. The second explanation is the removal of obstructions like non-framework species from the micropores, which consequently enhances the diffusivity of the reactant and product molecules. However, the major factor determining the enhanced catalytic performance of the dealuminated mordenites is the presence of mesopores [44]. In this way the one-dimensional mordenite micropores are interconnected by mesopores so that a two- or three-dimensional structure is obtained, as illustrated in figure 11. The presence of mesopores decreases the apparent length of the micropores, thereby alleviating diffusion limitation and preventing rapid deactivation. Despite the highly dealuminated structure, it was demonstrated that the catalytic action is still controlled by the shape selective properties of the mordenite 12 membered ring micropores [43].

Alkane hydroisomerization has become one of the most attractive routes for obtaining high-octane quality gasoline. The bifunctional zeolite type catalyst that is industrially applied uses mordenite containing small Pt particles. One of the drawbacks is that the most desired multiple branched products encounter large transport limitation in the one-dimensional pore system of mordenite [98]. To partially overcome this problem the mordenite is mildly acid-leached, resulting in an increase in the Si/Al ratio [48,98-102]. Ideally a Si/Al ratio is reached such that no aluminum cations are placed in the next nearest neighbor positions. In this way the cations are just isolated, which induces the highest intrinsic activity [103] and the highest framework stability [104]. Another large beneficial effect of the acid treatment is the introduction of mesopores in the zeolite [48]. The group of Sachtler [105] showed the potential positive effect of mesopores on the hydroisomerization activity. A higher hydroisomerization activity was observed for a catalyst with mordenite crystals that were locally destructed due to the growth of large Pt-particles inside. Tromp *et al.* [48] showed that

dealumination by mild acid leaching has a similar effect, because it generates mesopores in the mordenite crystals and consequently enhances the catalytic performance. From the above it can be concluded that both a shorter diffusion path length as well as an increase in the diffusion coefficient and/or an increase in the intrinsic activity may explain the large increase in catalytic activity.

Recently, it was demonstrated that it is possible to combine the measurement of adsorption, diffusion and reaction in one experimental set-up including a tapered element oscillating microbalance (TEOM) [106,107]. In this way the effect of acid leaching of the mordenite on the hydroisomerization of *n*-hexane was studied [107]. The *n*-hexane uptake-curves for an untreated Pt/mordenite (Pt/MOR1) with low Si/Al ratio and low mesoporosity, and for an acid-leached Pt/mordenite (Pt/MOR2) with a high Si/Al ratio and high mesoporosity were measured at reaction temperature. For the latter catalyst, the mesopores are visualized in figure 5. The uptake curves are displayed in figure 12, from which it is clear that the acid treatment significantly enlarges the rate and amount of *n*-hexane uptake. At stabilized uptake, more than a factor four increase in the hydroisomerisation rate of *n*-hexane was observed for Pt/MOR2. By applying an adapted Fickian diffusion model and the Thiele theory, it was determined that both an increase of the intrinsic activity as well as an alleviation of intracrystalline diffusion limitation caused the overall activity increase for Pt/MOR2. No noticeable difference in the intracrystalline diffusision coefficient was observed between Pt/MOR1 and Pt/MOR2. It was stated that the enhanced uptake after acid leaching predominantly arises from the shorter intracrystalline diffusion path resulting from the mesoporous structure. The overall increase in hydroisomerization activity as a result of the acid treatment was explained by the enlarged intrinsic activity and by the decrease in the intracrystalline diffusion path length, resulting from the mesoporous structure that enables an enhanced transport of reactant and product molecules.

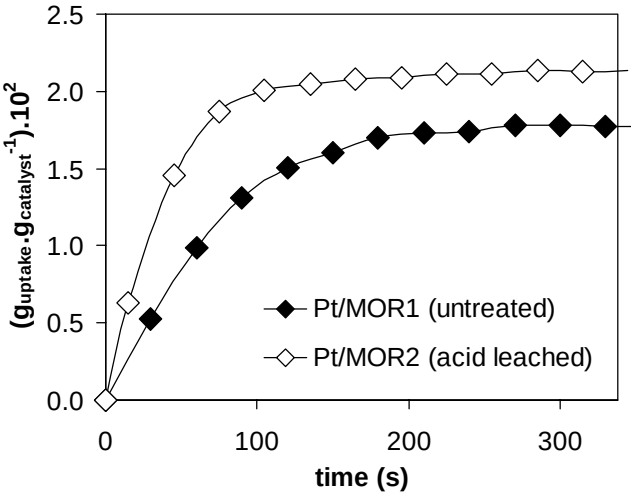

Figure 12. Uptake curves for *n*-hexane in Pt/mordenite before and after acid leaching, obtained at 523 K in a TEOM.

The above examples clearly demonstrate that the introduction of mesopores in a one-dimensional zeolite like mordenite is of major impact with respect to catalytic activity and stability. Part of this is accounted for by acidity enhancements, but the largest beneficial effect is the alleviation of diffusion limitation induced by the presence of mesopores turning the one-dimensional structure into a highly accessible multi-dimensional structure.

Conclusions

From this review it is clear that for some applications, like cracking of heavy oil fractions, cumene production, alkane hydroisomerization and more recently for the synthesis of fine chemicals, the presence of mesopores in zeolite crystals is of major importance. The creation of mesopores can be established via several routes from which steaming and acid leaching are the most commonly applied. Characterization of mesopores is mostly performed using nitrogen physisorption and electron microscopy. More recently, however, it was shown that electron tomography, a form of 3D-TEM, is able to reveal the three-dimensional shape, size and connectivity of the mesopores with great clarity. In order to assess the effect of mesopores on the transport properties of a zeolite catalyst, test reactions using the right probe molecules can be executed or alternatively one can monitor the uptake using a microbalance. Recently a combination of both methods in one set-up was shown to be highly effective to separate physical (transport) and chemical (acidity) effects.

In general, the generation of mesopores in zeolite crystals results in shorter intracrytalline diffusion path lengths and a higher external surface area. Accordingly, the presence of mesopores ensures an optimal accessibility and transport of reactants and products, while the zeolite micropores induce the preferred shape-selective properties. Therefore the combination of micropores and mesopores in one zeolite crystal renders some highly beneficial effects with respect to the catalytic performance.

Acknowledgements

Ries Janssen (Utrecht University) is kindly acknowledged for his contribution as a co-author of this chapter.

References

1. A. Corma, Chem. Rev. 95 (1995) 559.
2. C.R. Marcilly, Top. Catal. 13 (2000) 357.

3. J. Kärger and D.M. Ruthven, "Diffusion in Zeolites and Other Microporous Materials", John Wiley and Sons, New York (1992).
4. P.B. Weisz, Chemtech, 3 (1973) 498.
5. J. Crank, "The Mathematics of Diffusion", Clarendon, Oxford, 1975.
6. D.M. Ruthven and M.F.M Post, in "Introduction to Zeolite Science and Practice" (H. van Bekkum, E.M. Flanigen, P.A. Jacobs and J.C. Jansen, Eds.) 2nd edition, Elsevier Science, Amsterdam (2001).
7. W.O. Haag and D.H. Olson, US patent no. 4117026 (1978).
8. N.Y. Chen, W.W. Kaeding and F.G. Dwyer, J. Am. Chem. Soc. 101 (1979) 6783.
9. E.A. Schwabb and B.C. Gates, Ind. Eng. Chem. Fund. 11 (1972) 540.
10. K. Rajagopalan, A.W. Peters and G.C. Edwards, Appl. Catal. 23 (1986) 69.
11. W.O. Haag, R.M. Lago and P.B. Weisz, Faraday Disc. 72 (1982) 317.
12. P. Voogd and H. van Bekkum, Appl. Catal. 59 (1990) 311.
13. G. Bellussi, G. Pazzuconi, C. Perego, G. Girotti and G. Terzoni, J. Catal. 157 (1995) 227.
14. A. Corma, V. Fornes, S.B. Pergher, Th.L.M. Maesen and J.G. Buglass, Nature 396 (1998) 353.
15. C.C. Freyhardt, M. Tsapatsis, R.F. Lobo, K.J. Balkus Jr. and M.E. Davis, Nature 381 (1996) 295.
16. M. Yoshikawa, P. Wagner, M. Lovallo, K. Tsuji, T. Takewaki, C.Y. Chen, L.W. Beck, C. Jones, M. Tsapatsis, S.I. Zones and M.E. Davis, J. Phys. Chem. B 102 (1998) 7139.
17. A. Corma, M.J. Diaz-Cabanas, J. Martinez-Triguero, F. Rey and J. Rius, Nature 418 (2002) 514.
18. A. Karlsson, M. Stöcker and R. Schmidt, Micropor. Mesopor. Mat. 27 (1999) 181.
19. K.R. Kloestra, H. van Bekkum and J.C. Jansen, Chem. Comm. 23 (1997) 2281.
20. L. Huang, W. Guo, P. Deng, Z. Xue and Q. Li, J. Phys. Chem. B 104 (2000) 2817.
21. A. Corma, Chem. Rev. 97 (1997) 2373.
22. K. Sato, Y. Nishimura and H. Shimada, Catal. Lett. 60 (1999) 83.
23. U. Lohse and M. Mildebrath, Z. Anorg. Allg. Chem. 476 (1981) 126.
24. J. Scherzer, ACS Symposium Series 248 (1984) 157.
25. S. Morin, P. Ayrault, N.S. Gnep and M. Guisnet, Appl. Catal. A Gen. 166 (1998) 281.
26. E. Benazzi, J. Lynch, A. Gola, S. Lacombe and C.R. Marcilly, Proc 12th Int. Zeolite Conf. (1999) 2735.
27. J. Lynch, F. Raatz and Ch. Delande, Stud. Surf. Sci. Catal. 39 (1987) 547.
28. R.A. Beyerlein, C. Choi-Feng, J.B. Hall, B.J. Huggins and G.J. Ray, ACS Symposium Series 571 (1994) 81.
29. J. Lynch, F. Raatz and P. Dufresne, Zeolites 7 (1987) 333.
30. V. Patzelova and N.I. Jaeger, Zeolites 7 (1987) 240.
31. A. Zukal, V. Patzelova and U. Lohse, Zeolites 6 (1986) 133.
32. Y. Sasaki, T. Suszuki, Y. Takamura, A. Saji and H. Saka, J. Catal. 178 (1998) 94.
33. C. Choi-Feng, J.B. Hall, B.J. Huggins and R.A. Beyerlein, J. Catal. 140 (1993) 395.
34. R.A. Beyerlein, C. Choi-Feng, J.B. Hall, B.J. Huggins and G.J. Ray, Top. Catal. 4 (1997) 27.
35. R. Dutartre, L.C.D. Menorval, F. Di Renzo, D. McQueen, F. Fajula and P. Schulz, Micropor. Mat. 6 (1996) 311.
36. B. Chauvin, P. Massiani, R. Dutartre, F. Figueras, F. Fajula and T. Des Courieres, Zeolites 10 (1990) 174.

37. K.-H. Lee and B.-H. Ha, Micropor. Mesopor. Mat. 23 (1998) 211.
38. R.J. Pellet, D.G. Casey, H.-M. Huang, R.V. Kessler, E.J. Kuhlman, C.-L. O'Young, R.A. Sawicki and J.R. Ugolini, J. Catal. 157 (1995) 423.
39. R.M. Lago, W.O. Haag, R.J. Mikovsky, D.H. Olson, S.D. Hellring, K.D. Schmitt and G.T. Kerr, Stud. Surf. Sci. Catal. 28 (1986) 677.
40. C.R. Marcilly, Petrole et Techniques 328 (1986) 12.
41. D.A. Cooper, T.W. Hastings and E.P. Hertzenberg, US patent no. 5601798 (1997).
42. A.H. Janssen, A.J. Koster and K.P. de Jong, *Accepted in J. Phys. Chem. B.*
43. M.M. Olken and J.M. Garces, J.M., Proc. 9th Int. Zeolite Conf. (1993) 559.
44. G.R. Meima, CATTECH 2 (1998) 5.
45. P. Hudec, J. Novansky, S. Silhar, T.N. Trung, M. Zubek and J. Madar, Ads. Sci. Tech. 3 (1986) 159.
46. J.M. Garces, J.J. Maj, S.C. Rocke and J. Lee Guo-Shu, Eur. patent no. 0317907 (1989).
47. B.L. Meyers, T.H. Fleisch, G.J. Ray, J.T. Miller and J.B. Hall, J. Catal. 110 (1988) 82.
48. M. Tromp, J.A. van Bokhoven, M.T. Garriga Oostenbrink, J.H. Bitter, K.P. de Jong and D.C. Koningsberger, J. Catal. 190 (2000) 209.
49. H. Ajot, J.F. Joly, J. Lynch, F. Raatz and P. Caullet, Stud. Surf. Sci. Catal. 62 (1991) 583.
50. C. Coutanceau, J.M. Da Silva, M.F. Alvarez, F.R. Ribeiro and M. Guisnet, J. Chim. Phys. 94 (1997) 765.
51. R. Giudici, H.W. Kouwenhoven and R. Prins, Appl. Catal. A Gen. 203 (2000) 101.
52. M. Ogura, S. Shinomiya, J. Tateno, Y. Nara, E. Kikuchi and M. Matsukata, Chem. Lett. 8 (2000) 882.
53. M. Ogura, S. Shinomiya, J. Tateno, Y. Nara, M. Nomura, E. Kikuchi and M. Matsukata, Appl. Catal. A Gen. 219 (2001) 33.
54. M. Matsukata *et al*. in preparation.
55. C.A. Drake and A.-H. Wu, US patent no. 5952259 (1999).
56. J.M. Garces and D.M. Millar, US patent no. 6017508 (1998).
57. D. Goyvaerts, J.A. Martens, P.J. Grobet and P.A. Jacobs, Stud. Surf. Sci. Catal. 63 (1991) 381.
58. C.S. Triantafillidis, A.G. Vlessidis and N.P. Evmiridis, Ind. Eng. Chem. Res. 39 (2000) 307.
59. G.T. Kerr, A.W. Chester and D.H. Olson, Catal. Lett. 25 (1994) 401.
60. A. Carlsson, C. Madsen, I. Schmidt, J. Houzvicka and C.J.H. Jacobsen, Eur. patent no. 1106575 (2001).
61. C.J.H. Jacobsen, C. Madsen, J. Houzvicka, I. Schmidt and A. Carlsson, J. Am. Chem. Soc. 122 (2000) 7116.
62. I. Schmidt, A. Boisen, E. Gustavsson, K. Stahl, S. Pehrson, S. Dahl, A. Carlsson and C.J.H. Jacobsen, Chem. Mater. 13 (2001) 4416.
63. R.A. van Santen, P.W.N.M. van Leeuwen, J.A. Moulijn and B.A. Averill, Stud. Surf. Sci. Catal. 123 (1999) 543.
64. J.C. Groen, L.A.A. Peffer and J. Perez-Ramirez, Micropor. Mesopor. Mat. 51 (2002) 75.
65. S. Cartlidge, H.-U. Nissen and R. Wessicken, Zeolites 9 (1989) 346.
66. J. Rouquerol, D. Avnir, C.W. Fairbridge, D.H. Everett, J.H. Haynes, N. Pernicone, J.D.F. Ramsay, K.S.W. Sing and K.K. Unger, Pure Appl. Chem. 66 (1994) 1739.
67. A.J. Koster, U. Ziese, A.J. Verkleij, A.H. Janssen and K.P. de Jong, J. Phys. Chem. B. 104 (2000) 9368.

68. A.H. Janssen, A.J. Koster and K.P. de Jong, Angew. Chem. Int. Ed. 40 (2001) 1102.
69. D.M. Nace, Ind. Eng. Chem. Prod. Res. Dev. 9 (1970) 203.
70. A. Corma, Stud. Surf. Sci. Catal. 49 (1989) 49.
71. A. Hoek, T. Huizinga, A.A. Esener, I.E. Maxwell, W.H.J. Stork, F.J. van de Meerakker and O. Sy, Oil Gas J. april 22 (1991) 77.
72. P. O'Connor, A.W. Gevers, A.P. Humphries, L.A. Gerritsen and P.H. Desai, ACS Symposium Series 375 (1987) 318.
73. H.H. Kung, B.A. Williams, S.M. Babitz, J.T. Miller, W.O. Haag and R.Q. Snurr, Top. Catal. 10 (2000) 59.
74. E. Falabella S-Aguiar, M.L. Murta-Valle, E.V. Sobrinho and D. Cardoso, Stud. Surf. Sci. Catal. 97 (1995) 417.
75. A.I. Biaglow, D.J. Parrillo, G.T. Kokotailo and R.J. Gorte, J. Catal. 148 (1994) 213.
76. L.A. Pine, P.J. Maher and W.A. Wachter, J. Catal. 85 (1984) 66.
77. N. Cardona-Martinez and J.A. Dumesic, Adv. Catal. 38 (1992) 149.
78. J. Sommer, M. Hachoumy and F. Garin, J. Am. Chem. Soc., 116 (1994) 5491.
79. G. Yaluris, J.E. Rekoske, L.M. Aparicio, R.J. Madon and J.A. Dumesic, J. Catal. 153 (1995) 65.
80. J.W. Gosselink and J.A.R. van Veen, Stud. Surf. Sci. Catal. 126 (1999) 3.
81. P. O'Connor, P. Imhof and S.J. Yanik, Stud. Surf. Sci. Catal. 134 (2001) 299.
82. C.W. Kuehler, R. Jonker, P. Imhof, S.J. Yanik and P. O'Connor, Stud. Surf. Sci. Catal. 134 (2001) 311.
83. P. O'Connor and A.C. Pouwels, Stud. Surf. Sci. Catal. 88 (1994) 129.
84. R.H. Harding, A.W. Peters and J.R.D. Nee, Appl. Catal. A Gen. 221 (2001) 389.
85. I.E. Maxwell, J.K. Minderhoud, W.H.J. Stork and J.A.R. van Veen, in: Handbook of Heterogeneous Catalysis vol.4 (G. Ertl, H. Knözinger and J. Weitkamp, Eds.) Wiley-VCH, Weinheim (1997) 2017.
86. A.K. Hakuli, P. Imhof and C.W. Kuehler, Proc. Akzo Nobel Catalysts Symposium, Noordwijk (2001).
87. R. Mann, Catal. Today 18 (1993) 509.
88. W.F. Hölderich and H. van Bekkum, in: "Introduction to Zeolite Science and Practice" (H. van Bekkum, E.M. Flanigen, P.A. Jacobs and J.C. Jansen, Eds.) 2nd edition, Elsevier Science, Amsterdam (2001).
89. A. Corma, M.J. Climent, H. Garcia and L. Primo, Appl. Catal. 49 (1989) 109.
90. M. Spagnol, L. Gilbert, E. Benazzi and C.R. Marcilly, WO patent no. 9635655 (1996).
91. D.R. Corbin, E. Kumpinsky and A. Vidal, Eur. patent no. 316133 (1989).
92. W.F. Hölderich, J. Röseler, G. Heitmann and A.T. Liebens, Catal. Today 37 (1997) 353.
93. G.R. Meima, M.J.M. van der Aalst, M.S.U. Samson, J.M. Garces and G.J. Lee, Proc. 9th Int. Zeolite Conf. (1993) 327.
94. G.J. Lee, J.M. Garces; G.R. Meima and M.J.M. van der Aalst, US patent no. 325177 (1989).
95. H.W. Kouwenhoven and W.C. van Zijl-Langhout, Chem. Eng. Progress 67 (1971) 65.
96. J. Dwyer, Stud. Surf. Sci. Catal. 37 (1987) 333.
97. H.G. Karge and V. Dondur, J. Phys. Chem. 94 (1990) 765.
98. G.D. Lei, B.T. Carvill and W.M.H. Sachtler, Appl. Catal. A Gen. 142 (1996) 347.
99. P.B. Koradia, J.R. Kiovsky and M.Y. Asim, J. Catal. 66 (1980) 290.

100. I.E. Maxwell and W.H.J. Stork in: "Introduction to Zeolite Science and Practice" (H. van Bekkum, E.M. Flanigen, P.A. Jacobs and J.C. Jansen, Eds.) 2nd edition, Elsevier Science, Amsterdam (2001).
101. S.T. Sie, Stud. Surf. Sci. Catal. 85 (1994) 587.
102. A. Corma and A. Martinez, in: "Catalytic Activation and Functionalisation of Light Alkanes: Advances and Challenges" (E.G. Derouane, J. Haber, F. Lemos, F.R. Ribeiro and M. Guisnet, Eds.) Kluwer Academic, Dordrecht (1998) 35.
103. M. Guisnet, V. Fouche, M. Belloum, J.P. Bournonville and C. Travers, Appl. Catal. 71 (1991) 283.
104. M. Guisnet, V. Fouche, M. Belloum, J.P. Bournonville and C. Travers, Appl. Catal. 71 (1991) 295.
105. B.T. Carvill, B.A. Lerner, B.J. Adelman, D.C. Tomczak and W.M.H. Sachtler, J. Catal. 144 (1993) 1.
106. D. Chen, H.P. Rebo, K. Moljord and A. Holmen, Chem. Eng. Sci. 51 (1996) 2687.
107. S. van Donk, A. Broersma, O.L.J. Gijzeman, J.A. van Bokhoven, J.H. Bitter and K.P. de Jong, J. Catal. 204 (2001) 272 / chapter 4 of this thesis.

3

Application of a Tapered Element Oscillating Microbalance for Transient Uptake Measurements of Hydrocarbons over Zeolites

Abstract

The experimental background, operation and application of the Tapered Element Oscillating Microbalance (TEOM) is introduced and illustrated with two case studies. First, the TEOM is applied to perform uptake measurements for *n*-hexane over Pt/H-mordenite. By varying the sample amount and flow rate it is demonstrated that reliable adsorption/diffusion data are obtained. Second, it is shown that $SiCl_4$ modification of H-ferrierite decreases the rate of coke formation while the isobutene yield is enhanced.

Introduction

In 1980, Patashnick *et al.* [1] introduced the Tapered Element Oscillating Microbalance (TEOM), which had been developed at that time as a tool for the accurate real-time monitoring of the amount of particulate matter in the effluent streams of combustion systems. Since its introduction, the TEOM has been successfully applied in different fields of chemistry. Various environmental and health related studies have been conducted to establish the quantitative monitoring of all kinds of air polluting species in urban areas [2,3]. Moreover, the amount of particulate matter emerging from various diesel engine exhausts has been measured by applying filters in combination with a TEOM [4,5]. The major advantage of the TEOM is that it provides a packed sample bed, through which the feed or reactant gas is forced to flow [6]. In addition, it is able to operate at high temperature and pressures and can detect mass changes down to 1 μg. These factors make the TEOM a highly suitable tool to establish coking, adsorption and diffusion effects in the field of heterogeneous catalysis.

The TEOM has been used in catalysis research to *in situ* monitor the amount of coke deposition on various zeolite catalysts [6,7-13] and metal containing catalysts like Pt-Sn/Al_2O_3 [14], Ni/Al_2O_3 [15] and Pt-Cu/C [16]. Moreover, the TEOM has been applied to measure the adsorption and diffusion of hydrocarbons on zeolites [17-20]. Chen *et al.* [17] performed transient uptake measurements and derived numerical values for the diffusional time constant from these uptake curves. Zhu *et al.* [18-20] demonstrated that the TEOM can be easily used for transient uptake and desorption experiments as well as for steady state and equilibrium adsorption measurements. In this chapter the experimental background and operation of the TEOM will be further introduced. Moreover, the application of the TEOM for measuring the adsorption and diffusion of hydrocarbons, and the deposition of coke will be exemplified in two case studies.

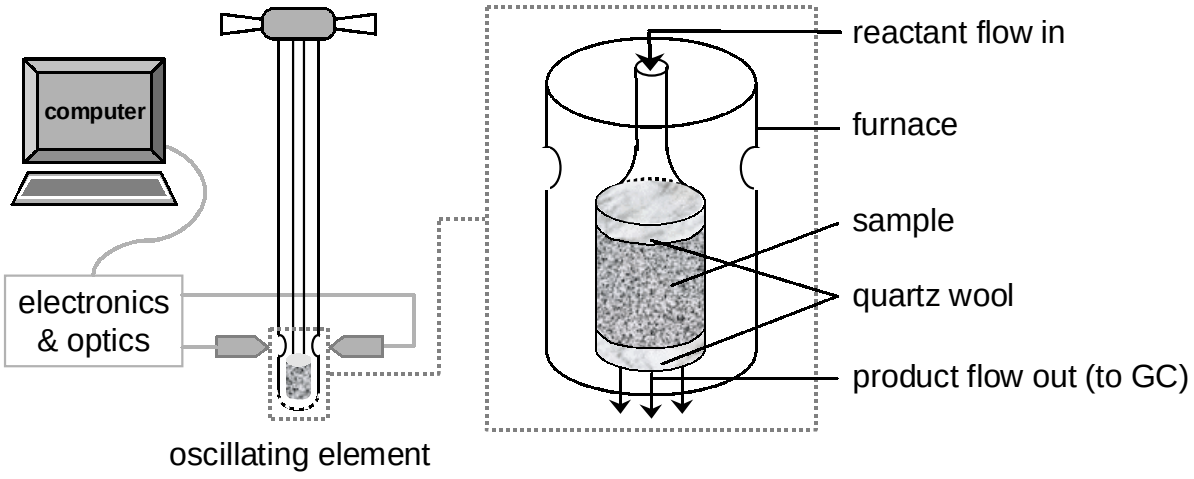

Figure 1. Schematic representation of the Tapered Element Oscillating Microbalance.

Description and operation of the TEOM

In figure 1 the TEOM (Rupprecht & Pataschnick TEOM 1500 PMA) is schematically depicted. The design is such that a stream of gas flows through a hollow quartz tube, the so-called tapered element, which contains a packed sample bed at its down-end. The sample particles are held in place between two layers of quartz wool with a meshed metal cup at the bottom end. The gas is directly purged through the sample bed, like in a down-flow fixed bed reactor, eliminating flow bypass problems that are often encountered in classical gravimetric instruments [6]. The tapered element holding the sample bed is mechanically forced into an oscillation that is controlled via an electronic feedback circuit. An optical device monitors the oscillation frequency and in this way the mass changes that occur due to interactions between the sample and the gas stream are directly computed.

The functioning of the TEOM is based on the relationship between the natural frequency *(f)* of the oscillating tapered element and its mass (*m*). Based on the operating principle, the total mass change detected (Δm) consists of the amount adsorbed by the sample (Δm_a) and a mass change caused by the variation in densities between the different gases used in the experiment (Δm_d):

$$\Delta m = \Delta m_a + \Delta m_d = K_0 \left[\left(\frac{1}{f_2} \right)^2 - \left(\frac{1}{f_1} \right)^2 \right] \qquad (1)$$

The subscripts 1 and 2 refer to the change of frequency with time because of alterations in the total mass and K_0 is the spring constant for the tapered element.

Depending on the type of experiment, two different strategies can be applied to correct for the mass change due to gas density differences. In figure 2 (on the next page) the two procedures that are employed in case of a coking and an adsorption experiment are illustrated. For the measurement of coke deposition on a catalyst, the sample is first pretreated in an inert gas flow, *e.g.* nitrogen, until no further mass change occurs. Then the flow is switched to the reactant and the actual coking reaction is executed until the desired coke-level is reached. Subsequently, without changing the temperature, the gas flow is switched back to the initial inert gas so that overall no mass change due to gas density differences is detected. In this way, the amount of coke is directly available as the 'read-out' mass change. Please note that this procedure necessitates a fully irreversible coke deposition. In the case of an adsorption/diffusion experiment, the previous procedure is not applicable because of the reversibility of the uptake. Therefore, blank experiments with a sample bed consisting of quartz particles and using

the same gases as in the actual adsorption experiment must be performed to establish Δm_d. After the actual uptake experiment, the amount of hydrocarbons sorbed by the sample, Δm_a, is then calculated as Δm minus Δm_d.

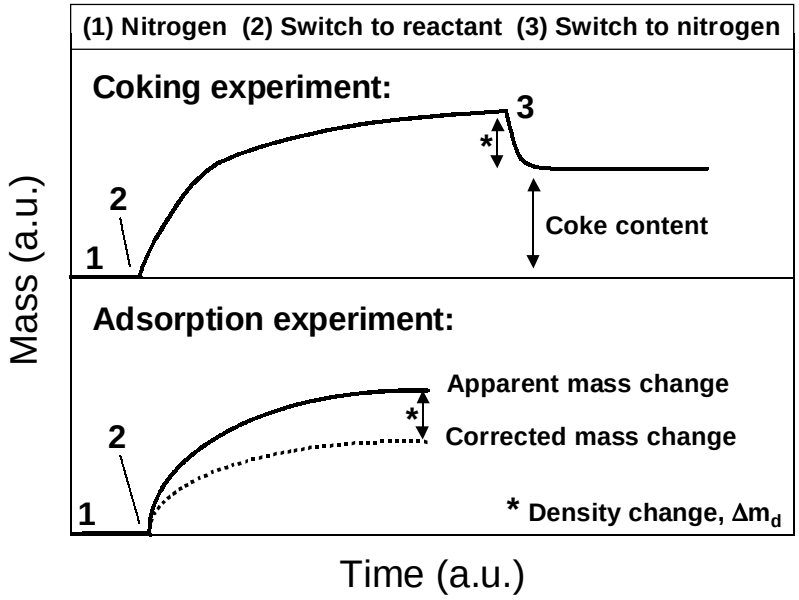

Figure 2. Experimental procedures for coking and adsorption experiments in the TEOM.

Application of the TEOM: two case studies

I: Adsorption of n-hexane on Pt/H-mordenite – variation of sample amount and flow rate

The Pt/H-mordenite (Pt/HMOR) sample was prepared as described by Tromp *et al.* [21]. Transient uptake experiments were performed for *n*-hexane over Pt/HMOR at 523 K and a total pressure of 1.3 bar. Prior to the actual uptake experiment, the samples were reduced *in situ* under H_2 at 623 K. Experiments were executed using two different sample amounts, namely 85 mg and 17 mg with a particle size of 150-425 μm. For the measurement with 85 mg sample also experiments with two different flow rates were performed, namely 21.7 ml.min^{-1} and 43.4 ml.min^{-1} with an H_2:*n*-C_6 ratio of 11 mol/mol. In this way it was investigated if consistent uptake data can be obtained using the TEOM set-up.

The experimental uptake curves for intracrystalline diffusion in the one-dimensional MOR crystals, may be described by a diffusion model for zeolite crystals having a slab geometry [22,23]:

$$\frac{m_t}{m_{eq}} = 1 - \frac{8}{\pi^2}\sum_{n=0}^{\infty}\frac{1}{(2n+1)^2} * e^{-\frac{(2n+1)^2\pi^2 t D_{uptake}}{4L^2}} \qquad (2)$$

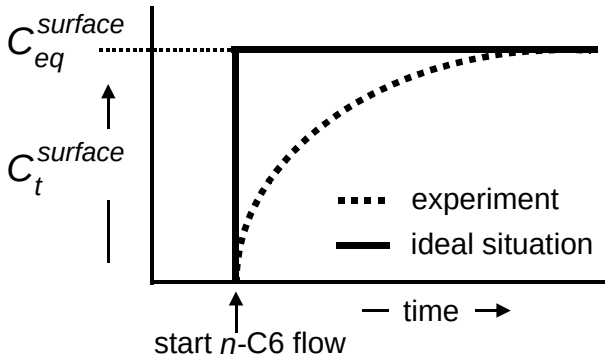

Figure 3. Schematic representation of the build-up of surface concentration in the TEOM sample bed, leading to a time delay in the uptake experiment.

The experimental uptake curves were initially fitted using this equation, however, acceptable fits were not obtained. It was revealed that the cause for the inconsistency between experiment and fit is the limited *n*-hexane feed rate, resulting in a concentration gradient over the sample bed. This implies that no immediate equilibrium is established at the surface of the crystals after the start of an uptake experiment, as visualized in figure 3. A mathematical approximation for the gradual build-up of the surface concentration may be best described by the following equation, which is adapted from Karge and Niessen [24]:

$$C_t^{surface} = C_{eq}^{surface} * \left(1 - e^{-\beta \cdot t}\right) \tag{3}$$

Here, β stands for a constant that is equal to the reciprocal value of the delay time. Combining equations 2 and 3 leaves the analytical solution for the transient diffusion equation:

$$\frac{m_t}{m_{eq}} = \int_0^t \left\{ \left[1 - e^{-\beta\left(t - t'\right)}\right] * \sqrt{\frac{D_{uptake}}{\pi L^2 t'}} * \sum_{n=0}^{\infty} \left[e^{-\frac{L^2}{t' D_{uptake}}(2n+2)^2} + e^{-\frac{L^2}{t' D_{uptake}}(2n)^2} - 2e^{-\frac{L^2}{t' D_{uptake}}(2n+1)^2} \right] \right\} dt' \tag{4}$$

This equation is applied to fit the raw uptake data obtained in the TEOM experiments. The fitting procedure yields the characteristic time for diffusion L^2/D_{uptake} and the time constant β.

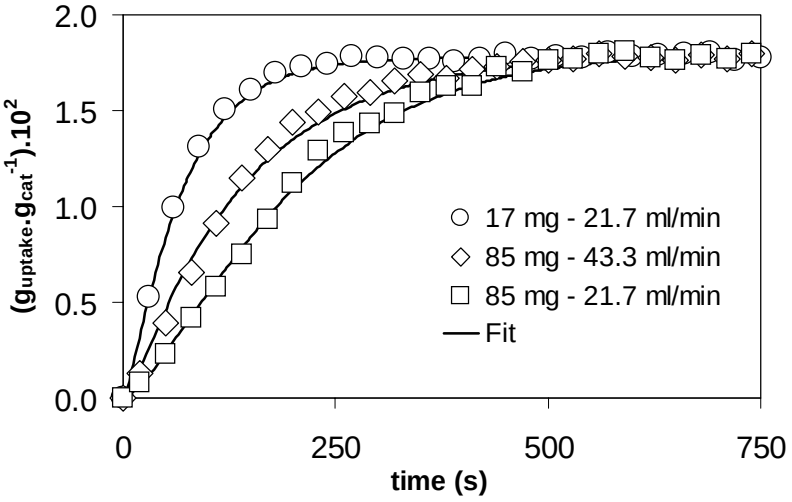

Figure 4. Experimental and fitted curves for the uptake of *n*-hexane over Pt/H-Mordenite at 523 K.

The experimental and fitted curves for the uptake of *n*-hexane are displayed in figure 4. From this it is clear that by doubling the feed of both H_2 and *n*-hexane, the equilibrium concentration of *n*-hexane in Pt/HMOR is established faster. Moreover, a five times lower sample amount results in an even faster establishment of the equilibrium uptake. It must be emphasized that for all experiments the same amount of *n*-hexane per gram sample is sorbed, indicating the good reproducibility of the apparatus. The complete set of fitting results for the performed experiments, including the quality of the fit, is collected in table 1. As is clear from the values obtained after fitting of the data, the delay constant β proportionally increased with doubling the feed or lowering the amount of catalyst while the same values for L^2/D_{uptake} were obtained. This indicates that the uptake experiments in all cases did not suffer from film diffusion and/or the presence of surface barriers, presumably because convective gas transport predominated in the packed bed reactor.

Table 1. Fitting results for the various *n*-hexane uptake experiments on Pt/H-mordenite.

Experiment	Mass (mg)	Flow (ml.min^{-1})	L^2/D_{uptake} (s)	β^{-1} (s)	Chi^2*
Small sample	17	21.7	154	21	$6*10^{-3}$
Large sample	85	21.7	147	109	$7*10^{-3}$
Double flow	85	43.4	158	58	$9*10^{-3}$

* $\mathrm{Chi}^2 = \sum_i \left(y_i^{obs} - y_i^{calc} \right)^2$, where *y* is the uptake- and *i* the time parameter (Note: $y_{max} = 1$)

II: Deposition of coke during n-butene reaction over ferrierite – effect of $SiCl_4$ treatment

Commercially available high silicon NH_4^+ ferrierite (Zeolyst Int. Si/Al 30) was activated in a dry nitrogen flow at 823 K for 12 hours to obtain the H^+ ferrierite (H-FER). Temperature programmed desorption-thermogravic analysis (TPD-TGA) on H-

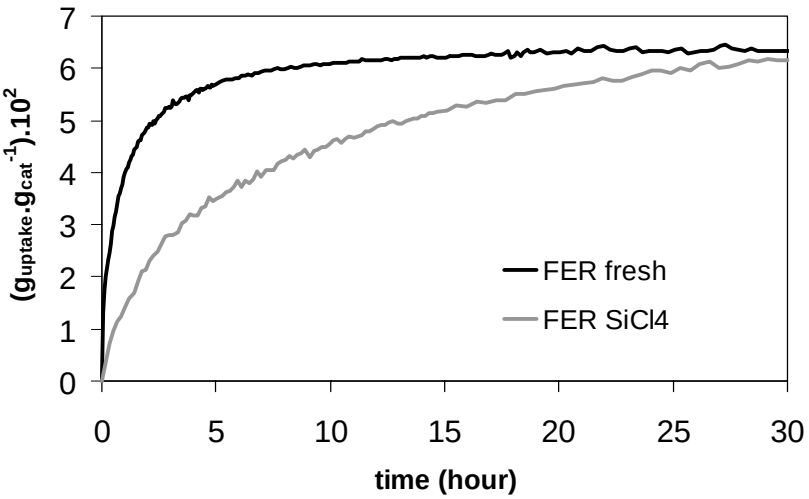

Figure 5. Uptake of carbonaceous deposits during the reaction of *n*-butene at 623 K on fresh ferrierite and $SiCl_4$ modified ferrierite.

FER using *n*-propylamine and *iso*-propylamine showed acid site concentrations of 0.53 $mmol.g^{-1}$ and 0.36 $mmol.g^{-1}$, respectively. The micropore volume is 0.132 $ml.g^{-1}$ as determined by nitrogen physisorption / t-plot analysis. H-FER was modified by chemical liquid deposition of silicon tetrachloride (H-FER-$SiCl_4$) following the procedure as described by Yue *et al.* [25]. In literature it is suggested that $SiCl_4$ modification and subsequent calcination lead to the formation of silicon species that decrease the Brønsted acid site concentration, especially in the pore mouths of the zeolite crystal [25,26]. Accordingly, the prepared H-FER-$SiCl_4$ sample displayed lower acid site concentrations of 0.45 $mmol.g^{-1}$ and 0.22 $mmol.g^{-1}$, as determined by TPD-TGA using *n*-propylamine and *iso*-propylamine respectively. However, the micropore volume accessible for nitrogen remained the same. The effect of the $SiCl_4$ treatment on the formation of carbonaceous deposits during the skeletal isomerization of *n*-butene to isobutene was monitored in a TEOM at 623 K and 1.3 bar. The tapered element was loaded with ~50 mg sample (90 - 150 μm). Prior to testing the samples were dried *in situ* in nitrogen at 623 K. During testing a pure *n*-butene gas-flow was used with a weight hourly space velocity (WHSV) of 20 $g_{n\text{-butene}}.g_{H\text{-}FER}^{-1}.h^{-1}$.

In figure 5 the uptake of carbonaceous deposits for both the fresh and the $SiCl_4$ modified sample are displayed. From this it is clear that the $SiCl_4$ treatment significantly reduces the rate of coke formation. Nevertheless, the final coke levels for both samples are similar, which indicates that after modification the complete micropore volume is still accessible for *n*-butene. This agrees with the nitrogen physisorption results and reveals that no complete pore blocking by silica species took place. The TPD-TGA results indicate that the Brønsted acid site concentration is lowered after the $SiCl_4$ treatment. Surprisingly, the decrease in *n*-propylamine uptake is less significant than for *iso*-propylamine. Additional infrared measurements also revealed a minor decrease in Brønsted acidity. These results might be explained by a

narrowing of part of the micropores due to the presence of small silica species, which hinder the more bulky *iso*-propylamine to completely enter the micropores of H-FER-$SiCl_4$. Recently Duncan and Möller [27] demonstrated comparable effects for ZSM-5 samples treated with tetraethoxysilane (TEOS).

Overall it is indicated that the lower formation rate of carbonaceous deposits during *n*-butene reaction over H-FER-$SiCl_4$ as monitored by the TEOM might be a result of the presence of small silica species. This might narrow the H-FER micropores and consequently prevent part of the hydrocarbons to pass. GC analysis of the products coming out of the TEOM-reactor at stabilized coke level reveals that the isobutene yield is about doubled for H-FER-$SiCl_4$, although the selectivity is lower as compared to the fresh H-FER. This last aspect is caused by a larger amount of cracking product, most likely because only small species are able to diffuse out of the modified micropores of H-FER-$SiCl_4$.

Notation

C_{gas}, C_{eq}	gas phase concentration, adsorbed concentration at equilibrium [$mol.m^{-3}$]
D_{uptake}	uptake diffusivity [$m^2.s^{-1}$]
f	frequency [s^{-1}]
K_0	spring constant [$g.s^{-2}$]
L	intracrystalline diffusion pathlength (= half length of crystal) [m]
m_t, m_{eq}	amount adsorbed at time t and equilibrium [$g.g_{cat}^{-1}$]
m	mass [g]
t, t'	time and time integration parameter [s]
β	delay constant [s^{-1}]

Acknowledgements

Dr. O.L.J. Gijzeman is acknowledged for providing the mathematical diffusion models; Dr. J.T. Miller (BP Research Center, Naperville IL) and Henk Jan Tromp are acknowledged for providing samples.

References

1. H. Patashnick, G. Rupprecht and J.C.F. Wang, ACS Symposium Series 25 (1980) 188.
2. G. Allen, C. Sioutas, P. Koutrakis, R. Reiss, F.W. Lurmann and P.T. Roberts, J. Air Waste Manage. 47 (1997) 682.
3. P.V. Tan, G.J. Evans, J. Tsai, S. Owega, M.S. Fila, O. Malpica and J.R. Brook, Environ. Sci. Technol. 36 (2002) 3512.

4. R.P. Jarrett, N.N. Clark, M.S. Gilbert and R. Ramamurthy, Powder Technol. 119 (2001) 215.
5. M.S. Gilbert and N.N. Clark, Int. J. Engine Research 2 (2001) 277.
6. D. Chen, A. Gronvold, H.P. Rebo, K. Moljord and A. Holmen, Appl. Catal. A Gen. 137 (1996) L1.
7. F. Hershkowitz, P.D. Madiara, Ind. Eng. Chem. Res. 32 (1993) 2969.
8. S.C. Fung, C.A. Querini, K. Liu, D.S. Rumschitzki and T.C. Ho, Stud. Surf. Sci. Catal. 88 (1994) 305.
9. K. Liu, S.C. Fung, T.C. Ho and D.S. Rumschitzki, J. Catal. 169 (1997) 455.
10. L.M. Petkovic and G. Larsen, Ind. Eng. Chem. Res. 38 (1999) 1822.
11. L.M. Petkovic and G. Larsen, J. Catal. 191 (2000) 1.
12. D. Chen, H.P. Rebo, A. Gronvold, K. Moljord and A. Holmen, Micropor. Mesopor. Mat. 35 (2000) 121.
13. S. Gomm, R. Glaser and J. Weitkamp, Chem. Ing. Tech. 73 (2001) 1584.
14. H.P. Rebo, D. Chen, E.A. Blekkan and A. Holmen, Stud. Surf. Sci. Catal. 119 (1998) 617.
15. J.N. Armor and D.J. Martenak, Appl. Catal. A Gen. 206 (2001) 231.
16. W. Zhu, J. Zhang, F. Kapteijn, M. Makkee and J.A. Moulijn, Stud. Surf. Sci. Catal. 139 (2001) 21.
17. D. Chen, H.P. Rebo, K. Moljord and A. Holmen, Chem. Eng. Sci. 51 (1996) 2687.
18. W. Zhu, J.M. van de Graaf, L.J.P. van den Broeke, F. Kapteijn and J.A. Moulijn, Ind. Eng. Chem. Res. 37 (1998) 1934.
19. W. Zhu, F. Kapteijn, J.A. Moulijn and J.C. Jansen, Phys. Chem. Chem. Phys. 2 (2000) 1773.
20. W. Zhu, F. Kapteijn and J.A. Moulijn, Micropor. Mesopor. Mat. 47 (2001) 157.
21. M. Tromp, J.A. van Bokhoven, M.T. Garriga Oostenbrink, J.H. Bitter, K.P. de Jong and D.C. Koningsberger, J. Catal. 190 (2000) 209.
22. J. Kärger and D.M. Ruthven, "Diffusion in Zeolites and Other Microporous Materials", John Wiley and Sons, New York, 1992.
23. J. Crank, "The Mathematics of Diffusion", Clarendon Press, Oxford, 1975.
24. H.G. Karge and W. Niessen, Catal. Today 8 (1991) 451.
25. Y. Yue, Y. Tang, Y. Liu and Z. Gao, Ind. Eng. Chem. Res. 35 (1996) 430.
26. P. Canizares, A. Carrero and P. Sanches, Appl. Catal. A Gen. 190 (2000) 93.
27. W.L. Duncan and K.P. Möller, Stud. Surf. Sci. Catal. 135 (2001) 3073.

4

The Effect of Acid Leaching on the Adsorption, Diffusion and Reaction of *n*-Hexane over Pt/H-Mordenite: a TEOM Study

Abstract

Uptake experiments under full catalytic conditions have been performed using a tapered element oscillating microbalance (TEOM). The effect of acid leaching on the diffusivity and reaction of *n*-hexane in Pt/H-Mordenite has been established from these experiments. For the acid leached Pt/H-Mordenite the hydroisomerization activity is four times higher than for the untreated Pt/H-Mordenite. Acid leaching gives rise to an acceleration of the uptake of *n*-hexane under reaction conditions. Analysis of the data implies the faster uptake to be predominantly accounted for by a shorter intracrystalline diffusion pathlength, as diffusivities are in the same range for both catalysts. The shorter pathlength results from the mesoporous structure of H-Mordenite generated by acid leaching. From the diffusivities, the pathlengths and by using the Thiele model, it is inferred that the weight-based intrinsic rate constant of acid leached Pt/H-Mordenite is twice that of the untreated Pt/H-Mordenite. The facilitated transport of reactants and products doubles the effectiveness factor, thereby also contributing to the overall activity enhancement for *n*-hexane hydroisomerization after acid leaching.

Introduction

Zeolites are microporous crystalline structures that are widely applied as adsorbents and solid acid catalysts in petroleum and chemical process industries. Transport through zeolitic micropores occurs by diffusion and often affects or even controls the overall rate of the process [1]. Optimization of catalytic and adsorption processes therefore requires knowledge of all phenomena that influence diffusional behavior of molecules in such materials. A number of techniques is available to experimentally determine diffusivities in zeolites, but none of them is suitable for simultaneously monitoring adsorption, diffusion and reaction. This illustrates the need for the development of an experimental procedure to monitor these phenomena concurrently in one set-up. A catalysis set-up including a tapered element oscillating microbalance (TEOM) offers the possibility to monitor adsorption and diffusion in a quantitative way, as has been shown by Chen *et al.* [2]. At the same time a TEOM provides the possibility to work under representative catalysis conditions, as the properties of a down-flow fixed bed reactor are maintained. Here we report a first-of-its-kind study using a TEOM in which adsorption and diffusion are measured under full catalytic conditions for the hydroisomerization of *n*-hexane over Pt/H-Mordenite.

Pt/H-Mordenite is a highly suitable catalyst for the hydroisomerization of linear alkanes to branched ones, although the limited intracrystalline molecular transport may significantly slow down the catalyst performance [3]. To this end, it is generally known that acid leaching of the mordenite structure enhances the hydroisomerization activity [3-7]. In addition, it has been shown that local destruction of the mordenite crystals by growing large Pt-particles inside also results in a higher hydroisomerization activity [8]. In a study by Tromp *et al.* [9] it was demonstrated that acid leaching leads to dealumination and the creation of mesopores that have recently been visualized by 3D-TEM [10]. This is accompanied by an enhanced catalytic activity for *n*-hexane hydroisomerization. Moreover the selectivity changed slightly to favor primary products [9]. The origin of the increased hydroisomerization rate after acid leaching of the mordenite may, in case of a diffusion limited reaction, be explained by the following options:

- An increase in the intracrystalline diffusion coefficient as a result of a faster molecular transport through the micropores.
- A decrease in the intracrystalline pathlength L related to the generation of mesopores, again resulting in a faster transport.
- An increase in the intrinsic activity, *i.e.* an enhancement of the *n*-hexane hydroisomerization rate per Brønsted acid site.

The present work deals with the adsorptive and diffusional behavior of *n*-hexane in an untreated as well as in an acid leached Pt/H-Mordenite and the simultaneous assessment of their influence on the hydroisomerization performance. We will report on the determination of diffusivities and intrinsic activities for the same Pt/H-Mordenite catalysts that were evaluated by Tromp *et al.* [9]. The *n*-hexane uptake curves are measured in a TEOM-reactor under full catalytic conditions. The experimental data obtained with the TEOM-set-up are fitted into an adapted theoretical model to acquire diffusion coefficients. The application of this method will be exemplified by performing check experiments in which the conditions for the *n*-hexane uptake are varied.

Based on both diffusivities as well as catalysis results, intrinsic activities are computed and evaluated. In the end it is shown that both a better accessibility of the crystals as well as an increase in intrinsic activity will contribute to the observed increase in hydroisomerization rate after acid leaching.

Experimental

TEOM

The operation of the tapered element oscillating microbalance [Rupprecht & Pataschnick TEOM 1500 PMA] is based on the relationship between natural frequency (*f*) of the oscillating tapered element, containing the catalyst, and its mass (*m*):

$$m_2 - m_1 = K_0\left[\left(\frac{1}{f_2}\right)^2 - \left(\frac{1}{f_1}\right)^2\right] \qquad (1)$$

K_0 is the spring constant for the tapered element used in the experiment and the subscripts 1 and 2 refer to the change of mass and frequency with time. One of the major advantages of the design is that it provides a packed catalyst bed through which all the gas is forced to flow, as depicted in Figure 1. For a detailed description of the TEOM we refer to Chen *et al.* [2] and Zhu *et al.* [11].

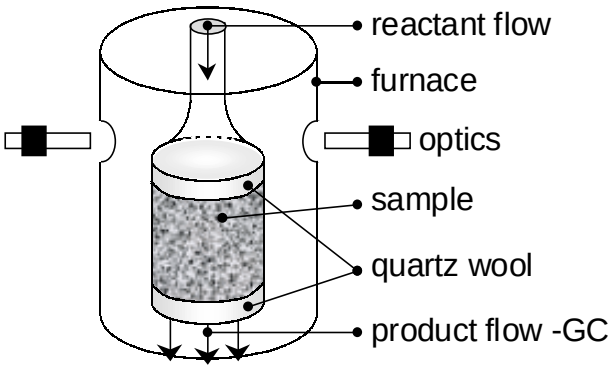

Figure 1. Schematic picture of the oscillating tapered element with the packed sample bed.

Table 1. Physicochemical characterization of the mordenite samples.

Sample	HMOR-P	HMOR-L
Mesoporous surface area (m^2 g^{-1})	30	89
Micropore volume (ml g^{-1})	0.19	0.18
Mesopore volume (ml g^{-1})	0.04	0.11
Si/Al ratio from XRF (mol mol^{-1})	6	20
Acid sites by *n*-propylamine TPD (mmol g^{-1})	2.1	1.1
Acid sites by isopropylamine TPD (mmol g^{-1})	1.4	1.1
Acid sites by ammonia TPD (mmol g^{-1})	2.3	0.7
Pt-Pt co-ordination number from EXAFS[#]	6.5 – 7.0	6.5 – 7.0

[#]Determined for the Pt/HMOR samples

Samples

The parent mordenite (HMOR-P) has a zeolite crystal size of 0.2 x 0.4 μm and Si/Al = 6. The acid leached mordenite (HMOR-L) has a lower bulk aluminum content, *i.e.* Si/Al = 20. Physicochemical properties of the H-Mordenite samples are presented in Table 1. Clearly acid leaching generates mesopores in the H-Mordenite crystals in line with earlier results from electron microscopy [9,10]. The 2 wt% Pt/H-Mordenite (Pt/HMOR) catalysts were prepared as described earlier by Tromp *et al.* [9].

Experiments

Hydroisomerization of *n*-hexane was carried out in the TEOM-reactor so that mass changes occurring during the catalytic action of the Pt/H-Mordenite can be monitored *in situ*, *i.e.* at high temperatures. A backpressure regulator maintained the pressure of the system at 1.3 bar. Mass flow controllers adjusted the incoming gas flows. The *n*-hexane (Merck) was injected into the system using an HPLC pump (Shimadzu LC-10AD). The reaction products were analyzed using a Shimadzu 17A gas chromatograph with a GS-GasPro capillary column (fused silica, 15 m x 0.32 mm). The system was heated to avoid condensation of gases.

Prior to testing, the samples were dried and reduced *in situ* in hydrogen at 623 K. Experiments were executed at 523 K and 1.3 bar using ~85 mg of sample with a particle size of 150 - 425 μm. Adsorption isotherms were determined under transient conditions by varying the *n*-hexane partial pressure at a total pressure of 1.3 bar and a constant H_2 flow. The transient uptake experiments were performed using an *n*-hexane flow of 0.078 $mmol.min^{-1}$ and H_2 flow of 20 $ml.min^{-1}$ (H_2:*n*-C_6 ratio 11 $mol.mol^{-1}$). After the *n*-hexane was added to the feed, t = 0 was defined as the last data-point before the first mass change detected by the TEOM. All mass changes were corrected for temperature- and gas density differences by performing blank runs over inert samples.

In between every experiment, the samples were regenerated in H_2 at 623 K to ensure a clean sample. To determine the influence of product formation on the uptake of *n*-hexane, measurements were also performed on samples without Pt. In addition, the *n*-hexane uptake measurements were performed with a lower *n*-hexane partial pressure (H_2:*n*-C_6 ratio 22 mol.mol^{-1}), a higher flow rate of both *n*-hexane and H_2 and using a lower amount of catalyst. In this way it was tested if consistent uptake data can be obtained using the TEOM set-up. The reversibility of the adsorption on the samples was checked as well by monitoring the amount of desorbed species following the uptake experiment.

The catalytic conversion of *n*-hexane over the Pt/H-Mordenites was determined at steady-state adsorption conditions in the TEOM, directly following an uptake experiment. Conversion is defined as the ratio of all products (≠ *n*-C_6) to all compounds detected. Selectivities are calculated as the ratio of a certain product to all products (≠ *n*-C_6). To be able to measure all samples at low conversions (< 5 %), the amount of catalyst and/or the *n*-hexane and H_2 flow were varied (the H_2:*n*-C_6 ratio was kept constant at 11 mol.mol^{-1}).

Theory

Fick's Second Law

The non-steady state diffusion of *n*-hexane in Pt/H-Mordenite is assumed to take place according to Fick's second law, which describes the change of the overall concentration inside the zeolite crystals as a function of time:

$$\frac{\partial C}{\partial t} = D * \left(\frac{\partial^2 C}{\partial x^2} \right) \tag{2}$$

However, it contains the inherent assumption that all molecules equally contribute to the process of stochastic displacement. For uptake measurements over zeolites this is usually not true, as molecules inside the zeolite crystals are present in two phases, a mobile phase and an immobile adsorbed phase. Hence, the diffusivity (*D)* in equation 2 corresponds to the uptake diffusivity based on the total concentration inside the zeolite crystals, *i.e.* including mobile as well as immobile species. To represent diffusivity for merely the mobile species in the zeolite one has to multiply the measured uptake diffusivity (D_{uptake}) with the ratio between all sorbed species at equilibrium (C_{eq}) and the mobile species at equilibrium, resulting in an intrinsic diffusivity [12]. In catalysis the diffusion process under steady state conditions is particularly relevant. Therefore, we take the concentration of mobile species to be equal to the concentration in the gas

phase (C_{gas}) since kinetic data are also based on the applied gas phase concentration. The following relation allows then the calculation of the intracrystalline steady state diffusivity (D_{ss}):

$$D_{ss} = \frac{C_{eq}}{C_{gas}} * D_{uptake} \tag{3}$$

As the steady state diffusivity is based on the gas phase concentration of the system, evaluation of diffusion and catalysis results may now be performed on the same concentration basis, which is of major importance as was stressed by Post [13]. Moreover, Garcia and Weisz [12] showed that possible deviations introduced by this assumption are small, even in the non-linear region of a Langmuir-type adsorption. In general, the obtained steady state diffusivities represent values that are consistent with catalytic diffusivities [12-16] and usually are two to four orders of magnitude larger than uptake diffusivities. However, it is important to realise that the steady state diffusivities do not necessarily represent intrinsic self-diffusivities as determined by for example PFG-NMR-studies. They describe net diffusivities based on the catalytic conditions applied including its effects on transport phenomena as scaled to reaction kinetics for the zeolite [16,17].

Fitting of the Uptake Curves

For crystals with slab geometry like mordenite, the experimental uptake curves may be described by the appropriate solution of Fick's second law [1,18]:

$$\frac{m_t}{m_{eq}} = 1 - \frac{8}{\pi^2} \sum_{n=0}^{\infty} \frac{1}{(2n+1)^2} * e^{-\frac{(2n+1)^2 \pi^2 t D_{uptake}}{4L^2}} \tag{4}$$

Where m_t and m_{eq} represent the amounts of adsorption at time t and equilibrium respectively and L is the intracrystalline diffusion pathlength. If the experimental uptake curves are fitted using this equation, no good fits are obtained, as the time delay of the set-up was not taken into account. The time delay occurs as a result of a concentration gradient over the catalyst bed, since no immediate constant concentration is established at the surface of the crystals after the start of the uptake experiment. The effect of this time delay on the experimental uptake curve may be approached by using the following equation [19]:

$$C_t^{surface} = C_{eq}^{surface} * \left(1 - e^{-\beta \cdot t}\right) \tag{5}$$

Where β stands for a constant, which is equal to the reciprocal of the delay time.

The occurrence of intercrystalline diffusion besides intracrystalline diffusion and the presence of a stagnant layer around the zeolite particles may slow down the observed diffusion as well [1,16,17]. However, based on check-experiments shown in the results section of this paper (*vide infra*), it is argued that the uptake experiments will not suffer from a large influence of these phenomena as convective gas transport predominates in the packed bed reactor using a TEOM (Figure 2).

The analytical solution for the transient diffusion equation including the correction for the time delay has been derived and reads:

$$\frac{m_t}{m_{eq}} = \int_0^t \left\{ \left[1 - e^{-\beta\left(t - t'\right)} \right] * \sqrt{\frac{D_{uptake}}{\pi L^2 t'}} * \sum_{n=0}^{\infty} \left[e^{-\frac{L^2}{t' D_{uptake}}(2n+2)^2} + e^{-\frac{L^2}{t' D_{uptake}}(2n)^2} - 2e^{-\frac{L^2}{t' D_{uptake}}(2n+1)^2} \right] \right\} dt' \qquad (6)$$

Mathematical information concerning the derivation and application of this equation is available from the authors. The experimental uptake data were fitted using this equation and the best fits yielded the parameters L^2/D_{uptake} and β. To determine D_{uptake} the intracrystalline diffusion pathlength L must be known. By applying equation 3, the obtained uptake diffusivity can be transformed into a steady state diffusivity.

Thiele Modulus and Rate Constants

The extent to which diffusional transport limits the reaction rate can be quantified by use of the Thiele relationship giving the effectiveness of a catalyst (η) as a function of the dimensionless Thiele modulus (ϕ):

$$\eta = \frac{\tanh \phi}{\phi} \qquad (7)$$

When the Thiele modulus is small, the effectiveness factor approaches unity. This means there is very little variation in reactant concentration throughout the zeolite crystal and the rate of the reaction is controlled by the intrinsic chemical kinetics. On the other hand, when the Thiele modulus is large, the reactant concentration will become significantly lower going from the outside to the inside of the zeolite crystal and the reaction is said to be diffusion controlled or diffusion limited [1]. To obtain the Thiele modulus, one first has to determine the apparent reaction rate constant. As the

hydroisomerization reaction is approximately first order in *n*-hexane [20], the volumetric first order rate constant based on the micropore volume may be calculated following:

$$k_v^{\text{apparent}} = -\frac{\phi_v}{V_{micropores}} \ln(1 - X) \tag{8}$$

The Thiele modulus can then be computed using:

$$\phi = L\sqrt{\frac{k_v}{D_{ss}}} \tag{9}$$

Note that steady state diffusivities are used in this equation as the Thiele model holds for k_v and D at identical concentration basis [13]. From the Thiele modulus the effectiveness factor can be determined using equation 7. The intrinsic rate coefficient is then computed by:

$$k_v^{\text{intrinsic}} = \frac{k_v^{\text{apparent}}}{\eta} \tag{10}$$

By filling out the obtained intrinsic rate constant in equation 9, subsequently followed by calculating equation 7 and 10 again, a better approximation of the intrinsic rate coefficient is acquired. This process is repeated until no noticeable change in the obtained intrinsic rate constant is observed.

Results

Uptake Experiments

The adsorption isotherms obtained at 523 K for *n*-hexane in Pt/HMOR-P and Pt/HMOR-L are depicted in Figure 2. For Pt/HMOR-L the isotherm was found to be fully reversible, however, for Pt/HMOR-P it was not, most likely as a result of the formation of branched products that remain trapped inside the crystals.

The fitting results of all *n*-hexane uptake experiments are collected in Table 2, with the experiment number denoted in the first column. All experimental uptake curves were fitted using equation 6, so that values for the uptake diffusional time constant (L^2/D_{uptake}) and the parameter β are obtained. To calculate the uptake diffusion coefficient, the square of the intracrystalline diffusion pathlength L is divided by the uptake diffusional time constant (L^2/D_{uptake}). For HMOR-P, L is 0.2 μm, established

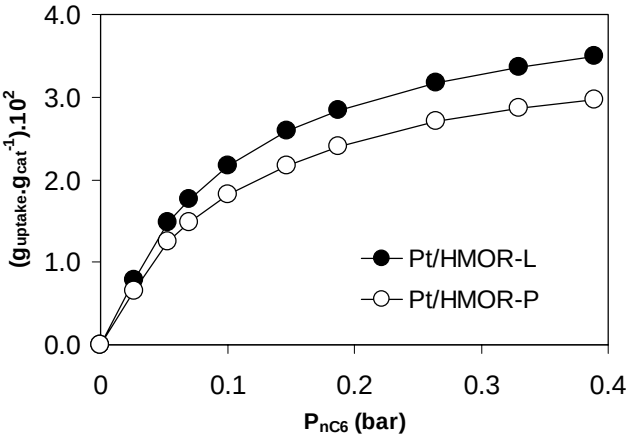

Figure 2. Adsorption isotherms of *n*-hexane in Pt/HMOR-P (exp. 2) and Pt/HMOR-L (exp. 7) determined under transient conditions at 523 K and a total pressure of 1.3 bar.

from transmission electron microscopy data [9]. For HMOR-L, L is estimated to be 0.06 μm by multiplying the ratio of the mesopore areas for HMOR-P and HMOR-L, determined by nitrogen physisorption (Table 1), with the L of HMOR-P. The steady state diffusivities are calculated by multiplying the uptake diffusivity by the ratio between all sorbed species at equilibrium and the gas phase concentration [12], according to equation 3.

Table 2. Results of *n*-hexane uptake experiments performed on (Pt)/H-MOR samples at 523 K and 1.3 bar.

Experiment		*Exp. conditions*			*Fitting results*						
No	Sample	Mass (mg)	Flow (ml.min^{-1})	H_2/nC_6 (mol.mol^{-1})	L^2/D_{uptake} (s)	β^{-1} (s)	Chi$^{2\,\#}$	L (m)	D_{uptake} (m^2.s^{-1})	C_{eq}/C_{gas}	D_{ss} (m^2.s^{-1})
1.	**HMOR-P**	85	21.7	11	139	125	$5*10^{-3}$	$2*10^{-7}$	$2.9*10^{-16}$	328	$1.0*10^{-13}$
2.	**Pt/HMOR-P**	85	21.7	11	147	109	$7*10^{-3}$	$2*10^{-7}$	$2.7*10^{-16}$	311	$0.8*10^{-13}$
3.		85	20.9	22	161	99	$8*10^{-3}$	$2*10^{-7}$	$2.5*10^{-16}$	412	$1.0*10^{-13}$
4.		85	43.4	11	158	58	$9*10^{-3}$	$2*10^{-7}$	$2.5*10^{-16}$	318	$0.8*10^{-13}$
5.		17	21.7	11	154	21	$6*10^{-3}$	$2*10^{-7}$	$2.6*10^{-16}$	301	$0.8*10^{-13}$
6.	**HMOR-L**	85	21.7	11	14	114	$8*10^{-3}$	$6*10^{-8}$	$2.6*10^{-16}$	409	$1.1*10^{-13}$
7.	**Pt/HMOR-L**	85	21.7	11	16	104	$6*10^{-3}$	$6*10^{-8}$	$2.2*10^{-16}$	396	$0.9*10^{-13}$
8.		85	20.9	22	19	88	$6*10^{-3}$	$6*10^{-8}$	$1.9*10^{-16}$	519	$1.0*10^{-13}$
9.		85	43.4	11	20	61	$8*10^{-3}$	$6*10^{-8}$	$1.8*10^{-16}$	400	$0.7*10^{-13}$
10.		17	21.7	11	21	25	$9*10^{-3}$	$6*10^{-8}$	$1.7*10^{-16}$	393	$0.7*10^{-13}$

$^{\#}\ \mathrm{Chi}^2 = \sum_i \left(y_i^{obs} - y_i^{calc}\right)^2$, where y is the uptake- and i the time parameter (Note: $y_{max} = 1$)

In order to visualize the influence of the acid leaching treatment on the *n*-hexane uptake, the curves for Pt/HMOR-P (No. 2) and Pt/HMOR-L (No. 7) are given in Figure 3. The curves are measured at 0.1 bar *n*-hexane partial pressure, hence at the border of the linear part of the respective isotherm. From Figure 3 it is obvious that the rate and amount of adsorption are significantly enlarged as a result of the acid treatment. In Figure 4 the fits for these experiments are displayed and it is demonstrated that the Fickian diffusion model given in equation 6 is appropriate to describe the uptake curves obtained with our experimental set-up. The linear behavior of the curves originates from the presence of the experimental time delay of the set-up, described by equation 5, as earlier reported by Karge and Niessen [19]. The presence of this time lag causes the absence of 'square root' behavior in the experimental and fitted uptake curves. To check the validity of the application of a Fickian diffusion model, uptake curves have also been conducted at lower *n*-hexane partial pressure, *i.e.* within the linear part of the isotherm. Experiments No. 3 and 8 in Table 2 represent the measurements performed at this lower *n*-hexane partial pressure of 0.05 bar (H_2/nC_6 molar ratio of 22). Since under these conditions similar values for the diffusivities are

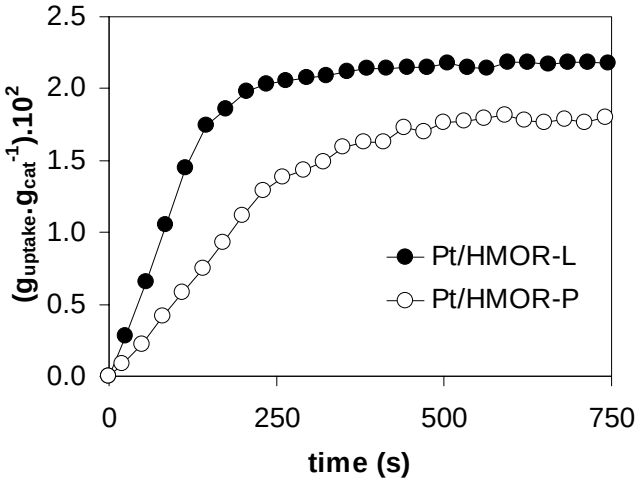

Figure 3. Experimental uptake curves for *n*-hexane over Pt/HMOR-P (exp. 2) and Pt/HMOR-L (exp. 7) using 85 mg sample and a H_2/nC_6 molar ratio of 11; *n*-hexane is introduced step-wise to the sample at time zero.

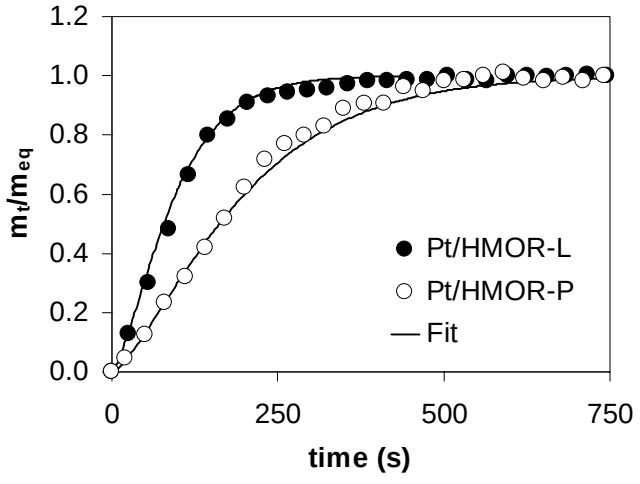

Figure 4. Experimental (normalized) and fitted curves for *n*-hexane over Pt/HMOR-P and Pt/HMOR-L for the experiments conducted with 85 mg sample and a H_2/nC_6 molar ratio of 11 (fits are obtained by the use of equation 6).

obtained as at 0.1 bar *n*-hexane partial pressure, it is inferred that a Fickian diffusion model as represented in equation 6 is applicable to evaluate the uptake data obtained in this study.

To check whether the occurrence of intercrystalline diffusion may play a role in these experiments, *n*-hexane uptake curves were also measured with a doubled flow rate of both *n*-hexane and H_2 and with a five times lower amount of catalyst as shown in Table 2 experiment No. 4, 9 and. 5, 10 respectively. From this it is clear that the parameter β^{-1} proportionally decreases with doubling the feed or lowering the amount of catalyst while the same values for L^2/D_{uptake} were obtained.

By studying samples without platinum the influence of product formation on the uptake of *n*-hexane was checked. Since similar values of L^2/D_{uptake} for both HMOR-L and Pt/HMOR-L (No. 6 and 7) and for HMOR-P and Pt/HMOR-P (No. 1 and 2) were obtained, it is concluded that the uptake measurements performed do not suffer from counter diffusion between reactant and product molecules.

From Table 2 it is clear that after acid leaching a decrease in diffusional time constants (L^2/D_{uptake}) is observed, *i.e.* the times to reach an equilibrium amount of uptake in the crystals is shorter. However, after taking into account the estimated diffusion pathlengths and applying equation 3, both samples display steady state diffusivities (D_{ss}) in the same order of magnitude. This implies the enhanced uptake after acid leaching to be predominantly due to a decreased diffusion pathlength *L*.

The total amounts of molecules that desorb following the uptake experiments have been determined for HMOR-P, Pt/HMOR-P HMOR-L and Pt/HMOR-L and are displayed in Figure 5. The reduced desorption of molecules for Pt/HMOR-P, as compared to HMOR-P, HMOR-L and Pt/HMOR-L is clearly illustrated and most likely arises from the formation of branched products which remain trapped as immobile species inside the parent mordenite crystals.

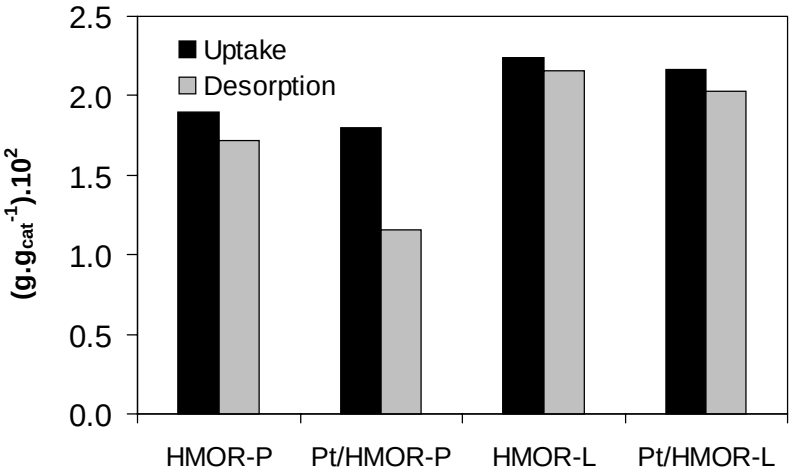

Figure 5. Amounts of uptake (adsorption) and desorption for HMOR-P, Pt/HMOR-P, HMOR-L and Pt/HMOR-L at 523 K and a H_2/nC_6 molar ratio of 11.

Table 3. Results for n-hexane hydroisomerization at 523 K, 1.3 bar and $H_2/nC_6 = 11$ mol.mol^{-1}.

Sample	Pt/HMOR-P	Pt/HMOR-L
Flow (ml min^{-1})	21.7	43.4
Sample amount (mg)	17	6
Conversion (mol %)	3.9	3.0
Relative activity	1	4.2
Selectivity to monobranched	0.78	0.82
Selectivity to dibranched	0.02	0.01
Selectivity to cracking products	0.20	0.17

Catalytic testing

In Table 3 the *n*-hexane hydroisomerization activities and product selectivities for Pt/HMOR-P and Pt/HMOR-L at 523 K are collected. Results are obtained under differential conditions (3 - 4% conversion) by varying the flow-rate and amount of catalyst. After acid leaching the relative activity per gram increases, confirming the results of Tromp *et al.* [9] and others [3,4,7]. Both samples show high selectivities to monobranched isomers, although dibranched isomers and cracking products were also formed. The acid leaching resulted in a slight increase in the selectivity to monobranched products while the selectivities towards dibranched- and cracking products decreased, which is in agreement with results from Chica *et al.* [21].

Based on the experimentally applied conditions and the differentially measured conversions, the Thiele modulus, effectiveness factor and apparent- and intrinsic rate constants are calculated for both Pt/HMOR-P and Pt/HMOR-L at 523 K using equations 7 to 10. Both the effectiveness factor and intrinsic activity are about doubled after the acid treatment. All numerical values are collected in Table 4.

Discussion

Diffusion

From the raw data in Figure 3 it is clear that the uptake of *n*-hexane is much faster in Pt/HMOR-L than in Pt/HMOR-P, indicating a higher accessibility as a result of the acid treatment. Fitting of the experimental data reveals the values for the diffusional time constant, L^2/D_{uptake}, and the time delay parameter β^{-1} as displayed in Table 2. To test whether irregularities like the occurrence of intercrystalline diffusivity appear during the uptake measurements, check-experiments have been performed and as expected β^{-1} proportionally decreased with doubling the feed or lowering the amount of catalyst while the same values for L^2/D_{uptake} were obtained.

Table 4. Rate constants and Thiele modulus determined by using equations 7 to 10.

Sample	T (K)	$k_{apparent}$ (s^{-1})	ϕ	η	$k_{intrinsic}$ (s^{-1})
Pt/HMOR-P	523	4.5	2.3	0.42	10.7
Pt/HMOR-L	523	18.7	1.0	0.77	24.2

Under the standard conditions applied here (85 mg sample, flow rate 21.7 ml min^{-1}) the values for β^{-1} are around 100 s, illustrating the time delay of the set-up. Based on the experimental conditions applied, the calculated minimum time to feed the required amount of *n*-hexane to a sample bed of 85 mg and establish a constant surface concentration should range from 10 to 40 s. The origin of the higher β^{-1} values observed results from the fact that in practice not all molecules in the feed stream adsorb in the uptake experiment. The experimental time delay causes the absence of 'square root' behavior in the experimental and fitted uptake curves.

The fitting results demonstrate that the faster uptake of *n*-hexane for Pt/HMOR-L results in lower values for the diffusional time constants under all conditions applied. Dividing the square of the intracrystalline diffusion pathlength L by the uptake diffusional time constant (L^2/D_{uptake}), provides an estimate of the uptake diffusion coefficients. For Pt/HMOR-P L = 0.2 μm, derived from transmission electron microscopy data [9]. For Pt/HMOR-L, L is not exactly known as by the acid treatment mesopores have been created resulting in a less ordered crystal structure. Nevertheless, based on nitrogen physisorption data the best estimate for the L of Pt/HMOR-L is 0.06 μm. This value seems to be reasonable when compared with a recently published 3D-TEM study in which the mesopores of Pt/HMOR-L were visualized [10].

The steady state diffusivities are calculated by multiplying the uptake diffusivities with the ratio between the adsorbed species at equilibrium and the gas phase concentration (Eq. 3). This ratio is applied to allow integration of the uptake results with the simultaneously monitored catalytic properties of the Pt/H-Mordenites. As is clear from Table 2, steady state diffusivities are in general two to three orders of magnitude larger than uptake diffusivities. This is consistent with diffusion data available on zeolites other than mordenite [12,13,15,16].

It has been shown in the literature that acid leaching may result in the destruction of the mordenite crystals accompanied by the formation of mesopores [22, 23]. For the acid leached sample [Pt/HMOR-L] we used in this study, Tromp *et al.* [9] and Koster *et al.* [10] have visualized this. In addition, it has been shown that the acid treatment resulted in dealumination, the formation of extra framework aluminum *i.e.* Lewis acid sites, local destruction of the 8-membered ring side-pockets and/or the selective removal of acid sites [9]. Despite the presence of all these phenomena, we observed no noticeable change in steady state diffusivities after acid leaching (Table 2), which

indicates that the one-dimensional mordenite structure is still intact. This suggests that the accelerated uptake of *n*-hexane after acid leaching, *i.e.* the lower diffusional time constant (L^2/D_{uptake}) is predominantly caused by the shorter intracrystalline diffusion pathlength L resulting from the mesoporous structure of Pt/HMOR-L. The absolute values for the steady state diffusivities are low as the numbers are based on the externally applied gas phase concentration and may be affected by counter diffusion effects, adsorption phenomena and/or single-file diffusion [8,24].

The uptake of alkanes over Pt/H-Mordenite has been suggested to proceed in the single-file diffusion regime [3,8], although conflicting data concerning this subject are available in literature [25-27]. In case this study would suffer from single-file diffusion, the Thiele model applied is no longer valid [24]. However, mordenite is a 12-membered ring zeolite and the kinetic diameter of *n*-hexane is 4.3 Å. The occurrence of single-file diffusion is not likely at low prevailing *n*-hexane pressure [26]. Moreover, counter diffusion with product molecules is shown to have minor influence since similar values for D_{ss} are obtained for samples with (Pt/HMOR) and without platinum (HMOR). This leaves us with adsorption phenomena as the cause of the low values for D_{ss}. In other words, the concentration of mobile species in the pores is to all appearances [much] lower than the applied gas phase concentration, meaning that the obtained steady state diffusivities do not necessarily represent the intrinsic self-diffusivities as determined by for example PFG-NMR-studies [17]. However, several authors have stressed that values for steady state diffusivities coincide with the numbers for catalytically derived diffusivities [12-16] and therefore the values we have obtained in this study describe the net transport phenomena occurring in our Pt/H-Mordenite samples under the catalytic conditions applied. To our knowledge, no PFG-NMR data on the diffusion of alkanes in mordenite are available in literature, probably because of the inappropriate (too long) time-scale for diffusion. In general, it must be stressed that differences in definitions of diffusivity can lead to different values of intracrystalline diffusivities and concentration dependencies respectively [16]. Considering the evaluation of results obtained by different groups, it is therefore important that one specifies the conditions and methods under which diffusion experiments are executed.

Catalysis

As is shown in Table 3 the *n*-hexane hydroisomerization activity per gram of catalyst is increased by a factor 4.2 after the acid treatment. This coincides with the higher accessibility of the Pt/HMOR-L (Figure 3) that displays a mesoporous crystal structure [9,10] with a higher amount of pore-inlets available for reaction. During hydroisomerization, methylpentanes will be formed as primary products. For Pt/HMOR-P, the transport of branched products through the crystals will be more difficult as the diffusion pathlength is longer, which results in the formation of

secondary products. The reduced desorption of products for Pt/HMOR-P as compared to Pt/HMOR-L is further illustrated in Figure 5. Opening up the crystal structure on a mesoscopic scale, as done by acid leaching, results in a faster exchange of reaction products and therefore a shift towards a higher methylpentane selectivity and a lower dimethylbutane selectivity, as summarized in Table 3. Under the conditions applied in this study the activity of the Pt/H-Mordenite catalysts will be affected by the intracrystalline transport, which implies that the accessibility of the active sites, but also their density and acidity are of major importance. From the computed effectiveness factors (Table 4) it is clear that there is a large increase in the amount of catalyst that is effectively used after acid leaching. Moreover, from the intrinsic rate constants it is deduced that the intrinsic activity on a weight basis is doubled. Part of the increase as a result of the acid treatment therefore is explained by this increase in intrinsic activity, which is caused by an enhancement of the activity per Brønsted acid site resulting from the lower framework-aluminum content for Pt/HMOR-L. The other part of the increase in hydroisomerization activity is caused by an alleviation of intracrystalline diffusion limitation, which is predominantly induced by the shorter intracrystalline diffusion pathlength L resulting from the mesoporous structure that enables an enhanced transport of reactant and product molecules. The activity enhancement caused by acid leaching in this work is explained $\sim$50/50 by intrinsic activity and mass transport. The exact balance between the two, of course, will be sensitive to both details of the MOR-crystals and the reaction conditions in question.

Conclusions

Using a tapered element oscillating microbalance (TEOM), it has been demonstrated for the first time that diffusivities can be established from uptake experiments performed under catalytic conditions. By applying an adapted diffusion model, uptake and steady state diffusivities for *n*-hexane in Pt/H-Mordenite have been obtained. The diffusion of *n*-hexane in Pt/H-Mordenite is not affected by counter diffusion between reactant and product molecules. These quantitative results have been used for studying the effect of acid leaching on the performance of Pt/H-Mordenite for *n*-hexane hydroisomerization.

Acid leaching largely accelerates the uptake and rate of hydroisomerization of *n*-hexane in Pt/H-Mordenite and in addition, an increase in primary reaction products is observed. An increase of the intrinsic activity and an alleviation of intracrystalline diffusion limitation of hydrocarbon molecules equally cause the overall activity increase after acid leaching. The faster mass transfer is predominantly accounted for by

a decrease of the intracrystalline diffusion pathlength resulting from the mesoporous structure created by acid leaching.

Notation

C_{gas}, C_{eq}	gas phase concentration, adsorbed concentration at equilibrium [mol.m^{-3}]
D_{uptake}, D_{ss}	uptake- and steady state diffusivity [m^2.s^{-1}]
f	frequency [s^{-1}]
k_v	volumetric rate coefficient [s^{-1}]
K_0	spring constant [g.s^{-2}]
L	intracrystalline diffusion pathlength [= half length of crystal] [m]
m_t, m_{eq}	amount adsorbed at time t and equilibrium [g.g$_{cat}^{-1}$]
m	mass [g]
t, t'	time and time integration parameter [s]
$V_{micropores}$	total micropore volume of the catalyst crystals [m^3]
x	distance [m]
X	conversion of *n*-hexane
β	delay constant [s^{-1}]
η	effectiveness factor
ϕ	Thiele modulus
ϕ_v	total volumetric flow of feed at actual conditions [m^3.s^{-1}]

Acknowledgements

Dr. Jeroen van Bokhoven (ETH Zürich), Moniek Tromp and Prof. Diek Koningsberger (Utrecht University) are acknowledged for initiating this work and helpful discussions; Dr. J. T. Miller (BP Amoco Research Center, Naperville IL) is acknowledged for providing the mordenites.

References

1. J. Kärger and D.M. Ruthven, "Diffusion in Zeolites and Other Microporous Materials", John Wiley and Sons, New York (1992).
2. D. Chen, H.P. Rebo, K. Moljord and A. Holmen, Chem. Eng. Sci. 51 (1996) 2687.
3. G.D. Lei, B.T. Carvill and W.M.H. Sachtler, Appl. Catal. A Gen. 142 (1996) 347.
4. P.B. Koradia, J.R. Kiovsky and M.Y. Asim, J. Catal. 66 (1980) 290.
5. I.E. Maxwell and W.H.J. Stork, in "Introduction to Zeolite Science and Practice" (H. van Bekkum, E.M. Flanigen, P.A. Jacobs and J.C. Jansen, Eds.) 2nd edition, Elsevier Science, Amsterdam (2001).

6. S.T. Sie, in "Advanced Zeolite Science and Applications" (J.C. Jansen, M. Stöcker, H.G. Karge and J. Weitkamp, Eds.), Elsevier Science, Amsterdam (1994).
7. A. Corma and A. Martinez, in "Catalytic Activation and Functionalization of Light Alkanes: Advances and Challenges" (E.G. Derouane, J. Haber, F. Lemos, F.R. Ribeiro and M. Guisnet, Eds.), Kluwer Academic, Dordrecht (1998) 35.
8. B.T. Carvill, B.A. Lerner, B.J. Adelman, D.C. Tomczak and W.M.H. Sachtler, J. Catal. 144 (1993) 1.
9. M. Tromp, J.A. van Bokhoven, M.T. Garriga Oostenbrink, J.H. Bitter, K.P. de Jong and D.C. Koningsberger, J. Catal. 190 (2000) 209.
10. A.J. Koster, U. Ziese, A.J. Verkleij, A.H. Janssen and K.P. de Jong, J. Phys. Chem. B 104 (2000) 9368.
11. W. Zhu, J.M. van de Graaf, L.J.P. van den Broeke, F. Kapteijn and J.A. Moulijn, Ind. Eng. Chem. Res. 37 (1998) 1934.
12. S.F. Garcia and P.B. Weisz, J. Catal. 121 (1990) 294.
13. D.M. Ruthven and M.F.M Post, in "Introduction to Zeolite Science and Practice" (H. van Bekkum, E.M. Flanigen, P.A. Jacobs and J.C. Jansen, Eds.) 2nd edition, Elsevier Science, Amsterdam (2001).
14. W.O. Haag, R.M. Lago and P.B. Weisz, Faraday Disc. 72 (1982) 317.
15. S.F. Garcia and P.B. Weisz, J. Catal. 142 (1993) 691.
16. J. Xiao and J. Wei, Chem. Eng. Sci. 47 (1992) 1143.
17. M. Bülow and A. Micke, Z. Phys. Chem. 189 (1995) 195.
18. J. Crank, "The Mathematics of Diffusion", Clarendon Press, Oxford (1975).
19. H.G. Karge and W. Niessen, Catal. Today 8 (1991) 451.
20. M. Guisnet, V. Fouche, M. Belloum, J.P. Bournonville and C. Travers, Appl. Catal. 71 (1991) 295.
21. A. Chica and A. Corma, J. Catal. 187 (1999) 167.
22. H. Stach, J. Jänchen, H.G. Jerschkewitz, U. Lohse, B. Parlitz, B. Zibrowius and M. Hunger, J. Phys. Chem. 96 (1992) 8473.
23. G.R. Meima, CATTECH 2 (1998) 5.
24. J. Kärger, M. Petzold, H. Pfeiffer, S. Ernst and J. Weitkamp, J. Catal. 136 (1992) 283.
25. A. van de Runstraat, J. van Grondelle and R.A. van Santen, J. Catal. 167 (1997) 460.
26. A. van de Runstraat, J.A. Kamp, P.J. Stobbelaar, J. van Grondelle, S. Krijnen and R.A. van Santen, J. Catal. 171 (1997) 77.
27. A. Rödenbeck, J. Kärger, K. Hahn and W.M.H. Sachtler, J. Catal. 183 (1999) 409.

5

Probing the Micropore Accessibility in Mordenite Crystals Using Adsorption and Diffusion Studies

Abstract

A novel approach, using the adsorption and diffusion of hydrocarbons, is presented to assess the accessibility of the micropores in the one-dimensional zeolite mordenite (MOR). The approach reveals a large discrepancy with the micropore accessibility probed by nitrogen physisorption. First, the accessibility of the micropores in 1-2 μm MOR crystals was established by examining the adsorption and diffusion of *n*-hexane using a tapered element oscillating microbalance (TEOM). It was demonstrated that a small amount of extra-framework aluminum (EFAl) species present in the MOR micropores induced a ~60 % decrease in the overall amount of adsorbed *n*-hexane, which was not observed using nitrogen physisorption. The characteristic time for diffusion, L^2/D, appeared to be decreased by 90% as compared to the value expected on the basis of the crystal size and literature data. Second, by performing line scans in a scanning electron microscope (SEM) equipped with an energy dispersive X-ray (EDX) facility, the blocking effect of such EFAl species on the uptake of hydrocarbons inside the MOR micropores was clearly visualized. With the EFAl present in the pores, the length of the crytsal open for reactants appeared to be 0.2 μm. After the removal of the EFAl by a mild treatment using oxalic acid, the uptake rate as well as the extent of adsorption of *n*-hexane was in line with a fully accessible micropore system. In general, it is demonstrated that it is of paramount importance for catalysis and diffusion research that the accessibility of the zeolite micropore volume is verified using the appropriate probe molecule.

Introduction

The zeolite mordenite (MOR) consists of parallel 12-membered ring (MR) channels with dimensions of 6.5 x 7.0 Å that are interconnected by 8 MR side pockets of 2.6 x 5.7 Å [1]. Because of the small size of the 8 MR channels it is difficult, if not impossible, for most hydrocarbon molecules to enter and therefore the MOR structure is generally regarded as one-dimensional [2-4]. One of the major applications of MOR is as a solid acid catalyst for the hydroisomerization of linear alkanes to branched ones for improving the octane quality of gasoline [5-7]. For this purpose the accessibility of the acid sites inside the micropores is of high importance. However, the adsorption of reactants and desorption of products, especially the preferred multiple branched ones, often suffer from diffusion limitation because of the one-dimensional pore system of MOR [3,8]. Moreover, several authors have suggested that in the case of a one-dimensional zeolite structure like MOR, crystal-growth defects and/or the presence of extra-framework alumina (EFAl) might block a large part of the micropore volume [9-12], making it unavailable for catalysis.

In a study by Hong and Fripiat [10] the adsorption of nitrogen and *n*-pentane on zeolite Y, ZSM-5 and MOR was compared with and without the presence of EFAl species. For zeolite Y and ZSM-5 minor differences were observed between nitrogen and *n*-pentane. However, for MOR the presence of EFAl species resulted in a significant decrease in the adsorption of *n*-pentane while almost no difference for nitrogen was detected. Hence, it was recognized that the use of nitrogen, although it is widely used as a probe to assess the surface area and micropore volume in zeolite catalysts, might give irrelevant information regarding the micropore accessibility for the hydrocarbons used in the reaction under study.

In the current study, a novel approach is presented to obtain detailed information on the micropore accessibility of MOR crystals. First, a tapered element oscillating microbalance (TEOM) is applied, which can monitor the rate and amount of hydrocarbon uptake at high temperature and under transient flow conditions [13,14]. In this way the reversible adsorption and diffusion of *n*-hexane is studied in order examine the extent of accessibility of the MOR micropores with and without EFAl species present. Second, scanning electron microscopy (SEM) in combination with energy dispersive X-ray analysis is applied to study the coke penetration depth on the MOR samples that were treated with *n*-butene, which is known to provoke coke formation inside zeolite micropores [15]. In this way a clear indication is obtained on the pathlength for free access from the crystal surface into the micropores with and without EFAl species present.

Experimental

H-Mordenite samples

Na-mordenite (NaMOR) with a Si/Al ratio of 5.5 was supplied by ExxonMobil. The Na^+ ions were exchanged for NH_4^+ ions to obtain the NH_4^+MOR by suspending 2.0 g NaMOR in a 200 ml aqueous solution of 1.0 M ammonium-nitrate at 353 K for 20 hours. After exchange the sample was filtered, washed and subsequently dried at 353 K for 12 hours. The exchange, washing and drying procedures were repeated twice. Inductive coupled plasma - atomic emission spectroscopy (ICP-AES) analysis showed the exchange to be complete. The obtained NH_4MOR was calcined in air by heating with a ramp of 1 K.min^{-1} up to 723 K, for 6 hours to obtain the H-form that will be referred to as HMOR.

Part of the HMOR sample was treated in a 100 ml aqueous solution of 0.1 M oxalic acid at 353 K for 1 hour. After this treatment the sample was filtered, washed and subsequently dried at 353 K for 12 hours and then calcined as described before. This treatment was executed twice and the obtained sample will be referred to as HMOR-ox.

The physicochemical characteristics of the two above prepared samples were obtained by nitrogen physisorption/t-plot analysis, ICP-AES, temperature programmed desorption - thermogravimetric analysis (TPD-TGA) using *n*-propylamine, scanning electron microscopy (SEM) in a Philips XL30FEG apparatus and ^{27}Al nuclear magnetic resonance spectroscopy (Al-NMR).

Experiments

Transient uptake measurements for *n*-hexane were performed at 523 K and a total pressure of 1.3 bar. Prior to the actual uptake experiment, the samples were dried *in situ* at 623 K. The measurements were executed in a TEOM reactor (Rupprecht & Pataschnick TEOM 1500 PMA) at 523 K using ~20 mg of sample (90-150 μm), *n*-hexane flow of 0.156 mmol min^{-1} and hydrogen flow of 40 ml min^{-1} (H_2:*n*C_6 ratio 11 mol/mol) at a total pressure of 1.3 bar. The *n*-hexane (Merck) is injected into the system using an HPLC pump (Shimadzu LC-10AD). Once the *n*-hexane is added to the system, the start of the uptake experiment (t = 0) is defined as the last data-point before the first mass change as detected by the TEOM. All mass changes have been corrected for gas density- and temperature effects by performing blank runs over inert samples. The experimental curves for *n*-hexane uptake in the HMOR crystals were fitted using an adapted Fickian diffusion model for crystals with slab geometry. This procedure is described in a previous study [14]. For further elaboration on the TEOM we refer to Chen *et al.* [13] and Zhu *et al.* [16].

Coked HMOR samples were prepared in the TEOM by the adsorption and reaction of *n*-butene during 20 hours at 623 K and 1.3 bar using a pure *n*-butene flow

with a weight hourly space velocity (WHSV) of 20 $g_{n\text{-}c4=}.g_{H\text{-}MOR}^{-1}.h^{-1}$. The tapered element was loaded with ~ 25 mg sample (particle size 90-150 μm) and prior to testing the samples were dried *in situ* in nitrogen at 623 K. The coked HMOR crystals were investigated in a SEM microscope (Philips XL30FEG) equipped with an EDX detector. By taking line scans over the HMOR samples the carbon (C) and zeolitic oxygen (O) signals were monitored. From this the C/O ratio was calculated in order to determine the penetration depth of the carbonaceous deposits into the 12 MR channels of the HMOR samples. In order to have no interfering carbon-signal, the regularly used carbon tape that covers the aluminum stub was replaced by a colloidal silver paste.

Results

Physicochemical characterization

The physicochemical characteristics of HMOR and HMOR-ox are collected in table 1. The ICP-AES results show that the mild treatment with oxalic acid causes an increase in the Si/Al ratio from 5.6 at/at to 8.0 at/at. No significant changes in the textural properties as determined by nitrogen physisorption were detected. Figure 1 shows a SEM image for HMOR, from which the crystal length is determined to be between 1 and 2 μm. After the treatment with oxalic acid, no changes in the crystal morphology were observed. Additionally, the HMOR samples were evaluated by Al-NMR and the results are displayed in figure 2. The signal at 55 ppm is ascribed to tetrahedral framework Al [17,18], although the tail below 50 ppm indicates that the peak also contains contributions from either distorted tetrahedral Al and/or EFAl species [18]. The broader peak around 0 ppm is generally ascribed to octahedral EFAl [17,18]. From the difference spectrum it is clear that upon the treatment with oxalic acid the overall amount of Al decreases and that almost all octahedral EFAl species are washed away. For the tetrahedral species that are removed, it is not clear if they are framework Al or EFAl species.

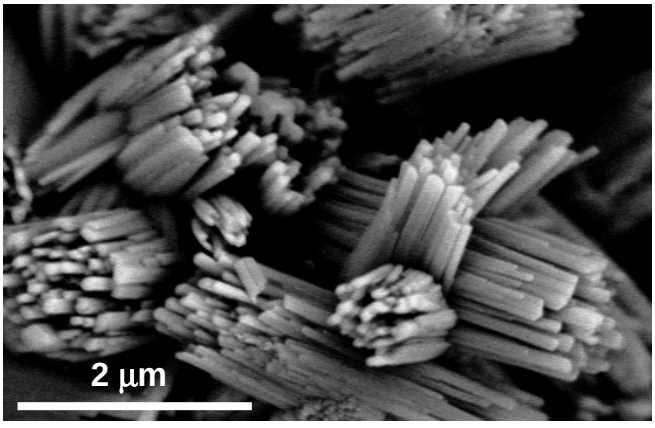

Figure 1. SEM image of the HMOR crystals.

Table 1. Physicochemical characteristics of the studied HMOR samples.

Sample	***H-MOR***	***H-MOR-ox***
Micropore volume ($ml.g^{-1}$)	0.16	0.17
Mesopore volume ($ml.g^{-1}$)	0.08	0.07
Mesopore area ($m^2.g^{-1}$)	67	52
Mean crystal length parallel to the 12 MR from SEM (μm)	1 - 2	1 - 2
Si/Al ratio (at/at) from ICP-AES	5.6	8.0
Acid sites by *n*-propylamine TPD-TGA ($mmol.g^{-1}$)	0.29	0.73
n-Hexane equilibrium uptake (wt%) at 523 K	0.56	1.53
n-Butene equilibrium uptake (wt%) at 623 K	3.7	8.2

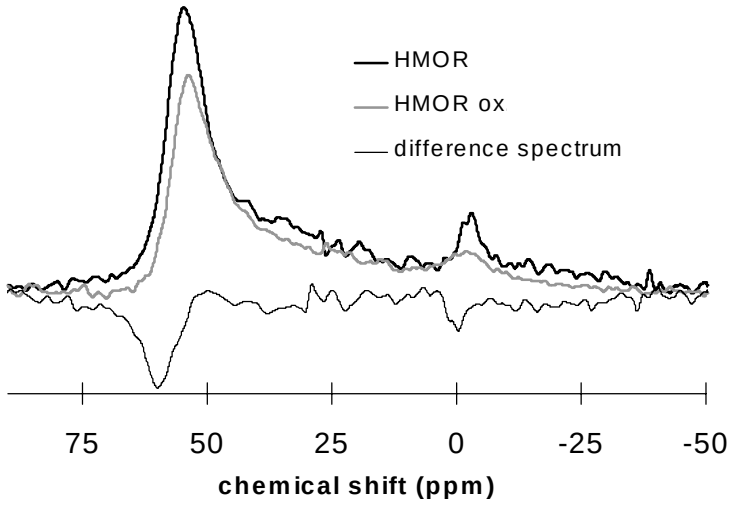

Figure 2. ^{27}Al-NMR spectra for HMOR and HMOR-ox normalized on their weight. Additionally the difference spectrum is shown.

Adsorption and diffusion of n-hexane

In figure 3 (on the next page) the *n*-hexane uptake curves for H-MOR and HMOR-ox are depicted. Obviously there is a significant difference in the equilibrium uptake of *n*-hexane between HMOR and HMOR-ox, 0.56 wt% and 1.53 wt% respectively (see also table 1). The higher amount of *n*-hexane adsorbed by HMOR-ox indicates a higher accessible micropore volume in this sample as compared to the HMOR sample. In a previous study [14], the uptake of *n*-hexane in a different HMOR sample having smaller crystals of ~0.4 μm was monitored. In order to set up a comparison with the current results, its uptake curve is also shown in figure 3 (referred to as HMOR small crystals). It is clear that the equilibrium uptake of the HMOR with small crystals sample lies significantly above that of HMOR, while only a minor difference is observed with the HMOR-ox sample.

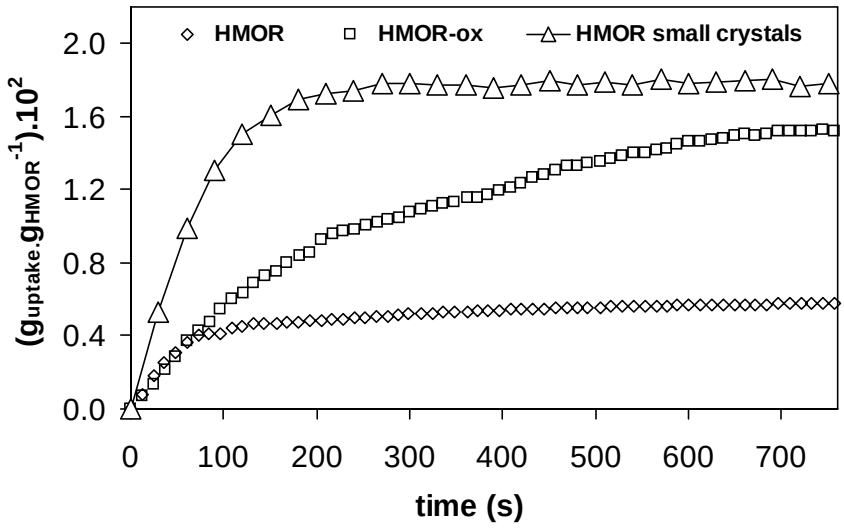

Figure 3. Experimental uptake curves for *n*-hexane over HMOR and HMOR-ox at 523 K. For comparison, the uptake data for a different HMOR sample with smaller crystals are shown.

From the *n*-hexane uptake curves, the characteristic time for diffusion or the so-called diffusional time constant L^2/D_{uptake} can be calculated, which is the square of the intracrystalline diffusion pathlength (crystal half-length *L [m]*) divided by the uptake diffusion coefficient (D_{uptake} $[m^2s^{-1}]$). Therefore the experimental uptake curves for HMOR and HMOR-ox were fitted according to the procedure described in an earlier study [14] resulting in values for L^2/D_{uptake} and the delay constant β. In figure 4 the experimental curves normalized to their equilibrium amount of uptake and the matching fits are presented. The complete set of fitting results is collected in table 2. From figure 3 and table 2 it is clear that after the oxalic acid treatment a large increase in L^2/D_{uptake} is observed, *i.e.* the time constant for the diffusion of *n*-hexane in the crystals of HMOR-ox is about ten times larger than for HMOR.

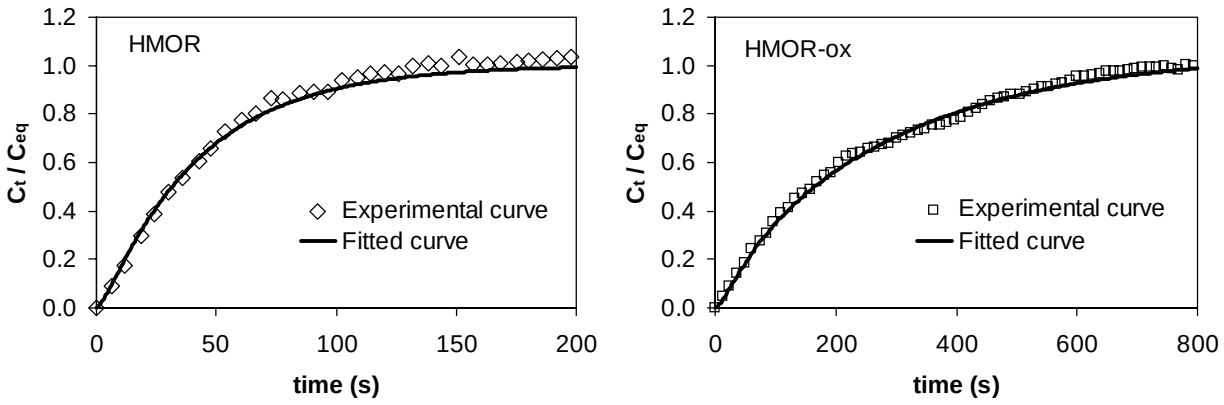

Figure 4. Experimental (normalized) and fitted curves for *n*-hexane uptake over HMOR at 523 K before (left) and after (right) treatment with 0.1 M oxalic acid.

Table 2. Fitting results for the *n*-hexane uptake curves over HMOR before and after the oxalic acid treatment.

Sample	L^2/D_{uptake} *(s)*	β^{-1} *(s)*	Chi^2 *	$L_{calculated}$ *(m)***
H-MOR	85	10	$5*10^{-3}$	$1.6*10^{-7}$
H-MOR-ox	797	10	$2*10^{-3}$	$4.9*10^{-7}$

* $Chi^2 = \sum_i \left(y_i^{obs} - y_i^{calc} \right)^2$, where y is the uptake- and i the time parameter (Note: $y_{max} = 1$).

** Assuming that $D_{uptake} = 3*10^{-16}$ $m^2 s^{-1}$, which is the value for HMOR with small crystals [14].

Adsorption and reaction of n-butene

The reaction of *n*-butene on the HMOR samples at 623 K leads to the formation of irreversibly present coke deposits. The coke content, as determined with the TEOM, for HMOR is 3.7 wt% and for HMOR-ox 8.2 wt%, revealing a similar trend as observed with the reversible *n*-hexane uptake measurements (see table 1). In figure 5 line scans are displayed that were obtained on representative coked HMOR and coked HMOR-ox crystals by scanning parallel to the direction of the 12 MR channels using SEM/EDX. The lines represent the atomic carbon to zeolitic oxygen (C/O) ratio as a function of scanning distance and provide an indication of the carbon distribution over the HMOR crystals before and after the oxalic acid treatment. For HMOR a high C/O ratio is observed close to the edge of the crystal, while the signal rapidly decreases going further from the edge towards the center of the crystal. This is in contrast to the C/O ratio that was monitored for HMOR-ox, which remains relatively constant over the scanned line with a C/O ratio that lies for large part above that of HMOR, which is in agreement with the higher coke content. The gradient of coke over the HMOR-ox crystal points to mass transfer limitation of the deposition process, which has been observed before with ferrierite (FER) [19].

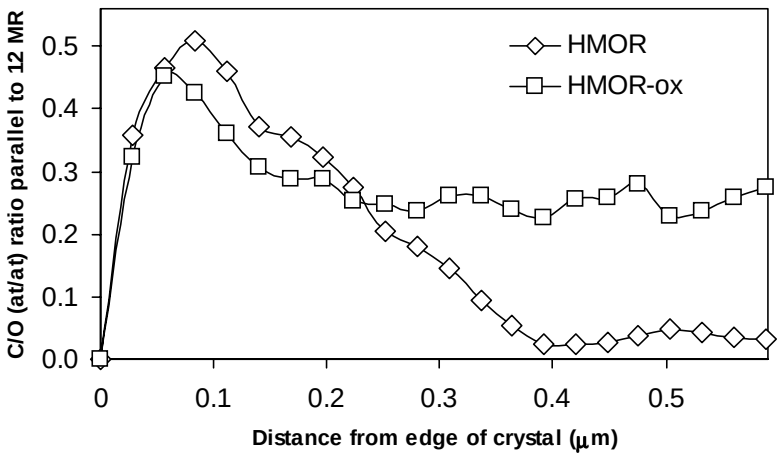

Figure 5. The atomic carbon to zeolitic oxygen (C/O) ratio as a function of scanning distance going from the edge to the inside of the crystal, as monitored by taking line scans using SEM/EDX.

Discussion

In literature it has been shown that crystal-growth defects and/or the presence of EFAl species may have large effects on the accessible micropore volume of a one-dimensional zeolite structure like MOR [9-12]. Moreover, such effects will become more significant when larger MOR crystals are used [10,12]. From the data presented in figure 3 it is clear that the uptake of *n*-hexane is higher in HMOR with small crystals (~0.4 μm) than in HMOR with 3 to 5 times larger crystals (1-2 μm). This indicates a higher accessibility of the micropore volume for the HMOR with small crystals. In order to enhance the accessibility of HMOR with larger crystals, a mild treatment with oxalic acid was performed, which is known to remove the EFAl species [20-22].

The removal of EFAl species by oxalic acid in HMOR-ox is confirmed by the Al-NMR results in figure 2, which demonstrates that oxalic acid washing leads to the abstraction of octahedral and some tetrahedral coordinated EFAl species. In good agreement with this the TPD-TGA results in table 1 display an increase in the number of Brønsted acid sites accessible for *n*-propylamine in HMOR-ox, as compared to HMOR. Moreover, ICP-AES analysis shows that the Si/Al ratio increases from 5.6 to 8.0 (table 1), which corresponds to a decrease in the alumina content from 17.5 wt% to 12.2 wt%. Considering that the removed species are predominantly EFAl located in the MOR micropores, it can now be calculated using a density for alumina of 3.5 $g.ml^{-1}$ [10], that these species will occupy a volume of ~0.015 $ml.g^{-1}$. Based on this, almost no change in the overall micropore volume is expected in the case that the used probe molecule is able to bypass the EFAl species. This is clearly the case for nitrogen, since the nitrogen physisorption/t-plot analysis results in table 1 did not reveal differences in the available micropore volume and/or mesopore volume between HMOR and HMOR-ox. Besides, it must be taken into account that nitrogen is able to enter the MOR crystal via the 8 MR side pockets. In contrast, *n*-hexane is not able to bypass the EFAl species present in the HMOR micropores and/or to enter via the 8 MR's in order to fill up the complete micropore volume. However, after the oxalic acid treatment of HMOR the *n*-hexane uptake for the resulting HMOR-ox approaches the level of HMOR with small crystals.

The fitting results in figure 4 and table 2 demonstrate that the diffusional time constant (L^2/D_{uptake}) for HMOR is much lower than for the HMOR-ox sample. This result can now be easily interpreted by the partial blocking of the micropores of HMOR with EFAl species. This induces an effectively shorter intracrystalline diffusion pathlength (L) for *n*-hexane and consequently the number for L^2/D_{uptake} is relatively low. This interpretation can be further verified by taking into account the uptake diffusion coefficient (D_{uptake}) of HMOR with small crystals that has been determined in a previous study [14] to be $3*10^{-16}$ m^2s^{-1}. By multiplying the values obtained for

L^2/D_{uptake} (see table 2) with the mentioned D_{uptake} and then taking the square root, good indication on the L for both HMOR samples under study is obtained. As displayed in table 2, the L after the oxalic acid treatment thus after the removal of EFAl species increases from 0.16 μm to 0.49 μm, hence by a factor of about 3. Taking into account the crystal length, which is known from SEM (figure 1), the value for L is expected to be between 0.5 and 1.0 □m. Evidently, the L value for HMOR-ox approaches this value, indicating that the micropore volume is largely accessible to *n*-hexane. This indicates a successful removal of EFAl from the zeolite micropores.

The larger accessibility of the micropore volume for HMOR-ox is further illustrated in figure 5. The SEM/EDX line scans reveal that for the HMOR sample, *n*-butene is not able to penetrate far into the 12 MR channels, while for HMOR-ox the complete micropore volume seems to be available. In this way the blocking effect of the EFAl species on the uptake of hydrocarbons inside the MOR micropores is clearly visualized. It is noted that the value for the accessible pore length from SEM of 0.2 μm corresponds nicely with the calculated value of 0.16 μm from the diffusion measurements.

The present results prove that when a one-dimensional zeolite like MOR is applied, the presence of a small amount of EFAl species, which itself only occupies less than 10 % of the micropore volume, may cause almost 60 % decrease in the micropore volume available for reaction. This may not affect the adsorption of a small molecule like nitrogen, which is able to pass the EFAl species and/or enter via smaller pores. But when a reactant like *n*-hexane is used, which is more relevant for catalysis purposes, the presence of EFAl has a major impact on the overall uptake. More specifically, the present results demonstrate that nitrogen does not indicate any change in the micropore and/or mesopore volume for HMOR with and without EFAl species present, while the adsorption of both *n*-hexane and *n*-butene reveals large differences. It is important to realize that with the use of one-dimensional zeolite structures, the chance on and the effect of crystal defects and/or the presence of EFAl species grows rather drastically with increasing crystal length.

Recently some diffusion related studies on large one-dimensional zeolite crystals like MOR have appeared [23,24]. With regard to these studies and future research, the present study demonstrates that thorough verification should be undertaken to check whether the complete micropore volume is available using a relevant probe molecule. Moreover, a novel approach has been presented that allows detailed assessment of the micropore length accessible for the reactant.

Conclusions

The accessibility of the MOR micropores was explored by examining the adsorption of *n*-hexane and *n*-butene using a TEOM. It was demonstrated that a small amount of EFAl species present in the MOR micropores induced a ~60 % decrease in the overall adsorption, which was not observed using nitrogen physisorption. Second, by performing SEM/EDX line scans the blocking effect of such EFAl species on the uptake of hydrocarbons inside the MOR micropores was visualized by a clear coke gradient over the crystal. After removal of the EFAl species by a mild oxalic acid treatment, the micropores were largely accessible to the hydrocarbons. Nitrogen physisorption did not reveal any changes in the micropore accessibility. This demonstrates that the use of nitrogen as a probe molecule may provide irrelevant information. On the other hand, the novel approach presented in this study allows detailed verification of the micropore accessibility for the reactant under study. In particular, the pathlength for free access of hydrocarbons from the crystal surface into the micropores could be deduced from diffusion studies (TEOM) and coke profiles (SEM/EDX).

Acknowledgements

Dr. An Verberckmoes (ExxonMobil) is kindly acknowledged for the synthesis and provision of the Na-mordenite; Katleen Hermans (ExxonMobil) for performing the ICP-AES and Al-NMR measurements; Dr. Jeroen van Bokhoven (ETH Zürich) for helpful discussion on the Al-NMR data; Arjan Plomp for modifying the samples and Marjan Versluijs (Utrecht University) for performing the SEM/EDX measurements.

References

1. Atlas of Zeolite Framework Types (Ch. Baerlocher, W.M. Meier and D.H. Olson, Eds.) 5th edition, Elsevier, Amsterdam (2001).
2. A.W. O'Donovan, C.T. O'Connor and K.R. Koch, Micropor. Mat. 5 (1995) 185.
3. G.D. Lei, B.T. Carvill and W.M.H. Sachtler, Appl. Catal. A Gen. 142 (1996) 347.
4. F. Eder, M. Stockenhuber and J.A. Lercher, J. Phys. Chem. B 101 (1997) 5414.
5. I.E. Maxwell and W.H.J. Stork, in "Introduction to Zeolite Science and Practice" (H. van Bekkum, E.M. Flanigen, P.A. Jacobs and J.C. Jansen, Eds.) 2nd edition, Elsevier Science, Amsterdam (2001).
6. S.T. Sie, in "Advanced Zeolite Science and Applications" (J.C. Jansen, M. Stöcker, H.G. Karge and J. Weitkamp, Eds.), Elsevier Science, Amsterdam (1994).
7. A. Corma and A. Martinez, in "Catalytic Activation and Functionalisation of Light Alkanes: Advances and Challenges" (E.G. Derouane, J. Haber, F. Lemos, F.R. Ribeiro and M. Guisnet, Eds.), Kluwer Academic, Dordrecht (1998) 35.

8. B.T. Carvill, B.A. Lerner, B.J. Adelman, D.C. Tomczak and W.M.H. Sachtler, J. Catal. 144 (1993) 1.
9. L.D. Fernandez, P.E. Bartl, J.L.F. Monteiro, J.G. Dasilva S.C. Demendez and M.J.B. Cardoso, Zeolites 14 (1994) 533.
10. Y. Hong and J.J. Fripiat, Micropor. Mat. 4 (1995) 323.
11. V. Zholobenko, A. Garforth, M. Makarova and J. Dwyer, Stud. Surf. Sci. Catal. 94 (1995) 560.
12. S. Moreno and G. Poncelet, Micropor. Mat. 12 (1997) 197.
13. D. Chen, H.P. Rebo, K. Moljord and A. Holmen, Chem. Eng. Sci. 51 (1996) 2687.
14. S. van Donk, A. Broersma, O.L.J. Gijzeman, J.A. van Bokhoven, J.H. Bitter and K.P. de Jong, J. Catal. 204 (2001) 272 / chapter 4 of this thesis.
15. S. van Donk, E. Bus, A. Broersma, J.H. Bitter and K.P. de Jong, Appl. Catal. A Gen. 237 (2002) 149 / chapter 7 of this thesis.
16. W. Zhu, J.M. van de Graaf, L.J.P. van den Broeke, F. Kapteijn and J.A. Moulijn, Ind. Eng. Chem. Res. 37 (1998) 1934.
17. R. Giudici, H.W. Kouwenhoven and R. Prins, Appl. Catal. A Gen. 203 (2000) 101.
18. T.-H. Chen, B.H. Wouters and P.J. Grobet, Eur. J. Inorg. Chem. 2 (2000) 281.
19. S. van Donk, F.M.F. de Groot, O. Stéphan, J.H. Bitter and K.P. de Jong, to be published / chapter 9 of this thesis.
20. M.R. Apelian and T.F. Degnan, US Patent 5.238.677 (1993), Mobil Oil Co.
21. M.R. Apelian A.S. Fung, G.J. Kennedy and T.F. Degnan, J. Phys. Chem. 100 (1996) 16577.
22. M. Müller, G. Harvey and R. Prins, Micropor. Mesopor. Mat. 34 (2000) 135.
23. F.J.M.M. de Gauw, J. van Grondelle and R.A. van Santen, J. Catal. 204 (2001) 53.
24. N.J. Noordhoek, D. Schuring, F.J.M.M. de Gauw, B.G. Anderson, A.M. de Jong, M.J.A. de Voigt and R.A. van Santen, Ind. Eng. Chem. Res. 41 (2002) 1973.

6

Butene Skeletal Isomerization over Solid Acid Catalysts: on the Beneficial and Harmful Effects of Carbonaceous Deposits

- a Review -

Abstract

Skeletal isomerization of *n*-butene to isobutene is mainly controlled by catalyst pore topology, acid strength, acid site density and location of the acid sites. It is established that the pore structure of the catalyst is the most important feature with regard to isobutene selectivity and stability. The most favorable activity versus selectivity and stability characteristics are displayed by the zeolite ferrierite, for which the presence of carbonaceous deposits coincides with the selective performance in butene skeletal isomerization. By-product formation, mainly propene, pentenes and octenes, as well as isobutene production initially takes place via oligomerization and cracking throughout the ferrierite crystals. After short time on stream the pore system of ferrierite is largely filled by aliphatic carbonaceous deposits, with catalysis primarily occurring at the pore mouths of the channels. At this stage cracking of these deposits is the origin of small amounts of by-products. With time on stream the deposits are converted into aromatic coke, thus further reducing reactivity and concomitant formation of non-selective products. It is emphasized that the observed increase of isobutene selectivity with time on stream is a direct consequence of the decrease of cracking reactions. Final deactivation of the catalyst is due to blockage of the pore mouth inlets by poly-aromatic compounds formed after prolonged time on stream.

Introduction

In oil refinery, fractions obtained from fluid catalytic cracking (FCC) and steam cracking contain linear butenes [1,2]. A growing demand for isobutene has provided a new purpose for these linear butenes because they can be converted into isobutene by skeletal isomerization. Main cause for this higher need has been the "Clean Air Act" legislation by the US government, which banned the use of lead containing compounds as fuel additives. However, without these additives the performance of the engine is deteriorated and alternatives like methyl-*tert*-butyl-ether (MTBE) and ethyl-*tert*-butyl-ether (ETBE) were needed [1,3]. These ethers contain oxygen in combination with a high octane number and hence are suitable as fuel additives. Production of MTBE and ETBE can be accomplished by etherification of isobutene with methanol or ethanol respectively. Main problem however is the supply of sufficient amounts of isobutene and therefore the interest for catalysts that selectively perform the skeletal isomerization of *n*-butene has been enlarged over the last decade. At present, MTBE is been banned from gasoline by some US states due to the detection of MTBE contaminated groundwater [4]. In Europe, however, MTBE is still used to enhance the octane quality of the gasoline. Next to the application of isobutene in etherification processes, it is also used as a building block for various polymers and other chemicals, like poly-isobutene, isobutylrubber, methacrolein and alkylated phenols and cresols [5].

The skeletal isomerization of butenes has received much interest, not only from an industrial point of view but also scientifically, since it is a difficult reaction to catalyze. Already in the seventies two reviews by Choudary [6,7] have been published dealing with catalysts like phosphoric acid, metal halides, alumina, aluminosilicates and phosphated and fluorinated aluminas. In 1993 a review by Butler and Nicolaides appeared [8] that emphasized on halogenated and non-halogenated amorphous catalysts. Since the Butler and Nicolaides review much has changed in the field of research as far as the catalysts that have been studied. In 1987 Barri *et al.* [9] reported on the high selectivity towards isobutene for Theta-1 (TON) as compared to ZSM-5 (MFI) and ZSM-23 (MTT). However, it was in the early nineties that the big breakthrough occurred when Shell co-workers discovered the exceptional selectivity and stability of the zeolite ferrierite (FER) [10]. Lyondell has commercially applied the ferrierite catalyst in the US for a limited period of time [1,4].

The application of microporous materials as selective catalysts for butene skeletal isomerization opened a completely new field of research. Moreover, with the introduction of microporous catalysts many mechanistic studies have been carried out. Especially much discussion is going on whether the isomerization over microporous materials proceeds via a monomolecular, pseudo-monomolecular or bimolecular reaction pathway [11-13]. Two comprehensive reviews concerning this subject have

recently been published by Houzvicka and Ponec [14], and by Meriaudeau and Naccache [15].

Numerous studies have indicated that the selective skeletal isomerization coincides with the formation of carbonaceous deposits [11,16-23]. Therefore this review will primarily concentrate on the role of carbonaceous deposits in butene skeletal isomerization. In order to give a comprehensive overview, amorphous and mesoporous acid catalysts as well as microporous materials will be taken into account. Above all, this review will focus on the zeolite ferrierite, as this has been the most intensively studied catalyst for butene skeletal isomerization over the last years. However, first the activity, selectivity and stability of various solid acid materials that have been applied in butene skeletal isomerization will be compared. Then the mechanism of coke formation and the location and nature of carbonaceous deposits will be explored. Furthermore, since the formation of coke and the prevailing reaction pathway in butene skeletal isomerization seem to be closely coupled, the impact of these deposits on catalysis will be extensively discussed. Finally, an overall scheme for the reaction of *n*-butene over ferrierite as a function of time on stream is presented.

Amorphous and mesoporous catalysts used for butene skeletal isomerization

In general it is thought that the skeletal isomerization runs over Brønsted acid sites, therefore the most important requirement for the catalyst seems to be proper acidity. Acid sites displaying intermediate acidity, higher than is needed for *cis-trans* isomerization and double-bond shift reactions and lower than used in protolytic cracking, are probably most suitable for skeletal isomerization [24].

Silica

The silanol groups on silica are too weakly acidic to catalyze the skeletal isomerization of butenes in a sufficient way. This means that treatment is needed to introduce a higher acidity on those compounds. Houzvicka *et al.* [25-27] treated silicas with phosphoric acid and after calcination, a catalyst containing 65 wt% of crystalline P_2O_5 was obtained. At very low space velocities and a rather high reaction temperature of 713 K this catalyst showed an isobutene selectivity of 90 %. Gao *et al.* [28] used a 23 wt% loading of 12-tungstophosphoric acid in order to make the silica acidic. With very short time on stream a very high activity but moderate selectivity was observed. With longer times on stream severe deactivation due to coking took place.

Alumina

η-alumina and γ-alumina display selective but low skeletal isomerization activity, as was shown in several publications [6,7,29-35]. In general alumina is Lewis acidic and not Brønsted acidic [36], as is thought to be necessary for the skeletal isomerization. Nevertheless, it was postulated that the skeletal isomerization over pure alumina predominantly runs over Lewis acid sites via π-allyl species, which are probably bound to the aluminum ions [31,32].

To make alumina more active in the skeletal isomerization, chemical modification is needed. Choudary *et al.* [29] found that fluorination of η-alumina, by impregnation of ammonium fluoride and drying at 110 °C, revealed a catalyst that exhibited a significant higher activity and stability compared to pure η-alumina, and still provided very good isobutene selectivity. Seo *et al.* [30] showed that the activity and selectivity of γ-alumina could be improved in a similar way. Other authors [25,31,37-39] carried out likewise halogenation procedures with fluoro-, chloro- and bromo-compounds to tune the acidity on alumina and obtained more or less the same results. Acidity of alumina can also be tuned by adding tungsten oxide [40-42]. Although this increases activity and selectivity, these catalysts are very liable to deactivation by coke formation.

The lifetimes of alumina catalysts can be lengthened when steam is added to the feed stream [35,37,40,41]. It was speculated by Szabo *et al.* [37] that water blocked the non-selective acid sites and consequently the catalyst lifetime was lengthened. However, it seems more likely that the addition of water results in a decrease in coke formation, thus enhancing the number of acid sites available for the formation of isobutene, as was suggested by Gielgens *et al*. [41]. Conversion of the active sites into less reactive and more selective ones may also take place as it was found that with longer times on stream especially the by-product formation decreased and a more selective catalyst was obtained [37,40].

Some research has focused on silylation [33,43] and zirconylation [44] of γ-alumina in order to improve activity and selectivity. For example Nilsen *et al.* [43] increased acidity on γ-alumina by the condensation of tetraethoxysilane. With increasing silicon coverage, a decrease in the number of Lewis acid sites and an increase of Brønsted acid sites was observed, which was accompanied by a higher activity. Therefore a correlation between the activity and the number of Brønsted sites was assumed. It was established that this correlation holds for silicon oxide contents not exceeding one monolayer.

Amorphous silica-alumina

In amorphous silica alumina (ASA) the amount of Brønsted acid sites can be varied by the silica/alumina ratio. These compounds display more activity than silicated alumina and pure alumina [24,26], but as was demonstrated Trombetta *et al.* [33] they exhibit

rather poor isobutene selectivity. Major by-products are propenes and pentenes, formed by the cracking of butene dimeric compounds.

Ordered mesoporous materials

Seo *et al.* [45] recently published a paper concerning the well-ordered mesoporous materials KIT-1 and MCM-41. The correlation between the Si/Al ratio and conversion and selectivity of these catalysts was investigated. It was observed that low Si/Al ratio's resulted initially in high conversions followed by rapid deactivation. On KIT-1, a high aluminum content gave rise to a decrease of the conversion and an increase of the selectivity with time on stream. But for the catalysts with lower aluminum content there was no change observed with time on stream. Similar results, but in a less pronounced way, were obtained for MCM-41.

Table 1. Amorpous and mesoporous catalysts with their catalytic performance in butene skeletal isomerization at atmospheric pressure.

Catalyst	T (K)	WHSV ($g.g^{-1}h^{-1}$)	Feed	$nC_4^=$ conv. (%)[a]	$iC_4^=$ sel. (%)[b]	TOS-max (h)[c]	Ref.
65 wt% P_2O_5/SiO_2	713	0.1	$N_2/nC_4^=$=20	47	90	40	25-27
23 wt% HPW/SiO_2	623	0.8	$He/nC_4^=$=10	85	33	0.2	28
η- Al_2O_3	723	5	$nC_4^=$	4	97	-	29
1 wt% F/η- Al_2O_3	723	5	$nC_4^=$	34	87	125	29
γ-Al_2O_3	723	3.1	$Ar/nC_4^=$=4.9	8	88	5	30
0.008 wt% F/γ-Al_2O_3	723	3.1	$Ar/nC_4^=$=4.9	33	95	5	30
4.5 wt% F/γ-Al_2O_3	723	1.9	$N_2/nC_4^=$=9	57	43	5	37
4.5 wt% F/γ-Al_2O_3	723	1.9	$N_2/nC_4^=/H_2O$=9/1/0.25	49	67	5	37
6 wt% WO_3/γ-Al_2O_3	633	1.5	$nC_4^=/H_2O$=40	43	85	1.2	40
2.7 wt% SiO_2/γ-Al_2O_3	748	2	$nC_4^=$	44	76	6	43
KIT-1 (Si/Al=14)	723	3.1	$Ar/nC_4^=$=4.9	26	60	5	45
KIT-1 (Si/Al=97)	723	3.1	$Ar/nC_4^=$=4.9	10	88	5	45
MCM-41 (Si/Al=102)	723	3.1	$Ar/nC_4^=$=4.9	14	81	5	45

a. Conversion = 100% [$\Sigma N_{products\ (\neq linear\ butenes)}$ / ΣN_{total}]

b. Selectivity = 100% [$N_{isobutene}$ / $\Sigma N_{products\ (\neq linear\ butenes)}$]

c. This is the highest value that is mentioned in the related reference.

Summary

In table 1, a selection of the previously mentioned amorphous and mesoporous catalysts with their activity, selectivity and stability at atmospheric pressures is given. From this it is clear that some of these catalysts show very high isobutene selectivities, but mostly only for a short time on stream. Main problem is namely that butenes are able to adsorb on the open surface. As a consequence they undergo severe deactivation because of dimerization and oligomerization reactions that will eventually lead to coke.

Activated alumina is probably the best known amorphous catalysts up to now. Snamprogetti [46] has developed a commercial process in which these catalysts are integrated. Nevertheless, for commercial application of these catalysts frequent regeneration cycles are needed in order to maintain high activity and selectivity.

Microporous catalysts used for butene skeletal isomerization

The discovery that microporous materials are selective catalysts for butene skeletal isomerization has opened a wide field of research. Zeolites are capable of performing the skeletal isomerization reaction at lower temperatures than most amorphous and mesoporous catalysts. Side reactions for butene skeletal isomerization, *i.e.* oligomerization and cracking, are controlled by zeolite acidity and geometrical constraints. Studies on a large number of zeolites have revealed that shape selectivity is the more important of these two parameters for enhancing isomerization over oligomerization. Pore diameters between 4.0 and 5.5 Å are required, which comprises zeolites exhibiting ten membered ring (10 MR) pores. Other parameters that may improve selectivity to isobutene are a high Si/Al ratio, high crystallinity and the absence of extra framework alumina [22,47].

The zeolite ferrierite

In 1992 the Shell-group discovered and patented the zeolite ferrierite (FER or ZSM-35) [10]. Their research revealed that ferrierite is a very selective and stable catalyst, resulting in high yields of isobutene at relatively low temperatures without the need of a diluted feed [10,16,20]. This exceptionally selective behavior of ferrierite has been related to its particular pore structure [16,48] where the 10 MR channels are interconnected with 8 MR channels, containing spherical cavities. The most striking result was the increase of isobutene selectivity with coke deposited on the catalyst [16,20]. On a fresh catalyst, high butene conversion of almost 100 % and a large number of by-products were reported. After prolonged reaction the conversion decreased to around 50 % while selectivity towards isobutene increased to 90 %. Several authors showed that this change in performance is related to the formation of carbonaceous deposits on the catalyst [20,47,49].

Ferrierite is by far the most extensively studied catalyst for butene skeletal isomerization, resulting in a large number of papers published over the last decade [16-23,47-67]. However, also other zeolites and microporous materials have been studied. Especially ten membered ring zeolites, like ZSM-5 (MFI), ZSM-22 (Theta-1 or TON) and ZSM-23 (MTT), have received a lot of attention.

The zeolite ZSM-5

Seo *et al.* [48] demonstrated that a ZSM-5 catalyst with similar acidity as a ferrierite catalyst, displays a higher butene conversion of around 55 % but a much lower selectivity of only 25 %. Houzvicka *et al.* [68,69] demonstrated that the stability of the ZSM-5 catalyst is rather well, but selectivity to isobutene will always be low because of extensive oligomerization reactions. The shape selectivity of the ZSM-5 zeolite, consisting of a two-dimensional pore system with only 10 MR channels that are somewhat larger than the ferrierite 10 MR channels, is apparently not sufficient to form isobutene selectively. Acidity of ZSM-5 may not be appropriate as well, which therefore may cause the formation of by-products. Hence the results obtained by Seo *et al.* can be attributed to structural differences and possibly acidity. Similar results and conclusions were obtained in other research papers [32,33,60,70].

The zeolites ZSM-22 and ZSM-23

Already in 1987, Barri *et al.* [9] reported on the high selectivity towards isobutene for ZSM-22 as compared to ZSM-5 and ZSM-23, which are all 10 MR zeolites. Later on, several other authors showed that by selecting the proper reaction conditions very high selectivities for both ZSM-22 [51,71-75] and ZSM-23 [60,70,76] catalysts can be obtained. Due to the one-dimensional topology, pore-blocking phenomena as a result of coking will lead to a rather fast decrease in activity for these zeolites as compared to ferrierite.

Modified zeolites

As was stated above, ZSM-5, ZSM-22 and ZSM-23 are less adequate for butene skeletal isomerization than ferrierite, due to structural characteristics and a less suitable acidity. However, when an intrinsically less selective zeolite than ferrierite is used, it has been shown by several authors that it is possible to improve isobutene selectivity by modifying the acid properties of the zeolite. For example, lowering the acid strength and/or density of the bridging OH groups by replacing trivalent framework aluminum with another trivalent cation, such as B, Ga or Fe, may result in an increase in isobutene selectivity. This was shown in some papers for ZSM-5 [53,68], ZSM-11 [77], ZSM-22 [71,74] and ZSM-23 [54]. Moreover, reducing the density of acid sites, for instance by increasing the Si/Al ratio, also results in a higher selectivity towards isobutene [69,71]. This has been explained by a reduction of undesired consecutive reactions like dimerization and cracking.

For ferrierite the Si/Al ratio has been increased by hydrothermal synthesis [20,22] or post-synthesis treatments [47,55]. These procedures generally lead to higher initial selectivities and lower deactivation rates. For unmodified ferrierites it was concluded that carbonaceous deposits are needed to achieve the exceptionally selective behavior.

Therefore some research has focused on modification of the pore diameter in order to simulate the presence of carbonaceous deposits and consequently enhance the initial selectivity [47,55,65-67]. Canizares *et al.* [67] reported on a rather large increase of the initial isobutene selectivity, as a result of chemical liquid deposition of silicon tetrachloride inside the ferrierite pores. The modified ferrierite showed a high activity and isobutene yield, already with short times on stream, and the stability remained as high as for the unmodified ferrierite.

Alumino-phosphates

Some research has focused on non-zeolitic types of microporous materials like various metal-alumino-phosphates [27,52,63,78-80]. For these structures moderate acidities and slightly narrower pore dimensions, as compared to 10 MR zeolites, result in very high isobutene selectivities. Cejka *et al.* [52] demonstrated for Co-APO-11 that already on a fresh catalyst the selectivity to isobutene is very high. However, as was illustrated by for example Yang *et al.* [80], these alumino-phosphates do not exhibit as high stabilities as the zeolite ferrierite and therefore a diluted butene feed is needed to maintain activity with time on stream.

Table 2. Microporous catalysts and their catalytic performance in butene skeletal isomerisation at atmospheric pressure.

Catalyst	Si/Al	Pores (Å)	T (K)	WHSV ($g.g^{-1}h^{-1}$)	Feed	$nC_4^=$ conv. (%)[a]	$iC_4^=$ sel. (%)[b]	TOS-max (h)[c]	Ref.
FER	57	3.5 x 4.8 (8MR) 4.2 x 5.4 (10MR)	623	2	Pure $nC_4^=$	50	90	1200	20
ZSM-5	27	5.3 x 5.5 (10MR) 5.1 x 5.5 (10MR)	623	-	$Ar/nC_4^==4.5$	55	25	1	48
ZSM-22	26	4.4 x 5.5 (10MR)	612	7.9	$N_2/nC_4^==8.3$	87	36	71	9
ZSM-22	53	4.4 x 5.5 (10MR)	673	200	$N_2/nC_4^==0.7$	28	80	5	74
Fe-ZSM-22	Si/Fe=56	4.4 x 5.5 (10MR)	673	25	$N_2/nC_4^==0.7$	16	92	5	74
ZSM-23	60	4.5 x 5.2 (10MR)	693	85.4	Pure $nC_4^=$	45	65	20	76
SAPO-11	Al/Si=11.2	3.9 x 6.3	723	1.1	$N_2/nC_4^==10$	56	65	2	80
CoAPO-11	Al/Co=75	3.9 x 6.3	620	4.5	$N_2/nC_4^==10$	39	98	24	52

a. Conversion = 100% [$\Sigma N_{products\ (\neq linear\ butenes)}$ / ΣN_{total}]
b. Selectivity = 100% [$N_{isobutene}$ / $\Sigma N_{products\ (\neq linear\ butenes)}$]
c. This is the highest value that is mentioned in the related reference.

Summary

All mentioned microporous catalysts, including their activity, selectivity and stability at atmospheric pressures, are displayed in table 2. From the above discussion it is established that the topology of the zeolite structure is the most important feature with regard to isobutene selectivity and stability. For example it has been shown that

10 MR zeolites are clearly more selective than 12 MR zeolites because of preventing extensive oligomerization reactions inside their narrower pores. Besides, there appear to be large mutual differences in product selectivities between 10 MR zeolites, depending on pore structure and acidity of the zeolite [9]. The one-dimensional 10 MR zeolites as ZSM-22 and ZSM-23 are more selective than the three-dimensional 10 MR zeolite ZSM-5. The non-zeolitic alumino-phosphates reveal high selectivities, but to maintain long time activity a diluted butene feed is needed. The two-dimensional zeolite ferrierite with 8 and 10 MR channels shows the most favorable activity versus selectivity and stability characteristics. These rather unique properties of ferrierite in the butene skeletal isomerization are thus a result of its particular pore structure, tolerating rather large amounts of carbonaceous deposits, while maintaining good activity and high selectivity. One critical remark, however, is that the initial isobutene selectivity is rather poor and some deposits are required in order to obtain high selectivities.

Deactivation of microporous catalysts by carbonaceous deposits

Hydrocarbon conversions over microporous catalysts often lead to some formation of carbonaceous deposits, which may influence the catalytic action [81]. The formation of carbonaceous deposits is a complicated process depending on several factors, like the nature of reactants and products, reaction temperature and time on stream. Moreover, for zeolites, the pore structure and the number, location and strength of the acid sites affect the coking behavior of these materials [82,83]. Skeletal isomerization over microporous materials is generally performed around 623 K, at which temperature initially aliphatic coke will be formed that is transformed into aromatics [84,85], see figure 1.

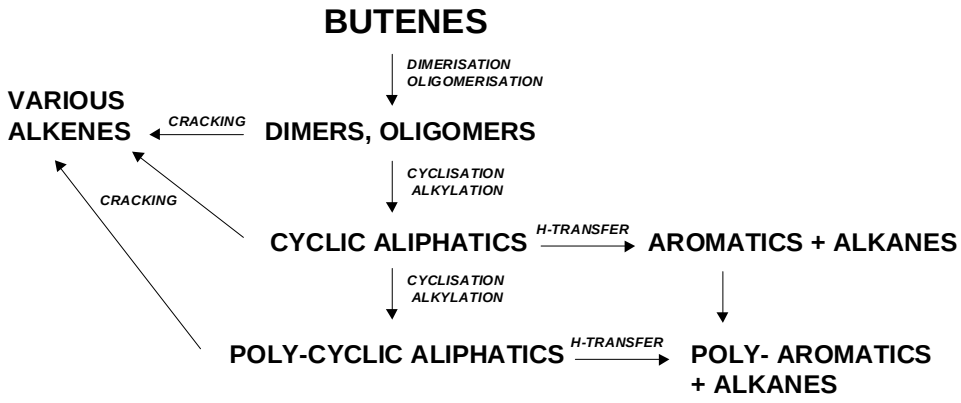

Figure 1. Scheme for the formation of carbonaceous deposits starting from butene.

Role of acidity

Irrespective of the reaction pathway, the protonation of butene by Brønsted sites is an important step, both for the reaction and for the formation of coke. Karge *et al.* [84,86] suggested that both Brønsted acid site density as well as acid strength affect both the catalytic activity of a zeolite and the initial rate of coke formation. The latter was confirmed by Houzvicka *et al.* [69], who compared the activity and selectivity of two ZSM-5 catalysts, where for one of them large part of the aluminum cations was replaced by boron cations in order to reduce the density of Brønsted acid sites. An IR study revealed that the bridged B-(OH)-Si groups behaved like silanol-groups that are not active in butene skeletal isomerization. A higher isobutene selectivity and less coke-formation were obtained for the boron substituted ZSM-5. From this observation it was concluded that the density of acid sites affected the contact-time of the butene molecules and the zeolite. The lower density of Al-(OH)-Si acid sites gives rise to a shorter contact-time and higher selectivity. Similar results were found by Wichterlova *et al.* [61] for ferrierite, although here the amount of OH groups was varied by dehydroxylation at temperatures ranging from around 670 to 990 K. In that case it was found that the isobutene yield in the skeletal isomerization is linearly proportional to the concentration of Brønsted acid sites present on ferrierite. This is in agreement with results obtained by Xu *et al.* [55]. Therefore, from these studies it can be concluded that there is a clear correlation between the number of Brønsted acid sites and the yield of isobutene during the butene skeletal isomerization.

Not only the acid site density but also the acid strength might have a significant impact on the formation of coke. In a study by Asensi *et al.* [71] the relation between acid strength and the formation of deposits for the ZSM-22 zeolite in butene skeletal isomerization was investigated. By replacing all trivalent aluminum cations by gallium and iron respectively, the Brønsted acid strength was decreased in the same order, while all other parameters were kept constant. It was shown that the activity of the zeolites increased with increasing acid strength, while isobutene selectivity decreased. Based on this study it can be stated that acid strength, at least in ZSM-22, has significant impact on the activity and selectivity in butene skeletal isomerization.

In addition to the acid site density and strength, also the location of the Brønsted acid sites is of significant importance for coke formation in butene skeletal isomerization [60]. It was shown by infrared spectroscopy [33,87] and neutron powder diffraction [88] that for ferrierite two different types of bridging OH groups are accessible for *n*-butene. One group is present in the 10 MR straight channels and the other in the side cavities, accessible through the 8 MR channels. The Brønsted acid sites in both 10 MR channels and cavities are more or less of the same acid strength. However, according to Zholobenko *et al.* [87], the number of Brønsted acid sites in the cavities will be much larger due to a preferential siting of framework aluminum cations

in the neighborhood of these cavities. Due to this higher number of Brønsted acid sites in the cavities, the 8 MR pores are very sensitive to coking and easily filled up and/or blocked by carbonaceous deposits.

The number and density of strong acid sites appear to be crucial for the rate of coke formation and the amount of coke deposited on the catalyst [83]. But also the nature and location of the coke already deposited is of influence. The rate of coke formation for *n*-butene over ferrierite was investigated by Petkovic *et al.* [56] by use of a tapered element oscillating microbalance (TEOM) in order to study the weight gain of the catalyst as a function of time on stream. Following this work, the rate of butene deposition on the zeolite ferrierite was studied in our own laboratory [89]. As is shown in figure 2, two different butene deposition mechanisms are operating. Initially pore blockage of the 8 MR channels will take place then followed by a much slower filling of the 10 MR channels, which most likely takes place via a site coverage mechanism. For the measurements executed at low butene partial pressures the filling of the 10 MR channels occurs very slowly as compared to the rate of deposition at higher butene partial pressure. Therefore it can be concluded that the transition from one mechanism into the other depends subtly on both temperature and butene partial pressure. This observed two-stage deposition mechanism corresponds very nicely to the two kind of acid sites, as suggested by Zholobenko *et al.* [87].

With regard to the formation of coke in general, it is established that Lewis acid sites are also of great influence. Based on infrared spectroscopy and ^{27}Al-NMR results, Wichterlova *et al.* [90] concluded that ferrierites dehydroxylate easily and therefore Lewis acid sites will frequently be present. In line with this observation it was stated that the stability of the ferrierite framework is not as high as for example for ZSM-5 and therefore extra-framework alumina species can be present. These extra-framework species are Lewis acidic and may enhance the acid strength of the zeolitic Brønsted sites [91]. As a consequence coking reactions may be enlarged [23].

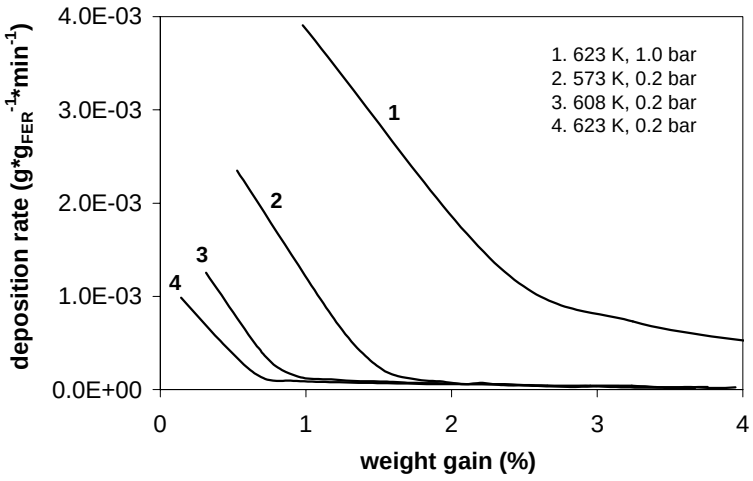

Figure 2. Deposition rates for butene over ferrierite at various temperatures and butene partial pressures.

Role of pore structure

For hydrocarbon conversions over zeolites, the majority of the coke will be deposited inside the micropores, as was shown by Karge *et al.* [84]. The deposited amount of coke formed during reaction of olefins, increased going from ZSM-5 to mordenite to faujasite, which corresponds to the increasing micropore volumes of these zeolites. Ghosh *et al.* [92] demonstrated that zeolites with different pore dimensions, exhibit different coking rates and a different nature of deposits. Therefore it can be concluded that coke formation is a shape selective process. Moreover, the topology of a zeolite is of large influence on the location of the carbonaceous deposits. Depending on the pore size dimensions and the presence of cavities, deactivation can occur due to the following incidents:

1. Site coverage, *i.e.* poisoning of the active sites by heavy carbonaceous products. This makes the individual active sites in pores, cavities or pore intersections unavailable for catalysis [93].
2. Pore blockage, *i.e.* deposition of carbonaceous compounds in cavities, intersections or channel entrances. In this way a complete pore can be made inaccessible because it is impossible for reactants to diffuse to the active sites inside the pore [93].
3. Structure alterations, by which the number and/or strength of the active sites is changed [94].

As micropores are normally not present on amorphous and mesoporous catalysts, site coverage is generally the main cause of deactivation in these catalysts. The steric constraints from the porous network in zeolites limit the formation of large bulky intermediates and therefore microporous catalysts are mostly deactivated by pore blockage. In general, the rate of deactivation on medium pore zeolites is lower than the rate of deactivation on open surface systems due to the beneficial effect of the micropores [95].

Location of deposits

An interesting and important problem related to coking in zeolites is the localization of carbonaceous deposits. Coke may be preferentially formed on the outer surface of the zeolite crystals or inside the zeolitic pore system. And furthermore, if deposits are mainly formed inside one can wonder where in the structure they are located. Various techniques, including adsorption measurements, X-ray photoelectron spectroscopy, electron microscopy and X-ray diffraction can be used to locate carbonaceous deposits in zeolites.

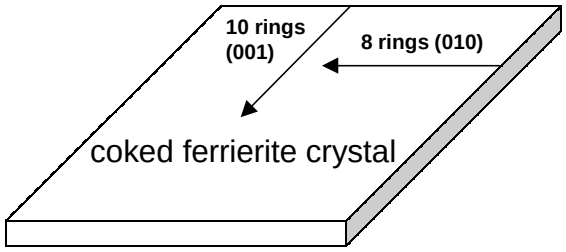

Figure 3. Scanning directions for STEM-EELS line scan experiments over aged ferrierite crystals.

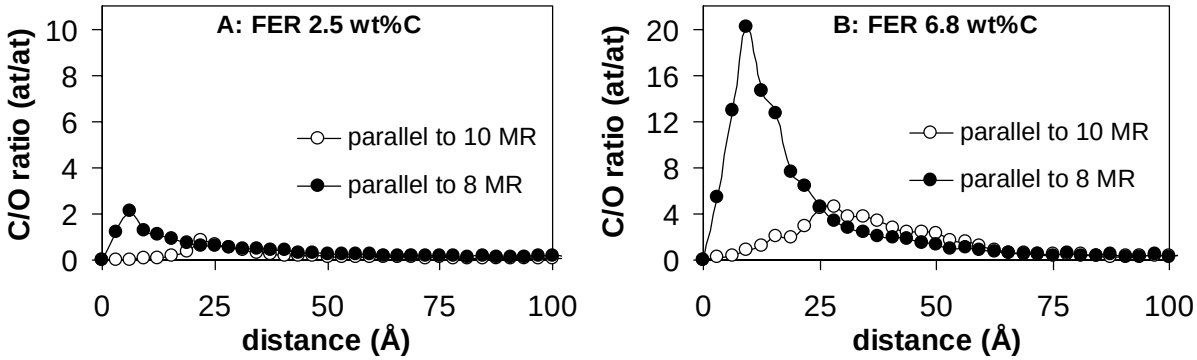

Figure 4. Atomic carbon to zeolitic oxygen ratios for coked ferrierite crystals as a function of scanning distance (distance = 0 for the edge of the crystal). (A) 2.5 wt% deposits; (B) 6.8 wt% deposits. Data are derived from STEM-EELS line scans parallel to the 8 MR and 10 MR channels, respectively. Note that there is a factor 2 difference in the y-axis scale between the two graphs.

To check the location of deposits in spent ferrierite crystals, some experiments were executed in cooperation with Dr. O. Stéphan [89], performing scanning transmission electron microscopy in combination with electron energy loss spectroscopy (STEM-EELS). Ferrierite crystals are very appropriate for STEM-EELS line scans, as they are plate-like. The measurements were performed in perpendicular directions over the ferrierite crystal, as is depicted in figure 3. The results are displayed in figure 4, in which the carbon to zeolitic oxygen ratio is shown as a function of scanning distance. For a sample holding 2.5 wt% deposits (fig. 4A), the line scan parallel to the 8 MR channels displays a large increase in the carbon to oxygen ratio towards the edge of the crystal. From this it is concluded that carbonaceous deposits largely block the pore inlets of the 8 MR channels. For the 10 MR channels also a slightly higher carbon to oxygen ratio has been observed, but a bit further from the edge of the crystals. Based on the nitrogen physisorption data in figure 5, giving information about the accessible micropore volume of the ferrierite crystals as a function of carbon content, and the TEOM data displayed in figure 2, it is concluded that the 10 MR channels are still partially accessible. For the highly coked sample, containing 6.8 wt% deposits (fig. 4B), the STEM-EELS results indicate that the 8 MR channels are completely blocked. The

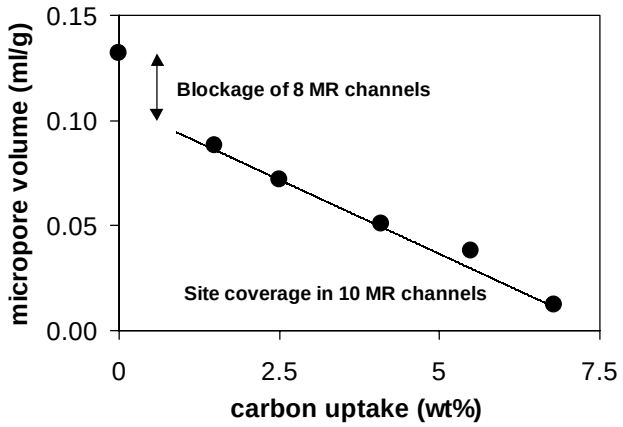

Figure 5. Micropore volumes of coked ferrierite samples, obtained by nitrogen physisorption.

amount of carbon in the 10 MR-direction also increases with the higher amount of deposits, although more moderately. Moreover, the maximum is located further into the crystal and it is therefore likely that the pore inlets remain accessible for butenes. These results again suggest the occurrence of a two-stage deposition mechanism, where pore blockage of the 8 MR channels is followed by a much slower filling of the 10 MR channels via a site coverage mechanism.

Both site coverage and surface coking can be confirmed by X-ray photoelectron spectroscopy (XPS) measurements from de Jong *et al.* [16,20]. It was demonstrated that with low carbon contents (< 6 wt%) first channel filling took place, followed by surface coking up to carbon contents around 9 wt%. In addition, transmission electron microscopy (TEM) experiments have been executed [20] on the completely spent ferrierite crystals. In figure 6 a TEM micrograph is displayed, from which it is revealed that the ferrierite crystals are bordered by a layer of amorphous material that is probably coke.

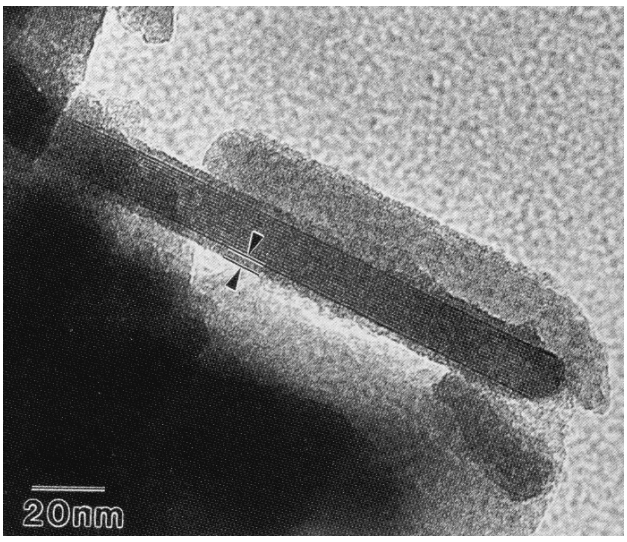

Figure 6. TEM micrograph of spent ferrierite crystals, size 250 nm with 20 nm thickness. Note that carbonaceous deposits have built up at the exterior of the crystal [20].

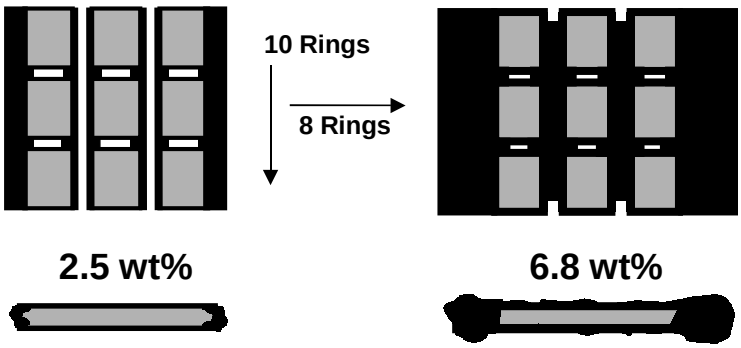

Figure 7. Schematic pictures of ferrierite crystals containing 2.5 wt% and 6.8 wt% coke respectively. Cross sections have been drawn such that the filling of both the 8- and 10 MR channels are outlined. Note that for the highly coked ferrierite, the inlets of the 10 MR pores remain accessible.

As mentioned earlier, according to Zholobenko *et al.* [87] there will be a higher number of Brønsted acid sites in the cavities as compared to the 10 MR channels. As a consequence these sites are very sensitive to coking and easily filled up and/or blocked by carbonaceous deposits. In agreement with this, it was concluded from our own results shown in figure 2 that a two-stage carbon deposition mechanism is taking place. The results of Zholobenko *et al.* correlate also very nicely with the STEM-EELS and nitrogen physisorption results [89]. Based upon all these results a schematic picture is made in figure 7 for the ferrierite crystals containing 2.5 wt% and 6.8 wt% coke respectively. Most important feature is that the pore inlets of the 10 MR channels remain accessible for butenes even if high amounts of carbonaceous species are deposited. In general it can be stated that both acid site density as well as pore topology influences the location of carbonaceous deposits inside the ferrierite crystals. It must be noted that it is difficult to discriminate between these two parameters because both seem to play a crucial role in the formation and location of carbonaceous deposits.

Nature of deposits

In order to investigate the nature of carbonaceous deposits, various techniques can be applied. In this respect ^{13}C-NMR is one of the most powerful techniques, as was stated by Bonardet *et al.* [96] in a recent review on deactivation of zeolites. It was shown that the chemical nature of deposits is largely dependent on the topology of the zeolite. Moreover they concluded that regardless the reactant, the chemical nature of the deposits would always be the same and only depend on the temperature and most of all the pore structure. ^{13}C-NMR spectroscopy is able to detect bindings between aromatic rings [85], alkylfragments and even tertiary carbenium ion-like species [97]. Disadvantage, however, is that the information is not quantitative and no distinction can be made between coke inside the porous network and on the outer surface.

Another very powerful technique is IR spectroscopy, as was shown by Ghosh *et al.* [92]. They investigated the nature of deposits formed during the reaction of propene over faujasite (12 MR with supercages), mordenite (12 MR) and ZSM-5 (10 MR). It was

stated that the chemical nature of the deposited compounds is largely dependent on the topology of the zeolite. At lower temperatures (< 600 K) mainly large branched oligomers were detected in faujasite, while smaller oligomers were detected for mordenite and ZSM-5. Higher temperatures (> 600 K) revealed poly-aromatics for faujasite, for mordenite both poly-aromatics and small aromatic molecules were found, while for ZSM-5 only small aromatics were detected. The aromatic nature of the carbonaceous deposits was also found for ferrierite by Xu *et al.* [23]. At the pore mouths and outer surface of zeolite crystals normally also some coke is deposited and it must be noted that mainly poly-aromatics will be formed here, as there is no pore restriction. For ferrierite this is confirmed by de Jong *et al.* [20] using electron energy loss spectroscopy.

Guisnet *et al.* [19,57] determined the structural composition of the coke deposited on ferrierite after various times on stream, thus with different amounts of coke deposited on the catalyst. The samples were analyzed by dissolving the ferrierite in hydrofluoric acid, so the internal coke compounds were liberated and could be analyzed by several techniques [82], without the disturbing signal of the zeolite lattice. Infrared and ^{1}H-NMR analysis revealed the presence of various alkyl-aromatics. To identify the coke components in more detail, GC-MS was applied and the results are displayed in table 3. It was clearly shown that the higher the coke content, the heavier the components. The compounds are distributed into seven families A to G, as is also summarized in table 3. Compounds A to C, containing two aromatic rings, are already formed at low coke contents while compounds exhibiting more aromatic rings, D to G, are formed at higher coke contents. It was suggested that with longer time on stream, the components A to C condense into poly-aromatic compounds.

Family	Gen. Formulae	Developed Structural Formulae	x
A	C_nH_{2n-12}	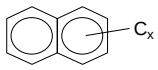	0-5
B	C_nH_{2n-14}		0-5
C	C_nH_{2n-16}	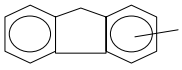	0-5
D	C_nH_{2n-18}	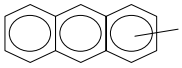	1-4
E	C_nH_{2n-20}	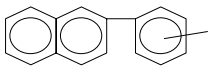	0-4
F	C_nH_{2n-22}	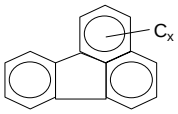	3-4
G	C_nH_{2n-26}	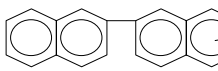	1-5

Table 3. Structures of the main components formed during butene skeletal isomerization over ferrierite. In the C_x sign, x stands for the number alkylgroups. Adapted from Andy *et al.*[57].

Finelli *et al.* [64] performed temperature programmed oxidation on coked ferrierite samples. Two different peaks were identified, one displaying aliphatic and the other aromatic character. With time on stream, so with longer coking of the samples, the aromatic peak increased while the olefinic one decreased. The decrease of hydrogen to carbon ratio, reported by de Jong *et al.* [20] and Xu *et al.* [23], indicate that the properties of the coke indeed change with time on stream.

Implications of coke formation on the reaction pathway for isobutene formation

For *n*-pentene and higher olefins it has been established that skeletal isomerization over zeolites runs via a monomolecular pathway, including an alkoxy-intermediate and a cyclopropane ring [102]. For butenes, however, this reaction pathway has been subject to a lot of discussion [11-13] as with the opening of the cyclopropane ring a primary carbenium ion is formed. Thermodynamically, the formation of isobutene from *n*-butene is favored at low temperature [98]. However, in practice these lower temperatures will result in side reactions and as consequence the selectivity to isobutene is poor. Major side reactions that occur are dimerization to several octenes, cracking of these octenes to propenes and pentenes, hydrogen transfer and coking [37]. The extent of undesired reactions can be decreased by applying low partial pressures of *n*-butene in the feed or by using high reaction temperatures. However, at higher temperatures the yield of isobutene is thermodynamically limited [99]. Therefore, taking into account both kinetics and thermodynamics, intermediate temperatures and low *n*-butene pressures are favored resulting in high isobutene selectivities as well as high *n*-butene conversions. In practice butene skeletal isomerization is mostly performed at 623 K and at this temperature thermodynamics predict a maximum relative isobutene to all butenes concentration of 51.5 %.

As was pointed out in the introduction, much discussion has been going on the prevailing reaction pathway in the skeletal isomerization of butene. Three major types of reaction pathways are proposed in literature and shortly summarized hereafter.

Bimolecular pathway

Butenes can undergo dimerization followed by isomerization and cracking, possibly leaving isobutene. Two types of bimolecular mechanisms can be distinguished, as is depicted in figure 8.

A. Dimerization: two linear butenes react to give a dimethylhexene and after isomerization and cracking, one isobutene and one *n*-butene are obtained. Some propenes and pentenes can be detected as by-products.
B. Codimerization: one linear butene reacts with an isobutene to give a trimethylpentene, after cracking two isobutenes are obtained.

Especially codimerization is a very selective and easy way to produce isobutene, as only tertiary and secondary carbenium ion species are involved. The initial small amount of isobutene that is needed for this reaction can be produced via the normal dimerization route. Several authors suggested that the bimolecular process would be the main route for the production of isobutene because propenes and pentenes, which also are formed via the bimolecular process, were found as major by-products [16,49].

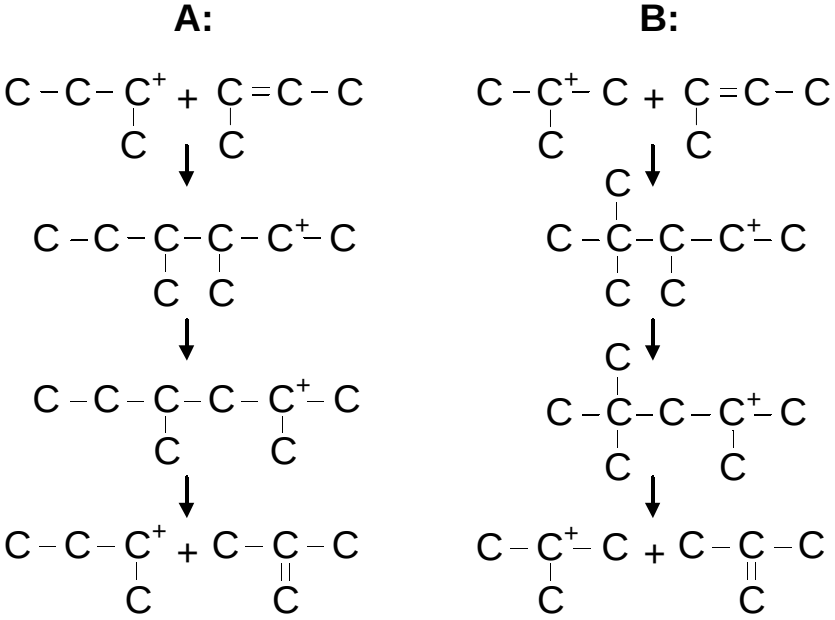

Figure 8. Scheme for the production of isobutene via bimolecular reaction pathways. (A) Non-selective dimerization pathway; (B) selective codimerization pathway.

Monomolecular pathway

In a monomolecular reaction pathway butene is isomerized over a plane Brønsted acid site, without the need of other butenes. The initial step of this reaction is the adsorption of butene on the Brønsted acid site resulting in a covalently bonded alkoxy-species, which is stable as was calculated by Kazansky [100]. By proton-transfer from the zeolite to the hydrocarbon a cyclopropyl cation is formed, then followed by the energetically and thermodynamically highly unfavorable ring opening to the primary carbenium ion [101] leading to isobutene [102]. The monomolecular pathway is shortly summarized in figure 9.

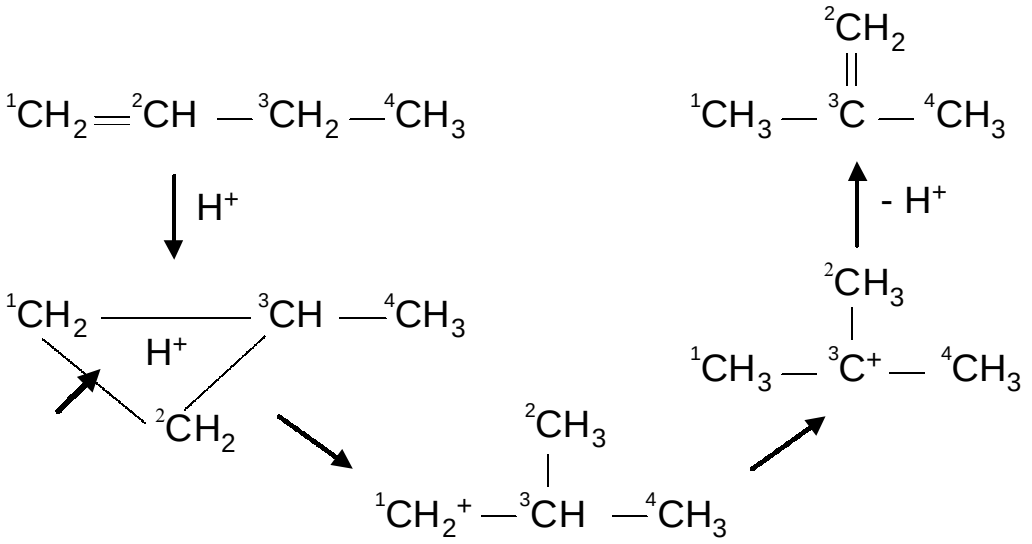

Figure 9. Monomolecular pathway for the production of isobutene.

At the prevailing reaction temperatures, a reaction pathway involving a primary carbenium ion should be questioned. Nevertheless a number of authors [11,17,25,26,30,50,71,78] suggested that butene skeletal isomerization would take place monomolecularly over an aged catalyst while on a fresh catalyst the isomerization could also take place bimolecularly. With time on stream and thus with coke deposited on the catalyst, the bimolecular pathway should decrease and the monomolecular pathway will become predominant. Recently some authors indicated that monomolecuar- and bimolecular reaction pathways are both contributing to the isobutene yield [21,51,52].

Pseudo-monomolecular pathway

Guisnet *et al.* [18,19,57] proposed a pseudo-monomolecular pathway in which the involvement of a highly unfavorable primary carbenium ion is avoided. As depicted in figure 10, the active site in this reaction pathway is formed by a carbenium ion that is

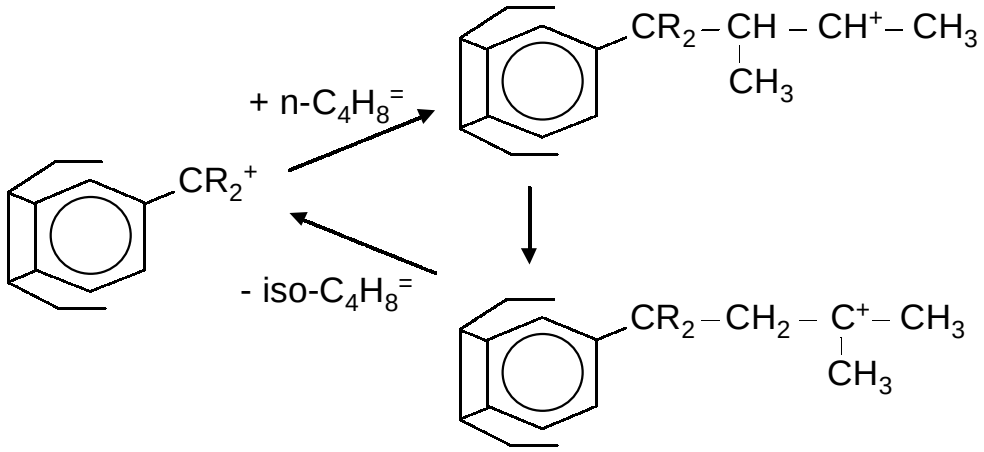

Figure 10. Pseudo-monomolecular reaction pathway as proposed by Guisnet *et al.* [18,19,57].

fixed in the coke deposited on the catalyst with increasing time on stream. Butene reacts with this carbenium ion to give a secondary carbenium ion and after a methyl- and hydride shift a tertiary carbenium ion is obtained. Finally β-scission of this intermediate produces an isobutene and with that the active site is regenerated.

Beneficial effect of deposits

Butene skeletal isomerization over a fresh ferrierite is accompanied by the formation of large amounts of by-products as propenes, pentenes and octenes, and to a lesser extent ethylene, hexenes, heptenes, propane, butanes and pentanes. On an aged ferrierite, both *n*-butene conversion and selectivity towards by-products are decreased as compared to the fresh catalyst, and consequently isobutene selectivity is raised. This is illustrated in figure 11 A and B adapted from de Jong *et al.* [20] and Cejka *et al.* [52] respectively. Moreover it is clearly demonstrated that despite the fact that the by-products yield is drastically decreasing with increasing time on stream, the yield in isobutene is almost invariable. From this it can be concluded that the non-selective dimerization pathway is prevailing with short times on stream, whereas with increasing time on stream an alteration in the prevailing reaction pathway occurs [11,16,20,23,49].

Meriaudeau *et al.* [17] and de Jong *et al.* [20] provided additional evidence for this change in the prevailing reaction pathway using ^{13}C-labeled butenes. They demonstrated that over a fresh ferrierite scrambling of the ^{13}C-label occurred. This clearly indicates that with short times on stream isobutene should be formed via the non-selective bimolecular dimerization-cracking pathway. However, over an aged ferrierite no scrambling was observed and isobutene could only be formed via a monomolecular, pseudo-monomolecualr and/or codimerization-cracking pathway. These experiments confirm that the non-selective dimerization pathway will dictate the catalytic action of ferrierite with short times on stream, whereas with longer times on stream this pathway will not be the main route for selective isobutene production.

The decrease in activity and the associated change in prevailing reaction pathway with increasing time on stream, suggest a reduction and/or change in the active sites due to irreversible butene deposition. Several authors have shown that this deposition of carbonaceous compounds can be correlated with the selective performance of ferrierite [11,16-23,50,55,57]. However, the exact role of carbonaceous deposits and especially its beneficial effect on the isobutene selectivity is still subject to much discussion. In the past years several suggestions have been given to explain the increase in isobutene selectivity with time on stream:

1. Enhancement of shape selectivity because of alterations in pore dimensions caused by carbonaceous deposits inside the 10 MR channels [11,23,50,67].

2. Creation of new highly active and selective sites, namely alkyl-aromatic tertiary carbenium ions blocked inside the zeolite pores, see figure 10 [18,19,57].
3. Preferential coking of the strongest and therefore non-selective acid sites inside the 10 MR channels [11,23].
4. Poisoning by coke of non-selective acid sites located at the outer surface of the crystals [21,22].
5. Decrease in Brønsted acid site density by deposition of carbonaceous deposits [55,61].

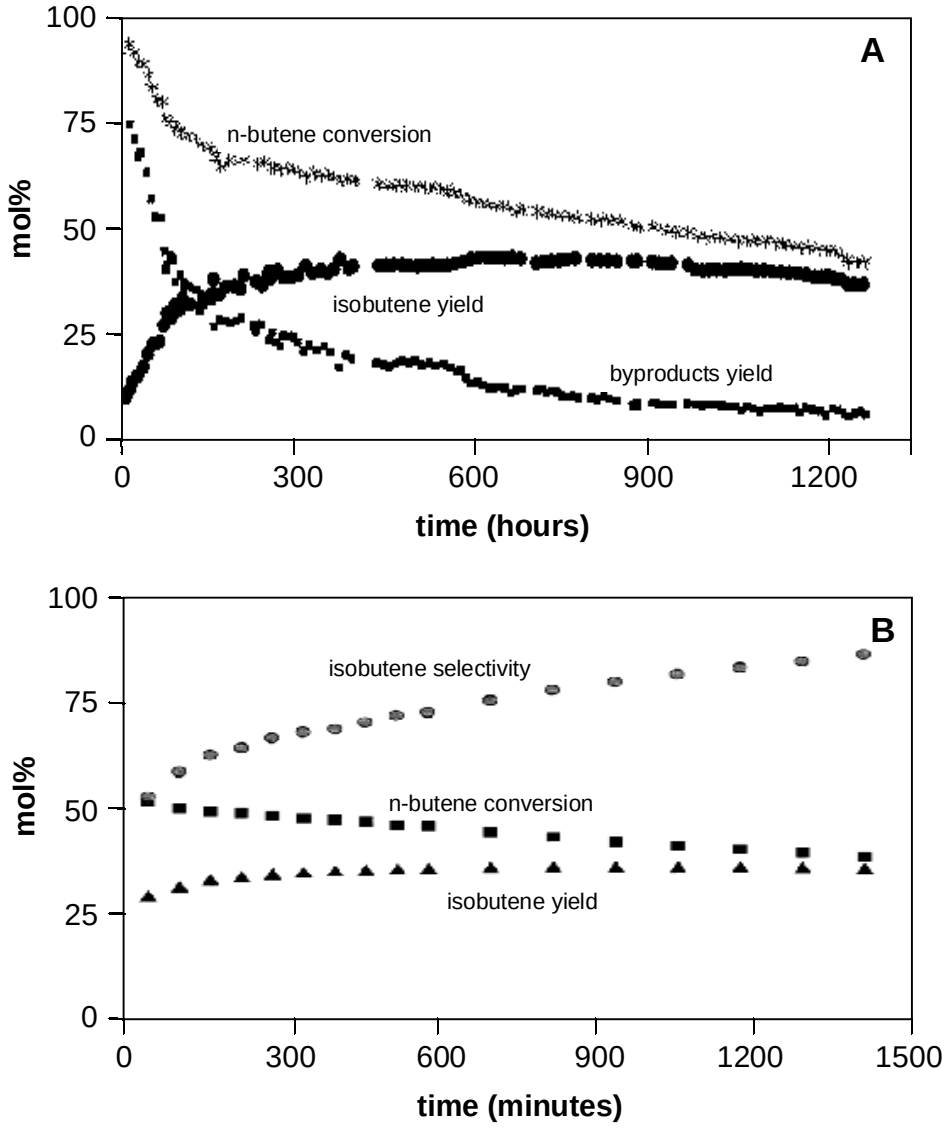

Figure 11. (A) Product yields and *n*-butene conversion versus time on stream, de Jong *et al.* [20]; (B) *n*-butene conversion and isobutene selectivity and yield versus time on stream, Cejka *et al.* [52].

Several authors [20,23,62] demonstrated that the pores of the ferrierite catalyst are almost completely filled or blocked, while isobutene selectivity is still increasing and isobutene yield stays invariable. Therefore it can be stated that suggestion 1 is no explanation for the increase in isobutene selectivity with longer times on stream, as for this explanation complete filling of the pores would decrease both isobutene selectivity and yield. Nevertheless, alterations in dimensions of the pore inlets by carbonaceous deposits may possibly contribute to an increase in isobutene selectivity.

Some authors reported on an increase in both isobutene selectivity and yield with increasing time on stream [19,20,23,57]. Based on this result Guisnet *et al.* [12,18,19,57] suggested a change in the prevailing reaction pathway for the production of isobutene. With short times on stream isobutene is mainly produced via a bimolecular pathway. But with longer times on stream, thus with coke deposited on the catalyst, the prevailing mechanism for isobutene production would change and it was suggested that the pseudo-monomolecular pathway, depicted in figure 10, would become predominant. At the same time bimolecular reactions would decrease due to poisoning of the non-selective acid sites, and this would explain the simultaneous decrease in the formation of propenes and pentenes. It should be noted, however, that at higher conversions the increase in isobutene yield with increasing time on stream could also be explained by the suppression of secondary non-selective dimerization-cracking reactions. Less butenes are converted into by-products, thus in order to reach thermodynamic equilibrium more isobutene may possibly be formed [11,13,62]. Therefore a pseudo-monomolecular pathway is not needed to account for the slight increase in isobutene yield and suggestion 2 is not necessary to clarify the observed increase in isobutene selectivity.

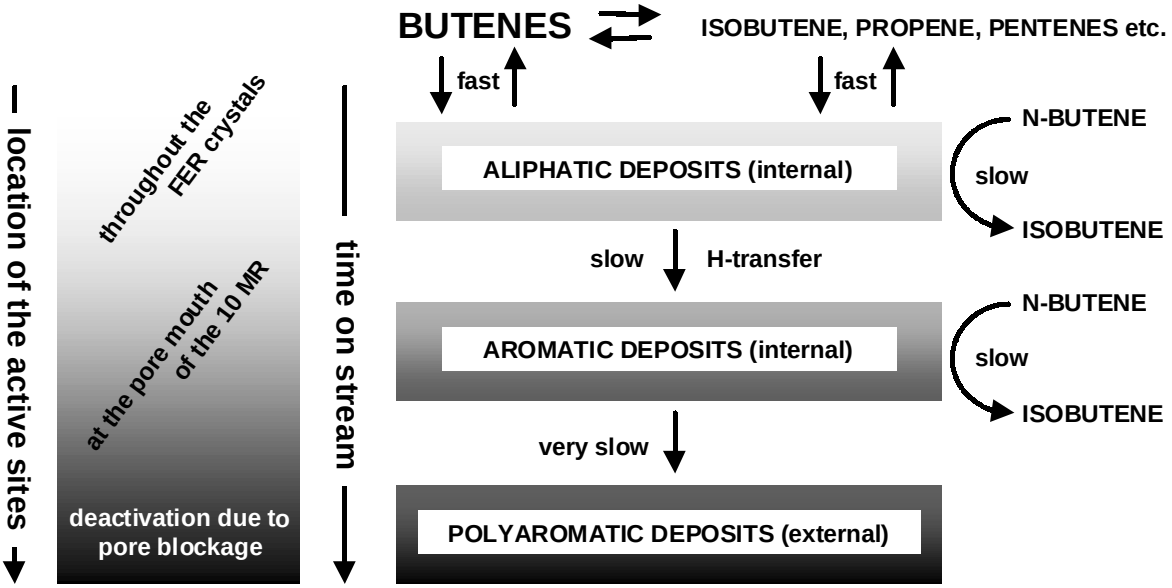

Figure 12. Schematic picture of possible reactions during *n*-butene skeletal isomerization as a function of time on stream; an indication of the locations of the active sites is shown as well.

Obviously, an increase in isobutene selectivity can be explained by the fact that sites, over which the non-selective bimolecular mechanism occurs, are poisoned by the deposition of carbonaceous deposits, as is stated in suggestions 3 and 4 [11,16-23]. Besides, solely the decrease in Brønsted acid site density (suggestion 5) can also account for the observed increase in selectivity [55,61,69]. According to the ^{13}C-scrambling experiments executed with long times on stream [17,20], isobutene could only be formed via a monomolecular, pseudo-monomolecualr and/or codimerization-cracking pathway, although this last pathway seems less likely in relation to suggestions 3, 4 and 5. In conclusion it must be stressed that suggestions 2 to 5, to various extents, may contribute to the exceptionally selective and stable behavior of ferrierite, for which the deposition of relatively large amounts of carbonaceous deposits can be experienced as beneficial [10,16,20].

Location of the active sites

Over a fresh ferrierite, initial formation of by-products as well as isobutene production occurs via oligomerization and cracking throughout the crystals. Although with short times on stream these reactions take place easily, their contribution to the overall reaction network decreases rapidly as a result of coke formation. After some time on stream when pores are practically filled and/or blocked with aliphatic deposits, cracking of these deposits is the origin of small amounts of by-products. With a constant carbon content and increasing time on stream, these aliphatic deposits are converted into aromatic coke, hence reducing reactivity and concomitant appearance of non-selective by-product formation. Further condensation of the aromatic coke will eventually hinder the catalytic action [57]. This idea is supported by the detection of poly-aromatics on the outer surface of spent ferrierite crystals by de Jong *et al.* [20].

The location of the selective isomerization sites will not be on the outer surface of the ferrierite crystals, as shape selectivity of the 10 MR channels plays a crucial role [16,48,50]. Selective sites can be located inside the 10 MR channels, but as channel filling already occurs with short times on stream and no major changes in isobutene yield are detected, it seems more likely that the shape selective Brønsted acid sites will be located in the pore mouths of the 10 MR channels. These sites are not very liable to deactivation, as very high lifetimes for the ferrierite catalyst have been reported [16,20]. Despite of the mentioned beneficial effects of carbonaceous deposits, extensive coking will eventually harm the selective catalytic action of the ferrierite as poly-aromatic compounds block the pore mouth inlets.

To summarize, reaction pathways as a function of time on stream are collected and depicted in figure 12. In addition, the above-discussed correlation between the occurring reactions, carbonaceous deposits and location of the active sites are visualized.

Concluding remarks

From the literature reviewed here it can be stated that the skeletal isomerization of *n*-butene to isobutene is mainly controlled by pore topology, acid strength, acid site density and location of the acid sites. It is established that pore topology of the catalyst is the most important feature with regard to coke formation and therefore as well for isobutene selectivity and catalyst stability.

Amorphous and mesoporous catalysts are able to display high selectivities towards isobutene, although with longer times on stream they undergo severe deactivation, as no micropores are present and more elevated temperatures are needed. Zeolites exhibiting 10 MR channels, and especially the zeolite ferrierite, display the most favorable activity versus selectivity and stability characteristics. The initial isobutene selectivity is rather poor, but with longer times on stream and thus with coke deposited on the catalyst, exceptionally high selectivity and stability are reached.

Irreversible deposition of butenes on a fresh ferrierite takes place in a two-stage mechanism. Initially blocking of the 8 MR channels occurs as a result of the higher acid site density in the cavities accessible through the 8 MR channels. Later on site coverage inside the 10 MR channels takes place. With time on stream, the deposits become more aromatic in nature and eventually poly-aromatic species are present.

The formation of carbonaceous deposits coincides with the selective behavior of ferrierite in butene skeletal isomerization. By-products formation, like propene, pentenes and octenes, as well as the production of isobutene initially take place via oligomerization and cracking throughout the ferrierite crystals. After some time on stream the pore system of ferrierite is largely filled with carbonaceous deposits and isobutene formation primarily occurs at the pore mouth inlets of the 10 MR channels. At this stage cracking of carbonaceous deposits is the origin of small amounts of by-products. Slow conversion of these deposits into more aromatic coke reduces reactivity and concomitant formation of non-selective products. It is emphasized that the overall observed increase of isobutene selectivity with increasing time on stream is a consequence of the decrease of cracking reactions. Final deactivation of the ferrierite is due to blockage of the pore mouth inlets by poly-aromatic compounds formed with prolonged time on stream.

References

1. P.J. Thomas, P.T. Stephen, Oil & Gas J. May 24 (1993) 54.
2. J.E. Naber, K.P. de Jong, W.H.J. Stork, H.P.C.E. Kuipers and M.F.M. Post, Stud. Surf. Sci. Catal. 84 (1994) 2197.
3. US Clean Air Act Amendments, Public Law (1990) 101.
4. A. Rhodes, Oil & Gas J. April 5 (1999) 39.

5. J.I. Kroschwitz and M.H. Grant (Eds.), Kirk-Othmer Encyclopaedia of Chemical Techmology, 4th edition, Wiley/Interscience, New York 1992 vol. 4 p. 722.
6. V.R. Choudary, Chem. Ind. Dev. 8 (1974) 32.
7. V.R. Choudary, Ind. Eng. Chem., Prod. Res. Dev. 16 (1977) 12.
8. A.C. Butler and C.P. Nicolaides, Catal. Today 18 (1993) 443.
9. S.A.I. Barri, D.W. Walker and R. Tahir, European Patent No. 247 802 (1987), to BP Company.
10. P. Grandvallet, K.P. de Jong, H.H. Mooiweer, A.G.T.G. Kortbeek and B. Kraushaar-Czarnetzki, European Patent No. 501 577 (1992), to Shell.
11. J. Houzvicka and V. Ponec, Ind. Eng. Chem. Res. 36 (1997) 1424.
12. M. Guisnet, P. Andy, N.S, Gnep, C. Travers and E. Benazzi, Ind. Eng. Chem. Res. 37 (1998) 300.
13. J. Houzvicka and V. Ponec, Ind. Eng. Chem. Res. 37 (1998) 303.
14. J. Houzvicka and V. Ponec, Catal. Rev. - Sci. Eng. 39(4) (1997) 319.
15. P. Meriaudeau and C. Naccache, Adv. Catal. 44 (1999) 505.
16. H.H. Mooiweer, K.P. de Jong, B. Kraushaar-Czarnetzki, W.H.J. Stork and B.C.H. Krutzen, Stud. Surf. Sci. Catal. 84 (1994) 2327.
17. P. Meriaudeau, R. Bacaud, L.N. Hung and T.A. Vu, J. Mol. Catal. A 110 (1996) L177.
18. M. Guisnet, P. Andy, N.S. Gnep, C. Travers and E. Benazzi, J. Chem. Soc. Chem. Commun. (1995) 1685.
19. M. Guisnet, P. Andy, N.S. Gnep, C. Travers and E. Benazzi, Stud. Surf. Sci. Catal. 105 (1997) 1365.
20. K.P. de Jong, H.H. Mooiweer, J.G. Buglass and P.K. Maarsen, Stud. Surf. Sci. Catal. 111 (1997) 127.
21. P. Meriaudeau, C. Naccache, L.N. Hung, T.A. Vu and G. Szabo, J. Mol. Catal. A 123 (1997) L1.
22. W-Q. Xu, Y-G. Yin, S.L. Suib, J.C. Edwards and C-L. O' Young, J. Phys. Chem. 99 (1995) 9443.
23. W-Q. Xu, Y-G. Yin, S.L. Suib and C-L. O' Young, J. Phys. Chem. 99 (1995) 758.
24. J-P. Damon, B. Delmon and J-M. Bonnier, J. Chem. Soc. Faraday Trans. 73 (1977) 372.
25. J. Houzvicka, O. Diefenbach and V. Ponec, J. Catal. 164 (1996) 288.
26. J. Houzvicka, S. Hansildaar, J.G. Nienhuis and V. Ponec, Appl. Catal. A Gen. 176 (1999) 83.
27. J. Houzvicka and V. Ponec, Appl. Catal. A. Gen. 145 (1996) 95.
28. S. Gao and B. Moffat, Catal. Lett. 42 (1996) 105.
29. V.R. Choudary and L.K. Doraiswamy, J. Catal. 23 (1971) 54.
30. G. Seo, N-H. Kim, Y-H. Lee and J-H. Kim, Catal. Lett. 51 (1998) 101.
31. Z.X. Cheng and V. Ponec, Catal. Lett. 25 (1994) 337.
32. M. Trombetta, G. Busca, S. Rossini, V. Piccoli and U. Cornaro, J. Catal. 168 (1997) 334.
33. M. Trombetta, G. Busca, S. Rossini, V. Piccoli, U. Cornaro, A. Guercio and R. Catani, R.J. Willey, J. Catal. 179 (1998) 581.
34. H.C. Woo, K.H. Lee and J.S. Lee, Appl. Catal. A. Gen. 134 (1996) 147.
35. J.W. Meyers and D.J. Strope, US Patent No. 4 436 949 (1984) Philips Petroleum Co.
36. C. Morterra, A. Chiorino, G. Ghiotto and E. Garrone, J. Chem. Soc. Faraday Trans. 75 (1979) 271.

37. J. Szabo, J. Perrotey, G. Szabo, J-C. Duchet and D. Cornet, J. Mol. Catal. 67 (1991) 79.
38. A. Melchor, E. Garbowski, M-V. Mathieu and M. Primet, J. Chem. Soc. Faraday Trans. 82 (1986) 1893
39. H. Sun and R.G. Gastinger, US Patent No. 4 654 463 (1987), to Atlantic Richfield Company.
40. B.G. Baker and N.J.Clark, Stud. Surf. Sci. Catal. 30 (1987) 483.
41. L.H. Gielgens, M.G.H. van Kampen, M.M. Broek, R. van Hardeveld and V. Ponec, J. Catal. 154 (1995) 201.
42. P. Patrono, A. La Ginesta, G. Ramis and G. Busca, Appl. Catal. A Gen. 107 (1994) 249.
43. B.P. Nilsen, J.H. Onuferko and B.C. Gates, Ind. Eng. Chem. Fundam. 25 (1986) 337.
44. J.C. Luy, J.C. Yori, A.A. Castro and J.M. Parera, React. Kinet. Catal. Lett. 36 (1988) 275.
45. G. Seo, N-H. Kim, Y-H. Lee and J-H. Kim, Catal. Lett. 57 (1999) 209.
46. G. Manara, V. Fattore and B. Notari, US Patent No. 4 038 337 (1977), to Snamprogetti.
47. R.J. Pellet, D.G. Casey, H-M. Huang, R.V. Kessler, E.J. Kuhlamn, C-L. O' Young, R.A. Sawicki and R.J. Ugolini, J. Catal. 157 (1995) 423.
48. G. Seo, H.S. Jeong, S.B. Hong and Y.S. Uh, Catal. Lett. 36 (1996) 249.
49. M. Guisnet, P. Andy, N.S. Gnep, E. Benazzi and C. Travers, J. Catal. 158 (1996) 551.
50. G. Seo, H. Seok Jeong, D-L. Jang, D. Lyun Cho and S. Bong Hong, Catal. Lett. 41 (1996) 189.
51. R. Byggningsbacka, N. Kumar and L.-E. Lindfors, J. Catal. 178 (1998) 611.
52. J. Cejka, B. Wichterlova and P. Sarv, Appl. Catal. A Gen. 179 (1999) 217.
53. P. Meriaudeau, V.A. Tuan, L.N. Hung and C. Naccache, Stud. Surf. Sci. Catal. 105 (1997) 1373.
54. P. Meriaudeau, V.A. Tuan, L.N. Hung, V.T. Nghiem and C. Naccache, J. Chem. Soc. Faraday. Trans. 94 (1998) 467.
55. W-Q. Xu, Y-G. Yin, S.L. Suib, J.C. Edwards and C-L. O' Young, J. Catal. 163 (1996) 232
56. L.M. Petkovic and G. Larsen, Ind. Eng. Chem. Res. 38 (1999) 1822.
57. P. Andy, N.S. Gnep, M. Guisnet, E. Benazzi and C. Travers, J. Catal. 173 (1998) 322.
58. P. Meriaudeau, V.A. Tuan,L.N. Hung and G. Szabo, J. Catal. 169 (1997) 397.
59. M.A. Asensi and A. Martinez, Appl. Catal. A Gen. 183 (1999) 155.
60. P. Meriaudeau, V.A. Tuan, L.N. Hung, C. Naccache and G. Szabo, J. Catal. 171 (1997) 329.
61. B. Wichterlova, N. Zilkova, E. Uvarova, J. Cejka, P. Sarv, C. Paganini and J.A.Lercher, Appl. Catal. A Gen. 182 (1999) 297.
62. M. Guisnet, P. Andy, Y. Boucheffa, N.S. Gnep, C. Travers and E. Benazzi, Catal. Lett. 50 (1998) 159.
63. P. Meriaudeau, V.A. Tuan,L.N. Hung and G. Szabo, Catal. Lett. 47 (1997) 71.
64. Z.R. Finelli, C.A. Querini, N.S. Figoli and R.A. Comelli, Appl. Catal. A Gen. 187 (1999) 115.
65. B.S. Kwak and J. Sung, Catal. Lett. 53 (1998) 125.
66. Z.R. Finelli, N.S. Figoli and R.A. Comelli, Catal. Lett. 51 (1998) 223.
67. P. Canizares, A. Carrero and P. Sanchez, Appl. Catal. A Gen. 190 (2000) 93.
68. J. Houzvicka, J.G. Nienhuis and V. Ponec, Appl. Catal. A Gen. 174 (1998) 207.
69. J. Houzvicka, R. Klik, L. Kubelkova and V.Ponec, Appl. Catal. A Gen. 150 (1997) 101.
70. C-L. O' Young, R.J. Pellet, D.G. Casey, J.R. Ugolini and R.A. Sawicki, J. Catal. 151 (1995) 467.

71. M.A. Asensi, A. Corma, A. Martinez, M. Derewinski, J. Krysciak and S.S. Tamhankar, Appl. Catal. A Gen. 174 (1998) 163.
72. M.W. Simon, S.L. Suib and C-L. O' Young, J. Catal. 147 (1994) 484.
73. R. Byggningsbacka, L-E. Lindfors and N. Kumar, Ind. Eng. Chem. Res. 36 (1997) 2990.
74. R. Byggningsbacka, N. Kumar and L-E. Lindfors, Catal. Lett. 58 (1999) 231.
75. R. Byggningsbacka, N. Kumar and L-E. Lindfors, Ind. Eng. Chem. Res. 38 (1999) 2896.
76. W-Q. Xu, Y-G. Yin, S. L. Suib and C-L. O' Young, J. Catal. 150 (1994) 34.
77. M.W. Simon, W.Q. Xu, S.L. Suib and C.L. O'Young, Microp. Mat. (1994) 477.
78. L.H. Gielgens, I.H.E. Veenstra, V. Ponec, M.J. Haanepen and J.H.C. van Hoof, Catal. Lett. 32 (1995) 195.
79. C.L. Lopez, F.J. Machado, J. Goldwasser, B. Mendez and K.Rodriguez, Zeolites 19 (1997) 133.
80. S-M. Yang, J-Y. Lin, D-H. Guo and S-G. Liaw, Appl. Catal. A Gen. 181 (1999) 113.
81. C.E. Snape, B.J. McGhee, S.C. Martin and J.M. Andresen, Catal. Today 37 (1997) 285.
82. M. Guisnet and P. Magnoux, Appl. Catal. 54 (1989) 1.
83. A. de Lucas, P. Canizares, A. Duran and A. Carrero, Appl. Catal. A Gen. 156 (1997) 299.
84. H.G. Karge and E. Boldingh, Catal. Today 3 (1988) 379
85. W.A. Groten, B.W. Wojciechowski and B.K. Hunter, J. Catal. 125 (1990) 311
86. H.G. Karge and E. Boldingh, Catal. Today 3 (1988) 53.
87. V.L. Zholobenko, D.B. Lukyanov, J. Dwyer and W.J. Smith, J. Phys. Chem. B 102 (1998) 2715.
88. A. Martucci, A. Alberti, G. Cruciani, P. Radaelli, P. Ciambelli and M. Rapacciulo, Microp. Mesop. Mat. 30 (1999) 95.
89. S. van Donk, F.M.F. de Groot, O. Stéphan, J.H. Bitter and K.P. de Jong, to be published / chapter 9 of this thesis.
90. B. Wichterlova, T. Tvaruzkova, Z. Sobalik and P. Sarv, Microp. Mesop. Mat. 24 (1998) 223.
91. Q. Wang, G. Gianetto and M. Guisnet, J. Catal. 130 (1991) 471.
92. K. Gosh and R.A. Kydd, J. Catal. 100 (1986) 185.
93. J.W. Beeckman and G.F. Froment, Ind. Eng. Chem. Fundam. 1 (1991) 245.
94. M. Guisnet and P. Magnoux, Catal. Today 36 (1997) 477.
95. S. Bathia, J. Beltramini and D.D. Do, Catal. Rev.- Sci. Eng. 31(4) (1989-1990) 431.
96. J.L. Bonardet, M.C. Barrage and J. Fraissard, J. Mol. Catal. A Chem. 96 (1995) 123.
97. J.P. Lange, A. Gutsze, J. Allgeier and H.G. Karge, Appl. Catal. 45 (1988) 345.
98. J.E. Kilpatrick, E.J. Prosen, K.S. Pritzer and F.D. Rossini, J. Res. Natl. Bur. Standards 36 (1946) 559.
99. Data of the National Bureau of Standards, Washington DC, USA.
100. V.B. Kazansky; Acc. Chem. Res. 24 (1991) 379.
101. D. Brouwer and J. Oelderik, Rec. Trav. Chim. Pays Bas 87 (1968) 1435.
102. V.B. Kazansky, Catal. Today 51 (1999) 419.

7

Butene Skeletal Isomerization over H-Ferrierite: TEOM and *in Situ* IR Study on the Role of Carbonaceous Deposits and the Location of Brønsted Acid Sites

Abstract

Butene skeletal isomerization over H-ferrierite is monitored in a catalysis set-up including a tapered element oscillating microbalance (TEOM) and using *in situ* infrared (IR) spectroscopy. For the first time the location and number of vacant Brønsted acid groups sited in the 10-, 8-, 6- and 5 membered rings (MR) of the H-ferrierite framework are established as a function of time-on-stream. By deconvolution of the acid site-band, it is determined that with proceeding reaction the 8 MR channels are blocked and the available micropore volume and Brønsted acidity on the aged H-ferrierite will be primarily located inside the 10 MR channels. When a maximum amount of hydrocarbons is deposited on the catalyst, vacant Brønsted acid sites are still present. Additionally, IR spectroscopy shows that with time-on-stream carbonaceous deposits are slowly converted from hydrogen-rich alkyl-aromatics into hydrogen-poor cyclopenta-fused-alkyl-aromatics, reducing by-product formation and therefore enhancing isobutene selectivity.

Introduction

A growing demand for isobutene as a raw material for methyl-*tert*-butyl-ether (MTBE), an octane enhancing fuel additive, has brought about large industrial and scientific interest for the skeletal isomerization of linear butenes to isobutene. The zeolite ferrierite in its acidic form (H-FER) containing 10-, 8-, 6-, and 5-membered rings (MR) [1] is an exceptionally selective and stable catalyst for this reaction [2,3]. The initial isobutene selectivity is rather poor, but with longer times-on-stream (TOS) very high selectivities and stabilities can be reached. The alteration in catalytic behavior is often associated with a change in the prevailing reaction pathway [4-8]. Evidence for this was provided by Meriaudeau *et al.* [5], de Jong *et al.* [6] and Cejka *et al.* [8] using ^{13}C-labeled butenes, demonstrating that over a fresh H-FER scrambling of the ^{13}C-label occurred whereas with prolonged TOS hardly any scrambling was observed. This points out that initially isobutene is formed via a non-selective dimerization-cracking pathway while in the long run isobutene is produced via either a monomolecular [5], a pseudo-monomolecular [7] and/or a selective dimerization-cracking pathway [3]. Although there is an ongoing debate on which of these pathways will be the main route for isobutene production [9-11], it is commonly established that the selective performance of H-FER coincides with the presence of carbonaceous deposits [4,6,7,12]. However, the role of these deposits and the importance of the H-FER Brønsted acid sites are not straightforward [9-15] and will be investigated in this study.

To correlate the amount of carbon deposited on H-FER with its catalytic performance in butene skeletal isomerization, a catalysis set-up including a tapered element oscillating microbalance (TEOM) is used. In literature, data on the final amount of carbon deposited on the catalyst as determined by *ex situ* methods are available [6,16,17]. Additionally, the formation of deposits with time has been monitored in conventional microbalances [4,18]. In such measurements, however, reactants are not forced to flow through the catalyst bed like in a down-flow fixed bed reactor. Consequently, the relation between the amount of carbonaceous deposits and the catalytic action can not be fully assessed. Chen *et al.* [19] clearly described the advantages of the application of a TEOM over conventional microbalances by studying the oligomerization of ethene over ZSM-5. Since all properties of a down-flow fixed bed reactor are maintained the TEOM offers the possibility to quantitatively monitor the formation rate and amount of carbonaceous deposits *in situ* [19-24], hence in real time, providing valuable information with respect to catalysis.

To establish the nature of carbonaceous deposits and the number of Brønsted acid sites and their locations as a function of TOS, *in situ* infrared (IR) spectroscopy is applied. Zholobenko *et al.* [14] and Domokos *et al.* [15] demonstrated for a fresh H-FER that it is possible to deconvolute the band corresponding to Brønsted acidity into

separate contributions. In that way the OH groups sited at the different locations in the framework were identified. Zholobenko *et al.* [14] applied computational and experimental techniques (ammonia TPD and accessibility studies) to interpret the IR spectra and reported five peaks that correspond to bridging OH groups vibrating in (1) the 10 MR channels, (2) the intersections between the 8 MR and 10 MR channels, (3) the 8 MR's, (4) the 6 MR's and (5) the 5 MR's. Domokos *et al.* [15] could not differentiate between the two different Brønsted acid sites in the 8 MR channels as detected by Zholobenko *et al.* [14]. However, they were able to distinguish the differently located Brønsted acid sites as a function of the extent of sodium-exchange. In this study it will be demonstrated for the first time that it is possible to distinguish the differently located Brønsted acid sites in the H-FER structure during butene skeletal isomerization. The relative numbers of the vacant Brønsted acid sites are determined as a function of the amount of carbonaceous deposits. Furthermore, when a maximum amount of coke is deposited on the catalyst the location of the vacant Brønsted acid sites is revealed, thus giving information on the location of the carbonaceous deposits.

Combining the information provided by *in situ* IR spectroscopy with the TEOM results, an overall image is obtained reflecting the role of carbonaceous deposits and the location and availability of Brønsted acid sites during butene skeletal isomerization over H-FER.

Experimental

Ferrierite

Commercially available high silicon NH_4^+ ferrierite (Zeolyst Int. Si/Al 30) was activated in a dry nitrogen flow at 823 K for 12 hours to obtain the H^+ ferrierite (H-FER). The sample displayed an acid site concentration of 0.53 mmol.g^{-1}, as determined by temperature programmed desorption - thermogravic analysis (TPD-TGA) using *n*-propylamine. Nitrogen physisorption / t-plot analysis shows an external surface area of 42 m^2.g^{-1} and a micropore volume of 0.132 ml.g^{-1}.

TEOM/catalysis

The catalytic experiments were performed in a tapered element oscillating microbalance (TEOM 1500 PMA, Rupprecht & Pataschnick) in order to monitor the formation of carbonaceous deposits *in situ*. The design of the TEOM reactor is such that it consists of a packed catalyst bed through which all the reactants are forced to flow. Because of its excellent sensitivity (in the microgram-range with a sample amount of 10-100 mg) and stability, the TEOM reactor provides the possibility to study real-time catalyst deactivation by uptake of carbonaceous deposits while performing

catalysis. The functioning of the TEOM is based on the relationship between the natural frequency (*f*) of the tapered element holding the catalyst, and its mass (*m*):

$$m_2 - m_1 = K_0\left[\left(\frac{1}{f_2}\right)^2 - \left(\frac{1}{f_1}\right)^2\right] \quad (1)$$

K_0 is the spring constant for the tapered element used in the experiment and the subscripts 1 and 2 refer to the alteration of mass and frequency with time. For a detailed description of the TEOM we refer to Chen *et al.* [19,21] and Hershkowitz and Madiara [20].

The tapered element was loaded with 53 mg of H-FER particles (90-150 μm). Quartz wool was used on top and bottom of the catalyst bed to keep the particles firmly packed. Measurements were performed at 623 K and 1.3 bar. Mass flow controllers adjusted the incoming gas flows. Reaction products were analyzed on-line using a Shimadzu 17A gas chromatograph with a Chrompack PLOT capillary column (fused silica-Al_2O_3/KCL, 50m x 0.32mm) equipped with a flame ionization detector. Prior to testing the samples were dried *in situ* in nitrogen at 623 K. All mass changes were corrected for temperature- and gas density differences by performing blank runs over inert samples. The weight hourly space velocity (WHSV) was varied from 4 to 27 g $_{n\text{-butene}}$.g $_{\text{H-FER}}^{-1}$.h^{-1} by adjusting the pure *n*-butene gas-flow (Hoek Loos, 1-butene, ≥ 99.5%). Conversion is defined as the molar ratio of all products (≠ *n*-butene) to all compounds detected. Selectivities are calculated as the molar ratio of a certain product to all products (≠ *n*-butene).

IR spectroscopy

IR spectra were recorded on a Perkin Elmer Spectrum One instrument during the skeletal isomerization of *n*-butene at atmospheric pressure and 623 K. The H-FER sample was pressed into a self-supporting wafer of approximately 3 mg and a diameter of 0.5 cm, by applying a pressure of 200 MPa. The wafer was placed in an *in situ* IR cell and heated up to 623 K in a helium flow (10 $ml.min^{-1}$) to remove adsorbed water. IR spectra during adsorption and reaction of *n*-butene on the sample were recorded using a 9 $ml.min^{-1}$ *n*-butene/helium flow ($P_{n\text{-butene}}$ / P_{total} = 0.225). The first 4 hours TOS an MCT detector recorded the spectra at a time interval of 5 minutes and during measurements 20 scans (22 seconds) were taken. After 4 hours spectra were recorded at a time interval of 5 hours using a MIR-TGS detector (100 scans, ~9 minutes). The spectra were measured in transmission mode from 4000 to 1000 cm^{-1} (4 cm^{-1} resolution) and after background subtraction (spectrum of the empty cell) normalized to the overtone lattice vibration of the dried H-FER between 1880-1860 cm^{-1} (A = 0.3), which

is a good measure of the thickness of the wafer. The OH stretch region (4000-3000 cm^{-1}) was deconvoluted using the Origin 6.1 software program, assuming Gaussian bandshapes.

Check experiments have been performed taking spectra of H-FER samples, aged *ex situ* in a normal down-flow fixed bed reactor. For these samples, the trend in the vacancy of Brønsted acid sites is very similar to the results that will be reported here, which confirms the present study to provide representative insight in the number of vacant Brønsted acid sites during *n*-butene reaction

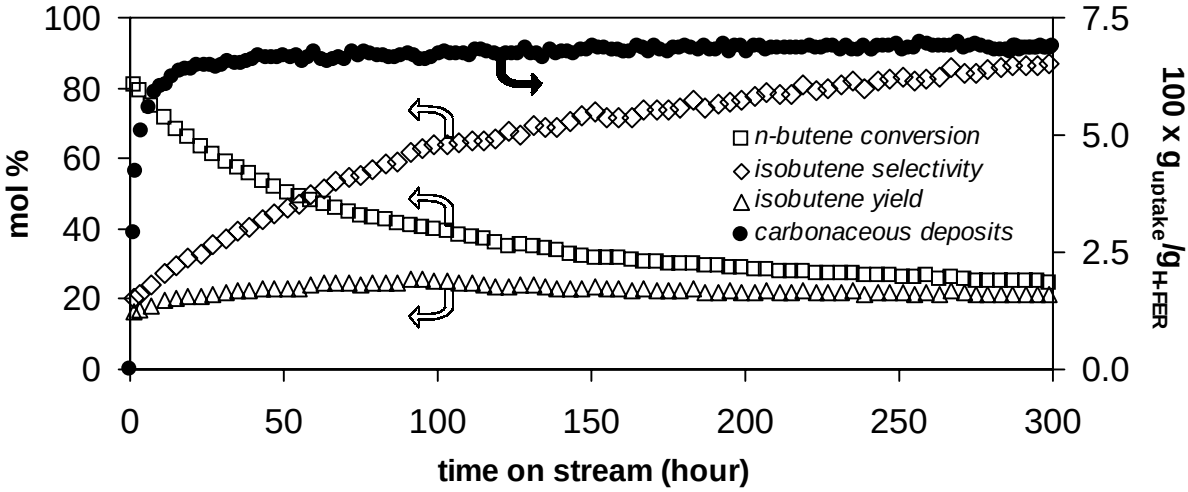

Figure 1. Catalytic performance and carbon uptake of H-FER during butene skeletal isomerization at 623 K, 1.3 bar and 4 g $_{n\text{-butene}}$.g $_{\text{H-FER}}^{-1}$.h^{-1} monitored in a TEOM-reactor.

Results

TEOM/catalysis

Figure 1 displays the catalysis results for butene skeletal isomerization over H-FER and the amount of carbonaceous species monitored *in situ* by the TEOM as a function of TOS. Already with short TOS a large amount of deposits is present on the catalyst, while the catalytic behavior is still liable to significant changes. In table 1 (on the next page) data are collected to exemplify the numerical changes in carbon uptake and catalytic performance of H-FER with TOS. Initially at 1 h TOS, the catalyst contains 2.5 wt% carbon and displays 81 % conversion, however, isobutene selectivity and yield are low, *i.e.* 20 % and 16 % respectively. In the region around 20 h TOS the amount of deposits levels off at 6.4 wt% while the conversion declines, the isobutene selectivity increases and the yield is slightly enhanced. With proceeding reaction the carbon content slowly increases to a final value around 6.8 wt% at 300 h TOS. It is important to note that during this slow weight gain, the *n*-butene conversion largely decreases to a

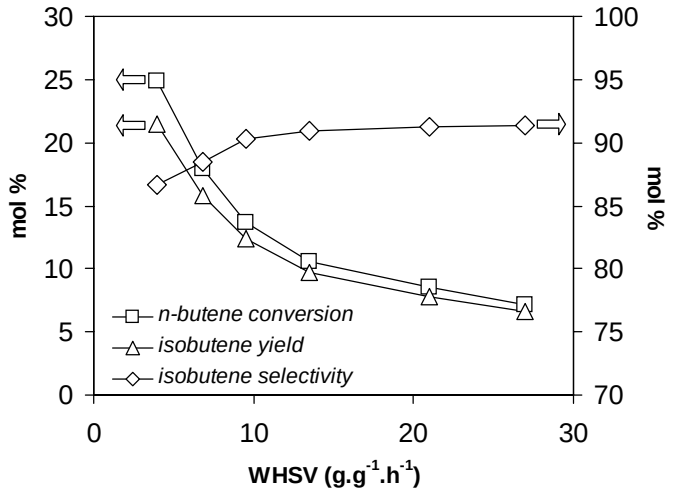

Figure 2. Conversion, yield and selectivity determined for aged and selective H-FER holding 6.8 wt% C at varying WHSV's, 623 K and 1.3 bar with $P_{n\text{-butene}} / P_{total} = 1$.

final value of 25 % at 300 h TOS and isobutene selectivity increases to 87 %. Hence, the change in activity and selectivity can not be directly related to the amount of carbonaceous deposits. Due to the opposite trends in conversion and selectivity, the net isobutene yield is almost constant with all TOS, although a shallow maximum is observed around 100 h TOS.

The carbon content of the final aged H-FER sample is 6.8 wt% as monitored by the TEOM. The deposition of carbonaceous deposits reduces the catalyst micropore volume to 0.013 $ml.g^{-1}$ and the external surface area to 19 $m^2.g^{-1}$. Hence, part of the pores of the aged and selective H-FER catalyst is still accessible for nitrogen. Since the kinetic diameters of nitrogen and *n*-butene are in the same range [4,6], one may assume that up to the same volume is accessible for butene molecules.

Over aged and selective H-FER, *i.e.* at 300 hours TOS, the WHSV was varied. In theory, this would result in net changes in conversion, selectivity and yield since the rates of the (pseudo)monomolecular and/or bimolecular reactions are different [25]. Figure 2 shows that increasing the WHSV, thus decreasing the contact time, enhances isobutene selectivity while both conversion and yield are diminished in a similar manner. These results are in good agreement with Byggningsbacka *et al*. [26].

Table 1. Effect of TOS on the carbon uptake, *n*-butene conversion, isobutene selectivity and yield during skeletal isomerization over H-FER at 623 K, 1.3 bar and WHSV = 4 g $_{n\text{-butene}}$.g $_{H\text{-FER}}^{-1}$.h^{-1}

TOS (h)	***Carbon uptake (wt%)***	***Conversion $nC_4^=$ (mol%)***	***Selectivity $iC_4^=$ (mol%)***	***Yield $iC_4^=$ (mol%)***
1	2.5	81	20	16
20	6.4	65	32	21
100	6.6	40	64	25
300	6.8	25	87	22

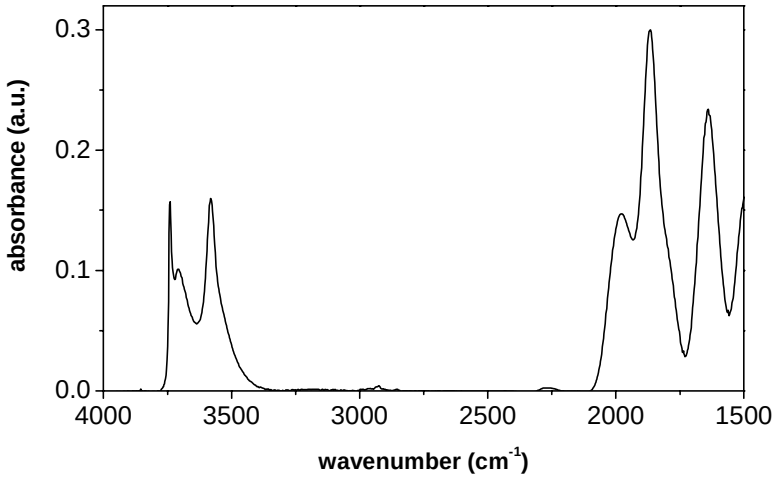

Figure 3. IR spectrum of H-FER obtained at T = 623 K under 10 ml/min He flow, after background subtraction (spectrum of the empty cell).

IR spectroscopy

In figure 3 the IR absorption spectrum of H-FER is shown. An intense band is found at 3580 cm^{-1}, which is assigned to the stretch vibration of the bridging Si-OH-Al hydroxyls, the Brønsted acid sites [14,15,27,28]. The signal at 3740 cm^{-1} is assigned to the stretch vibration of the terminal hydroxyls, the silanol groups [14,15,27,28]. An additional band is found at 3700 cm^{-1}, which originates from Lewis acidic non-framework aluminum species [28,29]. In the 2100 – 1500 cm^{-1} region the overtones of the H-FER lattice vibrations are found. Figure 4 displays the OH region of H-FER for the *in situ* recorded spectra at different TOS. With increasing TOS the total intensity of the OH band decreases, *i.e.* the number of acid sites reduces most likely because of irreversible deposition of carbonaceous species. Additionally, a broad band appears around 3300 cm^{-1}, which is assigned to Brønsted OH groups that are H-bonded to a C=C double bond. This band increases in intensity until 5 hours TOS and then reduces again.

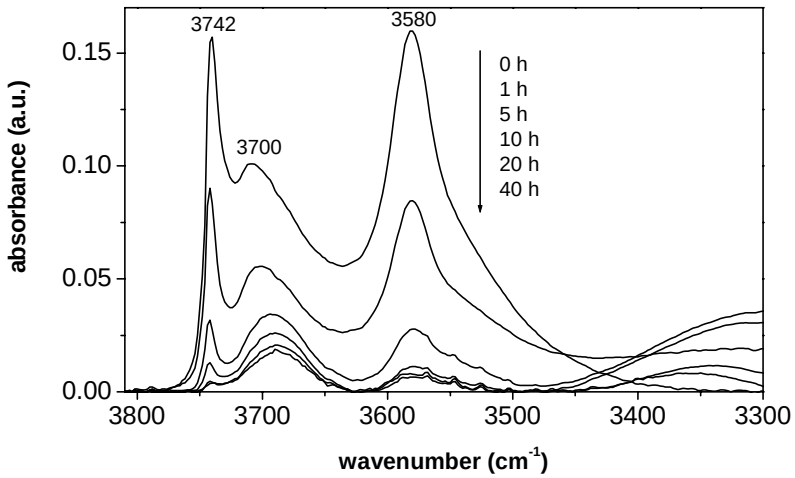

Figure 4. *In situ* IR spectra of the OH-region of H-FER without reaction and during *n*-butene reaction at various times on stream at 623 K, 1.0 bar and $P_{n\text{-butene}}$ / P_{total} = 0.225.

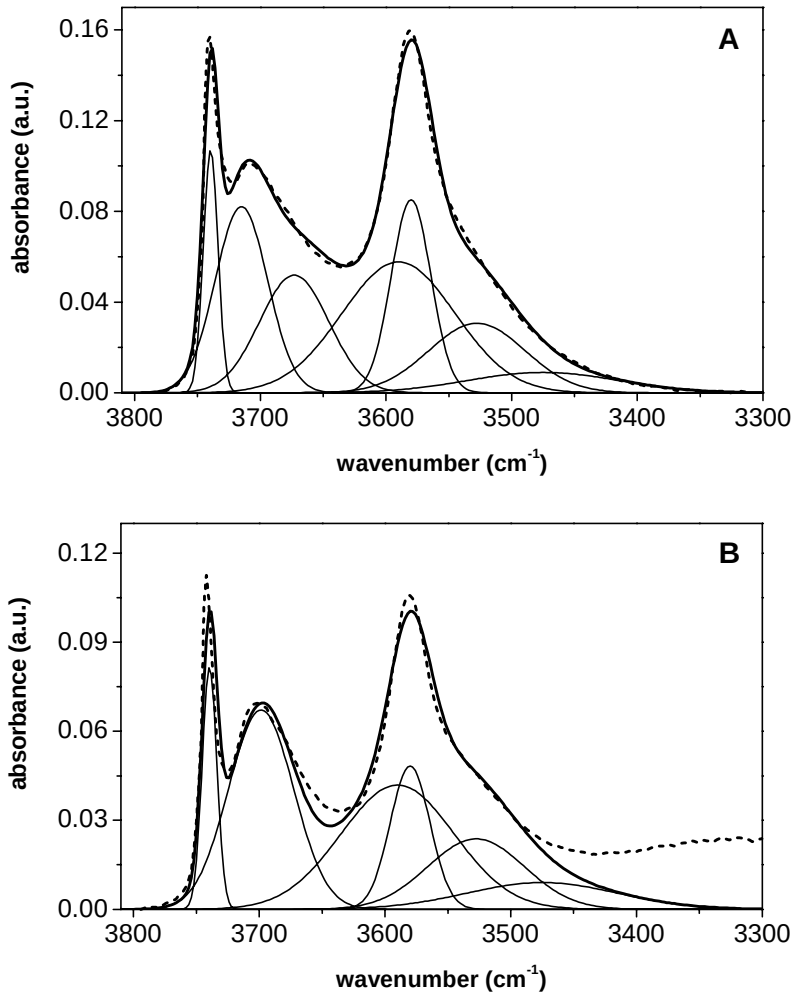

Figure 5. Deconvolution of the OH region of the H-FER IR spectrum (T = 623 K, under 10 ml/min He flow): -- experimental spectra; — computed spectra; — single components. (A) fresh H-FER, 0 h TOS. (B) aged H-FER at 1 hour TOS ($P_{n\text{-butene}}$ / P_{total} = 0.225).

In order to establish the contribution of the OH sites at different framework positions to the overall Brønsted acid band, the OH region of the IR spectrum for the fresh H-FER was deconvoluted. An excellent fit was obtained using the set of parameters proposed by Domokos *et al.* [15], taking into account the difference in experimental conditions. Figure 5A displays the deconvoluted OH region of the H-FER spectrum and in table 2 the matching assignments, peak positions, half-height bandwidths and integrated areas of the peaks are listed. At 3740 cm^{-1} the band of the silanol groups is found. The band assigned to non-framework aluminum is composed of two contributions, at 3715 cm^{-1} and 3673 cm^{-1}. The band corresponding to the Brønsted acidity is composed of four contributions. The first two bands at 3590 cm^{-1} and 3580 cm^{-1} are assigned to the bridging OH's in the 10 MR channels, and in the 8 MR channels, respectively. The third band at 3528 cm^{-1} is assigned to the Brønsted acid sites in the 6 MR's, pointing towards the 10 MR channels. The assignment of the band at 3475 cm^{-1} is ambiguous, but might be attributed to the OH groups in the 5 MR's [14,15].

Table 2. Parameters for the deconvolution of the OH region of the spectrum for fresh H-FER as shown in figure 5A, bandshapes are assumed to be Gaussian.

Acid site	*Peak position*	*Half-height bandwidth*	*Integrated area*
Silanol group	3740 cm^{-1}	11.8 cm^{-1}	1.58
Non-framework aluminum	3715 cm^{-1}	41.7 cm^{-1}	4.29
Non-framework aluminum	3673 cm^{-1}	55.1 cm^{-1}	3.58
Brønsted acid sites in 10 MR	3590 cm^{-1}	90.1 cm^{-1}	6.52
Brønsted acid sites in 8 MR	3580 cm^{-1}	31.6 cm^{-1}	3.37
Brønsted acid sites in 6 MR	3528 cm^{-1}	76.7 cm^{-1}	2.94
Likely Brønsted acid sites in 5 MR	3475 cm^{-1}	119.5 cm^{-1}	1.35

The OH regions of the spectra obtained with TOS were also deconvoluted such that the peak positions and half-height bandwidths were similar as for the fresh H-FER (table 2), with exception of the non-framework aluminum bands, which merge into one band at 3698 cm^{-1}. Figure 5B shows the deconvoluted OH region after 1 hour TOS. Until 5 hours TOS the deconvolution resulted in good fits, after that only the total number of Brønsted acid sites could be determined.

All the molar extinction coefficients of the Brønsted acid sites are assumed to be identical [15]. As a consequence, the relative number of vacant Brønsted acid sites in the different channels as a function of TOS can be determined using the results obtained by deconvolution of the OH regions of the aged H-FER samples. The total number of Brønsted acid sites as a function of TOS is represented in figure 6A. In figure 6B the relative band areas, *i.e.* the concentrations of the acid sites at the different locations relative to their respective initial concentration are shown as a function of TOS. After 20 hours TOS there is no significant further change in the number of acid sites. At this

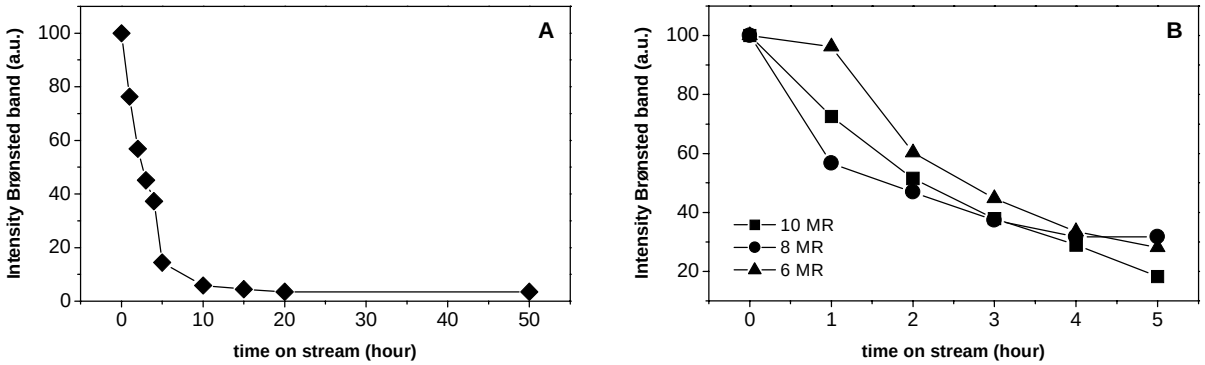

Figure 6. Number of vacant Brønsted acid sites on H-FER with TOS (T = 623 K, $P_{n\text{-butene}} / P_{total}$ = 0.225). (A) Total number, normalized on the number of Brønsted acid sites on fresh H-FER. (B) Number in the 10 MR channels (■), in the 8 MR channels (●), and in the 6 MR's pointing towards the 10 MR channels (▲). The relative numbers of sites are normalized on their respective initial number of sites.

stage almost all (97 %) silanol groups have been consumed, while around 15 % of the non-framework aluminum (Lewis acid sites) and 5 % of the Brønsted acid sites are still free (figure 4). Combining figure 6A and 6B it is implied that vacant Brønsted acid sites are still present in the 10 MR channels, in the 8 MR channels and in the 6 MR's pointing towards the 10 MR channels.

The *in situ* infrared spectra, displaying the region that characterizes carbonaceous species deposited on H-FER, are displayed in figure 7. The absorption at 1514 cm^{-1} corresponds to the carbon-carbon bond vibration of aromatics, at this stage such species are hydrogen rich *i.e.* non-condensed [30,31] and already moderately present after 1 h of exposure to *n*-butene. This band rapidly increases with a prolonged *n*-butene contact. After few hours, additional signals around and 1580 cm^{-1} and 1616 cm^{-1} appear that in combination with the band at 1514 cm^{-1} indicate the presence of hydrogen poor carbonaceous deposits [30,31]. Moreover, the peak around 1420 cm^{-1} indicates the presence of cyclopentane ring structures attached to aromatics. Also two contributions can be distinguished at 1438 cm^{-1} and 1352 cm^{-1}, induced by the bending modes of CH_2- and CH_3- aliphatic groups respectively [30-32]. Combination of these results suggests that with prolonged TOS cyclopenta-fused-aromatic ring structures with alkyl-groups are present on the catalyst, as was also demonstrated by Andy *et al.* [30].

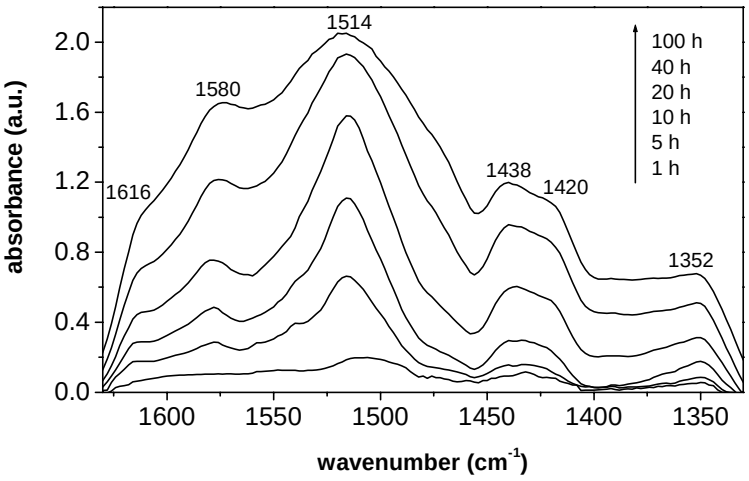

Figure 7. *In situ* IR spectra of carbonaceous deposits formed with TOS during the reaction of *n*-butene over H-FER. T = 623 K, P = 1.0 bar ($P_{n\text{-butene}}/P_{total} = 0.225$). The IR spectrum of the dried H-FER without deposits has been subtracted.

Discussion

On the location of the Brønsted acid sites

Figure 1 and table 1 demonstrate that the skeletal isomerization of *n*-butene over H-FER is accompanied by the formation of large amounts of carbonaceous deposits. Combining the results of figures 1, 4 and 7 it is clear that the initial deposition of carbon lowers the amount of Brønsted acid sites, resulting in a decrease of the overall *n*-butene conversion. The enhancement in isobutene selectivity shows that the

conversion drop is due to a suppression of non-selective dimerization-cracking reactions, which dominate the catalytic action with short TOS [5,6,8].

With respect to the alteration in the catalytic performance, discussion is focused on the role of carbonaceous deposits and the importance of the Brønsted acid sites and their locations [9-15]. Concerning this last aspect, this study demonstrates for the first time that deconvolution of spectra recorded *in situ*, thus during *n*-butene reaction, resulted in good fits (figure 5B) using the set of parameters obtained for fresh H-FER (figure 5A and table 2). In this way the contributions of the silanol groups, the non-framework aluminum and the different Brønsted acid sites have been distinguished, in good agreement with Domokos *et al.* [15]. Brønsted acid sites in the 10 MR channels, in the 8 MR channels, in the 6 MR's pointing towards the 10 MR channels and those that are assumed to be in the 5 MR's, are identified. Figures 4 and 6A indicate that with short TOS there is a reduction in the overall number of Brønsted acid sites. Figure 6B shows that in the first 3 hours TOS a fast decrease of the sites in the 8 MR channels occurs. This agrees with nitrogen physisorption results [12] that revealed that with low coke content (short TOS) there is a fast decrease in micropore volume attributed to a blockage of the 8 MR channels. As a result of such pore blocking effects not all the Brønsted acid sites in the 8 MR channels are consumed, hence there are still vacant sites present but most likely not accessible for *n*-butene. At the same time figure 6B shows that the acid sites located in the 10 MR channels and 6 MR's are deactivated at a lower rate. This again correlates with nitrogen physisorption results [12] showing that there is a slow linear decrease in micropore volume with higher coke contents, *i.e.* with longer TOS.

The TEOM results in figure 1 show that the amount of deposits on H-FER levels off around 20 h TOS. From the IR results in figure 6A it is clear that after 20 hours TOS no large changes in the total number of vacant Brønsted acid sites are observed. Furthermore, figure 4 reveals that when a maximum amount of deposits is present on the catalyst, almost all silanol groups are consumed, although some non-framework aluminum is still available. In the end, the catalyst micropore volume is 0.013 $ml.g^{-1}$ indicating that part of the pores of the selectively operating catalyst is still accessible. Combining figure 6A and 6B it is suggested that at this stage vacant Brønsted acid sites are still present in the 10 MR channels, the 6 MR's pointing towards the 10 MR channels and in the 8 MR channels. Although, it seems likely that the latter sites are inaccessible for the reactant when carbonaceous deposits are present on the catalyst. This implies that the available micropore volume and Brønsted acid sites will be mainly located inside the 10 MR channels. Domokos *et al.* [15] reported on the correlation between acid site locations in sodium exchanged H-FER samples and their catalytic performance. A clear structure-activity relationship was observed between the Brønsted acid sites located in the 10 MR channels and the selective formation of isobutene. This

agrees very well with the results reported in this study and with studies by other groups, implying that the 10 MR channels provide shape selectivity towards the formation of isobutene [7,13,33].

On the role of carbonaceous deposits

After the initially fast deposition of carbon, the TEOM results in figure 1 and table 1 reveal that with proceeding reaction a very slow increase in the amount of deposits from 6.4 wt% at 20 h TOS to a final value of 6.8 wt% takes place. Figure 7 indicates that in the beginning the deposits mainly consist of hydrogen rich alkyl-aromatic compounds. This suggests that at this stage, *i.e.* when carbonaceous deposits block large part of the acid sites, butene reaction with these alkyl-aromatic deposits and subsequent cracking is the origin of smaller amounts of by-products. Simultaneously with the slow growth in carbon content of H-FER, a relatively large decline in *n*-butene conversion occurs. Additionally, isobutene selectivity is enhanced, which indicates that parallel to the reactions running over the deposits a selectively operating isomerization pathway becomes prevailing.

The variations in conversions and selectivity coincide with a change in the nature of carbonaceous deposits as displayed in figure 7, revealing that the initially present hydrogen-rich alkyl-aromatic species are slowly converted into hydrogen-poor cyclopenta-fused-aromatic ring structures, which is in agreement with observations by Andy *et al.* [30]. These species are much less reactive resulting in less reaction with butenes, which mainly lead to by-product formation. Accordingly, a further enhancement in isobutene selectivity with prolonged TOS is induced.

Over the aged and selective operating H-FER catalyst the WHSV has been varied. Based on the results presented in figure 2 it is suggested that the conversion drop observed with increasing WHSV, can be ascribed to a reduction of non-selective reactions running over the deposits and/or Brønsted acid sites. Consequently, by-product formation but also part of the isobutene production is reduced. This last aspect induces the simultaneous decrease in isobutene yield although it is clear that with prolonged TOS larger part of the isobutene will be formed via a selectively operating reaction pathway. Therefore the slight selectivity enhancement observed by raising the WHSV, is explained by the increase of the ratio of the selective over the non-selective operating pathway(s). From this it is inferred that both secondary, *i.e.* bimolecular reactions over Brønsted sites and/or reactions running over the deposits, as well as primary reactions may lead to the overall production of isobutene. Although it is evident that the latter reaction pathway displays much higher selectivity and is prevailing with prolonged TOS.

Overall, it is revealed that at prolonged TOS a selective isomerization pathway directly producing isobutene from *n*-butene is operating over an aged H-FER catalyst,

containing 6.8 wt% of condensed aromatic deposits. The selective operation of H-FER coincides with the availability of some micropore volume and Brønsted acid sites, which will be mainly located inside the 10 MR channels. The present study can not completely clarify whether the latter sites are directly involved in the catalytic action, although it is evident that the sites for isobutene production over aged and selective H-FER are not very liable to deactivation, since very high lifetimes have been reported [3,6].

Conclusions

Monitoring butene skeletal isomerization over H-FER in a catalysis set-up including a TEOM proves that large amounts of carbonaceous deposits are already present with short TOS. In combination with *in situ* IR spectroscopy it is inferred that initial deposition of butenes lowers the amount of Brønsted acid sites, suppressing non-selective dimerization-cracking reactions and therefore decreasing the overall activity. Deconvolution of the IR acid band establishes for the first time the number of vacant Brønsted acid sites at different locations in the H-FER framework as a function of TOS. Four types of Brønsted OH groups located in 10-, 8-, 6- and 5 MR can be distinguished. With initial *n*-butene reaction, the 8 MR channels are rapidly blocked and the available micropore volume and Brønsted acidity on the aged H-FER will be primarily located inside the 10 MR channels. With proceeding TOS, when the amount of carbonaceous deposits is stabilized, butene reaction with these deposits and subsequent cracking is the origin of smaller amounts of by-products. IR spectroscopy indicates the deposits to be slowly converted into hydrogen-poor coke, reducing reactivity and concomitant appearance of by-product formation. In the end isobutene will be produced via a selectively operating reaction pathway over a stable H-FER catalyst holding 6.8 wt% deposits.

Acknowledgements

Eveline Bus is acknowledged for performing the IR experiments and helpful discussions. Dr. Tom Visser and Dr. Frank de Groot (Utrecht University) are acknowledged for helpful advises.

References

1. R.E. Morris, S.J. Weigel, N.J. Henson, L.M. Bull, M.T. Janicke, B.F. Chmelka and A.K. Cheetham, J. Am. Chem. Soc., 116 (1994) 11894.

2. P. Grandvallet, K.P. de Jong, H.H. Mooiweer, A.G.T.G. Kortbeek and B. Kraushaar-Czarnetzki, European Patent No. 501 577, to Shell (1992).
3. H.H. Mooiweer, K.P. de Jong, B. Kraushaar-Czarnetzki, W.H.J. Stork and S.C. Krutzen, Stud. Surf. Sci. Catal. 84 (1994) 2327.
4. W-Q. Xu, Y-G. Yin, S.L. Suib and C-L. O' Young, J. Phys. Chem. 99 (1995) 758.
5. P. Meriaudeau, R. Bacaud, L.N. Hung and T.A. Vu, J. Mol. Catal. A 110 (1996) L177.
6. K.P. de Jong, H.H. Mooiweer, J.G. Buglass and P.K. Maarsen, Stud. Surf. Sci. Catal. 111 (1997) 127.
7. M. Guisnet, P. Andy, N.S. Gnep, C. Travers and E. Benazzi, Stud. Surf. Sci. Catal. 105 (1997) 1365.
8. J. Cejka, B. Wichterlova and P. Sarv, Appl. Catal. A Gen. 179 (1999) 217.
9. J. Houzvicka and V. Ponec, Ind. Eng. Chem. Res. 36 (1997) 1424.
10. M. Guisnet, P. Andy, N.S, Gnep, C. Travers and E. Benazzi, Ind. Eng. Chem. Res. 37 (1998) 300.
11. J. Houzvicka and V. Ponec, Ind. Eng. Chem. Res. 37 (1998) 303.
12. S. van Donk, J.H. Bitter and K.P. de Jong, Appl. Catal. A Gen. 212 (2001) 97 / chapter 6 of this thesis
13. P. Mériaudeau, T.A. Vu, L.N. Hung and G. Szabo, J. Catal. 169 (1997) 397.
14. V.L. Zholobenko, D.B. Lukyanov, J. Dwyer and W.J. Smith, J. Phys. Chem. 102 (1998) 2715.
15. L. Domokos, L. Lefferts, K. Seshan and J.A. Lercher, J. Mol. Catal. A Chem. 162 (2000) 147.
16. G. Seo, H.S. Jeong, D-L. Jang, D.L. Cho and S.B. Hong, Catal. Lett. 41 (1996) 189.
17. G.N. Brascó and R.A. Comelli, Catal. Lett. 71 (2001) 111.
18. M. Guisnet, P. Andy, Y. Boucheffa, N.S. Gnep, C. Travers and E. Benazzi, Catal. Lett. 50 (1998) 159.
19. D. Chen, A. Gronvold, H.P. Rebo, K. Moljord and A. Holmen, Appl. Catal. A Gen. 137 (1996) L1.
20. F. Hershkowitz and P.D. Madiara, Ind. Eng. Chem. Res. 32 (1993) 2969.
21. D. Chen, H.P. Rebo, K. Moljord and A. Holmen, Chem. Eng. Sci. 51 (1996) 2687.
22. K. Liu, S.C. Fung, T.C. Ho and D.S. Rumschitzki, J. Catal. 169 (1997) 455.
23. L.M. Petkovic and G. Larsen, Ind. Eng. Chem. Res. 38 (1999) 1822.
24. L.M. Petkovic and G. Larsen, J. Catal. 191 (2000) 1.
25. L. Domokos, L. Lefferts, K. Seshan and J.A. Lercher, J. Catal. 197 (2001) 68.
26. R. Byggningsbacka, N. Kumar and L.-E. Lindfors, J. Catal. 178 (1998) 611.
27. W-Q. Xu, Y-G. Yin, S.L. Suib, J.C. Edwards and C-L. O' Young, J. Catal. 163 (1996) 232.
28. M. Trombetta, G. Busca, S. Rossini, V. Piccoli, U. Cornaro, A. Guerci, R. Catani and R.J. Wiley, J. Catal. 179 (1998) 581.
29. Y.S. Yin, A. Auroux and J.C. Vedrine, Appl. Catal. 37 (1988) 1.
30. P. Andy, N.S. Gnep, M. Guisnet, E. Benazzi and C. Travers, J. Catal. 173 (1998) 322.
31. Z.R. Finelli, C.A. Querini, N.S. Figoli and R.A. Comelli, Appl. Catal. A Gen. 187 (1999) 115.
32. C. Pazè, B. Sazak, A. Zecchina and J. Dwyer, J. Phys. Chem. B 103 (1999) 9978.
33. J. Houzvicka, S. Hansildaar and V. Ponec, J. Catal. 167 (1997) 173.

8

Probing the Accessible Sites for Butene Skeletal Isomerization over Aged and Selective H-Ferrierite with d_3-Acetonitrile

Abstract

Aged H-ferrierite (H-FER) samples with different contents of deposits were prepared and studied under differential catalytic conditions in a tapered element oscillating microbalance. Subsequently, these samples were examined using infrared spectroscopy to determine the nature of carbonaceous deposits and probing the type and number of accessible sites with d_3-acetonitrile. From these results, for the first time, we have been able to calculate turn-over-frequencies (TOF) for *n*-butene conversion and isobutene formation for both fresh and aged H-FER catalysts. It is observed that the deposition of carbonaceous species significantly lowers the number of accessible Brønsted sites. With short time-on-stream (TOS) cracking of the alkyl-aromatic deposits contributes to the overall isobutene production but simultaneously harms the selective catalytic action by inducing non-selective side-reactions. With prolonged TOS these deposits become non-reactive and as a result the TOF drops, while isobutene is produced with high selectivity. It is demonstrated that at this stage no carbenium ions are detected, while Brønsted OH acid sites are still accessible for d_3-acetonitrile on the extensively aged and highly selective H-FER. This indicates the latter sites to be responsible for the selective catalytic conversion of *n*-butene into isobutene.

Introduction

Zeolites containing 10-membered ring (MR) pores have proven to exhibit high selectivities for the skeletal isomerization of linear butenes into isobutene [1-4]. Especially the two-dimensional zeolite H-ferrierite (H-FER), for which 8 MR pores interconnect the 10 MR main channels, displays an exceptionally high selectivity and stability [5,6]. Nevertheless, the initial selectivity of H-FER is low, but increases with time-on-stream (TOS) when carbonaceous deposits largely fill the H-FER pores [4,7-9]. Over a fresh catalyst ^{13}C-labelling experiments have proven that non-selective bimolecular reactions, i.e. dimerization followed by cracking, dominate the catalytic action. However, in the same experiments it was established that over an aged catalyst with carbonaceous deposits present, the formation of isobutene occurs selectively and must take place via a different route [8,10,11].

A number of authors [10,12-15] therefore suggested a monomolecular reaction pathway, in which butene is isomerized over a plain Brønsted acid site of H-FER, to be the dominant reaction pathway for isobutene formation. The monomolecular formation of isobutene involves an energetically and thermodynamically highly unfavorable primary carbenium ion [16]. Therefore an alternative pathway, which does not involve a primary carbenium ion, was proposed by Guisnet *et al.* [9,17,18]. It was claimed that with prolonged TOS all Brønsted acid sites are inaccessible for reactants [18] and the creation of new highly active and selective sites was assumed to explain the enhanced isobutene selectivity. This so-called pseudo-monomolecular reaction pathway is thought to proceed over alkyl-aromatic tertiary carbenium ions that are captured inside the entrances of the zeolite pores.

In the current study the number and nature of the active sites available on aged H-FER catalysts are established and correlated with the catalytic performance in butene skeletal isomerization. Catalysis experiments are performed in a tapered element oscillating microbalance (TEOM), which resembles a down-flow fixed bed reactor and offers the possibility of quantitatively monitoring the formation of carbonaceous deposits *in situ* [19,20]. Several H-FER catalysts holding different amounts of deposits are evaluated and subsequently examined with infrared (IR) spectroscopy, in order to probe the available active sites. As a probe molecule d$_3$-acetonitrile (CD_3CN) is used, which is relatively small in size, as are the involved butene isomers.

In recent years CD_3CN has been widely employed in IR spectroscopic studies [21-28] because of its intermediate proton affinity [29] and the specific and high sensitivity of its ν(CN) stretching mode for interactions with different acid sites present in zeolites. Besides the ability to probe Brønsted and Lewis acid sites, Bystrov [21] and Jolly *et al.* [23] reported that CD_3CN could also probe secondary and tertiary carbenium ions. This makes it a highly interesting probe molecule to study the nature

of the active sites for isobutene formation on aged H-FER catalysts to be either Brønsted acidic protons or carbenium ions prefixed in the coke. Hence, by elucidating the nature and number of the active and selective sites and correlate this with catalysis, this study contributes to the longstanding discussion whether zeolite protons or carbenium ions are the active centers for butene skeletal isomerization over aged H-FER.

Experimental

Catalysis experiments in a TEOM

Commercially available high silicon-NH_4^+ ferrierite (Zeolyst Int. Si/Al 30) was activated in a dry nitrogen flow at 823 K for 12 hours to obtain the H^+ ferrierite (H-FER). The fresh H-FER displayed an acid site concentration of 0.53 mmol.g^{-1} as determined by temperature programmed desorption-thermogravic analysis (TPD-TGA) using *n*-propylamine. Nitrogen physisorption / t-plot analysis shows an external surface area of 42 $m^2.g^{-1}$ and a micropore volume of 0.132 ml.g^{-1}.

Catalytic conversion and selectivity were determined for H-FER samples holding different amounts of carbonaceous deposits. The measurements were executed in a tapered element oscillating microbalance (Rupprecht & Pataschnik TEOM 1500 PMA) in order to monitor the uptake of carbonaceous deposits during catalysis, hence *in situ*. For a detailed description of the TEOM we refer to Hershkowitz and Madiara [19] and Chen *et al.* [20]. The tapered element was loaded with 5 - 10 mg of H-FER particles (90 - 150 μm). Quartz wool was used on the top and bottom of the catalyst bed to keep the particles firmly packed. Measurements were performed at 623 K and 1.3 bar. Mass flow controllers adjusted the incoming gas flows. Reaction products were analyzed on-line using a Shimadzu 17A gas chromatograph with a Chrompack PLOT capillary column (fused silica-Al_2O_3/KCL, 50 m x 0.32 mm) equipped with a flame ionization detector. Prior to testing the samples were dried *in situ* in nitrogen at 623 K. All mass changes were corrected for temperature- and gas density differences by performing blank runs over inert samples.

Table 1 lists the content of carbonaceous deposits, the TOS, the applied weight hourly space velocity (WHSV) and the catalytic performance of the aged H-FER. The WHSV was varied by adjusting the pure *n*-butene gas-flow (Hoek Loos, 1-butene, ≥ 99.5%) in order to examine all samples at similar and low conversions (< 10 mol%). Conversion is defined as the change in mol% of linear butenes comparing the feed to the product mixture. Selectivities are calculated as the molar ratio of a certain product to all products (≠ *n*-butene). Immediately after the catalytic experiment the *n*-butene flow was switched off and after cooling down, the catalyst was unloaded from the

microbalance and subsequently studied by IR spectroscopy, probing the active sites with CD_3CN. Check experiments were performed which showed that the aged H-FER samples maintained their catalytic performance after cooling down to room temperature under nitrogen, exposure to air and subsequent reheating to the applied reaction temperature; this appeared to be the case for all samples. Moreover, nitrogen physisorption / t-plot analysis for the extensively aged H-FER6.8C shows an external surface area of 19 $m^2.g^{-1}$ and a micropore volume of 0.013 $ml.g^{-1}$.

Table 1. Carbon uptake, TOS, WHSV and performance of the aged H-FER samples at 623 K.

Sample	*Reaction conditions*		*Results uptake and catalytic performance*		
	TOS (h)	WHSV ($g_{C4=}.g_{H\text{-}FER}^{-1}.h^{-1}$)	Carbon uptake ($100.g_{uptake}.g_{H\text{-}FER}^{-1}$)	n-Butene conv. (mol%)	Isobutene sel. (mol%)
H-FER5.0C	4	169	5.0	9.5	35.5
H-FER6.6C	20	142	6.6	8.9	38.0
H-FER6.8C	300	21	6.8	8.5	91.2

IR spectroscopy: probing with CD_3CN

IR spectroscopy was performed using a Perkin Elmer Spectrum One instrument equipped with an *in situ* IR flow cell and an MCT detector. Measurements were performed on a fresh H-FER sample and on the aged H-FER samples listed in table 1. A self-supported wafer of approximately 3 mg with a diameter of 0.5 cm was prepared by applying a pressure of 200 MPa. The wafer was placed in a cylindrical oven and pre-heated to 623 K (the reaction temperature applied in the catalysis measurements) in a helium flow (10 $ml.min^{-1}$). Subsequently, the sample was cooled down to 448 K and the adsorption of CD_3CN (Acros, 99% purity) was started by switching the infrared cell inlet to a stream of CD_3CN (partial pressure 5-10 mbar) in He (10 $ml.min^{-1}$). The applied conditions were assessed based on experimental examination, revealing the highest possible temperature and lowest partial pressure at which the maximum number of Brønsted acid sites is probed. Spectra were measured in transmission mode from 4000 to 1000 cm^{-1} (4 cm^{-1} resolution) and after background subtraction (spectrum of the empty cell) normalized to the overtone lattice vibration of H-FER between 1880-1860 cm^{-1} (A = 0.3), which is a good measure of the thickness of the wafer. In order to quantify the amount of CD_3CN adsorbed on the Brønsted sites of the sample, the ν(CN) stretch region (2600-2100 cm^{-1}) was integrated after deconvolution using the Origin 6.1 software program. The extinction coefficients for all samples were assumed to be similar.

Results

Catalysis experiments in a TEOM

The results of the catalytic experiments performed in the TEOM on H-FER samples holding different amounts of carbonaceous deposits are collected in table 1. Results have been obtained under differential conditions at low (< 10 mol%) and similar conversions in order to compare the catalytic behavior of the aged H-FER samples in a quantitative way. Both H-FER5.0C and H-FER6.6C, measured at 4 h and 20 h TOS respectively, display low selectivities towards isobutene of around 37 mol%. For the extensively aged H-FER6.8C obtained at 300 h TOS, the isobutene selectivity is drastically enhanced to 91 mol%. This is an important feature since only a minor increase in uptake of carbonaceous deposits occurred going from H-FER6.6C to H-FER6.8C. Hence, the major increase in selectivity can not be directly related to the amount of carbonaceous deposits.

IR spectroscopy: probing fresh H-FER with CD_3CN

The fresh H-FER sample was studied with IR spectroscopy by *in situ* probing the active sites with CD_3CN. Figure 1 shows the IR spectra of fresh H-FER, of H-FER with adsorbed CD_3CN and the difference of these two spectra. The fresh H-FER spectrum displays a peak at 3742 cm^{-1} corresponding to the OH stretch vibration of the terminal silanol groups [30,31], mainly located on the external surfaces of the H-FER crystals. The band around 3580 cm^{-1} is built up of different Brønsted OH groups that are bridged between silicon and aluminum cations present in the H-FER structure [30,31]. A band around 3700 cm^{-1} [32] indicates the presence of non-framework aluminum species.

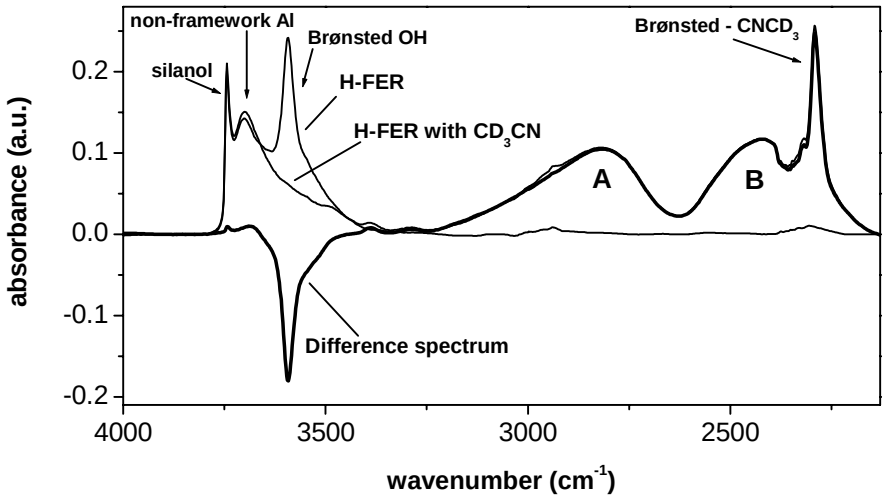

Figure 1. IR spectra of H-FER, H-FER with adsorbed CD_3CN and the difference spectrum, obtained at 5 mbar CD_3CN pressure in 10 ml.min^{-1} He-flow, T = 448 K.

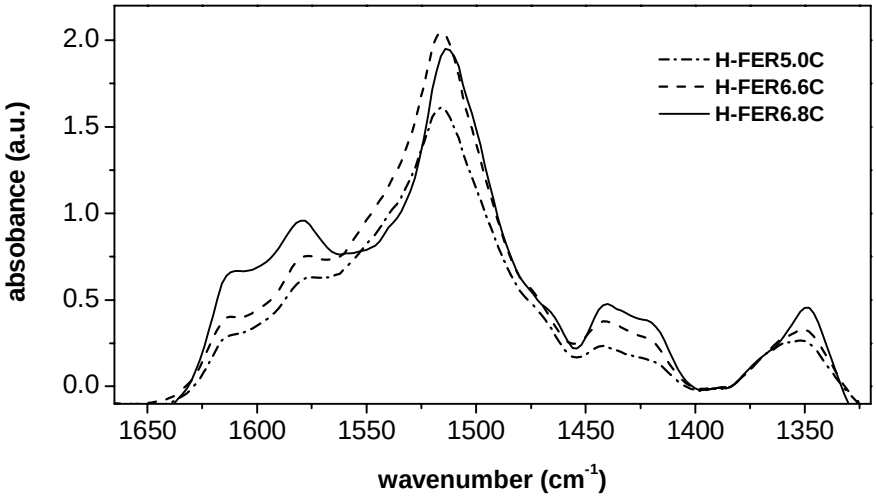

Figure 2. IR spectra of the carbonaceous deposits on H-FER5.0C, H-FER6.6C and H-FER6.8C. The spectra are obtained under a 10 ml.min^{-1} He-flow, T = 623 K and the spectrum of the dried H-FER (without deposits) is subtracted.

The spectrum after CD_3CN adsorption displayed in figure 1 shows the generally established A and B contours [22,24,25,28] to be present at ~2820 cm^{-1} and ~2420 cm^{-1} respectively, resulting from a large red shift of the ν(OH) due to moderate hydrogen bonding to the CD_3CN nitrogen [22,25]. The peak at 2292 cm^{-1} is assigned to the stretch vibration of ν(CN) co-ordinated to a Brønsted acid site [22-28]. A very small number of Lewis acid sites is also covered at the applied CD_3CN pressure, which results in a small shoulder at 2318 cm^{-1} [22,24,25,27,28]. Minor disappearance of the silanol-peak at 3742 cm^{-1} occurs and accordingly no peak of the stretch vibration of ν(CN) coordinated to a silanol group is observed, which if present should be around 2275 cm^{-1} [22,25,27,28].

IR spectroscopy: probing aged H-FER with CD_3CN

After catalysis, the aged H-FER samples were studied with IR spectroscopy. In figure 2 the regions that characterize the carbonaceous species deposited on H-FER are displayed for all aged samples. The absorption at 1514 cm^{-1} corresponds to the carbon-carbon bond vibration of hydrogen rich non-condensed aromatics [18,33]. However, by the appearance of additional bands around 1415 cm^{-1}, 1578 cm^{-1} and 1610 cm^{-1}, the presence of condensed aromatic deposits is indicated [18,33]. Moreover, the peak around 1420 cm^{-1} indicates the presence of cyclopentane ring structures. Also two contributions can be distinguished at 1442 cm^{-1} and 1350 cm^{-1} that are characteristic for the bending modes of CH_2 and CH_3 aliphatic groups respectively [18,33,34]. Going from H-FER5.0C to H-FER6.6C, figure 2 shows that all bands display a higher intensity due to the elevated content of deposits of the latter sample. Next, going from H-FER6.6C to H-FER6.8C, the band at 1514 cm^{-1} slightly decreases while the bands

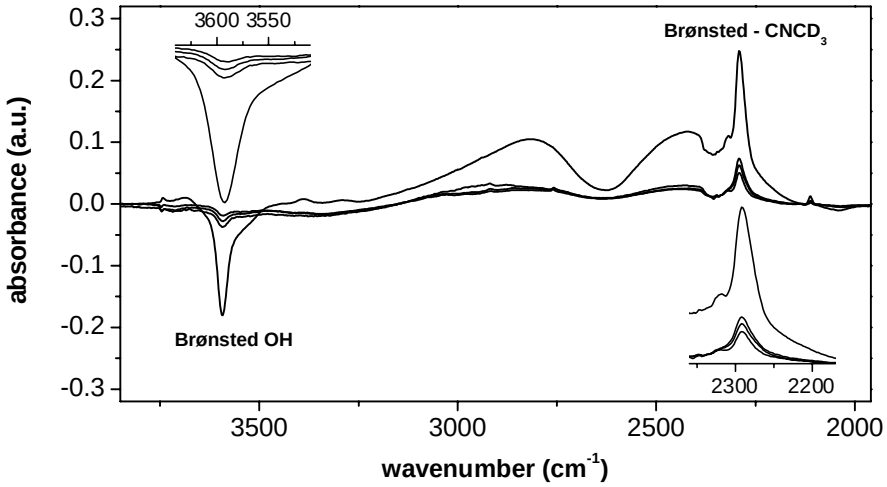

Figure 3. IR difference spectra of CD_3CN adsorbed on fresh H-FER, H-FER5.0C, H-FER6.6C and H-FER6.8C, obtained at 5-10 mbar CD_3CN pressure in 10 ml.min^{-1} He-flow, T = 448 K. Negative peaks correspond to the disappearance and positive peaks to the appearance of a vibration. The figure insets display a close-up of the Brønsted ν(OH) stretch region (left top) and the ν(CN) stretch region (right bottom). For explanation, see text.

that are characteristic for condensed aromatics clearly increase. Therefore, these results suggest that with extensive aging of H-FER the nature of carbonaceous deposits changes towards less hydrogen-rich species. In combination with the bands characteristic for cyclopentane and alkyl-groups it is suggested that with prolonged TOS condensed cyclopenta-fused-alkyl-aromatic ring structures are present on the catalyst, which is in perfect agreement with results from Guisnet *et al.* [18].

Subsequently, the aged H-FER samples were probed *in situ* with CD_3CN so that the number and nature of active sites was established. In figure 3 the difference spectra, *i.e.* the difference between the spectra with and without CD_3CN, are shown for fresh H-FER and for the differently aged H-FER samples. Upon adsorption of CD_3CN the band assigned to the Brønsted acid sites at 3580 cm^{-1} becomes negative, which illustrates the disappearance of Brønsted acid sites. For all samples it is observed that the disappearance of the Brønsted peak correlates with the appearance of the peak at 2292 cm^{-1}. Hence, the positive peak at 2292 cm^{-1} can be solely assigned to the stretch vibration of ν(CN) co-ordinated to a Brønsted acid site, as was also observed in other studies [22-28]. With increasing amount of carbonaceous deposits, the difference peak corresponding to the Brønsted sites becomes less negative and the difference peak for adsorbed CD_3CN becomes less positive. This indicates that the number of Brønsted acid sites that are accessible for CD_3CN is reduced upon *n*-butene reaction. Nevertheless, it is clear that still Brønsted acid sites are accessible, even for the extensively aged H-FER6.8C sample. In figure 4 the IR spectrum of H-FER6.8C with adsorbed CD_3CN is displayed and as a comparison the spectrum of CD_3CN adsorbed

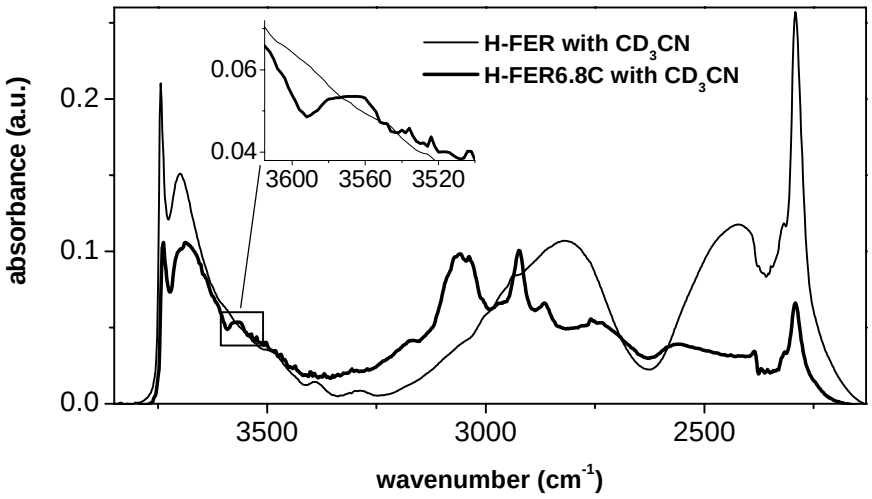

Figure 4. IR spectra of H-FER and H-FER6.8C with adsorbed CD_3CN, obtained at 5 mbar CD_3CN pressure in 10 ml.min^{-1} He-flow, T = 448 K. The figure inset illustrates the peak for the unperturbed Brønsted sites on H-FER6.8C that is left after CD_3CN-probing.

on fresh H-FER is also shown. In the H-FER6.8C spectrum a small Brønsted band is left after CD_3CN adsorption, which reveals that some Brønsted acid sites remain unperturbed upon probing, indicating that not all sites are accessible. The maximum of the small band that is left after probing is located at slightly lower frequencies (~ 3560 cm^{-1}) than the peak-maximum observed for fresh H-FER (~ 3580 cm^{-1}, see figure 1).

The specific and high sensitivity of the ν(CN) stretching mode at 2292 cm^{-1} allows quantification of the accessible Brønsted acid sites present in the aged H-FER samples. In table 2 the peak areas relative to the peak area of the fresh H-FER and the numbers of accessible Brønsted acid sites for the different H-FER samples are displayed. The number of accessible Brønsted acid sites for fresh H-FER was determined using *n*-propylamine TPD-TGA to be 0.53 mmol.g^{-1}. For the aged H-FER samples the numbers of accessible Brønsted acid sites are calculated by taking the ratio of CD_3CN peak areas of aged and fresh H-FER and multiply the outcome with the number determined for fresh H-FER. A large reduction of the number of accessible Brønsted acid sites is observed for the aged H-FER samples, hence upon *n*-butene reaction. For aged H-FER6.8C obtained with long TOS and containing a maximum amount of coke, still 14 % of the original number of Brønsted acid sites is accessible for CD_3CN. To determine whether the sites that are accessible for CD_3CN are also accessible for *n*-butene, all H-FER samples were additionally probed with *n*-butene. The changes in the Brønsted acid region resulting from butene adsorption are in good agreement with the results obtained for CD_3CN, although quantification is not possible due to a large contribution of weakly sorbed butenes that partially overlaps with the Brønsted OH band.

Table 2. CD_3CN peak areas and number of accessible Brønsted acid sites.

Sample	*Relative integrated area of CD_3CN peak at 2292 cm^{-1} (%)*	*Number of accessible Brønsted acid sites (mmol.$g_{H\text{-}FER}^{-1}$)*
H-FER	100	0.530 [2]
H-FER5.0C	25 [1]	0.133 [3]
H-FER6.6C	21 [1]	0.111 [3]
H-FER6.8C	14 [1]	0.074 [3]

1. Relative area normalized on the area for H-FER.
2. Number of Brønsted acid sites of H-FER is determined by *n*-propylamine TPD-TGA.
3. Number of Brønsted acid sites of aged H-FER = (area of CD_3CN peak / 100)∗number for H-FER

Bystrov [21] and Jolly *et al.* [23] reported that the adsorption of CD_3CN at low temperature on zeolite samples used in hydrocarbon conversions may result in the appearance of a sharp peak between 2387 cm^{-1} and 2377 cm^{-1}, characteristic for the vibration of ν(CN) bound to a carbocation. However, from figures 3 and 4 it is clear that no such contribution is observed, thus most likely no carbenium ions are present on the aged H-FER samples after they were heated to 623 K (the reaction temperature), cooled down to 448 K under a He-flow and then probed with CD_3CN. To further check the formation of carbenium ions as stable active sites in butene skeletal isomerization, H-FER has been aged *in situ* at 623 K, cooled down to 448 K under a He-flow and subsequently probed with CD_3CN at different TOS. In the spectra obtained during these experiments also no peaks were observed in the 2387 - 2377 cm^{-1} region.

Relation between catalytic performance and Brønsted acidity

The catalysis data presented in table 1 indicate that with longer TOS lower WHSV's are demanded to obtain similar *n*-butene conversions, indicating that the H-FER sample becomes less active upon aging. By taking into account the applied WHSV's for the differently aged H-FER samples, reaction rates for both the conversion of *n*-butene and the formation of isobutene are calculated and displayed in table 3. Figure 5 displays these reaction rates as a function of the number of accessible Brønsted acid sites on the aged H-FER samples, as probed by CD_3CN (see also table 2). By considering this number of accessible Brønsted acid sites, the reaction rates of the aged H-FER samples can be converted into turn-over-frequencies (TOF). The TOF's for *n*-butene conversion and isobutene formation are also collected in table 3, giving the moles of *n*-butene converted or moles of isobutene formed per mole accessible Brønsted acid sites per hour.

Table 3. Reaction rates and turn-over frequencies of the aged H-FER samples at 623 K.

Sample	*Reaction rates (g.g $_{H\text{-}FER}^{-1}$.h^{-1})*		*TOF's (mmol.mmol^{-1}.h^{-1})*	
	n-butene conversion[1]	isobutene formation[2]	*n*-butene converted[3]	Isobutene formed[3]
H-FER5.0C	16.1	5.7	$21.6*10^2$	$7.7*10^2$
H-FER6.6C	12.6	4.8	$20.3*10^2$	$7.7*10^2$
H-FER6.8C	1.8	1.6	$4.3*10^2$	$3.9*10^2$

1. Rate *n*-butene conversion = [(WHSV) ∗ (Conversion)] / 100.
2. Rate isobutene formation = [(Rate *n*-butene conversion) ∗ (isobutene selectivity)] / 100.
3. TOF = (rate / 56) / number of accessible Brønsted acid sites (see table 2).

Discussion

On the number, nature and location of the active sites

The observed reduction in intensity of the ν(CN) peak at 2292 cm^{-1} (figure 3) with increasing content of carbonaceous deposits indicates that upon *n*-butene reaction the number of accessible Brønsted acid sites in H-FER decreases. On a fresh H-FER the number of accessible Brønsted acid sites is 0.53 mmol.g^{-1}, while during *n*-butene reaction this number decreases for H-FER6.8C to a value of 0.074 mmol.g^{-1}, *i.e.* 14 % of the initial value (table 2). This agrees well with the decrease in micropore volume as determined by nitrogen physisorption going from 0.132 ml.g^{-1} on the fresh H-FER to 0.013 ml.g^{-1} on H-FER6.8C. The adsorption of CD_3CN on the aged H-FER samples induces a large but not complete reduction of the band assigned to the Brønsted acid sites at 3580 cm^{-1}, which is illustrated for H-FER6.8C in figure 4. This reveals that not all Brønsted acid sites in the aged H-FER sample are accessible for CD_3CN. Additionally, the maximum of the remaining Brønsted acid band for H-FER6.8C (figure 4) is shifted towards slightly lower frequencies as compared to fresh H-FER (figure 1). Since it is known that the OH groups in the 8 MR pores absorb at lower wavenumbers than those in the 10 MR channels [30,31], the observed shift implies that upon CD_3CN adsorption Brønsted sites remain vacant in the cages of the 8 MR pores. This indicates that with the formation of carbonaceous deposits at least part of the entrances of the 8 MR pores is blocked so that sites in these cages become inaccessible for both CD_3CN and butenes. As a result, the Brønsted sites that are still accessible for CD_3CN and butenes will be mainly located in the 10 MR channels, implying that only these sites are involved in the catalytic action. This result is in excellent agreement with Wichterlova *et al.* [35] and Domokos *et al.* [31], who reported on the correlation between acid site locations in sodium exchanged H-FER samples and their catalytic

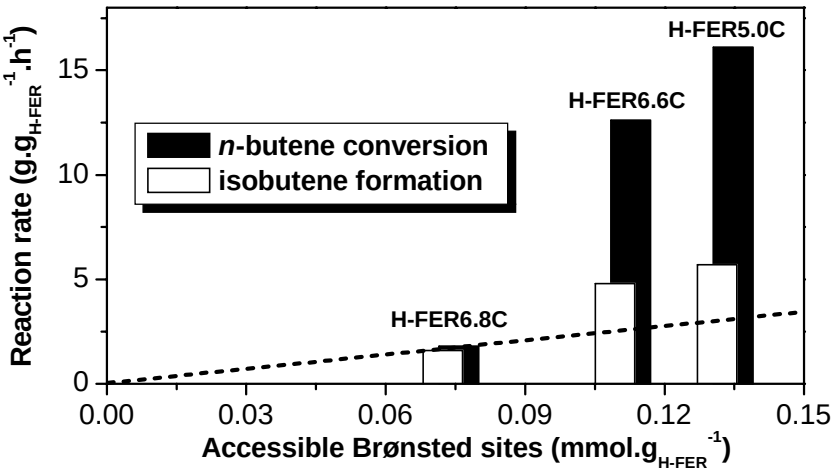

Figure 5. Reaction rates for *n*-butene conversion and isobutene formation as a function of the number of accessible Brønsted acid sites on the aged H-FER samples, as probed by CD_3CN. The dashed line (---) indicates the reaction rates one expects if catalysis on all samples would occur in linear correlation with the results obtained for H-FER6.8C and with the number of accessible Brønsted acid sites.

performances. In these studies a clear structure-activity relationship was observed between the presence of Brønsted acid sites in the 10 MR channels and the selective formation of isobutene. In our study we show that this structure-activity relation also exists under full catalysis conditions, *i.e.* when carbonaceous deposits fill a large part of the H-FER micropore volume.

In contrast to the results presented in our study, Guisnet *et al.* [18] claimed that on aged H-FER all Brønsted acid sites would be inaccessible for reactants on probing aged H-FER with ammonia (NH_3) at 323 K under vacuum. However, if one looks more closely into the spectra of Guisnet *et al.* [18], a slight decrease in the Brønsted band is observed upon NH_3 probing, indicating that at least a small number of Brønsted acid sites remains accessible after aging. This is, at least qualitatively, in agreement with the results obtained in the present study. The quantitative differences between the study of Guisnet *et al.* [18] and this study may be caused by selection of the probe molecule, the H-FER Si/Al ratio and the applied experimental conditions like temperature and pressure.

Based on the assumption that Brønsted sites are unavailable for the catalytic action on aged H-FER, Guisnet *et al.* [9,17,18] proposed that the enhancement of isobutene selectivity with TOS originated from the creation of alkyl-aromatic tertiary carbenium ions that are captured inside the entrances of the zeolite pores. Linear butenes would then react with these carbenium ions through a so-called pseudo-monomolecular reaction pathway in which a methyl- and hydride shift followed by β-scission produce

the isobutene. The present study does not reveal the presence of carbenium ions and hence the occurrence of a pseudo-monomolecular pathway seems less likely. This conclusion is supported by results of Mériaudeau *et al.* [36], who compared the skeletal isomerization of linear butenes and pentenes over aged H-FER. Their results demonstrated that *n*-pentene is isomerized much faster than *n*-butene. The observed difference in rates arises from the fact that the monomolecular skeletal isomerization of *n*-butene involves the formation of an energetically and thermodynamically highly unfavorable primary carbenium ion [16], while for *n*-pentene the monomolecular reaction occurs via a much more stable secondary carbenium ion. The experimentally observed rate difference indicates that the skeletal isomerization of both *n*-butene and *n*-pentene will probably not proceed via a pseudo-monomolecular reaction pathway, since then similar isomerization rates are expected.

Relation between catalytic performance and Brønsted acidity

The reaction rates for *n*-butene conversion and isobutene formation decrease with increasing coke content and decreasing number of accessible Brønsted acid sites (see table 3 and figure 5). However, no simple linear relationship is observed between the aged H-FER samples studied, as is indicated by the dashed line in figure 5. This is further emphasized by the fact that the TOF's in table 3 are not the same for all three samples. Nevertheless, large similarity for both H-FER5.0C and H-FER6.6C is observed, which suggests that despite their different contents in carbonaceous deposits identical reactions are prevailing on these catalysts. This analogous behavior is further illustrated by their similar isobutene selectivities displayed in table 1. In contrast, the isobutene selectivity for the extensively aged H-FER6.8C is much higher and the TOF's are significantly lower than for H-FER5.0C and H-FER6.6C. Simultaneously, only a minor increase in deposits was observed, going from H-FER6.6C to H-FER6.8C. Hence, the major increase in isobutene selectivity and the drastic decrease in reaction rates are neither directly related to the amount of carbonaceous deposits nor the number of Brønsted acid sites as figure 5 already indicated. Therefore, it becomes obvious that the nature of carbonaceous deposits largely affects the catalytic action and the dominant reaction pathway.

The nature of the deposits is deduced from the IR spectra of the carbon region as displayed in figure 2. The carbonaceous deposits change from alkyl-aromatic towards more condensed alkyl-aromatic species going from the shortly aged samples, *i.e.* H-FER5.0C and H-FER6.6C, to the extensively aged H-FER6.8C sample. This change in nature of coke with TOS has been observed before in other studies [7,8,33]. In general hydrogen rich carbonaceous deposits are more reactive than hydrogen poor ones and hence, cracking reactions of such reactive deposits will likely cause the higher TOF values for H-FER5.0C and H-FER6.6C in table 3. The discrepancies between the

TOF's of *n*-butene converted and isobutene formed clearly indicate that these reactions are not predominantly selective towards isobutene formation and additionally form by-products, resulting in low isobutene selectivities (table 1). This agrees very well with ^{13}C-labelling studies performed at short TOS [8,10,11], where it was suggested that with short TOS mainly non-selective bimolecular reactions dominate the catalytic action.

For H-FER6.8C, however, the reactivity of deposits and concomitant appearance of by-products is significantly reduced, resulting in a lower TOF for the conversion of *n*-butene. Furthermore, the similar TOF for the formation of isobutene indicates the high isobutene selectivity observed for H-FER6.8C. This again correlates to the ^{13}C-labelling experiments [8,10,11], in which it was observed that with extensive aging of the catalyst a change in the prevailing reaction pathway for the formation of isobutene occurred.

When we assume that the catalytic action on H-FER6.8C runs predominantly over the Brønsted acid sites available, the dashed line in figure 5 now indicates that half of the isobutenes obtained for H-FER5.0C and H-FER6.6C originates from other reactions than the selective one running over Brønsted acid sites. Likely the reactive carbonaceous deposits present on the mildly aged H-FER5.0C and H-FER6.6C induce such non-selective reactions. The suggestion that reactive deposits take part in the non-selective catalytic action agrees with earlier work of Xu *et al.* [7] and Finelli *et al.* [33].

Asensi *et al.* [14] showed that on a high-silica H-FER (Si/Al = 59, *i.e.* low number of Brønsted acid sites) high isobutene selectivities were reached without the substantial formation of deposits. Recently, an extensive kinetic study by Domokos *et al.* [37] confirmed that the presence of deposits is not crucial to achieve high isobutene selectivities and that isobutene is likely formed over Brønsted acid sites. However, it must be noted that at atmospheric or higher pressures, *i.e.* under conditions that are closer to industrial ones, the deposition of carbonaceous species can not be avoided as was shown by the group at Shell [6,8] and is demonstrated in table 1 and figure 2. During the complete catalytic action, the role of these deposits is rather ambiguous. According to figure 3, the deposition of carbonaceous species lowers the amount and density of accessible Brønsted sites, consequently suppressing non-selective bimolecular reactions. Nevertheless, the deposition of reactive species significantly contributes to the overall product formation, although not at all selectively since besides isobutene numerous by-products are formed. With extensive aging of H-FER, the high isobutene selectivity mainly stems from the fact that carbonaceous deposits have become non-reactive and *n*-butene is now exclusively transformed over the Brønsted acid sites left on aged H-FER. Additional effects like preferential deactivation of non-selective acid sites and/or a decrease in Brønsted acid site concentration as suggested by others [3,7,13,15,35] may contribute as well to the enhanced performance of aged H-FER.

Conclusions

Catalytically active H-FER samples with different amounts of deposits were prepared and studied under differential catalytic conditions in a TEOM. Subsequently, these samples were examined by IR spectroscopy, unraveling the nature of carbonaceous deposits and probing the number of accessible Brønsted acid sites using CD_3CN. The deposition of carbonaceous species significantly lowers the number of accessible Brønsted sites. With short TOS, reactive carbonaceous deposits largely contribute to the overall isobutene production but simultaneously harm the selective catalytic action by inducing non-selective reactions. With prolonged TOS the deposits become non-reactive and accordingly isobutene is produced with high selectivity. It is demonstrated that at this stage no carbenium ions are present, which excludes the occurrence of a pseudo-monomolecular reaction pathway. Additionally, Brønsted OH acid sites are still accessible on the extensively aged and highly selective H-FER, which presence indicates these sites to be responsible for the selective formation of isobutene from *n*-butene.

Acknowledgements

Eveline Bus is acknowledged for performing the IR experiments and helpful discussions. Dr. Tom Visser (Utrecht University) is acknowledged for helpful discussions.

References

1. A.C. Butler and C.P. Nicolaides, Catal. Today 18 (1993) 443.
2. J. Houzvicka, S. Hansildaar and V. Ponec, J. Catal. 167 (1997) 173.
3. P. Mériaudeau and C. Naccache, Adv. Catal. 44 (1999) 505.
4. S. van Donk, J.H. Bitter and K.P. de Jong, Appl. Catal. A Gen. 212 (2001) 97.
5. P. Grandvallet, K.P. de Jong, H.H. Mooiweer, A.G.T.G. Kortbeek and B. Kraushaar-Czarnetzki, European Patent no. 501677 to Shell (1992).
6. H.H. Mooiweer, K.P. de Jong, B. Kraushaar-Czarnetzki, W.H.J. Stork and B.C.H. Krutzen, Stud. Surf. Sci. Catal. 84 (1994) 2327.
7. W.-Q. Xu, Y.-G. Yin, S.L. Suib and C.-L. O'Young, J. Phys. Chem. 99 (1995) 758.
8. K.P. de Jong, H.H. Mooiweer, J.G. Buglass and P.K. Maarsen, Stud. Surf. Sci. Catal. 111 (1997) 127.
9. M. Guisnet, P. Andy, Y. Boucheffa, N.S. Gnep, C. Travers and E. Benazzi, Catal. Lett. 50 (1998) 159.
10. P. Mériaudeau, R. Bacaud, L.N. Hung and T.A. Vu, J. Mol. Catal. A 110 (1996) L177.
11. J. Cejka, B. Wichterlová and P. Sarv, Appl. Catal. A Gen. 179 (1999) 217.

12. G. Seo, H.S. Jeong, D.-L. Jang, D.L. Cho and S.B. Hong, Catal. Lett. 41 (1996) 189.
13. J. Houzvicka and V. Ponec, Ind. Eng. Chem. Res. 36 (1997) 1424.
14. M.A. Asensi and A. Martinez, Appl. Catal. A Gen. 183 (1999) 155.
15. G. Seo, M.-Y. Kim and J.-H. Kim, Catal. Lett. 67 (2000) 207.
16. D. Brouwer and J. Oelderik, Rec. Trav. Chim. Pays Bas 87 (1968) 1435.
17. M. Guisnet, P. Andy, N.S. Gnep, C. Travers and E. Benazzi, J. Chem. Soc. Chem. Commun. (1995) 1685.
18. P. Andy, N.S. Gnep, M. Guisnet, E. Benazzi and C. Travers, J. Catal. 173 (1998) 322.
19. F. Hershkowitz and P.D. Madiara, Ind. Eng. Chem. Res. 32 (1993) 2969.
20. D. Chen, A. Gronvold, H.P. Rebo, K. Moljord and A. Holmen, Appl. Catal. A Gen. 137 (1996) L1.
21. D.S. Bystrov, Zeolites 12 (1992) 328.
22. A.G. Pelmenschikov, R.A. van Santen, J. Jänchen and E. Meijer, J. Phys. Chem. 97 (1993) 11071.
23. S. Jolly, J. Saussey and J.C. Lavalley, Catal. Lett. 24 (1994) 141.
24. J. Kotrla and L. Kubelkova, Stud. Surf. Sci. Catal. 94 (1995) 509.
25. A. Zecchina, F. Geobaldo, G. Spoto, S. Bordiga, G. Ricchiardi, R. Buzzoni and G. Petrini, J. Phys. Chem. 100 (1996) 16584.
26. J.A. Lercher, C. Gründling and G. Eder-Mirth, Catal. Today 27 (1996) 353.
27. B. Wichterlová, Z. Tvaruzková, Z. Sobalik and P. Sarv, Microp. Mesop. Mat. 24 (1998) 223.
28. C. Pazé, A. Zecchina, S. Spera, G. Spano and F. Rivetti, Phys. Chem. Chem. Phys. 2 (2000) 5756.
29. R. Yamdagni and P. Kebarle, J. Am. Chem. Soc. 98 (1976) 1320.
30. V.L. Zholobenko, D.B. Lukyanov, J. Dwyer and W.J. Smith, J. Phys. Chem. B 102 (1998) 2715.
31. L. Domokos, L. Lefferts, K. Seshan and J.A. Lercher, J. Mol. Catal. A Chem. 162 (2000) 147.
32. M. Trombetta, G. Busca, S. Rossini, V. Piccoli, U. Cornaro, A. Guercio, R. Catani and R.J. Willey, J. Catal. 179 (1998) 581.
33. Z.R. Finelli, C.A. Querini, N.S. Figoli and R.A. Comelli, Appl. Catal. A Gen. 187 (1999) 115.
34. C. Pazè, B. Sazak, A. Zecchina and J. Dwyer, J. Phys. Chem. B 103 (1999) 9978.
35. B. Wichterlová, N. Zilkova, E. Uvarova, J. Cejka, P. Sarv, C. Paganini and J.A. Lercher, Appl. Catal. A Gen. 182 (1999) 297.
36. P. Mériaudeau, T.A. Vu, L.N. Hung and G. Szabo, J. Catal. 169 (1997) 397.
37. L. Domokos, L. Lefferts, K. Seshan and J.A. Lercher, J. Catal. 197 (2001) 68.

9

Monitoring the Location, Amount and Nature of Carbonaceous Deposits on Aged Zeolite Ferrierite Crystals Using STEM-EELS

Abstract

By the use of electron energy-loss spectroscopy performed in a scanning transmission electron microscope (STEM-EELS), detailed spatial information is obtained concerning the amount and nature of carbonaceous deposits formed inside the crystals of the zeolite ferrierite (FER) during the reaction of *n*-butene. In all cases, gradients in coke concentration over the crystal have been observed and quantified. An accumulation of coke is observed at the entrance of the 8 membered ring (MR) pores, while only little coke is present at the entrances of the 10 MR channels. At a higher coke content, further filling up of the complete micropore system occurs and the 8 MR pores become fully blocked. The 10 MR channels remain partially accessible for *n*-butene, with alkyl-aromatic species deposited near the inlets of these channels. With regard to the selective transformation of *n*-butene into isobutene, this supports the view that the catalytic action takes place in the pore mouths of the 10 MR channels. Overall it is demonstrated that the major benefit of STEM-EELS is the possibility to simultaneously determine the position-resolved amount and nature of carbonaceous deposits on intact zeolite crystals.

Introduction

Electron energy-loss spectroscopy (EELS) has proven to be a powerful technique in materials science and life sciences for detailed chemical characterization of nano-sized structures [1]. Gallezot *et al.* [2] demonstrated the use of EELS for studying carbonaceous species deposited on the outer surface of various zeolite crystals by performing the measurements in a scanning transmission electron microscope (STEM-EELS). In this way it was demonstrated that the carbonaceous species blocked the entrance of the zeolite pores. Moreover, by interpretation of the carbon K-edge fine structure, the nature of the deposits was qualitatively resolved to be poly-aromatic [2].

Carbonaceous deposits, often referred to as 'coke', are generally known to provoke catalytic deactivation of zeolites [3,4]. Besides deposition of coke at the outer surface, deactivation of zeolite catalysts may also be induced by carbonaceous species formed and deposited inside the zeolitic pore system. In that case the rate of deactivation and the location and nature of deposits inside the crystal is largely determined by the internal pore system of the zeolite [5-7]. Therefore, simultaneous determination of the location, amount and nature of carbonaceous deposits may significantly contribute to the understanding of deactivation phenomena in zeolite catalysis induced by coking. As a result of recent technical developments STEM-EELS provides the possibility to obtain highly detailed spatial information, not only at the outer surface of a coked zeolite crystal as revealed by Gallezot *et al.* [2], but in potential also inside the crystal. In this study it is demonstrated for the first time that by using STEM-EELS it is possible to unravel the influence of the pore structure on the coke deposition inside zeolite crystals. Additionally, by interpretation of the carbon K-edge fine structure an indication on the nature of the deposits is obtained.

The measurements are performed on crystals of the zeolite ferrierite (FER) that are aged during the catalytic conversion of *n*-butene into isobutene. FER consists of a two-dimensional pore network built up of 10-, 8-, 6- and 5-membered rings (MR) [8] and is a highly suitable catalyst for the skeletal isomerization of *n*-butene into isobutene [9]. For this reaction the selective formation of isobutene coincides with the presence of carbonaceous deposits [10-12]. However, the exact role of these deposits during the catalytic action is still under debate.

Therefore, information about the location, amount and nature of carbonaceous deposits in the zeolite crystals may contribute to a further understanding of the role of carbonaceous deposits in butene skeletal isomerization, and zeolite deactivation phenomena in general.

Table 1. Catalytic properties and micropore volumes of the aged FER samples.

Sample	*FER2.5C*	*FER6.8C*
Time-on-stream, h	1	300*
n-Butene conversion, mol%	81	24
Isobutene selectivity, mol%	20	87
Isobutene yield, mol%	16	22
Micropore volume**, $ml.g^{-1}$	0.072	0.013

* after several hours on stream the maximum amount of deposits is reached

** determined with N_2 physisorption, micropore volume for FER without deposits is 0.132 $ml.g^{-1}$

Experimental

Sample preparation

Commercially available high silicon-NH_4^+ ferrierite (Zeolyst Int. Si/Al 30) was activated in a dry nitrogen flow at 823 K for 12 hours in order to obtain the H^+ ferrierite (H-FER). Nitrogen physisorption and t-plot analysis for H-FER showed an external surface area of 42 $m^2.g^{-1}$ and a micropore volume of 0.132 $ml.g^{-1}$. Around 50 mg of FER (particle size: 90-150 μm) were aged during *n*-butene (Hoek Loos, 1-butene, ≥ 99.5%) reaction in a tapered element oscillating microbalance (TEOM, Rupprecht & Pataschnick 1500 PMA); reaction products were analyzed on-line using a gas chromatograph (Shimadzu 17A with a Chrompack PLOT capillary column of fused silica-Al_2O_3/KCL, 50m x 0.32mm). The TEOM reactor provides the possibility to study real-time catalyst deactivation induced by the deposition of carbonaceous deposits while monitoring the catalytic reaction. For a detailed description of the TEOM we refer to Hershkowitz and Madiara [13] and Chen *et al*. [14].

Two FER-samples with different amounts of carbonaceous deposits, exhibiting different catalytic properties, have been prepared in the TEOM at 623 K, 1.3 bar using a weight hourly space velocity of 4 $g_{butene} \cdot g_{ferrierite}^{-1} \cdot h^{-1}$. The first sample, obtained after 1 h time on stream, contains 2.5 wt% coke (FER2.5C) and displays a high *n*-butene conversion but a low selectivity to isobutene. The second sample, obtained after 300 h time on stream, contains 6.8 wt% coke (FER6.8C) and is less active but more selective towards isobutene. Their catalytic properties and micropore volumes as determined by nitrogen physisorption are summarized in table 1. FER2.5C and FER6.8C were extensively characterized using STEM-EELS, as described in the next paragraph.

STEM-EELS measurements

In order to investigate the carbon distribution on the aged H-FER crystals of FER2.5C and FER6.8C, carbon- and oxygen K edges were monitored by use of a 100 keV STEM instrument (VG HB 501) equipped with a field emission source and a

parallel Gatan 666 EELS spectrometer. The instrument is in operation in Orsay and produces EELS-spectra with 0.5 eV energy resolution and subnanometer spatial resolution within a typical acquisition time of a few hundreds of milliseconds. More specifically the subnanometer probe (typically 5 Å in diameter) can be positioned with an accuracy higher than 2 Å on the sample, and it can scan the sample digitally with spatial increments as small as 3 Å. For further details concerning the experimental set-up we refer to Stéphan *et al.* [15]. The aged H-FER crystals were first sonicated in ethanol and then dropped on a holey amorphous carbon layer supported on a copper grid. Parts of the crystals protruding out into vacuum were selected for EELS investigation. The FER crystals used in this study are very appropriate for STEM-EELS measurements since they are thin and plate-like with a size in the order of 1.0 x 0.4 x 0.05 μm, as depicted in figure 1. The two-dimensional pore network consists of 10 MR channels with a size of 5.4 x 4.2 Å and 8 MR channels of 4.8 x 3.5 Å [16] For both FER2.5C and FER6.8C one-dimensional line scans using a 5 Å probe size, 3.125 Å spatial increment and 400 ms of exposure time were recorded by taking spectra while ramping the electron probe parallel to the 8- and 10 MR channels of the crystals. For FER2.5C a large number of parallel-recorded line scans was combined providing two-dimensional elemental maps. This was not possible for FER6.8C since this sample was less stable in the electron beam.

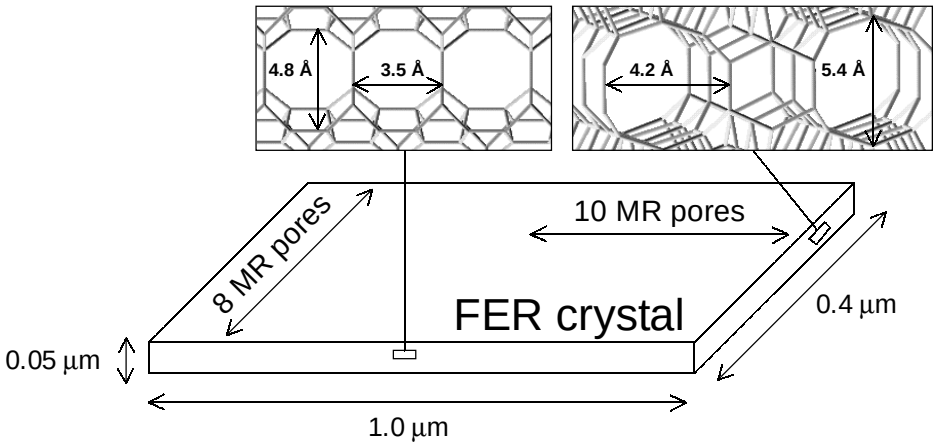

Figure 1. Schematic representation of a FER crystal, showing the average crystal-size and the directions and dimensions of the pores. Note: the kinetic diameter of *n*-butene is 3.0 x 4.7 Å.

Results

The atomic carbon and oxygen signals were monitored for FER2.5C and FER6.8C, and the results as a function of the scanning distance in the directions parallel to the 8 MR (top) and 10 MR channels (bottom) are displayed in figure 2. The first data-points shown in the graphs are also the first points detected on the zeolite crystals. All

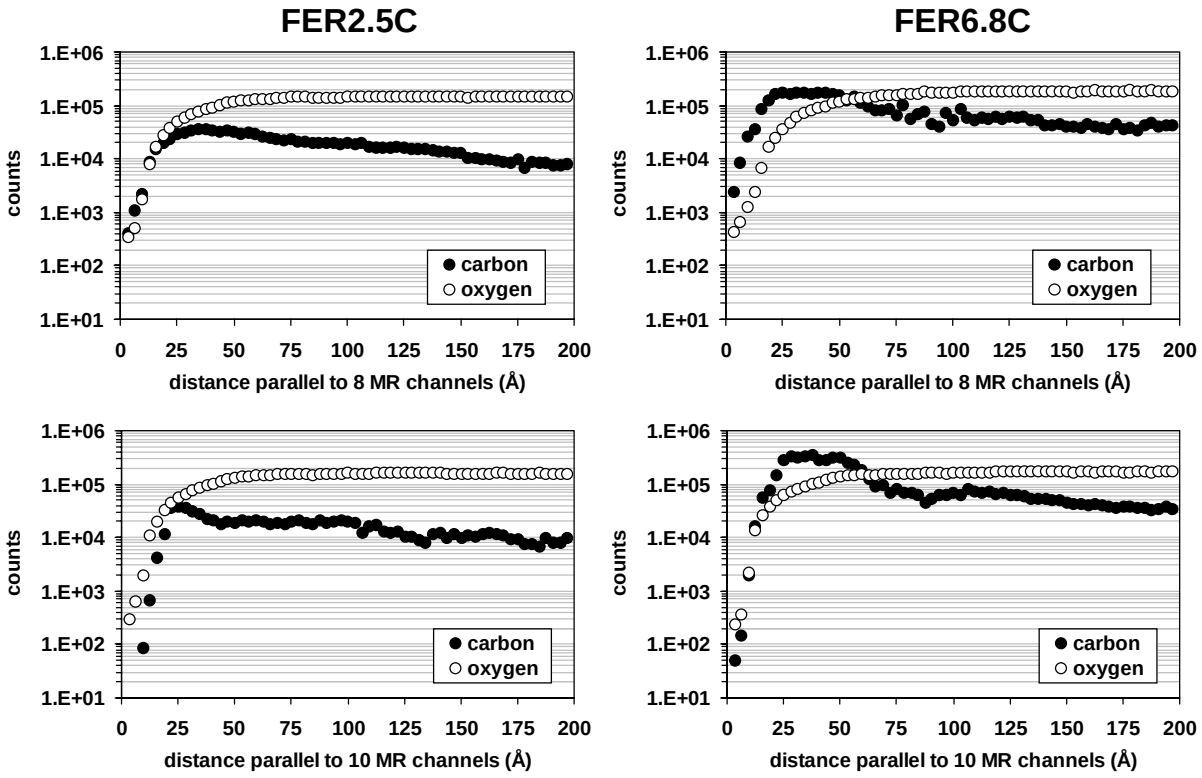

Figure 2. Carbon and oxygen signals for FER2.5C (left) and FER6.8C (right) as a function of scanning distance in the direction parallel to the 8 MR (top) and parallel to 10 MR channels (bottom). Note that the scale of the y-axis is logarithmic.

performed line scans indicate that it takes about 50 Å before a stable oxygen signal is detected. The increasing oxygen signal suggests that the edges of the crystals are not entirely flat but seem to be roughened in the direction perpendicular to the electron beam. Looking at the carbon signal, it becomes obvious that a significant amount of carbonaceous species is deposited throughout the FER crystal. Besides, it is evident that close to the pore mouths of the 8 MR channels more carbonaceous deposits are present than close to the pore mouths of the 10 MR channels.

In figure 3 (on the next page), line scans displaying the atomic carbon to zeolitic oxygen (C/O) ratios parallel to the direction of the 10 MR channels and the 8 MR channels as a function of scanning distance are displayed for both FER2.5C (top) and FER6.8C (bottom). In the graphs, the origin represents the last data-point detected just before the crystal, hence in vacuum. The second data-point in the graph is thus the first point detected on the zeolite crystal. Going from FER2.5C to FER6.8C, hence with increasing coke content, the scans parallel to the 8 MR channels show a large increase in the C/O ratio at the crystal edge which then declines going further into the crystal. In the direction of the 10 MR channels the C/O ratio also increases going from FER2.5C to FER6.8C, although more moderately.

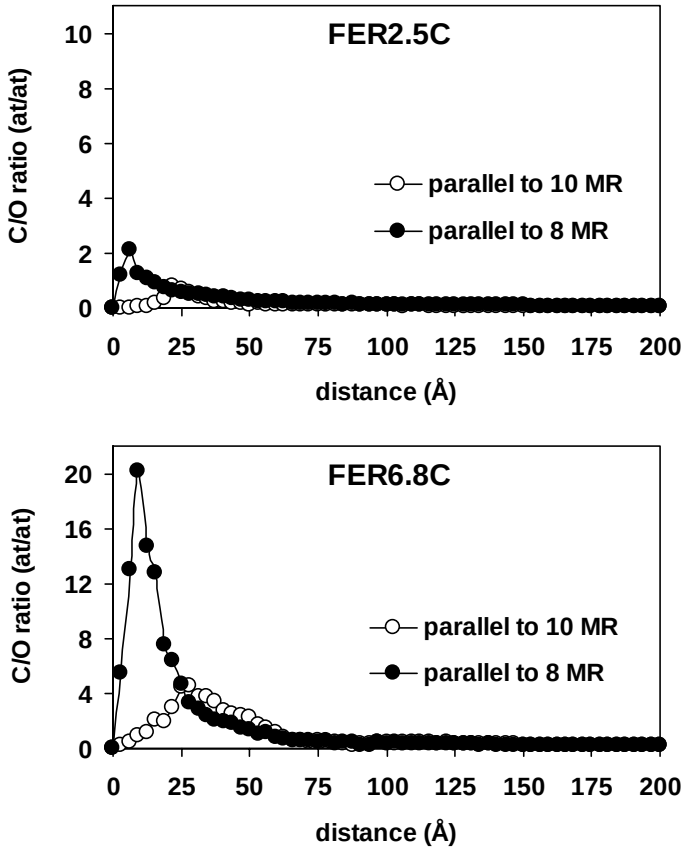

Figure 3. Atomic carbon to zeolitic oxygen ratios for FER2.5C (top) and FER6.8C (bottom) as a function of scanning distance. Line scans were taken parallel to the 8 MR and 10 MR channels, respectively. Note that there is a factor 2 difference in the y-axis scale between the top and bottom graph.

Figure 4 zooms in on the C/O ratio's detected further from the crystal edges, from 100 Å to 200 Å. For both FER2.5C (top) and FER6.8C (bottom) a clear gradient in the C/O ratio is observed, which stabilizes at around 175 Å. The C/O ratio at this position value coincides with the C/O ratio calculated from the bulk coke loading.

Figure 5 shows two-dimensional elemental maps for FER2.5C, which were obtained by combining a large number of parallel-recorded line scans. In this way figure 5 provides a clear image of the carbon distribution over part of the mildly aged FER2.5C crystals. It is important to take into account that the results obtained for the first 50 Å are largely determined by the roughened planes of the FER crystal.

In figure 6 the electron energy-loss spectra of the carbon K-edges detected at different locations in the FER6.8C crystals are displayed. The upper spectrum is obtained at ~ 20 Å from the edge of the crystal, hence close to the pore mouths of the 10 MR channels. The middle spectrum is obtained at ~ 50 Å and the bottom spectrum at ~ 100 Å from the crystal edge. To verify the nature of the carbonaceous species, the experimental spectra were evaluated using reference compounds [17]. All carbon K-edges resemble the spectra of amorphous carbonaceous compounds, implying the presence of poly-aromatic species. Moreover, for the spectrum obtained near the crystal edge, an extra small shoulder at 287 eV corresponding to the presence of aliphatic species and/or alkyl-groups is detected.

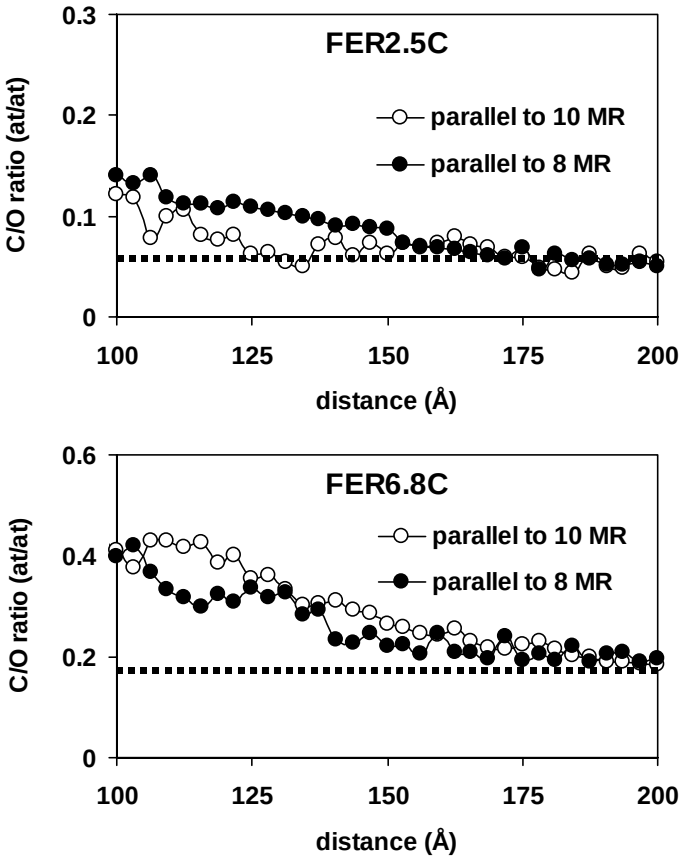

Figure 4. Atomic carbon to zeolitic oxygen ratios for FER2.5C (top) and FER6.8C (bottom) as a function of scanning distance from 100 Å to 200 Å. Line scans were taken parallel to the 8 MR and 10 MR channels, respectively. Dotted lines indicate the C/O ratio based on the overall coke content (see text). Note that there is a factor 2 difference in the y-axis scale between the top and bottom graph.

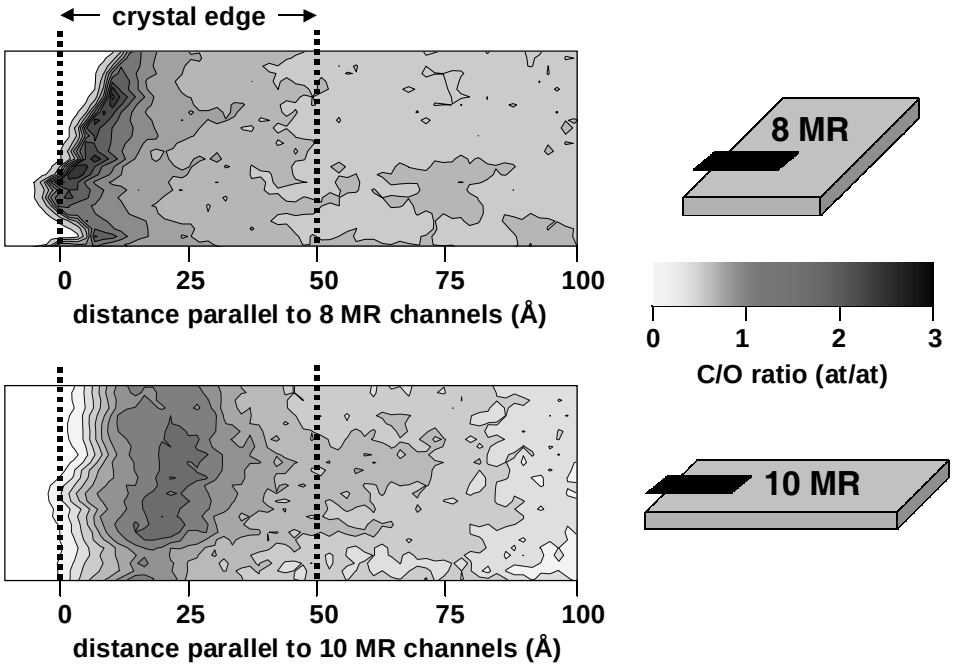

Figure 5. Two-dimensional elemental maps showing the atomic carbon to zeolitic oxygen (C/O) ratio over a representative crystal of FER2.5C, obtained by combining a large number of line scans parallel to the 8 MR channels (top) and 10 MR channels (bottom); the darker the area, the higher C/O ratio.

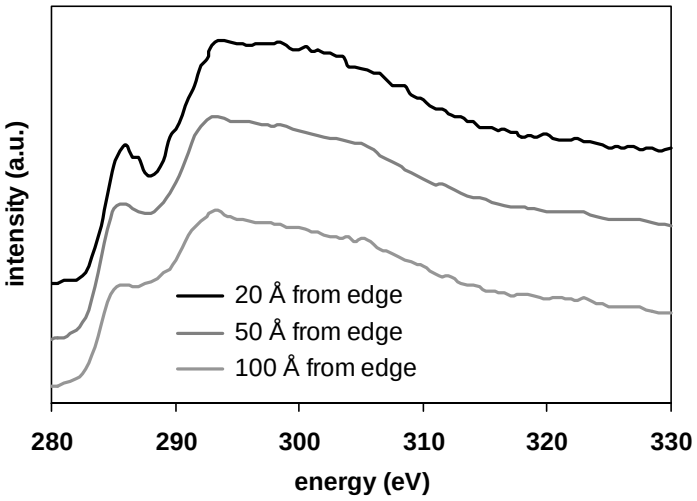

Figure 6. Carbon K-core edges for FER6.8C at various locations on the crystal, going from the edge at the 10 MR entrances (top spectrum) to the inside (bottom spectrum). For reasons of clarity we moved the baselines of the different spectra.

Discussion

The results displayed in figure 2 show that for FER2.5C, hence after 1 hour of *n*-butene reaction (see table 1), there is carbon present at all distances scanned in both the 8 MR (top) and 10 MR (bottom) directions. This reveals that the reaction of *n*-butene results in an immediate deposition of carbonaceous species throughout the crystal. With regard to the oxygen signal, the line scans indicate that it takes about 50 Å before a stable oxygen signal is detected. This suggests that the edges of the crystals are not straight but seem to be roughened in the direction perpendicular to the electron beam. At the same time, somewhat higher carbon signals are detected at the edges of the crystal in both the 8 MR and 10 MR directions, indicating that the pore mouths of both channels are sensitive to the deposition of carbonaceous deposits. Besides, by comparing the initial rise of the carbon signal with that of the oxygen signal, it becomes evident that the pore mouths of the 8 MR channels experience a more severe deposition of carbonaceous deposits than the inlets of the 10 MR channels. This is further illustrated in figure 3 (top), which shows that for FER2.5C the maximum of the atomic C/O ratio is significantly higher at the entrance of the 8 MR channels than at the entrance of the 10 MR channels. Moreover, figure 5 clearly visualizes that significant deposition of coke has occurred at the pore mouths of the 8 MR channels. Also at the entrances of the 10 MR channels some enrichment by coke species is observed, however, their location and amount indicate that the deposition has been less.

The higher sensitivity of the 8 MR channels towards the formation of coke may have two explanations. First, the diameter of an 8 MR channel is smaller than that of a 10 MR channel (see figure 1). As a result the *n*-butenes and/or the formed products will experience more steric hindrance in the 8 MR channels, which causes accumulation of polymeric species that subsequently induce coke formation. Second, it has been

demonstrated by infrared spectroscopy [12,18] that the Brønsted acid sites in the 8 MR channels are located at slightly lower wavenumbers, which suggests that they might be more acidic and therefore more sensitive to irreversible deposition of carbonaceous species. Nevertheless, figures 2, 3 (top) and 5 show that also at the entrances of the 10 MR channels of FER2.5C some accumulation of carbonaceous species is observed. Based on the nitrogen physisorption / t-plot analysis (table 1), which reveals that there is still a significant amount of free micropore volume, it is suggested that the 10 MR channels of FER2.5C remain partially accessible.

For FER6.8C, obtained after 300 hours *n*-butene reaction (see table 1), figures 2 and 3 (bottom) reveals a significant growth in the carbon signal throughout the crystal as compared to FER2.5C. Especially the considerable rise at the 8 MR pore inlets confirms the high sensitivity of the 8 MR channels for the deposition of coke. The carbon signal at the edge of the 10 MR channels has also increased, but the slower growth indicates that the thickness and severity of the deposited coke layer is significantly less. Nitrogen physisorption / t-plot analysis for FER6.8C (table 1) reveals that the micropore volume has decreased by a factor 10. Based on figures 2 and 3 (bottom) it is suggested that this volume will be primarily located in the 10 MR pore entrances and that the 8 MR channels will be completely blocked. Overall, this implies that the 10 MR channels remain to some extent accessible for *n*-butene, even with a high coke content. With regard to the selective transformation of *n*-butene into isobutene over aged and selective FER, this demonstrates that the catalytic action will primarily occur in the initial part of the 10 MR channels.

Essential information concerning the filling of the FER micropore volume is provided by figure 4, which zooms in on the C/O ratio's detected further from the crystal edge. This demonstrates that inside the FER crystal a smooth carbon gradient is present that levels off around 175 Å. At a distance of 100 Å the C/O ratio for FER2.5C is ~ 0.14 at/at, which increases to ~ 0.40 at/at for FER6.8C. Going even further towards the center of the crystal at 200 Å from the crystal edge, the C/O ratio for FER2.5C is ~ 0.05 at/at and for FER6.8C ~ 0.18 at/at. The validity of these numbers can be verified by calculating the theoretically expected C/O ratio's. For this calculation, the chemical composition of FER2.5C can be represented as 2.5 wt% coke ('CH') and 97.5 wt% FER ('SiO_2'), which then leaves a C/O ratio of ~ 0.06 at/at. In a similar way FER6.8C can be represented as 6.8 wt% coke ('CH') and 93.2 wt% FER ('SiO_2'), which results in a C/O ratio of ~ 0.17 at/at. The theoretically obtained numbers agree very well with the experimentally observed ones obtained at 200 Å from the crystal edge. Regarding the fact that the size of the FER crystals under study is ~10000 Å (parallel to 10 MR) by ~4000 Å (parallel to 8 MR), it is obvious that the number for the bulk C/O ratio will be predominantly determined by the numbers detected at 200 Å from the crystal edge. For this reason, the higher C/O ratio's

detected at the crystal edges are of minor influence on the bulk C/O ratio of the crystal. The good agreement between theory and experiment indicates the sensitivity and validity of the STEM-EELS technique for establishing C/O ratio's as a function of their location on aged zeolite crystals.

From the above discussion some indication is obtained on the growth of the coke going from FER2.5C to FER6.8C. The addition of reactants and/or products to the carbonaceous species already present will mainly occur via alkylation of butenes to aromatic coke in the initial part of the micropores, as is confirmed by the layer present at the crystal edges. Part of the butenes probably migrates further down into the zeolite channels, increasing more slowly the overall C/O ratio inside the crystal. The above coke deposition process is further confirmed by figure 6, which demonstrates that the carbonaceous species located around the C/O maximum in the 10 MR channels are both aromatic and aliphatic in nature, while the coke located further inside the crystal have been transformed into polyaromatic species. The nature of the coke on FER6.8C as detected by STEM-EELS is in good agreement with results obtained by infrared spectroscopy, revealing the presence of alkyl-aromatic species [12,19,20]. However, infrared spectroscopy is a bulk technique while it is now demonstrated by STEM-EELS that the aromatic species with aliphatic groups present are predominantly located at the initial part of the 10 MR channels.

Conclusions

STEM-EELS measurements were performed on FER crystals aged during the skeletal isomerization of *n*-butene into isobutene. From this it is evident that carbonaceous species are deposited throughout the zeolite crystals. However, the carbon profile is not homogeneous, since at the entrances of the 8 MR pores a large accumulation of coke is observed. For the 10 MR channels also some enrichment by coke is detected at the pore entrances. At a higher coke content, the micropores are further filled by carbonaceous species and the 8 MR pores become fully blocked. The 10 MR channels on the other hand remain partially accessible for *n*-butene, with alkyl-aromatic species deposited near the inlets of these channels. For that reason it is concluded that the selective transformation of *n*-butene into isobutene will take place in the primary part of the 10 MR channels. Overall, it is demonstrated that STEM-EELS is a powerful characterization technique for studying the location, amount and nature of carbonaceous deposits in zeolite crystals.

Acknowledgements

Dr. Odile Stéphan (Paris-Sud University) is acknowledged for performing and discussing the STEM-EELS measurements. Dr. Frank de Groot (Utrecht University) is acknowledged for helpful discussion and interpretation of the STEM-EELS data.

References

1. C. Colliex, M. Tencé, E. Lefèvre, C. Mory, H. Gu, D. Bouchet and C. Jeanguillaume, Mikrochim. Acta 114/115 (1994) 71.
2. P. Gallezot, C. Leclercq, M. Guisnet and P. Magnoux, J. Catal. 114 (1988) 100.
3. P. Magnoux, P. Cartraud, S. Mignard and M. Guisnet, J. Catal. 106 (1987) 242.
4. H.G. Karge and E. Boldingh, Catal. Today 3 (1988) 379.
5. A. de Lucas, P. Canizares, A. Duran and A. Carrero, Appl. Catal. A Gen. 156 (1997) 299.
6. A.R. Pradhan, J.F. Wu, S.J. Jong, W.H. Chen, T.C. Tsai and S.B. Liu, Appl. Catal. A Gen. 159 (1997) 187.
7. H.S. Cerqueira, P. Magnoux, D. Martin and M. Guisnet, Stud. Surf. Sci. Catal. 126 (1999) 105.
8. R.E. Morris, S.J. Weigel, N.J. Henson, L.M. Bull, M.T. Janicke, B.F. Chmelka, and A.K. Cheetham, J. Am. Chem. Soc. 116 (1994) 11894.
9. P. Grandvallet, K.P. de Jong, H.H. Mooiweer, A.G.T.G. Kortbeek and B. Kraushaar-Czarnetzki, European Patent no. 501577 (1992) to Shell.
10. W-Q. Xu, Y-G. Yin, S.L. Suib and C-L. O'Young, J. Phys. Chem. 99 (1995) 758.
11. K.P. de Jong, H.H. Mooiweer, J.G. Buglass and P.K. Maarssen, Stud. Surf. Sci. Catal. 111 (1997) 127.
12. S. van Donk, E. Bus, A. Broersma, J.H. Bitter and K.P. de Jong, Appl. Catal. A Gen. 237 (2002) 149 / chapter 7 of this thesis.
13. F. Hershkowitz and P.D. Madiara, Ind. Eng. Chem. Res. 32 (1993) 2969.
14. D. Chen, A. Gronvold, H.P. Rebo, K. Moljord and A. Holmen, Appl. Catal. A Gen. 137 (1996) L1.
15. O. Stéphan, A. Gloter, D. Imhoff, M. Kociak, K. Suenaga, M. Tencé and C. Colliex, Surf. Rev. Lett. 7(4) (2000) 475.
16. Atlas of Zeolite Framework Types (Ch. Baerlocher, W.M. Meier and D.H. Olson, Eds.) 5th edition, Elsevier, Amsterdam (2001).
17. A.P. Hitchcock and D.C. Mancini, J. Electron Spectrosc. 67(1) (1994) 1.
18. L. Domokos, L. Lefferts, K. Seshan and J.A. Lercher, J. Mol. Catal. A Chem. 162 (2000) 147.
19. P. Andy, N.S. Gnep, M. Guisnet, E. Benazzi and C. Travers, J. Catal. 173 (1998) 322.
20. C. Pazè, B. Sazak, A. Zecchina and J. Dwyer, J. Phys. Chem. B 103 (1999) 9978.

10A

Summary and Concluding Remarks

Zeolites are crystalline microporous materials that are widely applied as catalysts in industries like oil refining, basic petrochemistry and fine chemistry. They exhibit unique properties with respect to both activity and selectivity. Activity is mostly determined by the zeolite Brønsted acid sites and by the active metal-phase that may be present in the zeolite micropores. Selectivity is often provided by the zeolite micropores that range in size from 3 Å to 12 Å. Besides the highly favorable role in providing shape selectivity, the presence of micropores in some cases limits the catalytic performance of zeolites. This is caused by the restricted molecular transport rate inside the zeolite crystal, induced by the similarity between the size of the involved hydrocarbons and the micropore diameter. Accordingly, the hydrocarbons are in close contact with the walls of the zeolite micropores and diffusion occurs relatively slow. In many cases the effective slow diffusion in zeolite crystals limits the reaction rate and selectivity. One of the most effective ways to minimize diffusion limitation in zeolites is the generation of mesopores in the zeolite crystals. In this way the length of the zeolite micropores is effectively shortened and the molecular accessibility is largely enhanced.

From the review in **chapter 2** it is clear that for some applications, like cracking of heavy oil fractions, cumene production, alkane hydroisomerization and more recently the synthesis of fine chemicals, the generation of mesopores in zeolite crystals is an effective way to alleviate diffusion limitation. The creation of mesopores can be established via several routes from which steaming and acid leaching are most commonly applied. Characterization of mesopores is often performed using nitrogen physisorption and electron microscopy. Recently, it was shown that electron

tomography, a form of three-dimensional transmission electron microscopy (3D-TEM) is able to reveal the three-dimensional shape, size and connectivity of the mesopores with great clarity. In order to determine the effect of mesopores on the transport properties of a zeolite catalyst, test reactions using probe molecules can be executed or alternatively one can monitor the rate of uptake using a microbalance. In **chapter 3**, the experimental background and operation of the Tapered Element Oscillating Microbalance (TEOM) is introduced. It is demonstrated that with the TEOM reliable adsorption and diffusion data are obtained, which are independent on the amount of sample and/or the applied flow rate. Moreover, by using a catalysis set-up involving a TEOM, the measurement of adsorption, diffusion and reaction can be combined in one method. In this way it is possible to effectively separate physical (transport) and chemical (acidity) effects. This is further exemplified in **chapter 4**, in which the effect of acid leaching of the zeolite mordenite on the hydroisomerization of *n*-hexane, an important reaction for improving the octane quality of gasoline, was studied. Uptake experiments under full catalytic conditions were performed in a TEOM. From these data, uptake and steady state diffusion coefficients for *n*-hexane in Pt/H-mordenite have been obtained by applying an adapted Fickian diffusion model. Using the Thiele theory, it was determined that both an increase of the intrinsic activity as well as an alleviation of intracrystalline diffusion limitation caused the overall activity increase for the acid leached Pt/H-mordenite. Since no noticeable difference between the steady state diffusion coefficients is observed, it is stated that the enhanced uptake after acid leaching predominantly arises from the shorter intracrystalline diffusion pathlength resulting from the mesoporous structure.

In **chapter 5** the TEOM was applied to examine the accessibility of the micropores in the one-dimensional zeolite mordenite. Using the adsorption and diffusion of hydrocarbons, a novel approach is presented to assess the pathlength for free access of hydrocarbons from the crystal surface into the micropores. The approach reveals a large discrepancy with the micropore volume probed by nitrogen physisorption. It is demonstrated that a small amount of extra-framework aluminum (EFAl) species present in the mordenite micropores induced a large decrease in the overall adsorption of *n*-hexane, while no change was observed with nitrogen physisorption. Moreover, by monitoring line scans in a Scanning Electron Microscope equipped with Energy Dispersive X-ray (EDX) analysis, the blocking effect of such EFAl species on the irreversible uptake of *n*-butene inside the mordenite micropores was visualized by a clear coke gradient over the crystal. After removal of the EFAl species by a mild oxalic acid treatment, the micropores were largely accessible to both *n*-hexane and *n*-butene, while nitrogen physisorption did not reveal any changes. Overall, it was confirmed that it is of key importance for catalysis and diffusion research that the accessibility of the zeolite micropore volume is verified using the appropriate probe molecule.

Over the last decade a growing demand for isobutene has provided large industrial and scientific interest for the skeletal isomerization of linear butenes to isobutene. Isobutene is used in the petrochemical industry for the production of *e.g.* polyisobutene, methacrolein, synthetic rubber and methyl-*tert*-butyl-ether (MTBE), which can be used as an octane enhancing fuel additive. In **chapter 6** of this thesis a comprehensive review on the different catalysts that have been applied for this reaction is presented. Amorphous and mesoporous catalysts are able to display high selectivities towards isobutene, although with longer times on stream they undergo severe deactivation. Zeolites containing 10-membered ring (MR) pores have proven to exhibit high selectivities for the butene skeletal isomerization. Especially the two-dimensional zeolite ferrierite, for which the 10 MR main channels are interconnected by 8 MR pores, shows a remarkably high selectivity and stability. The initial isobutene selectivity is rather poor, because non-selective dimerization-cracking reactions that run over Brønsted acid sites dominate the catalytic action on a fresh ferrierite. However, with longer times on stream exceptionally high selectivity is reached and a highly selective reaction pathway prevails, which coincides with the presence of carbonaceous deposits, or so-called 'coke'. The nature of the selective reaction pathway over aged ferrierite and the role of the carbonaceous deposits are still under debate. It has been suggested that a monomolecular reaction pathway is responsible for the selective isobutene production. However, the direct conversion of *n*-butene into isobutene over a naked Brønsted acid site involves the formation of an energetically and thermodynamically highly unfavorable primary carbenium ion. An alternative pathway, in which no primary carbenium intermediate is formed, has been proposed as well. This so-called pseudo-monomolecular reaction pathway should run over alkyl-aromatic tertiary carbenium ions prefixed in the coke.

The aim of the studies described in chapters 7, 8 and 9 of this thesis was to contribute to the understanding of the nature and location of carbonaceous deposits and the number, nature and location of the active sites for the skeletal isomerization of *n*-butene over aged and selective ferrierite. The employed research strategies and the obtained results were as follows:

- In **chapter 7**, the catalytic performance of ferrierite as a function of the amount of carbonaceous species deposited was evaluated in a catalysis set-up including a TEOM. It was demonstrated that large amounts of carbonaceous deposits are already present with short time on stream. Using *in situ* infrared (IR) spectroscopy it was shown that deposition of butenes lowers the total amount of Brønsted acid sites. Moreover, by deconvolution of the IR acid band, the number of vacant Brønsted acid sites at different locations in the ferrierite framework was established as a function of time on stream. This revealed that with initial *n*-butene reaction, the 8 MR channels are rapidly blocked and the accessible micropore volume and

Brønsted acid sites on the aged ferrierite will be primarily located inside the 10 MR channels. When a maximum amount of hydrocarbons was deposited on the catalyst, vacant Brønsted acid sites were still present. The coke band as monitored with IR spectroscopy showed that with time on stream the deposits were slowly converted from hydrogen-rich alkyl-aromatics into hydrogen-poor cyclopenta-fused-alkyl-aromatics.

- In **chapter 8**, aged ferrierite samples with different contents of coke were prepared and studied under differential catalytic conditions in a TEOM. Subsequently, these samples were examined using IR spectroscopy to probe the type and number of accessible sites with d_3-acetonitrile. From these results, it was possible to calculate the turn-over-frequencies for *n*-butene conversion and isobutene formation for both fresh and aged ferrierite catalysts. It was observed that the deposition of carbonaceous species significantly lowers the number of accessible Brønsted sites. Moreover, on the most selective and aged ferrierite no carbenium ions were detected, while Brønsted acid sites were still accessible for d_3-acetonitrile. This indicates that the latter sites will be responsible for the selective catalytic conversion of *n*-butene into isobutene.
- In **chapter 9**, Electron Energy-Loss Spectroscopy performed in a Scanning Transmission Electron Microscope (STEM-EELS) was applied on ferrierite crystals aged during the skeletal isomerization of *n*-butene into isobutene. In this way detailed spatial information was obtained concerning the amount and nature of carbonaceous deposits formed inside the zeolite crystals. From this it became evident that carbonaceous species are deposited throughout the zeolite crystals. However, the carbon concentration was not homogeneous, since at the 8 MR pore entrances a large accumulation of coke was observed. For the 10 MR channels also some enrichment by coke was detected at the pore entrances. At a higher coke content, further filling up of the complete micropore system occured and the 8 MR pores became fully blocked. The 10 MR channels were still partially accessible for *n*-butene, with alkyl-aromatic species deposited near the inlets of these channels.

The results in chapters 7, 8 and 9 support the view that the selective catalytic action over aged ferrierite takes place in the pore mouths of the 10 MR channels. Moreover, since on the aged and selective ferrierite some Brønsted acid sites were still accessible and at the same time no aromatic carbenium ions were detected, it is suggested that the selective conversion of *n*-butene into isobutene will run over Brønsted acid sites located in these 10 MR pore mouths.

10B

Samenvatting en Conclusies

Zeolieten zijn kristallijne en microporeuze materialen die veel worden toegepast als katalysatoren in de aardolie raffinage, basis petrochemie en fijnchemie. Ze bezitten uitzonderlijke eigenschappen met betrekking tot activiteit en selectiviteit. De activiteit wordt vooral bepaald door de Brønsted zure plaatsen en door de metaalfase die aanwezig kan zijn in de microporiën van het zeoliet. De selectiviteit wordt met name bepaald door de grootte van de microporiën, die kan variëren tussen de 3 Å en 12 Å. De microporiën hebben dus een positieve rol door vormselectiviteit te bewerkstelligen, maar ze kunnen soms ook de katalytische activiteit van het zeoliet begrenzen. Dit wordt veroorzaakt door het feit dat de betrokken koolwaterstoffen en de diameters van de microporiën ongeveer even groot zijn, waardoor de moleculaire bewegingssnelheid van de koolwaterstoffen in de zeoliet kristallen vaak laag is. De koolwaterstoffen staan dus in direct contact met de wanden van de microporiën en dit heeft tot gevolg dat de diffusie relatief traag verloopt. In veel gevallen zorgt de trage diffusie ervoor dat zowel de activiteit als de selectiviteit negatief beïnvloed worden. Eén van de beste manieren om diffusie-limitering te minimaliseren is het creëren van mesoporiën in de zeoliet kristallen. Op deze manier wordt de lengte van de microporiën verkort en de moleculaire toegankelijkheid vergroot.

Uit het overzicht gegeven in **hoofdstuk 2** wordt duidelijk dat voor sommige toepassingen, zoals het kraken van zware aardoliefracties, de productie van cumeen, de hydroisomerisatie van alkanen en sinds kort ook de synthese van fijnchemicaliën, het creëren van mesoporiën in zeoliet kristallen een effectieve manier is om de diffusie-limitering te verminderen. Er zijn verschillende routes om mesoporiën aan te brengen, waarvan stomen en wassen met een sterk zuur het meest worden toegepast. De karakterisering van de mesoporiën gebeurt veelal met behulp van stikstoffysisorptie en elektronen microscopie. Onlangs werd elektronen-tomografie, een vorm van driedimensionale transmissie elektronen microscopie (3D-TEM) toegepast. Hierdoor bleek het mogelijk om de driedimensionale vorm, afmeting en onderlinge verbondenheid van de mesoporiën waar te nemen. Om het effect van de mesoporiën op het transport in de zeoliet katalysator te bepalen, kunnen er enerzijds test-reacties met probe-moleculen uitgevoerd worden of anderzijds kan de snelheid van opname gemeten

worden met behulp van een microbalans. In **hoofdstuk 3** is de experimentele achtergrond en de werking van de Taps Element Oscillerende Microbalans (TEOM) geïntroduceerd. Daarnaast is aangetoond dat met de TEOM betrouwbare adsorptie- en diffusie-data kunnen worden gemeten, die onafhankelijk zijn van de hoeveelheid monster en/of de toegepaste gasstroomsnelheid. Wanneer de TEOM wordt toegepast in een katalyse opstelling is het mogelijk om adsorptie, diffusie en reactie tegelijk in één systeem te bepalen. Op deze manier kunnen fysische effecten (transport) en chemische effecten (zuurheid) van elkaar gescheiden worden. Dit wordt geïllustreerd met de studie beschreven in **hoofdstuk 4** naar het effect van een behandeling van mordeniet met sterk zuur op de hydroisomerisatie van *n*-hexaan, een belangrijke reactie voor het verhogen van het octaangetal van benzine. De opname van *n*-hexaan werd bepaald in een TEOM onder volledig katalytische condities. Vervolgens werden met behulp van een aangepast diffusie model gebaseerd op de tweede wet van Fick, zogenaamde 'uptake' en 'steady-state' diffusie-coëfficiënten voor *n*-hexaan in Pt/H-mordeniet bepaald. Door het Thiele-model toe te passen werd daarna vastgesteld dat de activiteitstoename voor het zuurbehandelde Pt/H-mordeniet zowel werd veroorzaakt door een stijging in de intrinsieke activiteit alsmede een afname van de intrakristallijne diffusie-limitering. Aangezien er geen verandering werd waargenomen tussen de 'steady-state' diffusie-coëfficiënten voor en na zuurbehandeling, wordt de snellere opname van *n*-hexaan na zuurbehandeling vooral veroorzaakt door de kortere diffusie weglengte die een gevolg is van de aanwezigheid van mesoporiën.

In **hoofdstuk 5** is de TEOM toegepast om de toegankelijkheid van de microporiën in het ééndimensionale zeoliet mordeniet te bepalen. Een nieuwe benadering werd gepresenteerd waar gebruik wordt gemaakt van de adsorptie en diffusie van koolwaterstoffen om zo de padlengte voor vrije toegang in het kristal van buiten naar binnen vast te stellen. De nieuwe benadering laat een groot verschil zien met het microporievolume dat bepaald wordt met stikstoffysisorptie. Een kleine hoeveelheid 'extra-framework' aluminum (EFAl) veroorzaakte namelijk een grote afname in de totale adsorptie van *n*-hexaan, terwijl met stikstoffysisorptie deze afname niet werd waargenomen. Daarnaast werd met behulp van het meten van lijnscans in een Scannende Elektronen Microscoop (SEM) uitgerust met Energie Dispersieve Röntgen-analyse (EDX), aangetoond dat dit EFAl een blokkerend effect had op de irreversibele opname van *n*-buteen. Er werd namelijk een duidelijke koolgradiënt over het kristal waargenomen. Na het verwijderen van het EFAl met een milde oxaalzuurbehandeling waren de microporiën volledig toegankelijk voor zowel *n*-hexaan als *n*-buteen, terwijl er geen veranderingen waren waargenomen met stikstoffysisorptie. De resultaten bevestigen dat het zeer belangrijk is voor katalyse- en diffusie-onderzoek om de toegankelijkheid van het zeoliet microporievolume te verifiëren met behulp van een geschikt probe-molecuul.

In het afgelopen decennium is er een groeiende vraag geweest naar isobuteen. Dit heeft ervoor gezorgd dat er veel interesse van zowel industriële als wetenschappelijke aard was voor de skelet-isomerisatie van lineaire butenen naar isobuteen. Isobuteen wordt toegepast in de petrochemische industrie als bouwsteen voor onder andere polyisobuteen, methacrolëine, synthetische rubbers en methyl-*tert*-butyl-ether (MTBE), dat toegevoegd kan worden aan benzine om het octaangetal en de verbranding te verbeteren. In **hoofdstuk 6** is een overzicht gegeven van de verschillende katalysatoren die zijn toegepast in buteen-isomerisatie. Amorfe en mesoporeuze katalysatoren bezitten soms een hoge selectiviteit naar isobuteen maar deactiveren snel. Zeolieten met 10 'membered ring' (MR) kanalen laten de hoogste selectiviteiten zien in de buteen skelet-isomerisatie. Met name het tweedimensionale zeoliet ferrieriet, waar de 10 MR kanalen onderling worden verbonden door 8 MR poriën laat een uitzonderlijk hoge selectiviteit en stabiliteit zien. De aanvankelijke selectiviteit is niet zo hoog als gevolg van niet-selectieve dimerisatie- en kraakreacties over de Brønsted zure plaatsen van het relatief schone ferrieriet. Echter, met toenemende reactietijd wordt er een zeer hoge selectiviteit bereikt en de katalyse wordt gedomineerd door een bijzonder selectief reactiepad dat samenvalt met de aanwezigheid van koolafzettingen, of kortweg 'kool'. Er is veel discussie gaande over de aard van het selectieve reactiepad over ingekoold ferrieriet en de rol van de koolafzetting. Zo is gesuggereerd dat een monomoleculair reactiepad verantwoordelijk zou zijn voor de selectieve vorming van isobuteen. Maar de directe omzetting van *n*-buteen naar isobuteen over een kale Brønsted zure plaats houdt in dat er een energetisch en thermodynamisch zeer ongunstig primair carbenium ion wordt gevormd. Daarnaast is er ook een alternatief reactie pad voorgesteld, waarin de vorming van het primair carbenium ion wordt vermeden. Dit zogenaamde pseudo-monomoleculaire reactiepad zou plaatsvinden over alkylaromatische carbenium ionen die aanwezig zouden zijn in de koolafzettingen.

Het doel van de studies die staan beschreven in de hoofdstukken 7, 8 en 9 van dit proefschrift is om inzicht te krijgen in de aard en locatie van de koolafzettingen en om de hoeveelheid, de aard en de locatie van de actieve plaatsen te bepalen voor de skelet-isomerisatie van *n*-buteen over ingekoold en selectief ferrieriet. Hierbij werd de hiernavolgende onderzoeksstrategie gevolgd met bijbehorende resultaten:

- In **hoofdstuk 7** werden de katalytische eigenschappen van ferrieriet als functie van de hoeveelheid kool geëvalueerd in een katalyse opstelling met een TEOM reactor. Daarbij werd duidelijk dat er al na korte reactietijd een grote hoeveelheid kool aanwezig is. Met behulp van *in situ* infrarood (IR) spectroscopie werd aangetoond dat de afzetting van kool het aantal Brønsted zure plaatsen vermindert. Bovendien werd door middel van deconvolutie van de betreffende IR-band, het aantal lege Brønsted plaatsen op verschillende posities in het ferrieriet-rooster als een functie van de reactietijd bepaald. Hiermee werd aangetoond dat de 8 MR poriën al na korte

reactietijd worden geblokkeerd en dat het toegankelijk microporievolume zich voornamelijk in de 10 MR kanalen bevindt. Op het moment dat de maximale hoeveelheid kool aanwezig is, zijn er nog steeds lege Brønsted plaatsen aanwezig. De koolband die met IR spectroscopie werd waargenomen, laat zien dat met toenemende reactietijd de kool langzaam van waterstof-rijke alkylaromaten in waterstof-arme cyclopentaan-gekoppelde alkylaromaten wordt omgezet.

- In **hoofdstuk 8** werden ferrieriet monsters met verschillende hoeveelheden kool gemaakt en onder differentiële katalyse condities bestudeerd in de TEOM. Vervolgens werden deze monsters onderzocht met IR spectroscopie om het aantal en het soort toegankelijke plaatsen te bepalen met d_3-acetonitril. Met behulp van deze resultaten werden de omzetfrequenties voor de conversie van *n*-buteen en de vorming van isobuteen op schone en ingekoolde ferrieriet katalysatoren bepaald. Het aantal toegankelijke Brønsted zure plaatsen werd aanzienlijk verminderd door de afzetting van kool. Daarnaast werden op de ingekoolde ferrieriet die het meest selectief was geen carbenium ionen gedetecteerd, terwijl een klein aantal Brønsted plaatsen nog steeds toegankelijk bleek te zijn voor d_3-acetonitril. Dit duidt erop dat de Brønsted zure plaatsen verantwoordelijk zijn voor de selectieve omzetting van *n*-buteen naar isobuteen.
- In **hoofdstuk 9** werd Elektronen 'Energy-Loss' Spectroscopie uitgevoerd in een Scannende Transmissie Elektronen Microscoop (STEM-EELS) op ferrieriet kristallen die waren ingekoold tijdens de skelet-isomerisatie van *n*-buteen naar isobuteen. Met STEM-EELS kan gedetailleerde ruimtelijke informatie verkregen worden met betrekking tot de hoeveelheid en aard van de koolafzetting aanwezig in de zeoliet kristallen. Hieruit werd duidelijk dat de kool overal in het kristal aanwezig was, maar dat de concentratie niet overal hetzelfde was. Bij de toegang tot de 8 MR poriën was een duidelijke ophoping van kool aanwezig, terwijl bij de ingangen van de 10 MR kanalen slechts een kleine ophoping van kool te zien was. Bij een hogere koolbelading vond er een verdere opvulling van het microporievolume plaats en de 8 MR poriën werden volledig geblokkeerd. In dit stadium zijn echter de 10 MR kanalen nog deels toegankelijk voor *n*-buteen, waarbij er alkylaromaten aanwezig zijn dichtbij de porie ingangen.

De resultaten van hoofdstuk 7, 8 en 9 bevestigen het beeld dat de selectieve katalyse over ingekoold ferrieriet hoofdzakelijk plaatsvindt in de poriemonden van de 10 MR kanalen. Bovendien, omdat er geen carbenium ionen zijn gedetecteerd maar er tegelijkertijd nog wel Brønsted zure plaatsen toegankelijk zijn, lijkt het duidelijk dat deze Brønsted plaatsen in de 10 MR poriemonden de selectieve omzetting van *n*-buteen naar isobuteen katalyseren.

List of Publications and Presentations

Publications:

- S. van Donk, J.H. Bitter and K.P. de Jong 'Deactivation of Solid Acid Catalysts for Butene Skeletal Isomerization: on the Beneficial and Harmful Effects of Carbonaceous Deposits'
  Applied Catalysis A: General 212 (2001) 97-116.
- S. van Donk, A. Broersma, O.L.J. Gijzeman, J.H. Bitter and K.P. de Jong 'Transient Uptake Measurements using an Oscillating Microbalance: Effect of Acid Leaching on the Diffusivity of *n*-Hexane in Pt/H-Mordenite'
  Studies in Surface Science and Catalysis 135 (2001) 3112-3120.
- S. van Donk, A. Broersma, O.L.J. Gijzeman, J.A. van Bokhoven, J.H. Bitter and K.P. de Jong 'Combined Diffusion, Adsorption and Reaction Studies of *n*-Hexane Hydroisomerization over Pt/H-Mordenite in an Oscillating Microbalance'
  Journal of Catalysis 204 (2001) 272-280.
- S. van Donk, E. Bus, A. Broersma, J.H. Bitter and K.P. de Jong 'Butene Skeletal Isomerization over H-Ferrierite: a TEOM and in Situ IR Study on the Role of Carbonaceous Deposits and the Location of Brønsted Acid Sites'
  Applied Catalysis A: General 237 (2002) 149-160.
- S. van Donk, E. Bus, A. Broersma, J.H. Bitter and K.P. de Jong 'Unraveling the Nature and Location of the Active Sites for Butene Skeletal Isomerization over Aged H-Ferrierite'
  Studies in Surface Science and Catalysis 142 (2002) 573-580.
- S. van Donk, E. Bus, A. Broersma, J.H. Bitter and K.P. de Jong 'Probing the Accessible Sites for *n*-Butene Skeletal Isomerization over Aged and Selective H-Ferrierite with d_3-Acetonitrile'
  Journal of Catalysis 212 (2002), in press.
- S. van Donk, A.H. Janssen, J.H. Bitter and K.P. de Jong 'Generation, Characterization and Impact of Mesopores in Zeolite Catalysts'
  Catalysis Reviews, submitted.
- J.H. Bitter, A.A. Battiston, S. van Donk, K.P. de Jong and D.C. Koningsberger 'Accessibility of the Iron Species in Fe/ZSM5 Prepared via $FeCl_3$ Sublimation'
  Microporous and Mesoporous Materials, submitted.
- **The work described in Chapter 5 and Chapter 9 will also be submitted for publication.**

Oral presentations:

- S. van Donk, A. Broersma, O.L.J. Gijzeman, J.H. Bitter and K.P. de Jong 'Combined Diffusion, Adsorption and Catalysis Studies: *n*-Hexane Hydroisomerization over Pt/H-Mordenite in a TEOM'
  TEOM PMA 1500 European User Meeting, Zeist, November 2000.
- S. van Donk, A. Broersma, O.L.J. Gijzeman, J.H. Bitter and K.P. de Jong 'Monitoring Diffusion, Adsorption and Reaction in an Oscillating Microbalance: n-Hexane Hydroisomerization over Pt/H-Mordenite'
  2nd Netherlands' Catalysis and Chemistry Conference, Noordwijkerhout, March 2001.
- S. van Donk, A. Broersma, O.L.J. Gijzeman, J.H. Bitter and K.P. de Jong '*In Situ* Monitoring of Diffusion in an Oscillating Microbalance: *n*-Hexane Hydroisomerization over Pt/H-Mordenite'
  17th North American Catalysis Society Meeting, Toronto Canada, June 2001.

- S. van Donk, A. Broersma, O.L.J. Gijzeman, J.H. Bitter and K.P. de Jong 'The Effect of Acid Leaching on the Hydroisomerization Activity of Pt/H-Mordenite: Combined Adsorption, Diffusion and Catalysis Studies in an Oscillating Microbalance'
  Europacat V, Limerick Ireland, September 2001.
- S. van Donk, E. Bus, A. Broersma, J.H. Bitter and K.P. de Jong 'Unraveling the Nature and Location of the Active Sites on Aged Zeolite Ferrierite using *in Situ* Infrared Spectroscopy'
  3rd Netherlands' Catalysis and Chemistry Conference, Noordwijkerhout, March 2002.
- J.H. Bitter, A.A. Battiston, S. van Donk, K.P. de Jong and D.C. Koningsberger 'Accessibility of the Binuclear Iron Species in Over-exchanged Fe/ZSM5 Prepared by Chemical Vapor Deposition of $FeCl_3$'
  Russian-Dutch Catalysis Meeting, Novosybirsk, Russia, June 2002.
- S. van Donk, E. Bus, A. Broersma, J.H. Bitter and K.P. de Jong 'Unraveling the Nature and Location of the Active Sites for Butene Skeletal Isomerization over Aged H-Ferrierite'
  2nd FEZA Conference, Taormina – Giardini Naxos, Italy, September 2002.
- S. van Donk, E. Bus, A. Broersma, J.H. Bitter and K.P. de Jong 'Unraveling the Nature and Location of the Active Sites for Butene Skeletal Isomerization over Aged H-Ferrierite'
  NRSCC Workshop – Probing Catalytic Events, Utrecht, October 2002.

Poster presentations:

- S. van Donk, A. Broersma, F.M.F. de Groot, J.H. Bitter and K.P. de Jong 'Reactive Adsorption of Butenes on Ferrierite Crystals Monitored by an Oscillating Microbalance and Electron Microscopy'
  1st Netherlands' Catalysis and Chemistry Conference, Lunteren, January 2000.
- S. van Donk, O. Stéphan, F.M.F. de Groot, J.H. Bitter and K.P. de Jong 'Electron Energy Loss Spectroscopy: Monitoring the Location, Amount and Nature of Carbonaceous Deposits on Zeolite Crystals'
  2nd Netherlands' Catalysis and Chemistry Conference, Noordwijkerhout, March 2001.
- S. van Donk, A. Broersma, O.L.J. Gijzeman, J.H. Bitter and K.P. de Jong 'Diffusion and Reaction of *n*-Hexane in Pt/H-Mordenite: Transient Uptake Measurements Using an Oscillating Microbalance'
  13th International Zeolite Conference, Montpellier France, July 2001.
- S. van Donk, O. Stéphan, F.M.F. de Groot, J.H. Bitter and K.P. de Jong 'Electron Energy Loss Spectroscopy: Monitoring the Location, Amount and Nature of Carbonaceous Deposits on Zeolite Crystals'
  13th International Zeolite Conference, Montpellier France, July 2001.
- S. van Donk, E. Bus, A. Broersma, J.H. Bitter and K.P. de Jong 'Determination of the Amount, Location and Nature of Active Sites for Butene Skeletal Isomerisation over Aged Zeolite Ferrierite'
  TOCAT 4, Tokyo Japan, July 2002.
- S. van Donk, O. Stéphan, F.M.F. de Groot, J.H. Bitter and K.P. de Jong 'Resolving the Location, Amount and Nature of Carbonaceous Species Deposited on Zeolite Crystals Using STEM-EELS'
  TOCAT 4, Tokyo Japan, July 2002.
- J.H. Bitter, A.A. Battiston, S. van Donk, K.P. de Jong and D.C. Koningsberger 'Accessibility of the Iron Species in Fe/ZSM5 Prepared via $FeCl_3$ Sublimation'
  2nd FEZA Conference, Taormina – Giardini Naxos, Italy, September 2002.

Dankwoord

Promoveren: 4 jaar onderzoek doen – 4 jaar leren. Het eindresultaat is hier en ik ben er best trots op. Uiteraard heb ik de nodige hulp gehad en nu is het moment daar om diegenen te bedanken die op wetenschappelijke en/of vriendschappelijke wijze hun bijdragen hebben geleverd.

Krijn, mijn promotor, toen ik je eens op een congres vroeg of je het naar je zin had, antwoordde je: "Ach het congres vind ik tot nu toe niet zo bijzonder, maar ik geniet met name als ik jullie hier bezig zie jullie werk te presenteren." Dat typeert exact jouw enthousiasme en betrokkenheid, en daarmee heb je mij altijd enorm weten te motiveren. Ik heb ontzettend veel van je geleerd en vond het heel leuk om samen met jou mijn promotieonderzoek vorm te geven.

Harry, copromotor, onze discussies 's ochtends vroeg bij de koffie en 's middags bij de thee hebben veel bijgedragen aan de interpretatie van de verschillende resultaten en een leuke werk atmosfeer. Thanks Dr. B.!

Fred, TEOMetgezel, met jouw technisch vernuft heb je me heel wat werk uit handen genomen en er voor gezorgd dat ik veel mooie metingen heb kunnen doen. Bovendien heb ik me altijd zeer vermaakt tijdens alle meetuurtjes op jouw domein. Dank je wel!

Zeer belangrijk in dit proefschrift zijn de bijdrages van de studenten die met mij hebben gewerkt. Eveline, jij bent de hoofdvakstudente die elke AiO zich wenst! Heel veel dank voor alle mooie IR metingen waaruit hoofdstuk 7 en 8 zijn voortgekomen; succes met jouw promotie in Zürich en ik wens je een net zo goede student toe als jij voor mij was. Henk Jan, bedankt voor het geploeter om die ferrierieten kapot te krijgen, helaas zonder succes. Misschien ben je gewoon te rustig en te vriendelijk voor zulk grof werk...? Maar in hoofdstuk 3 zul je zien dat het silyleren wel lijkt gelukt. Arjan, jij hebt mordeniet onder handen genomen en daarmee de basis gelegd voor hoofdstuk 5, bedankt. Patrick en Armanda, dank jullie wel voor het schrijven van jullie informatieve scripties.

De resultaten in dit proefschrift zijn het gevolg van veel mooie metingen die ik gelukkig niet allemaal zelf heb hoeven doen. John, hartelijk dank voor alle stikstof fysisorptie metingen en compu-care. Helaas ben je er niet meer, maar jouw enthousiasme zal me altijd bij blijven. Ad M., ook jij hebt heel wat fysisorptie metingen voor mij gedaan, waarvoor dank. Odile, merci infiniment pour les formidables mesures STEM-EELS qui ont conduit au chapitre 9. Marjan, dank je voor het SEMmen met als hoogtepunt het werk in hoofdstuk 5! An, voor hoofdstuk 5 heb jij de mordeniet stalen gesynthetiseerd en daarnaast de ICP-AES en NMR metingen mogelijk gemaakt, heel veel dank daarvoor.

Ook heb ik regelmatig gebruik mogen maken van de kennis en wijze raad van mensen die al iets langer 'in het vak' zitten. Onno, dank voor het beschikbaar stellen van jouw wiskundig brein en het maken van 'Zeo-diff' waardoor de interpretatie van de uptake-data een stuk makkelijker werd. Frank, hartelijk dank voor het mogelijk maken van de STEM-EELS metingen en het helpen interpreteren van de resultaten. Jeroen, jij was altijd geïnteresseerd in mijn werk en ik vond het leuk en leerzaam om dat met jou te bespreken,

veel succes in Zürich! Tom, dank je wel voor de wijze infrarood-raad en natuurlijk ook het beschikbaar stellen van je tuin voor de meest sfeervolle BBQ van de afgelopen jaren! Ook wil ik op deze plaats Michiel, Moniek, Marjolein en Ries bedanken voor hun hulp bij de speurtocht naar foutjes in het manuscript van dit proefschrift.

Dan kom ik nu langzaam toe aan het minder wetenschappelijk gedeelte van dit dankwoord. Als eerste mijn kamergenoten Andrea en Moniek, dank jullie wel voor veel gezelligheid, koffie & thee! Alle andere (EX)collega's en met name Mikey-Mike, Jan de B..man, Moniek (je bent een lieverd!), Marije (redheaded woman), Rosmans, Julio (dit jaar is het weer mijn beurt met de Teammaster!), Review-Ries, Marjolein en Harry: heel erg bedankt voor de gezelligheid bij koffie- en lunchpauzes, BBQ's, kerstdiners, Long Island Ice Tea's, etentjes, feestjes en congresbezoeken. Vanzelfsprekend kan ik hier de heldenprestatie met de Gouden Generatie niet onvermeld laten, daar kan het Oranje van nu nog wat van leren! Op het secretariaat was het ook altijd gezellig, dank jullie wel Dymph en Monique, en nu maar hopen dat ik opgevolgd word door die stoere blonde viking?!

En jawel, nu ben ik echt aangeland bij het niet wetenschappelijke gedeelte van dit dankwoord. Want om goed te kunnen werken is ontspanning van levensgroot belang! Het leven buiten de vakgroep is daarom altijd ontzettend belangrijk voor mij geweest en ik wil dan ook alle Vriendjes & Vriendinnetjes bedanken voor de vele leuke en gezellige etentjes, weekendjes, Poort-avonden, terrasbezoekjes, concertjes, schilderavonden, Balgevoel-momenten, oud & nieuw-, sinterklaas- en andersoortige feestjes. Zonder jullie zou mijn leven er de afgelopen 4 jaar een stuk saaier uit hebben gezien!

Iel, paranimfomaan, jij bent een fantastische vriendin! Dank je wel voor je trouwe vriendschap, gezelligheid en oprechtheid. Ook al zijn we het misschien niet steevast eens, ik hecht altijd zeer veel waarde aan jouw oordeel!

Mike, paranimf, jij bent een vriend uit duizenden! We hebben al veel samen meegemaakt: van spruitjes tot Spanje, van studeren tot promoveren, van oranje pannenkoeken tot tennis en nog veel meer. Dank je wel voor je jarenlange vriendschap en je telkens weer verrassend nuchtere kijk op zaken!

Papa, ik vind het moeilijk om vanaf deze plaats de juiste woorden te vinden, maar ik hoop vooral dat je beseft hoe belangrijk je voor me bent.

Lieve Oma, ik weet dat het leven zonder Opa een stuk minder leuk is, maar ik vind het heel fijn dat jij er nog steeds bent – je bent een schat! Opa, ik denk vaak aan je, bedankt voor het overdragen van het 'chemie-gen' en ik hoop dat je de oranje omslag mooi vindt...

Mam, Hen (thanx voor de hulp bij de omslag!), Nannie, Jopie en Ruth, het is in de afgelopen jaren heel fijn geweest om thuis te komen en steeds zoveel gezelligheid te vinden. Jullie zijn er altijd voor mij en dat is van onschatbare waarde, dank je en ik hou van jullie!

Anne, ma jolie chérie, tu es la meilleure chose qui me soit jamais arrivée, et avec la fin de nos doctorats, le moment de vivre ensemble en un seul et même endroit (au lieu d'être séparés de 1099.3 km!) est enfin venu. Notre premier rêve est devenu réalité, ma princesse! Et maintenant, allons ensemble vers notre futur fait d'amour...

Sander xx

Curriculum Vitae

Sander van Donk werd op 28 oktober 1973 geboren te Hillegom. In 1993 behaalde hij het VWO diploma aan het Stedelijk Gymnasium te Haarlem. In september van datzelfde jaar begon hij met de studie scheikunde aan de Universiteit Utrecht, waar hij in 1994 zijn propedeuse diploma met genoegen behaalde. In 1998 studeerde hij af met genoegen, na universitaire stages bij de secties Gecondenseerde Materie (Prof. A. Meijerink) en Anorganische Chemie & Katalyse (Prof. D.C. Koningsberger) en een bedrijfsstage bij Engelhard in de Meern.

Vanaf 1999 was hij werkzaam als Onderzoeker in Opleiding bij Prof. K.P. de Jong en Dr. J.H. Bitter in de sectie Anorganische Chemie & Katalyse van de Universiteit Utrecht. Het promotieonderzoek heeft geleid tot het proefschrift dat u nu in handen heeft. Tijdens deze promotietijd kreeg hij in september 2001 een prijs toegekend door Akzo Nobel Catalysts, en in maart 2002 ontving hij de NRSCC prijs voor de beste presentatie op de 'Netherlands Catalysis and Chemistry Conference'. Per 1 januari 2003 zal hij in dienst treden als 'research chemist' bij Akzo Nobel Catalysts te Amsterdam.

Sander van Donk was born on the 28th of October 1973 in Hillegom. In 1993 he received his diploma of the Secondary Grammar School 'Stedelijk Gymnasium' in Haarlem. In September of that year he started with his chemistry studies at Utrecht University and in 1994 he passed his propadeutic degree with credit. In 1998 he obtained his master's degree with credit after university traineeships at the departments of Condensed Matter (Prof. A. Meijerink) and Inorganic Chemistry & Catalysis (Prof. D.C. Koningsberger) and an industrial traineeship at Engelhard in de Meern.

Since 1999 he has worked as a PhD-student under the supervision of Prof. K.P. de Jong and Dr. J.H. Bitter in the department of Inorganic Chemistry & Catalysis at Utrecht University. The PhD-research resulted in the thesis that you hold at this very moment. During his PhD research Akzo Nobel Catalysts awarded him a prize in September 2001, and in March 2002 he received the NRSCC prize for the best presentation at the 'Netherlands Catalysis and Chemistry Conference'. Starting January 1st 2003, he will work as a research chemist with Akzo Nobel Catalysts in Amsterdam.